ANNALES
UNIVERSITATIS SCIENTIARUM BUDAPESTINENSIS DE ROLANDO EÖTVÖS NOMINATAE

SECTIO GEOLOGICA

TOMUS XXII.
1980

REDIGUNT
B. GÉCZY
J. KISS
L. STEGENA

BUDAPEST
1980

ANNALES
UNIVERSITATIS SCIENTIARUM BUDAPESTINENSIS DE ROLANDO EÖTVÖS NOMINATAE

SECTIO BIOLOGICA
incepit anno MCMLVII

SECTIO CHIMICA
incepit anno MCMLIX

SECTIO GEOLOGICA
incepit anno MCMLVII

SECTIO GEOGRAPHICA
incepit anno MCMLXV

SECTIO HISTORICA
incepit anno MCMLVII

SECTIO IURIDICA
incepit anno MCMLIX

SECTIO LINGUISTICA
incepit anno MCMLXIX

SECTIO MATHEMATICA
incepit anno MCMLVIII

SECTIO PAEDAGOGICA ET PSYCHOLOGICA
incepit anno MCMLXX

SECTIO PHILOLOGICA
incepit anno MCMLVII

SECTIO PHILOSOPHICA ET SOCIOLOGICA
incepit anno MCMLXII

THE TRACE ELEMENTS AND THE CONTROLLING PETROLOGICAL – MINERALOGICAL FACTORS IN THE SEDIMENTARY ROCKS OF THE NORTHERN AND NORTHEASTERN CSERHÁT MOUNTAINS

ANDÓ J.

Petrological – Geochemical Department Eötvös Loránd University
H – 1088 Budapest, Múzeum krt. 4/A

Received 2 June 1980

SUMMARY

Sedimentological units, relatively homogenous formations can be identified in the surficial Tertiary detrital sediments in the northern and eastern parts of the Cserhát by lithostratigraphic mapping and reconstruction of the environmental factors of sedimentation (Andó, 1973, 1975). The mean values of different trace element contents in these units, as well as weighted averages for the surficial formations of this region have been determined. Affinity factors were calculated by comparing the respective trace element content to the abundance of each lithological units in the surface exposures. These factors reflect the favourable enrichments of the different trace elements in the lithological units. It is illustrated, that the average trace element content of the region is lower than those typical for the sedimentary rocks. The samples were separated by several methods (i. e. to light and heavy mineral fractions, according their magnetic susceptiblity, grain size), and these fractions were assayed. The results were evaluated by comparing them to the clay mineral types and $CaCO_3$ contents of the respective samples and the local trace element enrichments. The anomalies have mostly been proved to be absorptive rather than detrital enrichments.

Regional geology

The main features of the geology of NNE-Cserhát Mountains is presented here in order to give the necessary geological background for the geochemical data and the methods applied.

A Tertiary basin has been developed between the Veporides and the Gemerides, and was filled by Paleogene and Neogene sediments. This basin has been subdivided into different parts by later tectonic and magmatic events as well as surface erosion. These parts now belong to the Börzsöny, Cserhát and Mátra mountains. The Upper Oligocene psammitic sediments on the surface in the NNW-Cserhát underlie the volcanic pile of the Börzsöny Mts on the eastern margins, maintaining the same bedding directions. Good correlation exists between the corresponding igneous and sedimentary rocks of the eastern Cserhát and the western Mátra Mountains.

Upper Oligocene – Lower Miocene sediments, subvolcanic andesite dikes are found on the surface of the emerged, eroded western, northern and central parts of the Cserhát. The eastern, southeastern parts are in subsided position and characterised by younger, Middle-Upper Miocene and Pliocene sediments and Upper Miocene strato-volcanic series.

Drill hole data from the peripheries have revealed that the subsidence of the metamorphic basement and the beginning of the marine sedimenta-

LITHOSTRATIGRAPHIC MAP OF THE NORTHERN AND EASTERN CSERHÁT MOUNTAINS

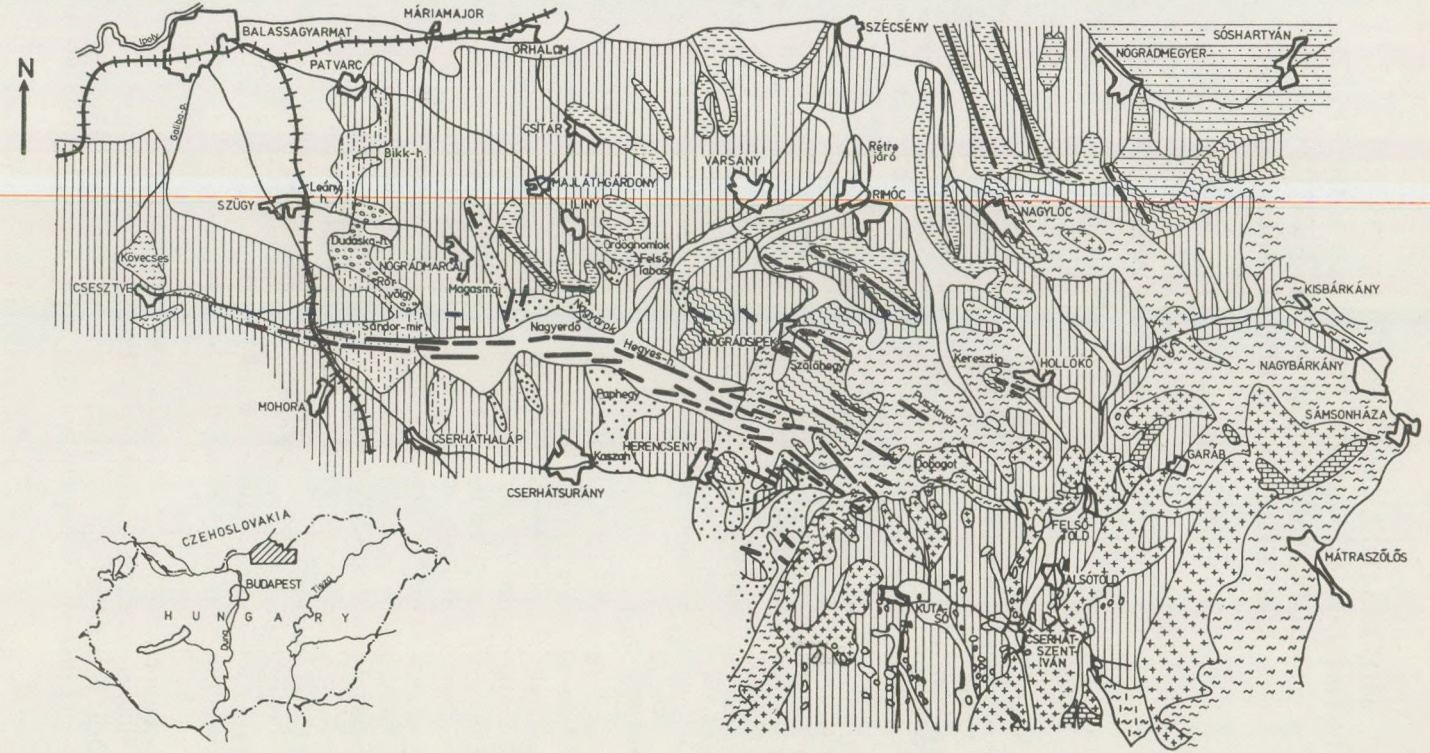

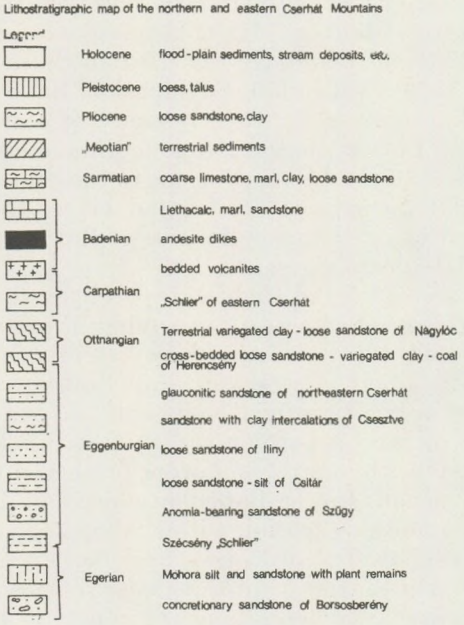
Lithostratigraphic map of the northern and eastern Cserhát Mountains
Legend
Holocene
flood-plain sediments, stream deposits, etc.
Pleistocene
loess, talus
Pliocene
loose sandstone, clay
„Meotian"
terrestrial sediments
Sarmatian
coarse limestone, marl, clay, loose sandstone
Lithacalc, marl, sandstone
Badenian
andesite dikes
bedded volcanites
Carpathian
„Schlier" of eastern Cserhát
Ottnangian
Terrestrial variegated clay - loose sandstone of Nagyłóc
cross-bedded loose sandstone - variegated clay - coal of Herencsény
glauconitic sandstone of northeastern Cserhát
sandstone with clay intercalations of Csesztve
Eggenburgian
loose sandstone of Iliny
loose sandstone - silt of Csitár
Anomia-bearing sandstone of Szügy
Szécsény „Schlier"
Egerian
Mohora silt and sandstone with plant remains
concretionary sandstone of Borsosberény

Fig. 1.

tion started in the Middle Oligocene. Thickness data of the Middle Oligocene sequence (Kiscelli Agyag) of alternating claystone, clay – marl, silty clay – marl represent the eastward deepening of the Paleogene catchment basin. These sediments are not exposed on the surface.

Lithoral, shallow bathyal conditions have been developed in the Upper Oligocene – Lower Miocene periods, with abundant lateral facies changes. The inherited relief of the basin-floor, however, predetermined the facies relationships of the contemporaneous sediments. Complete off-shore detrital Oligocene – Lower Miocene series was formed in the ENE parts of the Cserhát. The Upper Oligocene deltaic – shoreline sedimentation in the western areas was followed by intense uplifting and the development of terrestrial conditions. The boundary between the Upper Oligocene (Egerian) and Lower Miocene (Eggenburgian) stages – similarly to the Middle-Upper Oligocene boundary – is hard to define in the continuous sequences (*Báldi* 1973). Stratigraphic evaluations have shown that the western areas were characterised by easterly trending regression in the uppermost Oligocene and Lower Miocene, while marine sedimentation was maintained up to the end of the Lower Miocene in the eastern region.

The terrestrial formations (variegated clays, fluvial sands, gravel, rhyolite tuffs) indicating the completeness of this regression are found in thin layers in isolated exposures.

East of the area (Nógrád coal-field) paralic coal-measures have been formed in significant thicknesses, overlying the terrestrial sediments. In the NNE-Cserhát this formation is represented in reduced thickness, with gradual wedging-out in westward direction (Ottnangian stage). The coal measures and/or the terrestrial sediments are covered by the silt-clay marine sequence of the Carpathian stage. These rocks have been completely eroded away in the north, but were preserved in the eastern parts beneath the Carpathian, Lower Badenian volcanics. Interarc basins have formed in the post-volcanic period, with shallow marine limestones (Lajta Limestone) and shallow bathyal clays and marls, in the Badenian and Sarmatian stages. The marine sediments were replaced by lake, lacustrine and deltaic detrital, clayey deposits in the course of the general uplifting at the end of the Sarmatian stage.

Brackish water environment, embayed lacustrine conditions were developed in the Pannonian stage extending to the line of the Pásztó and Alsótold basins, as result of the renewed marine transgression, with pelitic, clay marl sediments.

As it is seen from this description, Upper Oligocene – Lower Miocene, less frequently Middle Miocene detrital sediments are exposed on the surface in the NNE-Cserhát (Fig. 1).

The trace element distribution in the lithological units

The geochemical investigations were preceded by lithostratigraphic mapping and detailed sedimentological analyses. Sedimentological types, representing larger regions, have been determined. The methods, and some of the results have already been discussed earlier (*Andó*, 1973, 1975).

Thus only a brief summary of the petrological characteristics and facies recoonstrucion is presented here (Table 1).

The lithostratigraphic units are genetically uniform and relatively homogenous as far as their lithology and geochemistry is concerned. Thus the average trace element content for each unit were initially determined (Table 2.).

Assaying has been made by emission spectral analysis method using a Q – 24 type quartz-spectrograph. The semi-quantitative evaluation was carried out by means of concentration vs. intensity scales – the so-called spd or Y-scales. The method was decribed in details by Ms. *Nagy – Balogh* J. (1971). The principle of the processing and interpretation of the approximately 550 assays were similar to that of our earlier investigations (*Andó* 1973).

Systematic, but generally moderate differences have been found amongst the trace element contents of the different formations. However, the comparison of these differences with published data should be dealt with caution. In order to establish a realistic basis for comparison, a summarised mean value for all of the surface rocks of the studied area was calculated, from the individual average values of each units. Since the abundances of the rock types in surface exposures are different, and their continuation towards the depth is virtually unknown, the trace element averages in the calculations of the summarised mean values were weighted by the surface areal abundance of rock types.

In principle the application of such a calculation is verified by the fact that the increasing grain size of the detrital sediments shows linear and reversed correlation with their specific gravity and porosity values, respectively. Since these effects mutually eliminate each other, the unit weight of the natural detrital sediments is more or less uniform, 2.3 – 2.5 g/cm^3. Therefore, in these rocks the relationship between the mass and volume is approximately constant, and the volume can be considered as adequate weighting factor in the calculations of average trace element contents. Since the actual volumes of the litho-stratigraphic units are unknown, this parameter is replaced by their surface abundance. In this way the weighted averages of trace element contents of the surface rock types in the northern and eastern Cserhát areas were calculated. The surface abundances were determined from lithostratigraphic maps (Fig. 1.).

The soils were excluded from sampling since the thin soil cover is generally weathered and reworked, and their trace element content do not represent the underlying bedrocks.

Vinogradov's (1962) data for average trace element contents of the sedimentary rocks were used for comparisons (Table 2, rows 20 – 21.). These data were also derived from detrital sediments, hence provided a reliable basis for the evaluations. The comparative evaluations revealed, that only the silver shows significant enrichment (d = 31), the concentrations of the other elements are in reasonable agreement with the sedimentary average values of the Earth's crust, with enrichment factors ranging from 0.3 to 1.5. From those elemets, which have shown enrichment,

Table 1.

The main characteristics of the surficial sedimentary formations of the Northern, and Northeastern Cserhát

Formation	Lithological character	Age	Environment of deposition
Borsosberény concretion sandstone	coarse to medium grained pebbly soft sandstone with concretions and fossiliferous bands	Upper Oligocene (Egerian)	deltaic lithoral
Mohora silty sandstone with plant fossils	fine grained silty sandstone with plant fossils (overlain by the Szügy standstone)	Egerian	fore-deltaic deltaic, lagunar
Szécsény "slir" formation	Calcareous siltstone, clayey and sandy siltstone	Egerian-Eggenburgian	deep sublithoral to shallow sublithoral
Szügy sandstone with Anomias	Medium to coarse grained sandstone, fine grained siltstone, pebbly, cross-bedded sandstone	Eggenburgian	shallow sublithoral to lithoral
Csitár loose sandstone and siltstone	Pebbly sandstone, coarse to medium grained with Ostreas, siltstone and pebble intercalations (on top of the Szécsény "slir")	Eggenburgian	lithoral – shallow sublithoral
Iliny loose sandstone	Fine grained loose sandstone, siltstone (overlying the Szécsény "slir")	Eggenburgian	shallow to medium sublithoral
Csesztve sandstone with intercalated clays	Fine to coarse grained sandstone, occasionally crossbedded, with clay intercalations	Eggenburgian	shallow sublithoral
NE Cserhát glauconitic sandstone	Fine to coarse grained loose sandstone	Eggenburgian	shallow sublithoral
Herencsény sandstone-variegrated clay	Coarse grained crossbedded and gray loose or massive sandstone, silty sandstone	Ottnangian	deltaic, lithoral, terrestrial
Nagylóc sandstone-variegated clay			
Garáb "slir" formation	Clay and sandy calcareous sandstone	Carpathian (Middle Miocene)	medium to deep sublithoral

Trace elements of sedimentary formations cropping out in the Northern and Eastern Cserhát area

		r		Co	Ni	Cu	Ag	Zn	Ga	Sn	Pb	V	Cr	Mn	Ti	Mo	Li	Be	Ba	Sr	B
1	Borsosberény concreation sandstone	1,1	a	10,0	14,5	14,5	0	50,0	7,3	0	24,0	10,8	60,8	685,0	3200,0	0	0	0	295,0	135,0	11,0
			b	0,6	0,5	0,5		0,5	0,7		1,6	0,3	1,0	1,0	1,7				0,8	0,4	0,4
			c	0,5	0,4	0,4		0,4	0,6		1,5	0,2	0,9	0,9	1,6				0,7	0,4	0,4
2	Mohora slity sandstone with plant fossils	2,6	a	26.0	62,0	16,0	0	100,0	8,0	0	9,0	61,0	97,0	533,0	5943,0	0	0	0	460,0	226,0	16,0
			b	3,8	4,7	1,3		2,2	1,7		1,4	3,0	3,8	1,8	7,6				3,0	1,7	1,4
			c	1,5	1,8	0,5		0,8	0,6		0,5	1,2	1,5	0,7	2,9				1,1	0,6	0,6
3	Szécsény "slir" formation	5,4	a	20,0	55,0	46,0	0	98,0	14,0	3,6	15,0	109,0	103,0	448,0	4670,0	3,3	0	0	683,0	434,0	36,0
			b	6,0	8,7	7,5		4,5	1,1	5,4	4,9	12,3	8,4	3,1	4,7	5,9			9,2	6,7	6,8
			c	1,1	1,6	1,4		0,8	11,9	1,0	0,9	2,3	1,6	0,6	0,9	1,1			1,7	1,2	1,3
4	Szügy sandstone with Anomias	1,7	a	8,2	16,0	15,0	0	16,0	4,9	8,2	9,3	25,0	53,0	419,0	1071,0	4,2	0	0	336,0	271,0	31,0
			b	0,8	0,8	0,8		0,2	0,7	3,9	1,0	0,9	1,4	0,9	0,9	2,4			1,4	1,3	1,8
			c	0,5	0,5	0,5		0,1	0,4	2,3	0,6	0,6	0,8	0,6	0,6	1,4			0,8	0,8	1,1
5	Csitár loose sandstone and silstone	0,6	a	4,2	34,0	12,0	0	49,0	7,5	0	13,0	79,0	77,0	990,0	3750,0	0	0	0	340,0	280,0	39,0
			b	0,1	0,6	0,2		0,3	0,4		0,5	1,0	0,7	0,8	1,1				0,5	0,5	0,8
			c	0,2	1,0	0,4		0,4	0,6		0,8	1,6	1,1	1,2	1,8				0,8	0,8	1,3
6	Iliny loose sandstone	0,9	a	15,0	38,0	40,0	0	93,0	16,0	3,1	13,0	114,0	67,0	726,0	2709,0	2,9	0	0	601,0	295,0	28,0
			b	0,9	1,0	1,1		0,7	1.2	0,8	0,7	2,1	0,9	0,8	1,2	0,9			1,3	0,8	0,9
			c	0,8	1,1	1,2		0,8	1,3	0,8	0,8	2,4	1,0	0,9	1,3	1,0			1,5	0,8	1,0
7	Csesztve sandstone with intercalated clays	1.1	a	18,0	24,0	55,0	0	104,0	11,0	3,8	16,0	21,0	62,0	1030,0	1809,0	0	0	0	295,0	168,0	38,0
			b	1,1	0,8	1,8		1,0	1.0	1,2	1,1	0,5	1,0	1,4	1,0				0,8	0,5	1,5
			c	1.7	0.7	1.0		0,9	0,9	1,0	1,0	0,4	0,9	1,3	0,9				0,7	0,5	1,3
8	NE Cserhát glauconitic sandstone	17,2	a	21.0	29.0	18.0	17.0	212,0	20,0	6,0	12,0	23,0	37,0	1215,0	2260,0	3,4	166,0	0	394,0	318,0	12,0
			b	20,2	14,6	9,4	94,2	31,0	27,9	28,4	12,6	8,2	9,6	26,6	19,2	19,4	40,1		16,8	15,7	7,2
			c	1,2	0,8	0,5	5,5	2,8	1,6	1,7	0,7	0,5	0,6	1,5	1,1	1,1	2,3		1,0	0,9	0,4
9	Nagylóc sandstone – variegated clay	0,5	a	23,0	80,0	40,0	0	130,0	15,0	8,0	104,0	74,0	70,0	1600,0	3505,0	0,5	0	260,0	730,0	590,0	48,0
			b	0,6	1,2	0,6		0,6	0,6	1,1	3,2	0,8	0,5	1,0	0,9	0,1		29,2	0,2	0,9	0,8
			c	1,3	2,3	1,2		1,4	1,2	2,2	6,4	1,5	1,0	2,0	1,7	0,1		58,3	1,8	1,7	1,6
10	Herencsény sandstone – variegrated clay	0,6	a	15,0	25,0	24,0	0,2	80,0	11,0	4,3	16,0	21,0	50,0	496,0	1518,0	0,8	55,0	14,0	302,0	127,0	38,0
			b	0,5	0,4	0,4	0,04	0,4	0,5	0,7	8,6	0,3	0,5	0,4	0,5	0,2	0,5	1,6	0,4	0,2	0,8
			c	0,8	0,7	0,7	0,1	0,7	0,9	1,2	1,0	0,4	0,7	0,6	0,7	0,2	0,8	2,6	0,7	0,4	1,3
11	Garáb "slir" formation	19,4	a	19,0	45,0	47,0	0,12	119,0	16,0	4,0	15,0	87,0	78,0	491,0	3330,0	4,3	24,0	3,6	584,0	675,0	49,0
			b	20,6	25,4	27,6	0,8	19,6	25,2	21,4	17,8	35,2	22,8	12,1	3,2	27,7	6,5	15,7	28,1	37,6	33,1
			c	1,1	1,3	1,4	0,03	1,0	1,3	1,1	0,9	1,8	1,2	0,6	0,2	1,4	0,3	0,8	1,4	1,9	1,7
12	Lajta limestone and sandstone	1,8	a	16,0	12,0	27,0	0,8	60,0	6,0	0	6,0	26,0	19,0	2900,0	825,0	9,0	0	0	299,0	1152,0	14,0
			b	1,6	0,6	1,5	0,5	0,9	0,9		0,7	1,0	0,5	6,6	0,7	5,3			1,3	5,9	0,9
			c	0,9	0,3	0,8	0,2	0,5	0,5		0,4	0,5	0,3	3,7	0,4	2,9			0,7	3,3	0,5
13	Badenian marl and siltstone	0,4	a	15,0	45,0	37,0	1,2	10,9	16,0	2,4	16,0	78,0	70,0	597,0	2000,0	102,0	0	0	686,0	2438,0	40,0
			b	0,3	0,5	0,5	0,2	0,4	0,5	0,3	0,4	0,7	0,4	0,3	0,4	13,6			0,7	2,8	0,6
			c	0,8	1,3	1,1	0,4	0,9	1,3	0,6	1,0	1,6	1,0	0,7	1,0	3,4			1,7	6,9	1,4
14	Sarmatian fossiliferous limestone	0,7	a	10,0	17,0	30,0	0,9	56,0	8,0	5,6	11,0	16,0	19,0	5387,0	343,0	0	0	0	408,0	1357,0	29,0
			b	0,4	0,4	0,6	0,2	0,3	0,5	1,1	0,5	0,2	0,2	4,8	0,1				0,8	2,7	0,7
			c	0,6	0,5	0,9	0,3	0,5	0,6	1,5	0,7	0,3	0,3	6,8	0,2				1,0	3,9	1,0
15	Sarmatian clay and marl	0,6	a	14,0	28,0	24,0	0,7	103,0	13,0	2,4	12,0	60,0	64,0	441,0	1778,0	4,7	0	0	312,0	600,0	35,0
			b	0,5	0,5	0,4	0,1	0,5	0,6	0,4	0,4	0,8	0,6	0,3	0,5	0,9	0	0	0,5	1,0	0,7
			c	0,8	0,8	0,7	0,2	0,9	1,0	0,7	0,7	1,2	1,0	0,6	0,9	1,6			0,8	1,7	1,2
16	Pannonian sediments	0,2	a	12,0	35,0	28,0	0,6	100,0	5,0	0	8,0	80,0	80,0	80,0	1600,0	0	0	0	205,0	100,0	13,0
			b	0,1	0,2	0,2	0,04	0,2	0,1		0,1	0,3	0,2	0,02	0,2				0,1	0,1	0,1
			c	0,6	1,0	0,8	0,2	0,8	0,4		0,5	1,6	1,2	0,1	0,8				0,5	0,3	0,4
17	Loess	32,3	a	18,0	38,0	35,0	0,3	98,0	10,0	1,0	23,0	44,0	88,0	815,0	3230,0	1,0	0	0	333,0	186,0	33,0
			b	32,5	35,8	34,2	3,1	26,9	26,2	8,9	45,4	29,6	42,8	33,5	51,5	10,7			26,7	17,2	37,1
			c	1,0	1,1	1,1	0,1	0,8	0,8	0,2	1,4	0,9	1,3	1,0	1,6	0,3			0,9	0,5	1,1
18	Recent sediments, quicksand	12,9	a	13,0	9,0	29,0	0	90,0	5,0	0	9,0	10,0	24,0	281,0	722,0	0	0	0	207,0	107,0	10,0
			b	9,4	3,4	11,3		9,9	5,2		7,1	2,7	4,7	4,6	4,6				6,6	4,0	4,5
			c	0,7	0,3	0,9		0,8	0,4		0,5	0,2	0,4	0,3	0,3				0,5	0,3	0,3
19	Weighted average of trace elements			17,9	34,3	33,0	3,1	117,6	12,3	3,6	16,4	48,0	66,4	786,3	2025,4	3,0	71,2	4,5	402,6	348,6	28,8
20	Vinogradov's sedimentary averages			20,0	95,0	57,0	0,1	80,0	30,0	10,0	20,0	130,0	100,0	670,0	4500,0	2,0	60,0	3,0	800,0	450,0	100,0
21	Enrichment factor			0,9	0,4	0,6	31,0	1,5	0,4	0,4	0,6	0,4	0,7	1,2	0,4	1,5	1,2	1,5	0,5	0,8	0,3

Notes: a = average trace element content of the rock type (g/t)
b = proportional amount of trace element in the lithological type
c = affinity factor (af)
r = surficial abundance of rock types (%)

$$af = \frac{\text{proportional amount of trace element in the lithological type (b)}}{\text{surficial abundance (r)}}$$

$$d = \text{enrichment factor} = \frac{a}{\text{Vinogradov-value}}$$

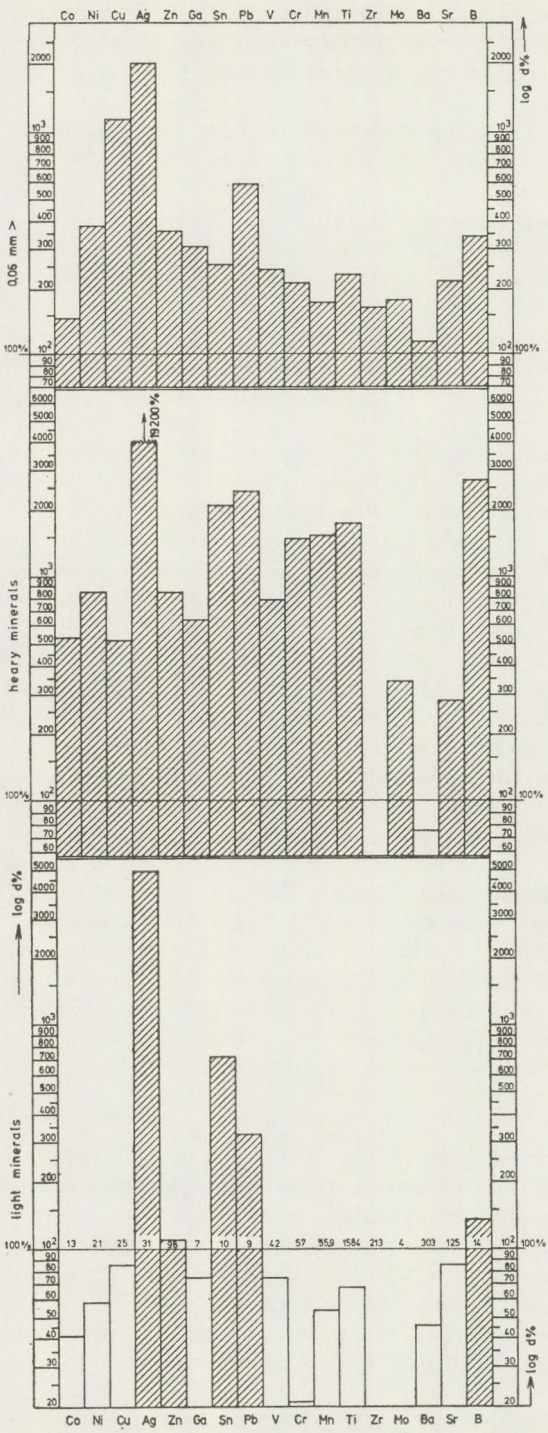

Fig. 2. The comparison of the minor element enrichments in the separated 0.1 – 0.2 mm and – 0.06 mm fractions

d = the rate of enrichment compared to the whole sample (the initial sample = 100%). The actual values of the concentrations are shown at the bottom of the diagram, on the line of the respective concentration values of the whole rock sample. Number of samples: 22, h = heavy

and their concentration was higher than the sedimentary average value, only the Zn and Mn was found to be evenly distributed. The Mo, Be, Li values were strongly dispersed, with enrichments being related to certain rock types.

Besides the trace element contents of the individual rock types, affinity factors were calculated, by dividing these average values with the surface abundances of the respective rock types. This factor indicates the rate of enrichment in the different lithological units. (Table 2. rows *a* and *b*). As it is seen, the greatest amounts of trace elements were assigned to the Oligocene glauconitic sandstone, the Carpathian "slir" Formation (siltstone, sandstone), and the loess, in accordance with their great surficial abundance. Despite of the limited extension on the surface, the terrestrial variegated clays at Nagylóc contain the majority of the Be, while the molybdenum has been enriched mainly in the Badenian marlsiltstone unit.

The actual enrichments compared to the background values of the environment are reflected by the affinity factors, independently from the actual volume of rocks. For these affinity factors – 1.0 values are the most abundant, similar to the mean values of the enrichment factors calculated for the whole area. Values over 2.0 were encountered in the silstone containing plant fossils at Mohora (Ti; af = 2.9), the "slir" formation at Szécsény (V; af = 2.3), the sandtone containing Anomia bivalves (Sn; af = 2.3), the loose sandstone at Iliny (V; af = 2.4), the glauconitic sandstone (Ag; af = 5.5; Zn; af = 2.8; Li; af = 2.3), the tuffitic variegated terrestrial sediments (Be; af = 58.3; Pb; af = 6.4; Ni; af = 2.3; Sn; af = = 2.2), the rocks associated with the coal measures at Herencsény (Be; af = 2.6), the Lithothamnium – limestone (Mn; af = 3.7; Sr; af = 3.3), the Badenian siltstone (Sr; af = 6.9; Mo; af = 3.4), and in the Sarmatian fossiliferous limestone (Mn; af = 6.8; Sr; af = 3.9). Only moderate minor element enrichments were recorded in the Carpathian "slir" formation and in the Pleistocene loess. For the "slir" formation 1.0 – 2.0 affinity factors were calculated, reflecting a slight but universal trace element enrichment. The siderophile Ni is enriched only in the terrestrial (tuffitic) sediments, the calcophile elements in the terrestrial and the shallow sublitoral coarse detrital sediments, the pegmatophile elements in the fine grained sediments and carbonates (Mn), the lithophile Be in the terrestrial paralic, while the Sr in the carbonate formations.

Mineralogical – Petrological factors affecting the trace element distribution

As can be seen from the earlier sections, the minor element enrichments were mainly observed in the silt – pelite grade sediments, though in cases anomalous concentrations have been recorded in other rock types too. These characteristics were approached by assaying separated fractions of rocks and evaluation of the variation of clay mineral and carbonate compositions with the trace element contents. Though the applicability of this method is limited, the number of data was insufficient for more accuate estimations, like multiple correlation.

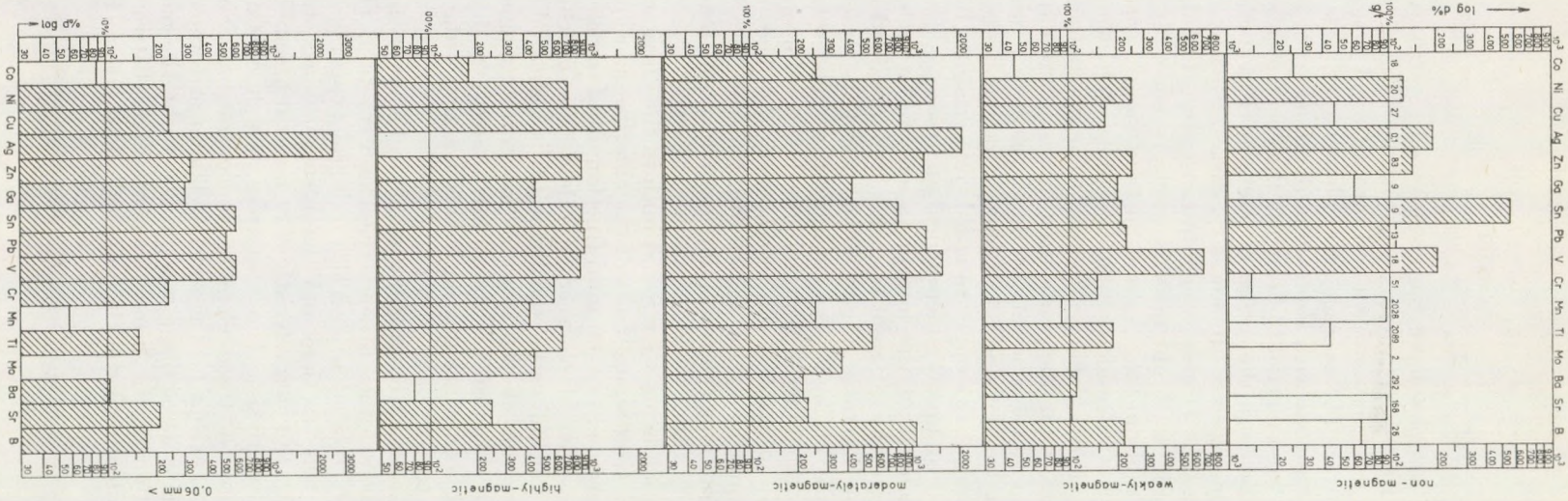

Fig. 3. The comparison of the magnetically separated 0.1 – 0.2 mm and – 0.06 mm fractions
d = enrichment compared to the whole sample (the initial sample = 100%). Number of samples: 9

A number of samples have been separated to 0.2–0.1 and –0.06 mm fractions. The 0.2–0.1 fraction was further subdivided into heavy and light minerals using bromoform and into different magnetic fractions by magnetic separator. The average trace element contents of these fractions were then correlated with the results obtained from the whole rock samples. The data were plotted to illustrate the enrichments as well as the distribution of elements in the different fractions (Fig. 2 and 3).

The finer grain sizes are abundantly characterised by higher amount of trace elements,. The largest concentrations were found in the heavy mineral fractions (Fig. 2). Light mineral fractions generally have d-values lower than 100%, and only the Ag and Sn show significant enrichment in this fraction. Most of the siderophile, calcophile and lithophile elements were accumulated in the "heavy minerals". The anomalous behaviour of Zr, i. e its concentration in the pelite sized fraction, is due to its extremely fine grain size. The lower amounts of Ba in the heavy mineral fractions indicate, that this element does not occur as independent mineral phase. The boron, however, shows opposite trend, reflecting its linkage to tourmaline as indicated by micro-mineralogical analyses.

Further refinement of the interpretation of the factors controlling the concentrations of the different elements were obtained by the evaluation of the magnetic fractions (Fig. 3). The "magnetic" fraction" refers to oxides and silicates of high iron content, the "moderately magnetic" fraction represents the minerals containing inclusions of magnetic minerals, or encrusted by ferrous material dia- or epigenetically. The "non-magnetic" fraction includes quartz, calcite, muscovite, feldspar, etc. With separate analyses of each fractions the respective concentration trends were determined.

Significant enrichments were found both in the "magnetic" and "moderately magnetic" (containing most of the chlorites and glauconite) fractions. In the fine grained (–0,06 mm) fraction all of the elements but Co, Mn and Mo have given above-average values. The geochemical significance of inclusion rich minerals and limonites is indicated by the higher concentrations of several elements in the "moderately magnetic" fraction. The "non-magnetic" fraction has shown less than 100% d values, though the Ag and Sn has been concentrated in this fraction – like in the "light mineral" fraction too.

The increased adsorptive capacity seems to be a relevant explanation for the higher concentrations in the –0,06 mm fraction. This adsorptive capacity is strongly related to the clay mineral types. 55 samples have been analysed for this fraction, and the average values were plotted on diagrams along with the characteristic clay mineral assemblages (as identified by thermical analysis). Those samples, which contained kaolinite, have shown the lowest trace element concentrations. Similar is true for montmorillonite, except for Cu and Ba. The most complex illite/montmorillonite+kaolinite assemblage was proved to be the most favourable for the concentration of the minor elements. The distribution of Co is seemingly independent from the clay mineral composition (Figs. 4 and 5).

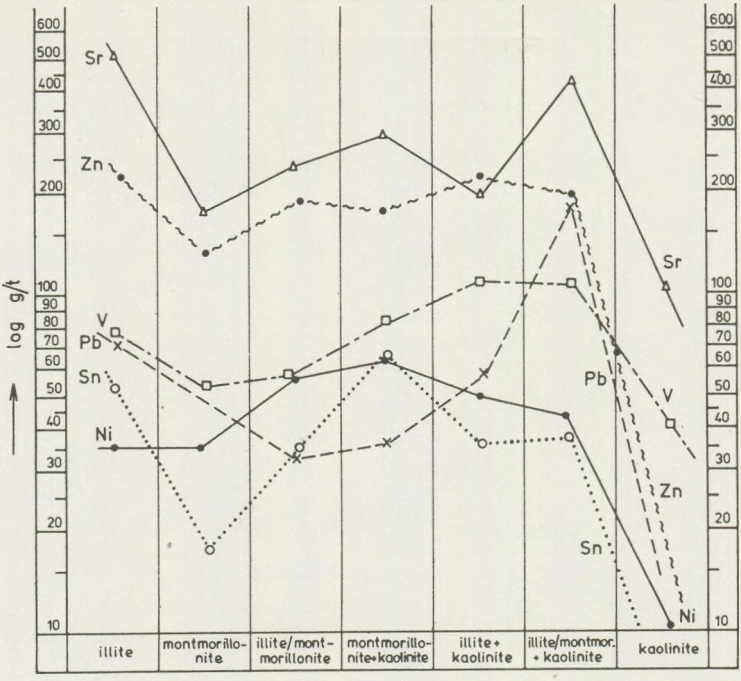

Fig. 4. The Ni, Zn, Pb, Sn, V and Sr content of the -0.06 mm fractions as a function of the clay mineral composition

The above detailed evaluation of the fine grain sized fraction should be handled as initial data for establishing the mineralogical, geochemical models to interprete these enrichments. Further improvements can be achieved if the amounts of the different clay minerals, the silt fraction, as well as the role of the diagenetic and epigenetic minerals (calcite, limonite) will also be encountered.

The detrital sediments contain varying amount ($0-40$ weight percent) of carbonate minerals (dominantly calcite, less dolomite).

The amount of carbonates of fossil or diagenetic origin is generally small. Larger amounts occur as syngenetic carbonate component. Since the carbonate minerals may have significant role in the enrichment of minor elements, the relationship of the $CaCO_3$ content and the trace element concentrations has been investigated. Choosing 5 percent class intervals, 259 samples were grouped according their $CaCO_3$ content, and the averages of the minor element concentrations were calculated for each of these groups. The data were plotted on diagrams, using logarithmic scale (Figs. $6-9$).

The interpretation of these plots were resulted in the following enrichment types:

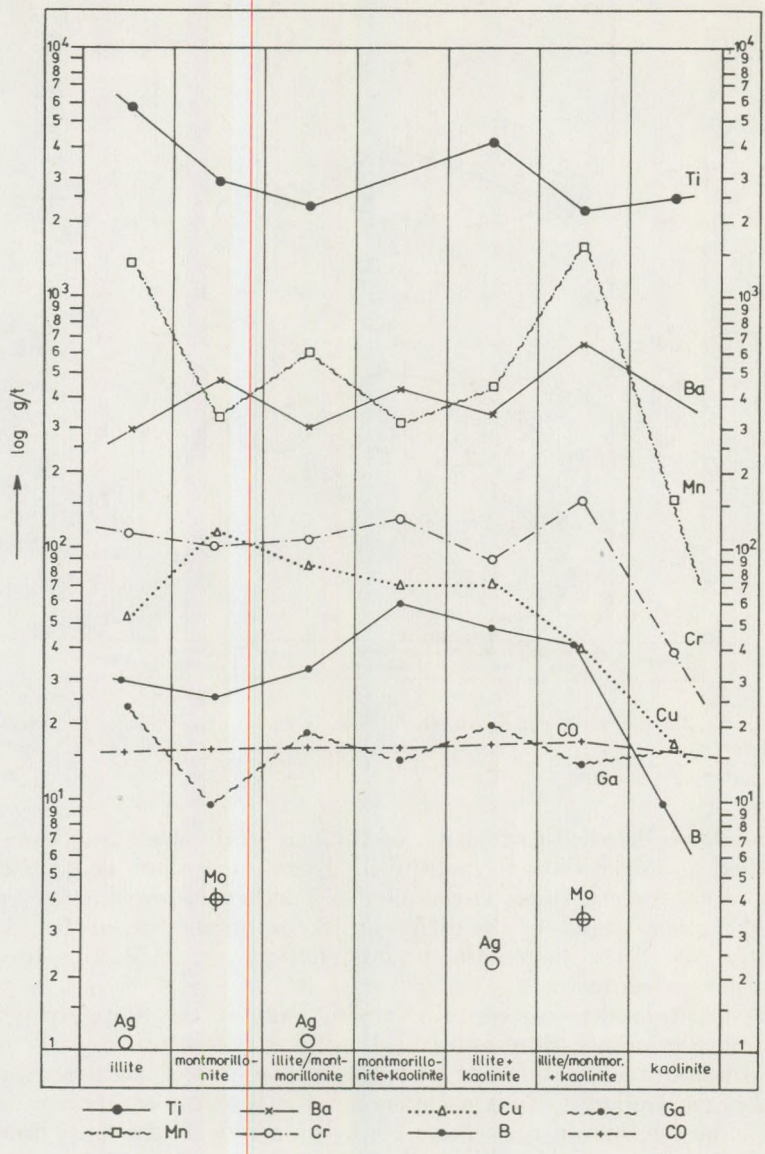

Fig. 5. The Co, Cu, Ag, Ga, Cr, Mn, Ti, Mo, Ba, B content of the -0.06 mm fractions as a function of the clay mineral composition

(1) The minor element content logarithmically increases with $CaCO_3$ content (the plot is rising from bottom left towards the upper right corner). These elements are mainly related to the carbonate minerals.

(2) The trace element content remains unchanged at higher $CaCO_3$ contents (i. e. with the decreasing amount of detrital components). In this case the plot is subvertical, and indicates the relation of the given element to both (detrital and carbonate) fractions.

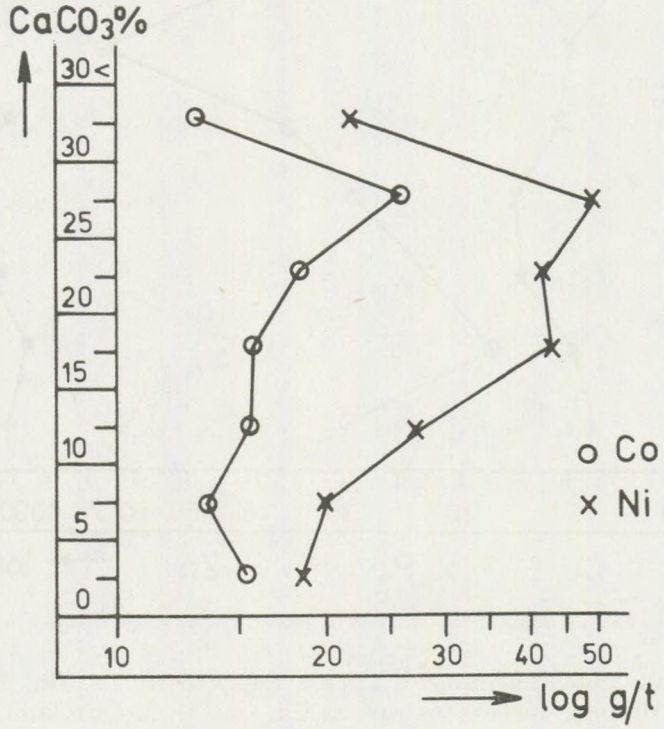

Fig. 6. The Co and Ni contant vs. the $CaCO_3$ content of the investigated detrital rocks

(3) The trace element content is inversely proportional with the amount of carbonates, the element is related to the detrital components.

These typical cases are simplified, since a greater complexity of the effecting factors should be considered. The curves show several unexplained variations, and serve only as rough estimates of the main trends. As an example, the multiple relationship among the ratio of the carbonate and silicate fractions, and the mineralogical composition of the silicate fraction can be mentioned. With increasing amount of the $CaCO_3$ content the role of the clay minerals also increases. Therefore, the specific minor element content of the detrital fraction changes with the amount of carbonate in the rocks.

Most elements decrease if the $CaCO_3$ content exceeds 30 percent. This fact might indicate the difference in the trace element concentrations of diagenetic and syngenetic calcites.

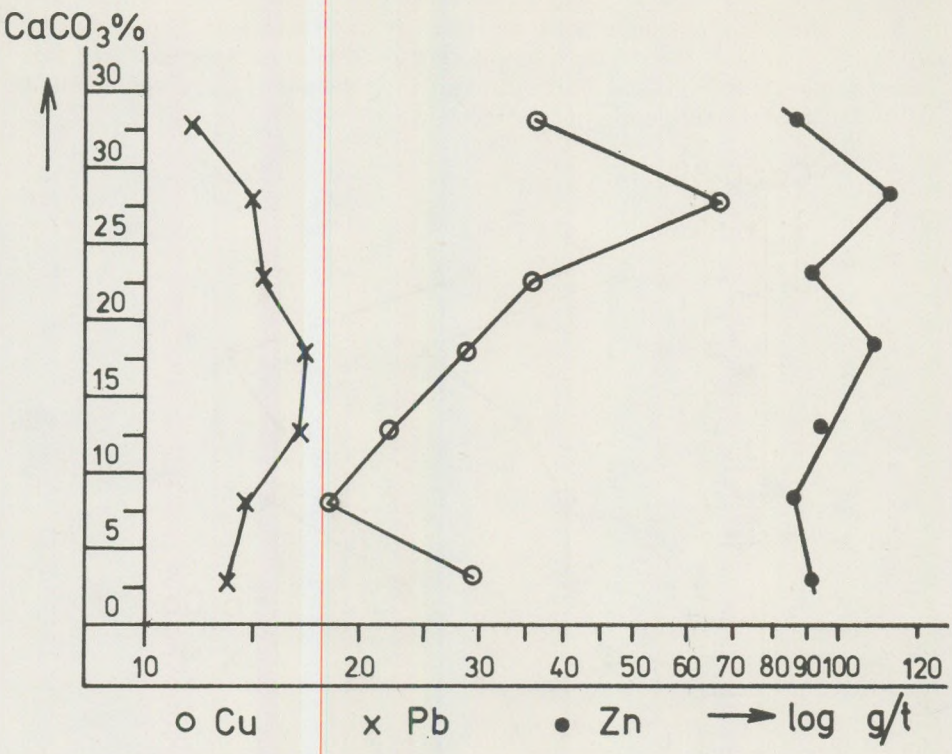

Fig. 7. The Cu, Pb, Zn content vs. the $CaCO_3$ content of the investigated detrital rocks

From the above mentioned, Type 1 refers to Ni, Cr, Mn, Ti, Sr and Ba (gently dipping curves), as well as Cu, Ga (?), Mo, Sn, and V (sharp curves); Type 2 includes Co and Zn, while Type 3 is characteristic of Pb.

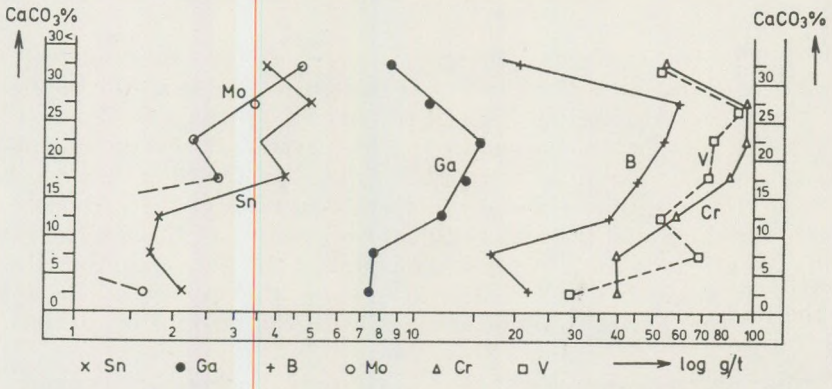

Fig. 8. The Ga, Mo, Sn, Cr, V and B content vs. the $CaCO_3$ content of the investigated detrital rocks

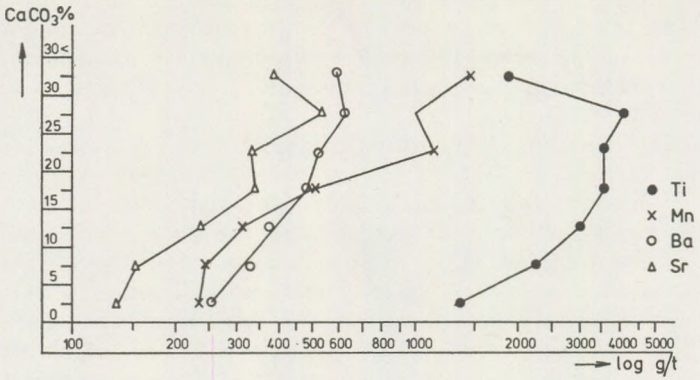

Fig. 9. The Mn, Ti, Ba and Sr content vs. the $CaCO_3$ content of the investigated detrital rocks

Most of these studies were carried out on -0.2 mm fractions. For some samples, the $0.125-0.250$ mm and the $0.25-0.50$ mm fractions were also assayed. Surprisingly large enrichments of Ag, Cu, Sn and Zr, moderate concentrations of Pb and Zn were observed in the $0.25-0.50$ mm fraction. This fact indicates the necessity of investigations of the coarse grain sizes.

It should be mentioned that the "heavy minerals" and magnetic fractions comprise $0.1-10$ percent, the fine grained fractions $1-95$ percent, the carbonate fraction $0-50$ percent of the weight of the total rock mass.

With these considerations kept in mind, the interpretation of the relative enrichments of the different elements is attempted in the following sections (Table 2).

The siderophile *Co* enrichments in sediments are generally derived from basic, ultrabasic igneous source rocks. Micromineralogical analyses have precluded this possibility here, therefore no special interpretation of the weighted average value (19.3 g/t) and affinity factor is needed. The glauconitic sandstone, terrestrial variegated clays, the siltsone pelitic sediments (the "slir" formation and the siltsones with plant fossils at Mohora) are characterised by slightly larger than 1 affinity factors. These enrichments are related to the heavy mineral and the magnetic or moderately magnetic fractions. In the terrestrial sediments it occurs in trivalent form, linked to limonite.

The nickel, *Ni*, shows only marginal concentration (d = 0.4) in the area. Despite this fact that in sediments characterised by over 1.0 values of affinity factor for Co, the nickel content is also higher. This is the case for the Badenian marls, siltstones too. Among these rocks only the terrestrial variegated clays show more considerable concentration (af = 2.3). The Ni is mainly concentrated in the illite/montmorillonite mixed-layered clay minerals, and less frequently in diagenetic carbonates. In the terrestrial sediments the volcanogenic heavy minerals (pyroxenes, magnetite) may also have important role in the accumulation.

The copper, *Cu* average is also low in the Northern and Eastern Cserhát. With an 1 7 maximum value of affinity factors, no anomalous enrichments can be encountered. The pelitic (dominantly illite or illite-montmorillonite) sediments show slightly higher values, possibly due to adsorptive enrichments.

The data for silver, *Ag* show large variation, thus its regional weighted average value (d = 31) is of little meaning. The highest concentrations have been encountered in the glauconitic sandstone (af = 5.5). This enrichment needs further study. Accordingly the analyses of separated rock fractions of the following types of enrichments were observed: clay minerals (adsorptive), the moderately magnetic and magnetic fractions (mainly in glauconite by adsorption); light minerals (presumably in quartz).

The low concentrations of zinc, *Zn* (d = 1.5) are mainly due to the abundant fine grained sediments, with affinity factors around 1,0. Local enrichments have been found in the glauconitic sandstone, linked to the moderately magnetic galuconite and chlorite components.

The regional average value of the gallium, *Ga* is very low (d = 0.4). Owing to its genetic relationship with alumina, it is mainly concentrated (and represented by over 1.0 and maximum 1.6 af values) in the pelitic sediments.

The distribution of tin, *Sn* shows large variation. Its regional average value is similarly low (d = 0.4), local enrichments were encountered in the shoreline, shallow water marine as well as terrestrial sediments (max. af value is 2.3). The submicroscopic inclusions in light minerals (quartz) may play significant role in the Sn enrichment. The areal distribution of Sn shows ENE – WSW arrangement, subparallel with the dike swarms in the Northern Cserhát. Tin minerals have not been identified microscopically. The tourmaline, which is abundant in the sediments, indicate granitic source area (*Andó* 1973).

The areal average of lead, *Pb* is less than the sedimentary average value (d = 0.8). It is mainly concentrated in the heavy and magnetic mineral fractions. Owing to the small amount of these fractions, the adsorptive enrichment in clay minerals is probably the main concentrating factor. The significant enrichment in the terrestrial variegated sediments is presumably related to the potassium-rich volcanogenic components.

Erratic distributions were observed in the case of the vanadium, *V*, which is characterised by relatively low areal average value. Affinity factors with values larger than 1.0 were found primarily in pelitic rock types. The main concentrating phases were found to be the clay minerals (especially the complex, kaolinite containing assemblages).

Though high concentrations were formed in the heavy and magnetic fractions, their effect on the bulk of the rocks is significantly lower.

The areal average value of chrome *Cr*, is small, similarly to that of the vanadium. This similarity is also valid for those rocks which are relatively enriched chromium though affinity factors are somewhat smaller.

The manganese, *Mn* shows most frequent enrichments in the sediments of the area. Moderate anomalies were observed in both the detritic and

carbonate sediments, The medium to coarse grained sandstones, conglomerates contained the largest number of Mn anomalies among the detrital sediments. Sometimes the thin manganese oxide lamellae, encrustations are easily visible, indicating high energy oxic sea water during precipitations. The enrichments in the postvolcanic carbonates are also large (af = = 3.7 – 6.8).

The carbonate and manganese contents of the sediments show direct relationship. Thus in the Eastern Cserhát the Mn oxides which are found as fissure fillings in the Lajta limestone were probably originated from the manganese released from limestones during surficial weathering, and were precipitated in form of oxides.

The titanium, *Ti* occurs in relatively small amounts mainly in psammitic rocks. It is mostly linked to titano-magnetite, ilmenite, rutile, anathase, biotite, garnet minerals, as identified by micro-mineralogical analyses. This fact explains its concentration in medium grained sandstones. The Ti content in the terrestrial variegated sediments is related to the volcanogenic components.

The scarce data for molybdenum, *Mo* indicates that the relatively small average enrichment has resulted from a few local anomalies. Generally the pelitic sapropelites are the favourable concentrating sedimentary rocks for molybdenum. The coarse- and fine grained detrital sediments in the Cserhát are far from this type, recently available data are insufficient for proper evaluation of these enrichments.

The lithium, *Li* data exhibit considerable scattering. Its areal average (d = 1.2) can not be considered as representative of all studied formations. Its strong affinity to glauconitic sandstone is presumably due to the abundantly high Li content in glauconite.

The areal average of barium, *Ba* does not reach the Vinogradov value (d = 0.5). No high affinity factors were observed (max. af = 1.8). Despite the occasional appearence of barite, the highest concentrations were found in fine grained pelitic fractions, indicating adsorptive bonds, but systematic relationship between the barium and clay mineral compositions was not found. Its relationship with diagenetic carbonate minerals is indicated by the increasing amount of *Ba* with rising carbonate content up to 20 weight percent of carbonates.

The areal average of strontium, *Sr* is roughly equal to the sedimentary average values (d = 0.8). Up to 30% carbonate content its amount proportionally increases. This indicates connection with calyey-silty carbonate rocks ("slir" formation) and limestones (affinity factors in the latter rock types being 3.3 – 6.9).

Further increase in carbonate, content is not associated with simultaneous enrichment of *Sr*. This fact, along with other geochemical considerations indicates the affinity of barium to the biogenic carbonates, though its adsorptive enrichment in clay minerals is also significant.

The amount of boron, *B*, does not reach the Vinogradov values in any of the studied rock types. Weak relative enrichments were found in

the psammitic and pelitic rocks (max. af = 1.7). The tourmaline of the heavy mineral fractions as well as adsorption on clay minerals are presumably responsible for the concentration of boron.

REFERENCES

A n d ó J. (1973): A szállítási-leülepedési térszín vizsgálata a log-normál szemcsepopulációk elemzése alapján. Földtani Közlöny 103. Budapest

A n d ó J. (1973): Geochemical Investigation of Sedimentary Rocks in the Northern Cserhát Hills. Ann. Univ. Sci. Budapestiensis de R. Eötvös, Sectio Geologica 16.

A n d ó J. (1975): Method for a Common Evaluation of Petrographical and Paleontological Investigation of Detrital Sedimentary Formations. Annales Univ. Sci. Budapestiensis de R. Eötvös Sectio Geologica 19.

B á l d i T. (1973): Mollusc Fauna of the Hungarian Upper Oligocene (Egerien). Akad. Kiadó, Budapest

N a g y n é B. J. (1971): Vorrichtung zur halbquantitativen Auswertung von Emission spektren. Spectrochimica Acta 26. B.

N e m e c z (1973): Agyagásványok. Akad. Kiadó, Budapest

ГЕОТЕРМИЧЕСКАЯ МОДЕЛЬ ЗЕМНОЙ КОРЫ В ПАННОНСКОМ БАССЕЙНЕ

Л. БОДРИ

Кафедра геофизики Будапештского Ун-та им. Л. Этвеша, Будапешт (Венгрия)

20. V. 1981

ABSTRACT

A geothermal model of hyperthermal zone of the Pannonian basin is constructed. On the basis of results of seismic measurements along five deep seismic sounding profiles on the territory of the basin and surrounding areas and also of measurements of heat flow, heat production by radioactive elements and thermal conductivity of rocks, the variation of temperature with depth and maps of Moho-temperatures and heat flux through this surface are calculated and constructed respectively. It is shown by numerical model calculations that the heat anomaly of the Pannonian basin indicated by a number of surface measurements is mainly of mantle origin. Inhomogeneities of the heat flow on the territory of the basin deepen down to the upper mantle and temperature on the Moho-surface here has values is average by 400 – 500 °C more than those in the surrounding areas. Heat flux through the Moho under the Pannonian basin also anomalously high, compared with values in the surroundings the basin; it is increased here by about 40 – 50 m Wm^{-2}. On the basis of results of present calculations, it can be emphasized that beneath the Pannonian basin probably not only te upper mantle but also a part of the lower crust are partially molten.

В работе была построена геотермическая модель гипертермальной зоны Паннонского бассейна. На основании результатов сейсмических измерений вдоль пяти профилей ГСЗ на территории бассейна и в окружающих его районах с привлечением измеренных значений теплового потока, генерации тепла радиоактивными элементами и теплопроводности пород были расчитаны распределения температуры с глубиной, построены карты теплового потока и температур на поверхности Мохо. Численное моделирование показало, что в создании тепловой аномалии, определенной в Паннонском бассейне по приповерхностным измерениям решающую роль играет верхняя мантия. Неоднородности теплового потока прослеживаются вплоть до верхней мантии, температуры поверхности Мохо достигают 800 – 1000 °C, что в среднем на 400 – 500° превышает Мохо-температуры в окружающих бассейн районах. Разница в тепловых потоках с поверхности Мохо между бассейном и окружающими районами доходит до 40 – 50 милливатт/м². Имеются все основания полагать, что не только верхняя мантия, но и часть нижней коры под Паннонским бассейном находится в состоянии частичного расплавления.

Введение

Паннонский бассейн, западная часть Карпатского бассейна — молодой депрессии, расположенной на юго-востоке Европы и окруженной горными цепями Альп, Карпат и Динарид, является так называемой гипертермальной зоной. Паннонский бассейн характеризуется высокой гидротермической активностью, чрезвычайно развитой аномалией тепло-

вого потока, поскольку измерения теплового потока на территории бассейна дают значения от 70 до 110 милливатт/м² [Čermak and Hurtig, 1977], а в некоторых отдельных случаях тепловой поток достигает значений 130—135 милливатт/м² [Boldizsár, 1975], в то время как средний тепловой поток окружающих территорий не превышает 50—60 милливатт/м². Можно отметить также высокие значения температурного градиента (в среднем, 50—60 °С/км и 70—80 °С/км в юго-западной и северо-восточной части Паннонского бассейна), полученные при обработке данных по водяным и нефтяным скважинам [*Bélteky* and *Korim*, 1971; *Juhász*, 1977], а также соответствующие этим градиентам температуры в водяных скважинах либо измеренные непосредственно [*Bélteky* and *Korim*, 1971], либо полученные из данных по ионной концентрации в термальных водах описываемого региона [*Bodri*, 1979].

Наличие указанной тепловой аномалии делает весьма интересным построение геотермической модели Паннонского бассейна, то есть с привлечением результатов сейсмических измерений вдоль профилей ГСЗ, измерений теплового потока, генерации тепла и теплопроводности пород конструирование теплофизической модели исследуемой зоны (модели генерация тепла — теплопроводность как функция глубины) и на ее базе вычисление распределения температур в коре и верхней мантии, экстраполяция наблюдаемой картины теплового потока вплоть до верхней мантии, определение, в какой мере тепловой поток имеет глубинное происхождение и в какой мере он связан с корой. Построение и первичная интерпретация такой модели и было целью настоящей работы.

Математическая модель

В математической формулировке задачи, характеризующие горизонтальные температурные неоднородности, ставятся как стационарные двумерные задачи вида

$$\frac{\partial}{\partial x}\left(K\frac{\partial T}{\partial x}\right)+\frac{\partial}{\partial z}\left(K\frac{\partial T}{\partial z}\right)+A(x,z)=0 \qquad (1)$$

с граничными условиями

$$\frac{\partial T}{\partial x}(x=0,\ L;\ z)=0$$

$$T(x,z=0)=T_0(x) \qquad (2)$$

$$K(x,z=H)\frac{\partial T}{\partial z}(x,z=H)=q^*(x)$$

где (x, z) — сетка декартовых прямоугольных координат,
T — температура,
$K(x, z, T)$ — теплопроводность,
$A(x, z)$ — генерация тепла на единицу объема,

L – длина профиля,
H – его глубина,
T_0 – поверхностная температура,
$q^*(x)$ – тепловой поток с нижней границы профиля.

Легко показать, что для исследуемых глубин кривизной поверхности Земли можно пренебречь. В Паннонском бассейне не производилось измерения радиоактивности и теплопроводности пород под тонким (не свыше 2 км глубиной) слоем, поэтому в данной работе необходимо было сделать ряд допущений относительно глубинного распределения этих функций.

Теплопроводность K считалась зависящей от типа породы и от температуры. Как известно, теплопроводность пород с увеличением температуры убывает, причем температурный коэффициент $C = \frac{1}{K}\left(\frac{\partial K}{\partial T}\right)_P$, где P – давление, довольно постоянен. Из этой зависимости грубо следует формула для температурной поправки вида

$$K = K_0/(1 + cT), \tag{3}$$

где K_0 – теплопроводность при 0 °С. Значения температурного коэффициента c брались по работам *Birch* and *Clark* [1940] и *Roy* [1963]. Считалось, что зависимостью теплопроводности от давления для изучаемых глубин можно пренебречь [Roy, 1963; Любимова, 1968].

Функция генерации тепла A первоначально бралась в виде ступенчатой функции постоянной для каждой породы и изменяющейся с глубиной лишь по мере изменения строения изучаемого профиля. Однако предварительные расчеты показали, что при таком допущении генерация тепла в верхней коре получается нереально высокой [*Bodri*, 1976], поэтому в настоящей работе было использовано более общее с геохимической точки зрения, предложенное *Lachenbruch* [1971] послойное экспоненциальное убывание функции генерации тепла. При этом потолку каждого слоя приписывалось значение, лабораторно измеренное для породы, составляющей слой. Это допущение сыграло существенную роль, в основном, лишь для гранитного слоя. В верхней мантии генерация тепла считалась постоянной.

В качестве поверхностной температуры $T_0(x)$ в работе бралась среднегодовая температура поверхности, которая хорошо известна на территории Паннонского бассейна из метеорологических наблюдений. Следует отметить, что на указанной территории эта температура достаточно стабильна от года к году и составляет 9–11 °С.

Для уравнения (1) была составлена симметричная разностная схема. Конечно-разностный аналог общего уравнения теплопроводности решался методом поточечной сверхрелаксации на прямоугольной неравномерной сетке. Точность решения составляла не менее 0,01°. Значение температуры для каждой последующей итерации получалось с помощью формулы

$$T_{\text{нов}} = T_{\text{стар}} + R(T^*_{\text{нов}} - T_{\text{стар}}) \tag{4}$$

в каждой точке сетки. Здесь $T_{\text{стар}}$ – значения температур с предыдущей итерации, $T^*_{\text{нов}}$ – новые значения, вычисленные по конечно-разностному аналогу уравнения (1), R – ускоряющий множитель, больший единицы, вычислялся в процессе итерации. Описанный процесс повторялся вплоть до получения конвергентного решения. Несколько затрудняло итеративную процедуру, во-первых, то, что теплопроводность, входящая в урав-

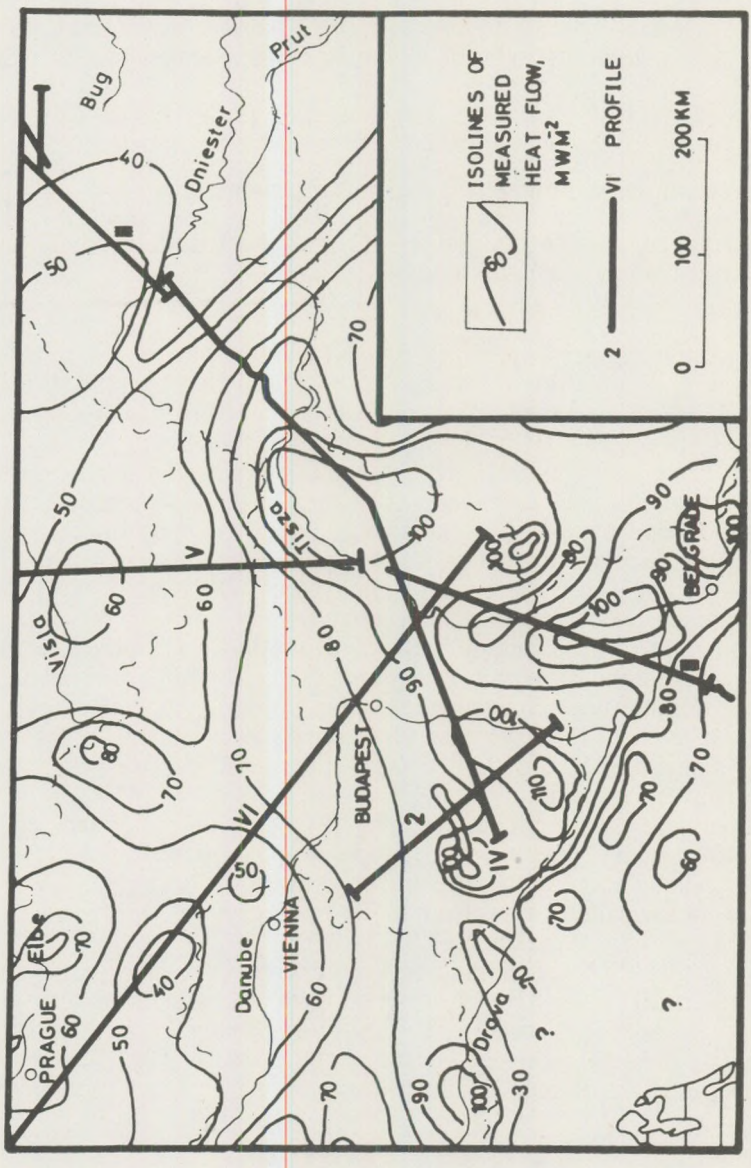

Fig. 1. Heat flow map of the Pannonian basin and surrounding areas indicating also the deep seismic sounding profiles considered.

Рис. 1. Карта теплового потока в Паннонском бассейне и окружающих его районах с нанесенными на ней профилями ГСЗ

нение (1), сама являлась функцией искомой температуры, а во-вторых, то, что поток с нижней границы профиля, фигурирующий в граничных условиях (2), заранее не был известен.

Что касается температурной зависимости теплопроводности, то в процессе получения конвергентного решения приходилось расчитывать эффективное значение теплопроводности в соответствии с полученной температурой. Приведение теплопроводности к эффективному значению производилось не в каждой итерации, а только после достижения хорошей конвергенции для эффективной теплопроводности, принятой перед этим.

Для определения условия на нижней границе профиля использовался известный поверхностный тепловой поток $q_0(x)$ (Рис. 1). В первом приближении задача получения распределения температуры решалась, как описано выше, с произвольным потоком $q^*(x)$. После ее решения вычислялся поверхностный тепловой поток, и если расчитанный поток не совпадал с наблюдаемым, то поток соответствующим образом изменялся, чтобы уменьшить эту разницу. После этого процедура получения конвергентного решения для температуры повторялась. Описанный процесс представлял собой дополнительную итерационную процедуру, которая повторялась до тех пор, пока вычисленный на поверхности тепловой поток не совпадал с наблюдаемым.

Теплофизическая модель Паннонского бассейна

На рис. 1 представлено расположение пяти профилей ГСЗ, пересекающих территорию Паннонского бассейна. Относительно густое покрытие профилями столь маленького района сыграло существенную роль в детальности построения распределения теплофизических параметров с глубиной. Геологическая интерпретация профилей была взята по данным *Beránek* et al [1972] и *Mituch* and *Posgay* [1972]. При этом использовались не только результаты сейсмического зондирования, но и результаты прикладной геофизики и глубинного бурения. Как уже упоминалось, бассейн представляет собой молодую депрессию, которая как морфологически, так и с точки зрения строения коры, полностью изолирована. Значительная часть бассейна заполнена осадками верхнего мела (в основном, известняки и доломиты) и неогеновым молассом, причем толщина осадочного комплекса составляет, в среднем, 3 км, но может достигать и 6—7 км. Фундамент сложен породами, стратиграфически охватывающими период от докембрия до нижнего мела. Самые старые породы — это, в основном, сильно метаморфизированные кристаллические сланцы (гнейсы, слюдистые сланцы, амфиболиты, кварциты и т. д.). Палеозой характеризуется менее метаморфизированными породами. Старый палеозойский фундамент бассейна состоит, главным образом, из филлитов и сланцев. Породы нового палеозоя также мало метаморфизированы или вообще не метаморфизированы (обычные или глинистые сланцы, известняки, песчаники, конгломераты). Мезозойский комплекс характеризуется, как правило, карбонатными фациями (известняки и

доломиты, затем мергели, песчаники и спорадически эруптивные породы). Верхнемеловой — палеогеновый — неогеновый комплекс имеет примерно горизонтальное простирание. Глубина фундамента изменяется от нуля до 10 км. Далее расположен гранитный слой, глубина потолка которого изменяется от 4 км до 10 км. Потолок слоя габбро, то есть поверхность Конрада, проходит на глубине 15—20 км. Одна из наиболее интересных черт коры бассейна состоит в том, что гранитный слой обычно имеет нормальную или несколько повышенную толщину, в то время как слой габбро необычно тонок. Поверхность Мохо в Паннонском бассейне расположена на небольшой глубине 24—28 км. Ее топография имеет довольно спокойный характер.

В таблице 1 представлены параметры теплофизической модели, использованной при расчете представленных ниже распределений температуры с глубиной по всем пяти профилям, пересекающим бассейн. В таблице 1 параметры разбиты на группы в соответствии с обозначениями слоев, данных на представленных ниже рисунках распределения

Табл. 1.

Параметры теплофизической модели Паннонского бассейна
Values of thermal parameters used in present calculations

Зона	Обозначение	Теплопроводность (ВТ/М °К)	Генерация тепла (10^{-6} ВТ/М^3)
Осадочный комплекс	1		
Паннонского бассейна			
Неогеновые осадки		1,9	1,4
Мезозойские осадки		2,2	1,3
Карпатский флиш		3,1	1,2
Фундамент	2		
Мезозойский комлекс, главным образом, карбонаты		2,5	1,3
Палеозойские метаморфические породы		2,5	1,3
Докембрийские кристаллические породы		2,9	1,6
Магматические породы	3		
сиениты		2,2	3,0
граниты		2,9	3,0
базальты		2,2	0,9
Гранитный слой			
высокое содержание урана	4	2,9	3,0
низкое содержание урана	5	2,9	1,3
Слой габбро	6	2,2	0,5
Верхняя мантия	7	4,3	0,004

температуры с глубиной вдоль исследуемых профилей. Однако с целью избежать излишнего загромождения этих рисунков, геологическая структура профилей была намечена на них лишь условно и не отражала вполне тонкой структуры, применявшейся при расчетах. Поэтому в таблице 1 к зоне с одним и тем же условным обозначением могли относиться несколько значений теплопроводности и генерации тепла. Поскольку прямых измерений генерации тепла и теплопроводности пород на самой территории бассейна известно мало, то наличествовавшие данные пришлось существенно дополнить результатами аналогичных измерений по соедним районам. Таблица 1 составлена на основании данных *Любимовой* [1968], *Kappelmeyer* and *Haenel* [1974], *Čermák* [1975], *Buntebarth* [1975], *Buntebarth* [1976], *Rybach* [1976], *Кутас* [1977].

Теплопроводность и генерация тепла в верхней мантии была приянта соответствующей перидодиту.

Геотермическая модель Паннонского бассейна

На рисунках 2, 3, 4 представлены результаты расчетов распределения температуры вдоль пяти профилей ГСЗ, показанных на рисунке 1. Обшим для геотермики всех представленных профилей следует считать то, что тепловая аномалия, определенная в Паннонском бассейне по приповерхностным наблюдениям хорошо развита вплоть до верхней мантии. Если в окружающих Паннонский бассейн районах ход изотерм обусловлен, в основном, генерацией тепла в верхней коре, то есть практически только строением коры, то в самом бассейне влияние генерации тепла в тонкой коре существенно размывается влиянием теплового потока, приходящего из мантии. Строение изотерм в Паннонском бассейне почти полностью повторяет ход мантийного теплового потока. Если на периферии Карпатского бассейна кора дает 75–80% наблюдаемого потока, по выходе из бассейна на некоторых территориях даже до 90% то в Паннонском бассейне вклад коры редко доходит до 40%, а 60–70% наблюдаемого потока обеспечивает верхняя мантия. Что является очень важной чертой, поскольку обычно основные вариации наблюдаемого теплового потока на континентах связаны, главным образом, с неравномерным распределением радиоактивных элементов в верхней коре, а мантийная составляющая теплового потока стабильна даже в пределах обширных территорий. Не только глубинные температуры в этом районе, но даже приповерхностные температуры очень велики. В некоторой степени причиной этого является некоторый изолирующий эффект, вызываемый толстым слоем осадков с низкой теплопроводностью, однако основная причина, как и прогретости бассейна в целом, – высокая величина потока из верхней мантии. Подъем изотерм под Паннонским бассейном по сравнению с окружающими областями чрезвычайно резок, что приводит к появлению значительных горизонтальных градиентов температуры. Этот факт почти исключает возможность применения для моделирования температур в этом районе часто используемого в геотермической литературе одномерного варианта [$T = T(z)$] уравнения (1).

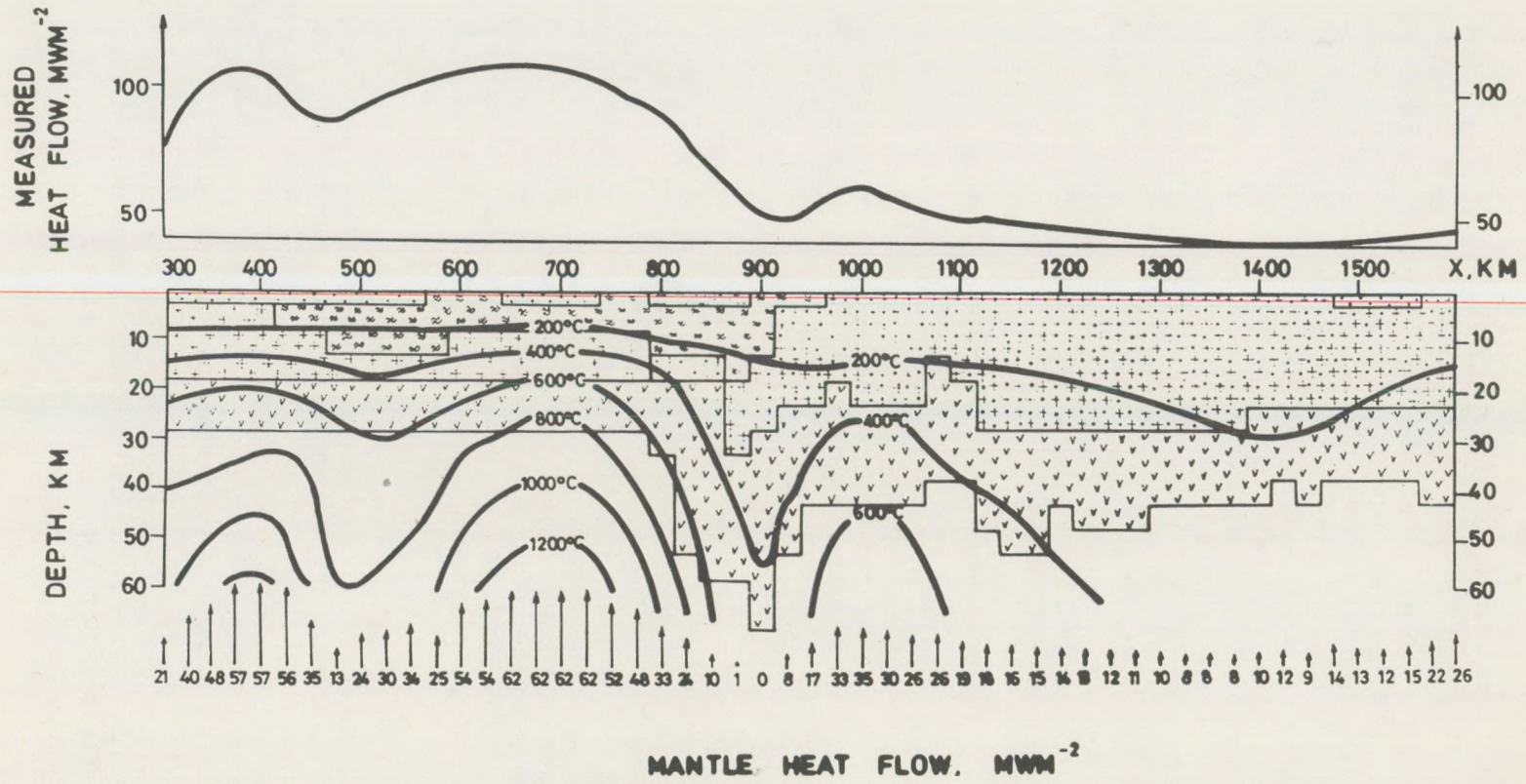

Fig. 2. Geotherms along DSS-profile IP – III. (notations explaned in the text).

Рис. 2. Распределение температуры вдоль профиля ГСЗ IP-III (объяснение обозначений в тексте)

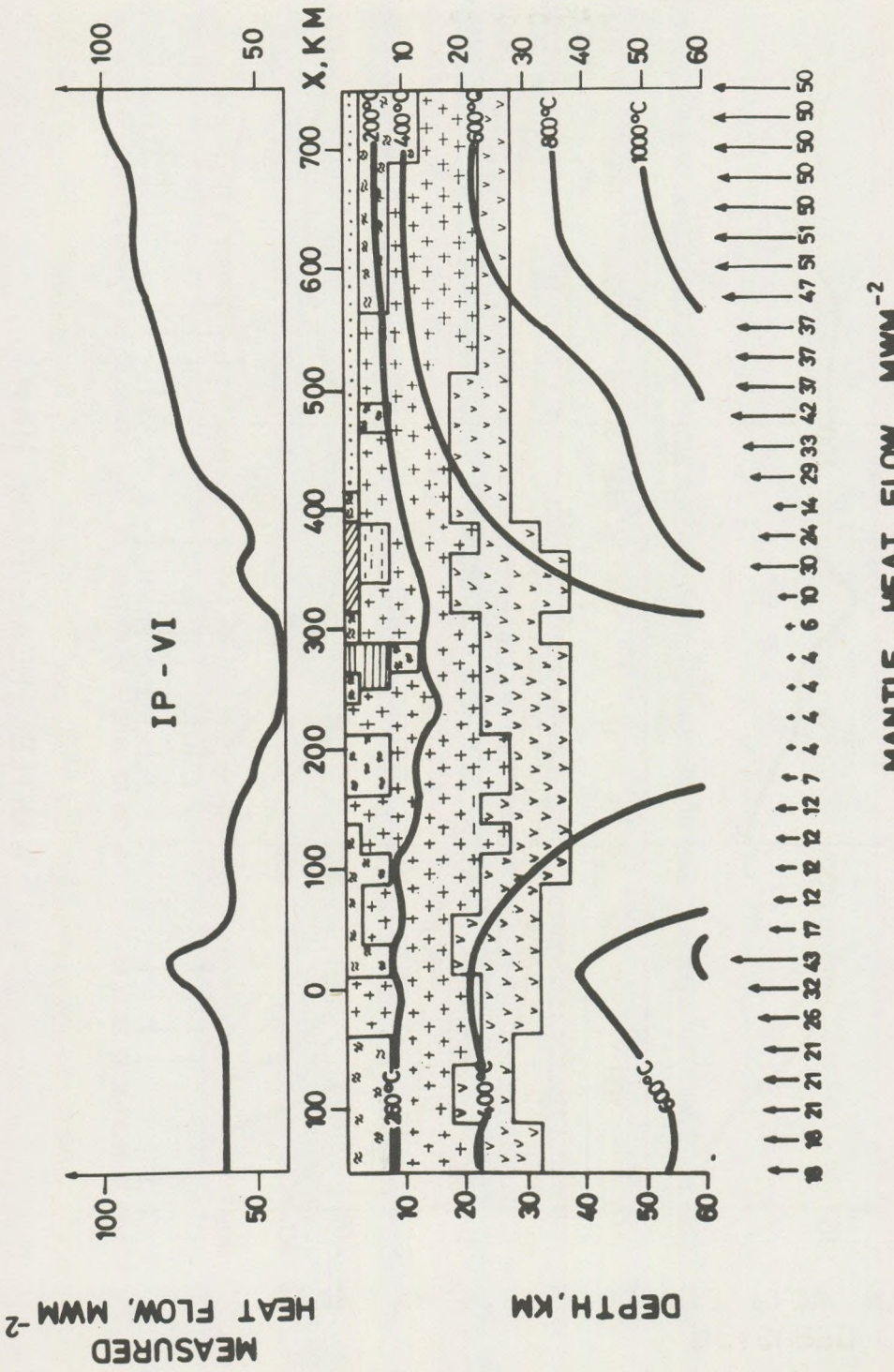

Fig. 3. Geotherms along DSS-profile IP – VI.

Рис. 3. Распределение температуры вдоль профиля ГСЗ IP-VI

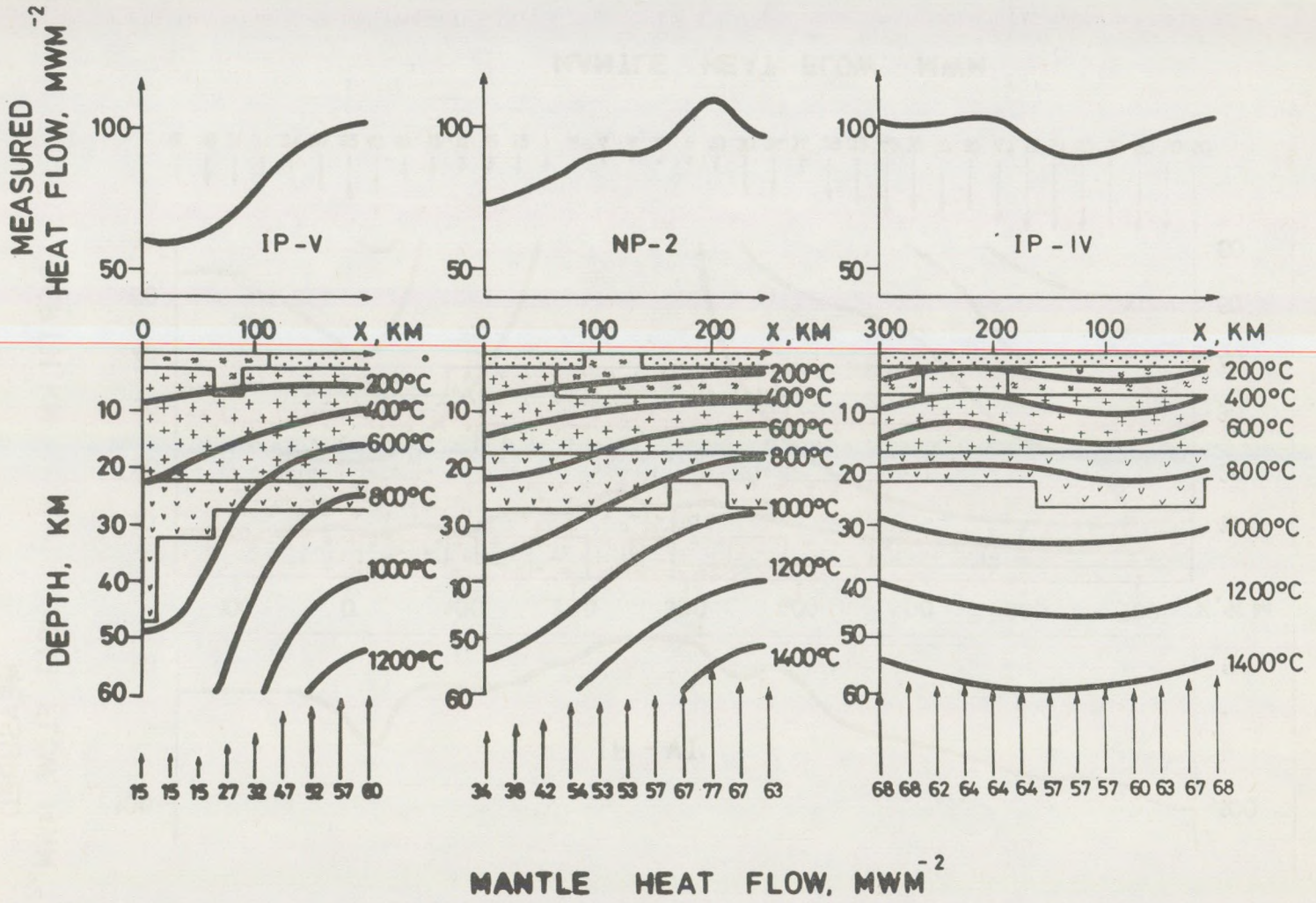

Fig. 4. Geotherms along profiles IP – V, NP – 2 and IP – IV. *Рис. 4.* Распределение температуры вдоль профилей ГСЗ IP-V, NP-2, IP-I V

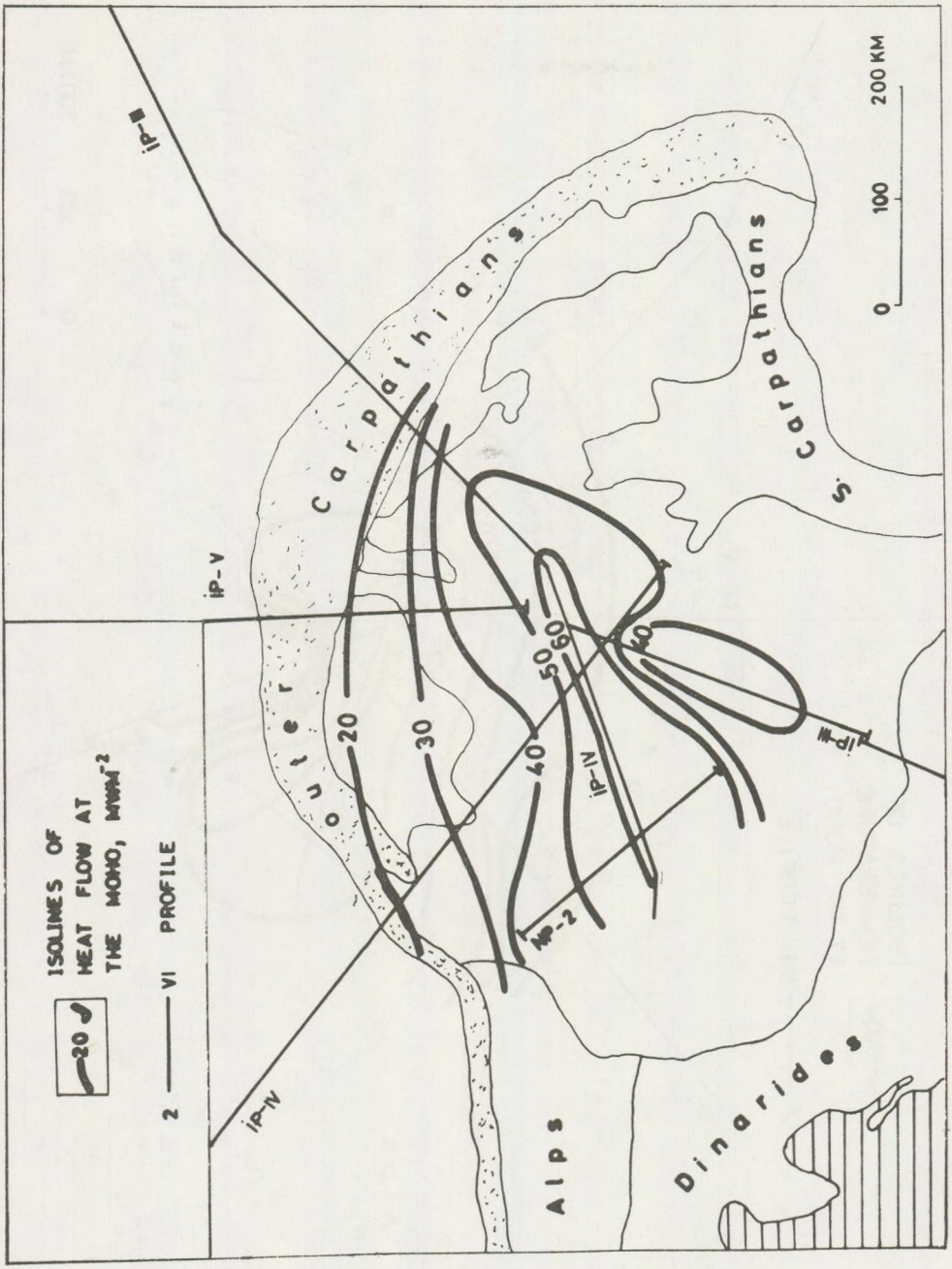

Fig. 5. Map of heat flow through the Moho in the Pannonian basin.

Рис. 5. Карта теплового потока с поверхности Мохо в Паннонском бассейне

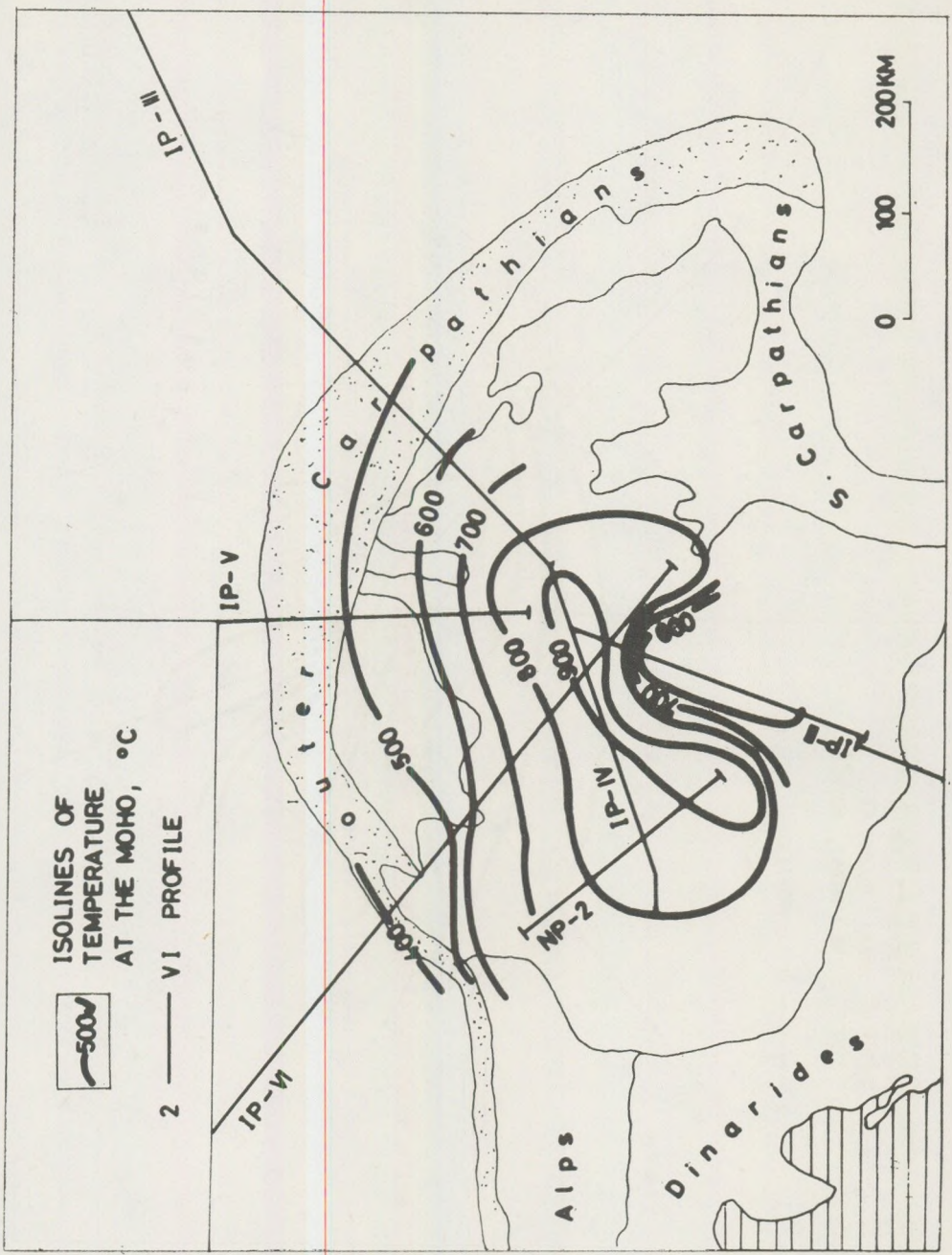

Fig. 6. Temperature distribution on the Moho-surface under the Pannonian basin.
Рис. 6. Карта температуры поверхности Мохо в Паннонском бассейне

Большая густота покрытия Паннонского бассейна профилями ГСЗ позволила также на основании проделанных расчетов построить для него карты теплового потока и температур на поверхности Мохо, представленные на рис. 5 и 6. Очевидна сильная прогретость верхней мантии бас сейна. Мохо-температуры достигают значений 800—1000 °С, по сравнению с 400—600 °С вне исследуемой зоны. На периферии бассейна изолинии потока и температуры, в основном, повторяют контуры геологических структур. В самом же бассейне экстраполяция потока и температуры на уровень Мохо дала более простую по сравнению с поверхностным потоком картину, хотя основные черты карты поверхностного потока присутствуют и на карте потока и температур на поверхности Мохо. Вместо ряда локальных максимумов была получена единая протяженная зона повышенных потоков и температур с простиранием СВ-ЮЗ, по обе строны от которой поток плавно спадает. Локальный минимум на южной периферии Большой Венгерской Равнины сохранился неизменным. Существование значительных региональных неоднородностей температуры, сконцентрированных на относительно небольшой территории Паннонского бассейна, по-видимому, будет иметь важное значение при интерпретации его геотектонической эволюции (как и в случае других гипертермальных зон: островные дуги-окраинные моря, рифтовые зоны и т. д.).

Сравнивая полученные в верхней мантии температуры с кривой пиролитового солидуса *Clark* and *Ringwood* [1964], легко заметить, что температуры плавления достигаются уже на сравнительно небольших глубинах, то есть верхняя мантия под Паннонским бассейном, вероятно, частично расплавлена. Указывает на высокие и возможность частичного расплавления также малая глубина слоя высокой проводимости (40—60 км), *Ádám* [1976] и высокая граница слоя низких скоростей — 74,5 км [*Bisztricsány*, 1974] для Карпатского бассейна, хотя с другоий стороны сейсмические скорости в коре и верхней мантии под бассейном и затухание нормальное. Кроме того, в зоне максимальной прогретости (ось СВ-ЮЗ, по которой почти полностью проходит профиль IP-III) не только в верхней мантии, но и в нижней коре могут достигать ся температуры, достаточные для плавления базальта, [*Yoder* and *Tilley*, 1962]. Возможно, что вероятность даже настоящего частичного плавления базальтового слоя в какой-то мере связана с уже упоминавшейся выше пониженной толщиной этого слоя в Паннонском бассейне. Зона минимальных глубин поверхности Мохо [*Mituch* and *Posgay*, 1972] также имеет простирание СВ-ЮЗ и совпадает с зоной максимальной прогретости.

Заключение

Совместный анализ геотермических данных и результатов геофизических, геологических и геохимических исследований показал, что в образовании тепловой аномалии Паннонского бассейна решающую роль играет верхняя мантия. Составляющая теплового потока, появляющаяся благодаря генерации тепла в коре, дает не более одной трети

наблюдаемого потока. Из-за почти горизонтального характера границ основных слоев, эта составляющая сохраняет устойчивые значения в пределах почти всей обширной территории бассейна. Сложный характер вариаций наблюдаемого потока и его повышенная величина почти полностью связаны с неравномерностью потока, приходящего из верхней мантии и в значительной степени повторяют его.

Более чем вероятно существование, по крайней мере в прошлом, в верхней мантии Паннонского бассейна других источников тепла, помимо радиоактивного нагрева. Поскольку настоящая форма бассейна является результатом крупномасштабных тектонических движений, имевших место в этом районе с триасса по миоцен, можно предположить, что образование тепловой аномалии явилось следствием процесса вторичной вынужденной конвекции, неизбежно возникающей в вязкой астеносфере при любого рода перемещениях в ней твердых литосферных плит. Отличительной чертой процесса вторичной вынужденной конвекции, хорошо изученного для систем островная дуга – окраинное море, например, *Oxburgh* and *Turcotte* [1968], *Andrews* and *Sleep* [1974], *Bodri* and *Bodri* [1978], является то, что литосфера ведет себя в этом случае как упругое тело, а астеносфера может моделироваться как очень вязкая жидкость. То есть астеносфера в достаточной мере обладает свойствами жидкости для того, чтобы в ней могли возникнуть конвективные течения, но тем не менее она имеет достаточно большую вязкость, для того чтобы напряжения, вызванные конвективными потоками, индуцированными нисходящей океанической литосферной плитой на границе взаимодействия литосфера-астеносфера достигали и превышали несколько сотен МРа. Механически это означает превышение предела прочности материала литосферы, растяжение и разлом литосферных плит, а с точки зрения геотермики приводит к тому, что на всей подошве литосферы и материала лито феры, растяжение и разлом литосферных плут, а с точки частью в астеносфере вблизи погружающейся плиты и на восходящей ветви конвективного потока (например, под окраиным морем) преобладающим становится механизм нагревания трением. Тепловой поток существенно возрастает, температуры достигают температур плавления. Менее существенную роль, зависящую от скорости субдукции и вязкости астеносферы, играет механизм переноса тепла при макроскопическом движении горячего материала. В результате действия механизма нагревания трением все районы вторичной вынужденной конвекции отличаются повышенной термической активностью. При этом легко показать, что из-за малой теплопроводности литосферы картина теплового поля, порожденного конвекцией не теряет своих основных черт даже через 10–20 млн.лет после прекращения конвекции [*Bodri* and *Bodri*, 1979]. В принципе, анализ современного теплового поля Паннонского бассейна мог бы дать существенную информацию о конвективных движениях в прошлом, хотя малая изученность динамики процессов взаимодействия континентальных плит в настоящее время еще не позволяет с абсолютной точностью связать наблюдаемые геотермические скачки с конкретной конфигурацией конвекционного потока.

В заключение отметим, что рассмотренная модель распределения теплофизических свойств и температуры в коре Паннонского бассейна не является единственно возможной. По мере накопления фактического материала предложенная в настоящей работе геотермическая модель, которую пока можно считать лишь первым приближением к реальным условиям, осуществляющимся в Паннонском бассейне, будет пересматриваться, уточняться и усложняться.

Уточнение математической постановки задачи, более детальное измерение теплофизических свойств пород в пределах отдельных тектонических зон бассейна в нормальных и повышенных термодинамических условиях, установление эмпирических зависимостей, например, величины теплового потока от возраста геологических структур или зависимости между физическими параметрами и составом пород, наряду с оценками геотермических градиентов и температур независимыми методами, позволит существенно уменьшить неоднозначность интерпретации геотермических данных.

ЛИТЕРАТУРА

Andrews, D. J. and Sleep, N. H., (1974.) Numerical modelling of tectonic flow behind island arcs. Geophys. J. R. Astron. Soc., 38: 237–251.

Ádám, A., (1976). Connection between geoelectric and geothermal parameters in the earth. In: A. Ádám (Editor-in-Chief), Geoelectric and Geothermal Studies (East-Central Europe, Soviet Asia). KAPG Geophysical Monograph, Budapest, pp. 567–571.

Beránek, B., Weiss, J., Hrdlicka, A., Dudek, A., Zounkova, A., Suk, M., Feifar, M., Militzer, H., Knothe, H., Mituch, E., Posgay, K., Uchman, J., Sollogub, V. B., Chekunov, A. V., Prosden, D., Milovanovic, B. and Roksandic, M. (1972). The results of the measurements along the international profiles. In: Gy. Szénás (Editor), The Crustal Structure of Central and Southeastern Europe Based on the Results of Explosion Seismology. Geophys. Transaction of Hung. Geophys. Inst. R. Eötvös, Special Edition, Budapest, pp. 133–139.

Bélteky, L. and Korim, K. (1971). A hazai hévízfeltárás eredményei (1965–1970). In: K. Stelczer (Editor-in-Chief), Magyarország Hévízkútjai II. VITUKI Special Edition, Budapest, pp. 7–255.

Birch, F. and Clark, H. (1940): The thermal conductivity of rocks and its dependence on temperature and composition. *Am. J. Sci.*, 258: 529–558.

Bisztricsány, E. (1974): The depth of of the LVL in Europe and some adjacent regions. Geofizikai Közlemények, 22:61–68.

Bodri, L. (1976): Deep temperature and heat flow in the Pannonian basin. Ph. D. Thesis, Eötvös Universitity, Budapest.

Bodri, L. (1979): Application of ion-geothermometers SiO_2, Na–K–Ca and Na–K–Ca–Ca–CO_2 for estimation of temperature in water-wells of the Pannonian basin (unpublished).

Bodri, L. and Bodri, B. (1978): Numerical investigation of tectonic flow in island-arc areas. In: M. N. Toksöz (Editor), Numerical Modeling in Geodynamics. Tectonophysics, 50: 163–175.

Bodri, L. and Bodri, B., (1979.) Induced convection – a possible source mechanism of heat anomaly of the Pannonian basin. Acta Geol. Hung., 21:277–285.

Boldizsár, T. (1975): Research and development of geothermal energy production in Hungary. Geothermics, 4: 44–56.

Buntebarth, G. (1975): Geophysikalische Untersuchungen über die Verteilung von Uran, Thorium und Kalium in der Erdkruste sovie deren Anwendung auf Temperaturberechnungen für Verschiedene Krustentypen. Ph. D. Thesis, Univ. of Clausthal.

Buntebarth, G. (1976): Temperature calculations on the Hungarian seismic profile-section NP–2. In: A. Ádám (Editor-in Chief), Geoelectric and Geothermal Studies (East-Central Europe, Soviet Asia). KAPG Geophysical Monograph, Budapest, pp. 561–566.

Clark, S. P. and Ringwood, A. E. (1964): Density distribution and constitution of the mantle. Rev. Geophys., 2: 35–88.

Čermák, V. (1975): Temperature-depth profiles in Czechoslovakia and some adjacent areas derived from heat flow measurements, deep seismic sounding and other geophysical data. Tectonophysics, 26: 103–119.

Čermák, V. and Hurtig, E. (Editors) (1977): Preliminary Heat Flow Map of Europe. A Contribution to International Geodynamics Project. Edited by the the Geophysical Institute, Czechosl. Acad. Sci., Praha.

Juhász, P., (1977): Olajipari fúrások karotázshőmérséklet értékeinek feldolgozása. Magyar Geofizika, 18: 201–210.

Kappelmeyer, O. and Haenel, R., (1974.): Geothermics with Special Reference to Application. Gebrüder Borntraeger, Berlin-Stuttgart, 327 pp.

Kutas, R. I. (1977): Thermal model of the crust of the Ukrainian Shield along DSS-profile VIII. Geophys. Collection Acad. Sci. USSR, Naoukova dumka, Kiev, 80: 3–10 (in Russian).

Lachenbruch, A. H. (1971): Vertical gradients of heat production in the continental crust. Theoretical detectability from near-surface measurements. J. Geophys. Res., 76: 3842–3851.

Lubimova, E. A. (1968): Thermal Studies of the Earth and Moon. Naouka, Moscow, pp. 280 (in Russian).

Mituch, E. and Posgay, K. (1972): The results of DSS measurements in the cooperating countries: Hungary. In: Gy. Szénás ((Editor), The Crustal Structure of Central and Southeastern Europe Based on the Results of Explosion Seismilogy. Geophys. Transactions of Hung. Geophys. Inst. R. Eötvös, Special Edition, Budapest, pp. 118–131.

Oxburgh, E. R. and Turcotte, D. L. (1968): Problem of high heat flow and volcanism associated with zones of descending mantle convective flow. Nature, 218: 1041–1043.

Roy, R. F. (1963): Heat flow measurement in the United States. Ph. D. Thesis, Harvard Univ., Cambridge, Mass.

Rybach, L. (1976): Radioactive heat production in rocks and its relation to other petrophysical parameters. PAGEOPH., 114: 309–317.

Yoder, H. S. and Tilley, C. E. (1962): Origin of basalt magmas; an experimental study of natural and synthetic rock systems. J. Petrol., 3: 342–532.

STRUCTURE OF PRECIOUS OPAL FROM ČERVENICA

DÓDONY, I.

Mineralogical Department of Eötvös Loránd University, Budapest, Múzeum krt. 4/A

TAKÁCS, J.

Hungarian Academy of Sciences, Laboratory for Geochemical Research, Budapest, Budaörsi út 45.

Received: 6. October 1980.

ABSTRACT

The present paper expounds the structural basis of the unique play of colour of the precious opal from Červenica making use of the results of thermal, X-ray diffraction and in the first place, electron and light optical examinations. Underlining the role of optical space lattice in the generation of anisotropic colours, we presented the peculiarities of the morphological elements building up this lattice which differ from the results obtained previously. On this basis we interpreted the different play of colour of precious opals coming from different sites and referred to the possibility of their separation. With the aid of the employed preparation of samples and on the basis of the selective solubility in HF of the material we explained the formation of the optical lattice in the precious opal from Červenica.

Generalizing our examinations we stated that the effect of optical diffraction – superposing itself onto the light optical parameters of the mineral – has to be reckoned with in all the minerals where periodical inhomogeneities falling into the order of magnitude of the light wave-lenght are found.

Introduction

Schafarzik (1913) – referring to the works of *Behrens*, *Bauer* and *Quincke* – supposed a periodic change of the refractive index in precious opal in accordance with the order of magnitude of light wave-length. For the correct explanation of the play of colour the first data were supplied by the detailed investigations of *Baier* (1932). On the basis of the anisotropy of colours he proved indirectly the lamellar structure of the – otherwise X-ray amorphous – precious opal which he regarded as pseudomorph after calcite.

With the development of examination methods *Pense* (1963) and simultaneously *Sanders* (1964) made visible the optical lattice consisting of periodically repeated grains in the three directions of space by means of electron microscope using replica method. In Australian opals *Sanders* detected spherical grains of 1500 to 3500 Å. Furthermore, he stated (1968) that these are linked according to the closest cubic and hexagonal symmetry and with clearly visible intervals, respectively.

The diffraction of light – on the lattice of periodically located voids – was discussed by Baier (1966) with reference to his earlier work and by *Sanders* (1968) on the basis of measurements made with the aid of his optical diffractometer. With this method, the structure of precious opals

from different sites and of synthetic ones can be well described. According to Sanders (1976), the star opals of Idaho contain, in addition to the symmetry above, dislocations and stacking faults in a great relative frequency.

Periodical inhomogeneities of the order of magnitude of light wavelength – detected in the last decade – are frequent in minerals (*Wenk*, 1976). Thus optical phenomena derived from the structure of precious opal can be generalized in mineral optics.

The present paper discusses the structural basis of the unique play of colour of the precious opals from Červenica (so-called Hungarian opals). The samples available were collected by ourselves in the Joseph-mine situated in Libanka Mountain in the proximity of Červenica from the fissure of pyroxene-andesite. The geological structure of the region was discussed by *Schafarzik* (1913).

The samples contain homogeneous, bluish-white, opaque milky opals and precious opals of violet-blue, green, yellow, red colour play in a bluish-grey potch. The colours appear in patches of >0.1 mm contacting each other and giving a macroscopically homogeneous impression.

In the course of our work, we employed thermal analyses, X-ray diffraction, light- and electron microscopic examinations.

Examinations

In the X-ray diffraction records of the samples a so-called "glass peak" of a great half-width can be detected at around 4.1 Å (Fig. 1) indicating the short-range order of the material.

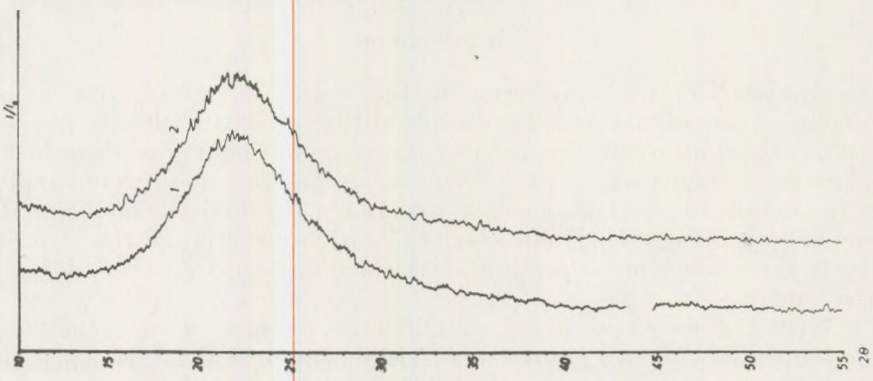

Fig. 1. X-ray pattern of the milky (1) and the precious (2) opals.

In the course of thermal analyses the precious opal lost its water content at a maximum temperature of 423 K, while milky opal at 473 K. The water content amounted to 6.8 per cent in the first case and to 5.7 per cent in the second (Fig. 2).

Accordingly, there is no interpetable difference between these two varieties.

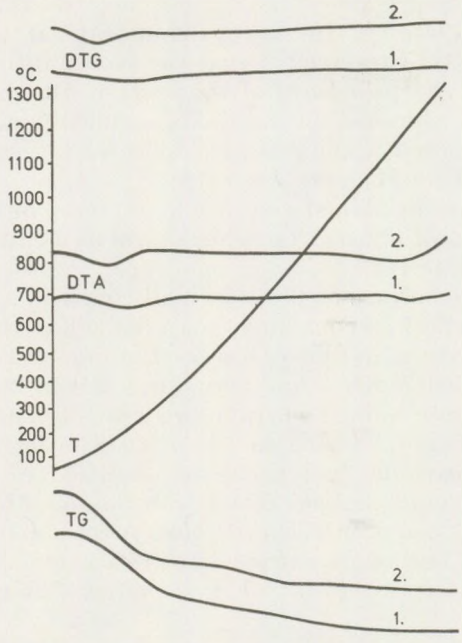

Fig. 2. DTG, DTA, TG curves of the milky (1) and the precious (2) opals.

TEM examinations

The exposures were made with the aid of an electron microscope type JEOL JEM 100 U with an accelerating voltage of 80 and 100 kV.

The morphology of fresh fracture surfaces was studied by means o the carbon replica method.

For direct examination of opal material two kinds of preparation were employed. The so-called drop preparation: a drop taken from a thin suspension in distilled water of the fine-ground sample material and evaporated on an amorphous carbon supporting film of approximately 100 Å thickness. By means of this method the fragments of the material which is suitable to transillumination by electron beam can be examined.

By pulverization we lose, however, the possibility of studying the characteristics found in larger areas. For the latter purpose, we took opal slides polished on both sides to $20-30$ μm thickness and further thinned by dissolving them with HF.

The electron diffraction pictures made from the drop preparations revealed the samples, in accordance with X-ray diffraction, being amorphous. In the amorphous basic material quantitatively negligible high-cristobalite can be defined from both opal varieties by means of SAED. Despite their small size (about 1 μm), they are no monocrystals. The diffraction pattern seen in Plate I/1 was made from an area of 0.4 μm diameter. Supposing that each diffraction point comes from the entire selected area, a Multi-Beam DF of the diffracted beams leads us to a topo-

graphic projection Plate I/2. In case of the instrument used, the disadvantage of the picture thus received is that the beams diffracted in different orders do not give sharp features of the surface. On the other hand, the different contrasts obtained in crystallographically different directions can clearly be discerned within the selected area i. e. we have no monocrystal even within the diameter of 0.4 μm.

The milky opal examined on carbon replicas forms a statistically random aggregation of spherical morphological elements of the same size: 0.08 to 0.25 μm (Plate I/3).

On the fracture surface of precious opal coursed "spotlike" voids can be detected in the otherwise continuous material (Plate I/4). Their periodicity varies locally within and also between the lines (Plate II/1). The size of areas of the same symmetry and periodicity is 1 to 20μm.

In the small slides thinned with HF to a few 100 Å angular morphological elements are found, located in geometrical order of low symmetry (Plate II/2). Their irregular, polygonal shapes differ from one another but their irregular, polygonal shapes differ from one another but their sizes are almost identical (between 2500 and 6000 Å) in a given area and orientation (Plate II/3). The single morphological elements show no crystalline structure. On the basis of their diffraction picture, their microstructure is amorphous.

Light optical examinations

Under polarizing microscope milky opal is optically isotropic. Under crossed nicols, the 50 to 60 μm thick slide of precious opal produces, various interference colours in patches contacting each other. In general, the extinc-

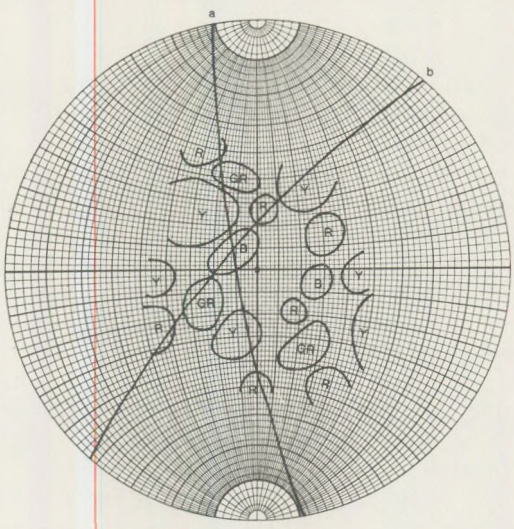

Fig. 3. Stereographical projection of the different colour of one gem opal's patch. B = blue, GR = green, Y = yellow, R = red.

tion of patches of 0.1 – X mm is not unified either. Similarly to the polysynthetic twin-lamellar structure of albite – when turning the stage – every second of the parallel bands change their colours simultaneously. The breadth of the bands amounts to X – 20 μm and their orientation varies from patch to patch.

Applying convergent light-beam (conoscope) it was stated that the precious opal of Červenica is optically biaxial, the value of 2V varying between 10 and 30°.

The anisotropy of the colours of one patch was investigated by means of a universal stage under unpolarized light. The diffracted colours of the opal slide enlighted by a light-beam falling upon it under varying angles of incidence can only be measured – as a result of the geometry of the universal stage – under a 100° cone angle. The flashing colours did not appear in discrete spots but in diffuse patches which were fixed in a Vulf-net (Fig. 3.). The light patches in the figure were evaluated as optical diffractogrammes.

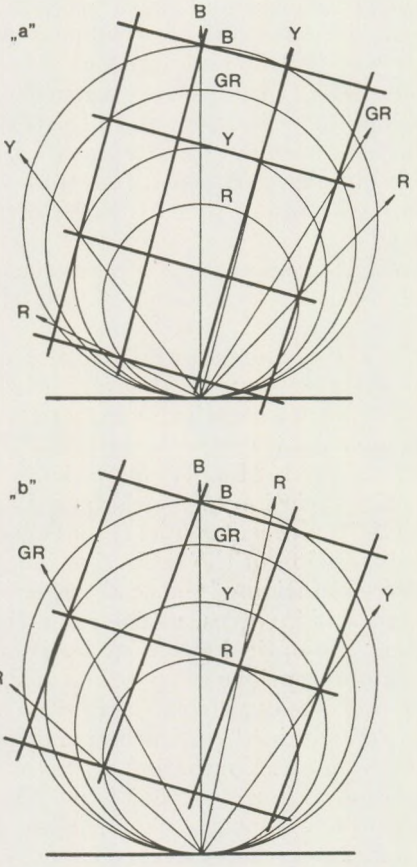

Fig. 4. Constructed reciprocal lattice sections from "a" and "b" planes in Fig. 3.

The parameters and the symmetry of the reciprocal lattice plotted by means of the Ewald-spheric method can be mutually co-ordinated with those experienced at the electron microscopic examinations (Fig. 4.). When plotting, the diffuse character of diffraction spots and the estimation of the wave-length of the individual colours, consequently the fluctuation of the radius length of Ewald-spheres were considered.

Interpretation

Numerous researchers dealt with the origin of the colour of precious opal. First indirectly then directly, they stated the connection between colours and structure in a correct manner. The present paper aims at supporting their results in this respect.

On the statistically inordinate particles of milky opal white light diffuses uniformly in every direction. In precious opal on the lattice of ordinate particles, the components of different wave-length of light are diffracted – according to their wave-length – in different directions; this is defined by the periodicities and the symmetry of the optical lattice.

In the course of our electron and light optical examinations, however, we experienced a number of differences in respect of the details. Contrary to the Australian opals, the precious opals of Červenica are not built up by spherical but by angular morphological elements filling the whole space.

The shapes of adjoining particles differ from one another while the Australian specimens are composed – within a given area – of uniform, isometric elements.

On the morphological elements of the precious opals from Červenica no primary particles of about 100 Å, as mentioned by *Darragh* et al. (1966), are found.

The solubility in HF of the material varies locally. As a result, simultaneously dissolved surfaces present identical brightness in the electron microscopic pictures. Parts of identical contrast form a network as found in the replicas. Varying solubility proves the periodical change of the composition and density of opal. Mrs. Wojnarovich (Thesis of candidature, 1980) defined the radial variation of the composition of glass fibres.

In our opinion, in the precious opal from Červenica the light scattering is caused by the variation of the refractive index. In spite of its amorphous structure the composition of the opal material changes periodically in every direction and this involves, at the same time, a variation of the refractive index. Thus, the optical space lattice is created by the parts of different indices. Our observations support the assumptions of *Schafarzik* (1973) in case of the precious opal from Červenica.

The specimens we examined possess varying periodicity in different directions and low symmetry. Comparing with the results of the optical analysis, the 2V obtained also shows that it may be orthorhombic at the maximum. The Ewald-plotting supports a triclinic symmetry in contrast to the hexagonal and cubic respectively closest packing of Australian opals.

The diffuse colour patches of the light diffractogramme fixed in the Vulf-net can be correlated unanimously with the values of the periodicity of the morphological elements varying in a given direction. The location and number of patches indicate a low symmetry of order.

In the replica pictures the stripped appearance of the individual coloured patches originates from the fact that the periodicity of the optical lattice remains constant within a short distance (< 20 μm) only in one given direction.

If different sites can be characterized according to precious opals of different symmetries, they can be separated – on the basis of evaluating the diffraction of the measured light patches – by means of a universal stage. This procedure is non-destructive and in addition much cheaper and more easily available than TEM examinations.

The morphological elements of different shape, periodicity and symmetry explain also the different play of colour of various precious opals. Spherical elements give a more uniform light diffusion than angular ones, consequently the intensity of colours is greater in the former case to which a higher order may also contribute. In the latter case, the intensity of the colours occuring in a greater solid angle interval is smaller, their appearance is more "velvety".

An optical lattice of small periodicity and high symmetry results in the reduction of the number of colours. Low symmetry and greater periodicity cause the appearance of more colours.

Researchers discussing precious opal, e. g. *Baier* (1932), *Sanders* (1975) made their investigations also upon so-called Hungarian opals. As – on the basis of their publications – their results are different from those we obtained, concerning the symmetry and the shape of morphological elements, there are the following alternatives:

- either they did not examine Hungarian opals,
- or, and this is more probable, the samples were not taken from the mines from which we collected ours.

In the latter case, the precious opals coming from various mines of the surroundings of Červenica consist of morphological elements of different order and shape. Consequently, they can be separated according to their sites on the basis of their structure.

Discussion

Generalizing our investigations we can state that the phenomenon of optical diffraction appears in all minerals containing periodical ihnomogeneities of a size falling into the order of magnitude of light wave-length. The play of colour of labradorite and moonstone (adular) can also be attributed to similar reasons. Much more significant is this phenomenon, however, for light microscopic examinations in general application. The most important rock forming minerals e. g. pyroxenes, amphiboles and feldspars often contain periodical inhomogeneities falling into the order

of magnitude of light wave-length. In such cases the effect of optical diffraction is superposed onto the optical parameters of the mineral resulting in an irregular image of the axes and an anomalous 2V. The deviations from the light optical defining curves of individual mineral groups can be interpreted also in light of this fact.

* * *

Plate I.

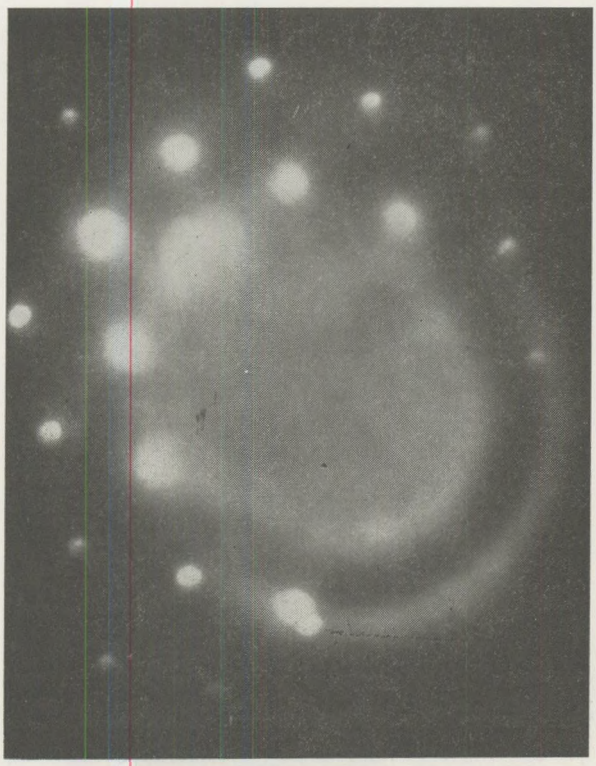

1. SAED pattern of the high-cristobalite. The electron-beam parallel with the [111].

Plate I/a.

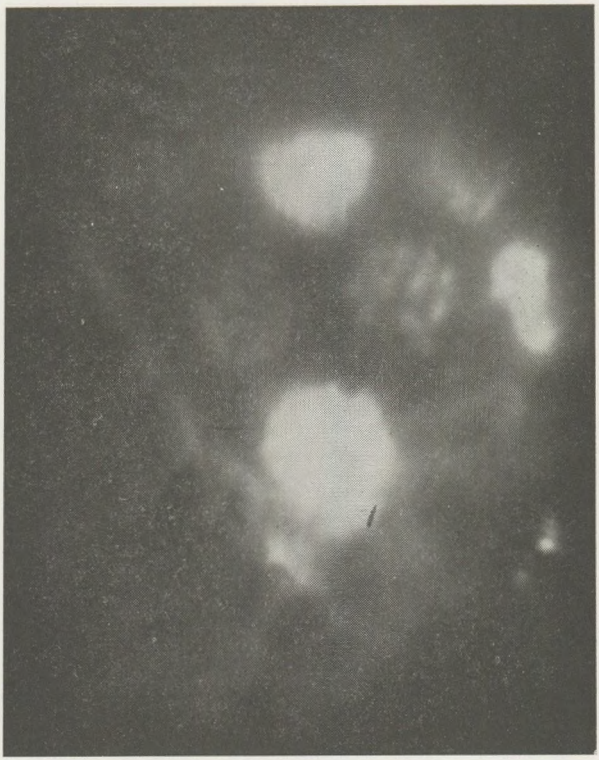

2. Multi-Beam DF image from the same grain as are shown in Plate I/1

Plate I/b.

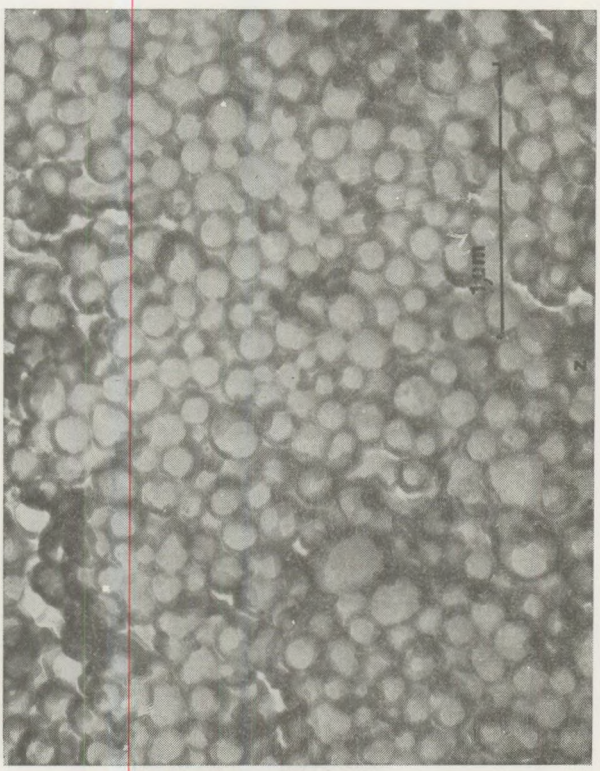

3. Electron micrograph of the milky opal's replica.

Plate I/c.

4. Electron micrograph of the precious opal's replica.

Plate II.

1. Electron micrograph of the precious opal's replica.

Plate II/a.

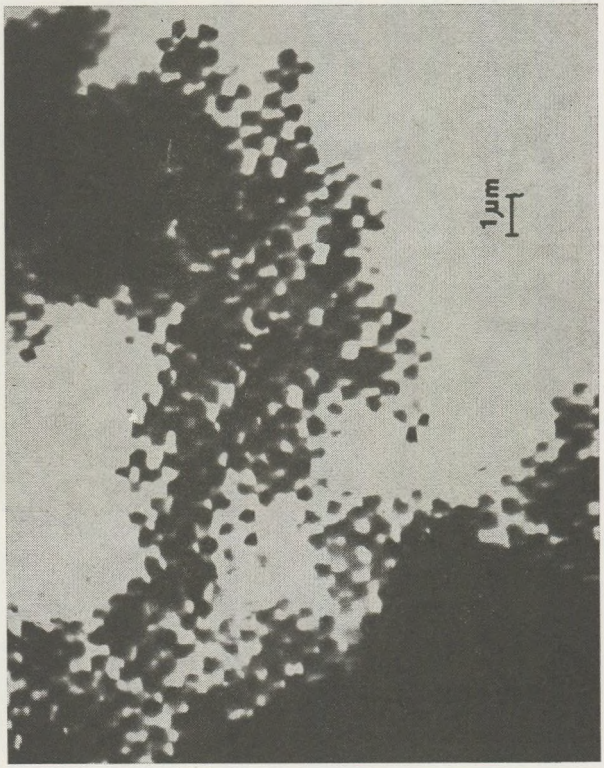

2. Electron micrograph of the HF thinned precious opal.

Plate II/b.

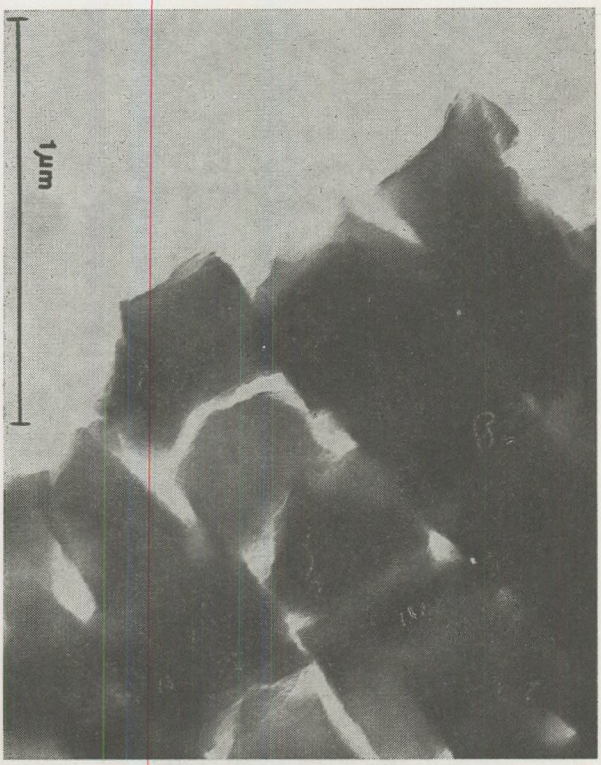

3. Electron micrograph of the HF thinned precious opal.

REFERENCES

Schafarzik, F. (1913): A magyar nemesopálról. Természettudományi Közlöny, XLV 576–577 f., p. 1–25.
Baier, E. (1932): Die Optik der Edelopale. Z. Kristallogr., A 83, p. 183–218.
Pense, J.)1963): Elektronenmikroskopischer Beitrag zur Optik der Edelopale. Fortschr. Min., 41, p. 166.
Jones, J. B., Sanders, J. V., Segnit, E. R. (1964): Structure of opal. Nature, 204, p. 990–991.
Sanders, J. V. (1968): Diffraction of light by opals. Acta Cryst., A 24, p. 427–434.
Baier, E. (1966): Diffraction lattices in precious opal. Experientia, XXII/3, p. 129–133.
Sanders, J. V. (1976): The structure of star opals. Acta Cryst., A 32, p. 334–338.
Wenk, H. R. (ed.) (1976): Electron microscopy in mineralogy. Springer-Verlag, Berlin–Heidelberg–New York.
Sanders, J. V. (1975): Microstructure and Crystallinity of Gem Opals. Amer. Min., 60, p. 749–757.

DATA FOR EVALUATING SOLAR ENERGY IN HUNGARY

FELMÉRY L.

Department of Meteorology, Eötvös Loránd University
H – 1088 Budapest, Múzeum krt. 4.

Received: 12. February 1981.

SUMMARY

The study presents data about the possible application of solar energy in Hungary. Climatic characteristics have been established and presented in tables from 20 years long measurement series (1950 – 1970). The climatic potential of solar radiation is discussed in details.

"Sharing the Sun" was the headline of the conference held by the International Solar Energy Society in Winnipeg, Canada, between 15th and 20th August, 1976. A remarkable sentence from its subjectmatter: "The sun offers great hope of alleviating the world's energy problems, but research and development on a massive scale are necessary before this as yet untapped energy source can be usefully harnessed".

The direct application of solar energy for power production in a given country needs complex and extensive research activity. The first step is to determine the solar energy potential of the local climate. It is the duty of climatology. The second step is a technical one, namely to develop adequate receptors or adapt them from well-developed industrial countries. The third step is to do thorough, careful prognostic calculations. That is as important as the former two. These technical and economic considerations generally have the impact of intense disputes and gave birth to controversial opinions. To cite a sceptical view: "... the transformation and accumulation of solar energy, as well as its storing for night and winter is certainly an unprofitable, irrational and technically difficult task. In my opinion the soft solar energy is rather a source of the past than the future." (*Marx Gy.*, Népszabadság, 1978. Dec. 24.) Simultaneously it is known that the government's energy strategy in the U.S. aims to reach a 20 percentage share of solar energy in the power consumption of the country. Several methods are known already for the conversion of solar energy into suitable forms: as from the most simple *collectors* through the *sun-boilers*, heated by solar radiation, to the *solar cells*, which are the most promising methods for direct power production. Hungary has also started the technical researches, carried on in the Architectural Research Institute.

The present study deals only with the climatological aspects of this problem, and discusses the potential of solar radiation energy in the climate

of Hungary. The interpretation is based on the data of a 20 years long period of homogenous solar radiation observations of the Martonvásár – Erdőhát Meteorological Station from 1951 to 1970. This station represents a *medium situation*, both in its geographical ($\varphi = 47°21'$ N; $\lambda = 18°49'$ E., H = 150 m), and in its air quality aspects. This latter means that, at a 30 km distance from Budapest, the airpollution of the metropolitan area has little influence, but the undisturbed natural environment still not prevails owing to the proximity of the Százhalombatta industrial area. Thus the conditions do not meet the requirements for air-quality standards of the regional background, but practically this is the situation over the majority of the area of our country. So this series of data can be accepted as a representative sample.

Detailed data have been published recently about solar radiation in Hungary, providing valuable contribution to our climatological knowledge (*Major*, 1976). In this publication calorical data are presented for a 15 years period (1958 – 1972) in form of figures (diagrams), maps and tables. These presentations do not provide directly applicable informations for climatic characteristics suitable for further planning. Our homogenous data of the 20 years long observation in suitable detailed tables may serve valuable supplementary informations for these purposes.

The data are grouped on annual, monthly, daily and per hour tables in order to meet the demands of technical design. The data represent the values of global (direct and diffuse) radiation on horizontal units in J. cm^{-2}. (If these values are multiplied by 10, the values can be converted to the more common dimensions of kJ m^{-2}).

Table 1 and 2 show the average values of global radiation in monthly, daily and per hour basis, the minimum and maximum values, and the standard deviations of the values. Table 3 summarizes the duration probabilities of the daily values. As Table 2 includes the percentage distribution of the per hour values, too, the three tables provide almost all of the necessary informations for designing problems. For example it can be seen from Table 3 that a small amount of thermical energy can be counted in whole January, 31 days (100%), but the daily average values of solar radiation reaches the 628 J (150 cal) level only in 3 days during January. Further on if we divide this 628 J daily average value (9,8%, approximately 10%) with the percentage values of Table 2, we get, that in January, between 12°° and 13°° the probability of having a $+116$ J $cm^{-2}h^{-1}$ (28 cal) radiation is 10%, etc. etc.

Table 1.

Monthly averages of global radiation
($J\ cm^{-2} \cdot month^{-1}$)
(20 years long averages)

	I.	II.	III.	IV.	V	VI.	VII.	VIII.	IX.	X.	XI.	XII.
1.	11 145	16 911	32 042	47 118	59 231	65 775	66 855	58 042	40 424	26 055	12 238	7 762
2.	7 381	11 757	22 559	38 795	44 430	58 929	55 484	50 170	30 082	20 235	4 899	4 915
(in year)	(1952)	(1952)	(1964)	(1965)	(1957)	(1963)	(1960)	(1968)	(1951)	(1964)	(1962)	(1959)
3.	14 143	23 195	48 760	55 705	82 275	81 680	83 087	70 811	45 866	33 365	15 374	11 095
(in year)	(1954)	(1956)	(1953)	(1953)	(1958)	(1957)	(1952)	(1958)	(1956)	(1959)	(1969)	(1967)
4.	6 762	11 438	26 201	16 910	37 845	22 751	27 603	20 641	15 784	13 130	10 475	6 180

1. Summarized monthly averages
2. Minimum value of the month
3. Maximum value of the month
4. Range Δ

Table 2.
The average per hour and daily

Hours		4–5	5–6	6–7	7–8	8–9	9–10	10–11	11–12	12–13	13–14
I.	J cm^{-2}	–	–	–	1.2	7.0	2 5.0	45.3	60.4	65.5	57.8
	%	–	–	–	0.3	2.0	7.1	12.8	17.1	18.5	16.3
II.	J cm^{-2}	–	–	0.3	4.3	22.4	50.9	76.4	93.1	97.0	91.2
	%	–	–	–	0.8	4.1	9.4	14.0	17.1	17.8	16.8
III.	J cm^{-2}	–	1.0	4.1	25.8	63.2	101.7	128.6	142.4	140.6	130.7
	%	–	0.1	0.4	2.6	6.3	10.1	12.8	14.2	14.0	13.0
IV.	J cm^{-2}	–	10.3	27.4	71.3	118.1	154.9	178.4	187.6	187.5	174.3
	%	–	0.7	1.8	4.7	7.7	10.1	11.7	12.3	12.3	11.4
V.	J cm^{-2}	2.9	18.7	60.7	105.2	149.5	181.0	198.9	208.0	206.0	192.9
	%	0.2	1.0	3.3	5.7	8.1	9.8	10.7	11.2	11.1	10.4
VI.	J cm^{-2}	5.4	31.7	80.2	123.2	165.9	201.8	223.5	231.7	228.2	211.4
	%	0.3	1.5	3.8	5.8	7.8	9.5	10.5	10.9	10.7	9.9
VII.	J cm^{-2}	5.0	25.5	69.1	117.6	165.0	197.6	217.3	228.2	227.3	216.5
	%	0.2	1.2	3.3	5.6	7.9	9.5	10.4	10.9	10.9	10.4
VIII.	J cm^{-2}	0.4	8.8	44.4	95.9	143.6	180.9	207.3	215.6	209.3	199.7
	%	–	0.5	2.4	5.3	7.9	10.0	11.4	11.9	11.5	11.0
IX.	J cm^{-2}	–	2.5	17.6	57.4	104.7	141.9	167,1	178.4	173.3	159.5
	%	–	0.2	1.3	4.4	8.0	10.8	12.8	13.6	13.2	12.2
X.	J cm^{-2}	–	–	2.9	21.8	55.7	91.3	117.2	129.4	123.5	111.0
	%	–	–	–	2.7	6.9	11.2	14.4	15.9	15.2	13.7
XI.	J cm^{-2}	–	–	0.4	4.6	17.2	36.0	54.0	64.5	61.1	54.0
	%	–	–	0.1	1.3	4.8	10.0	15.1	18.0	17.0	15.1
XII.	J cm^{-2}	–	–	–	0.8	7.1	20.5	35.6	46.1	45.6	39.4
	%	–	–	–	0.3	2.9	8.4	14.5	18.8	18.6	16.1

1. Average summarized daily values
2. Min. summarized daily values
3. Max. summarized daily values
4. Standard deviation of summarized daily values σ

values of global radiation ($J \cdot cm^{-2}$)

14–15	15–16	16–17	17–18	18–19	19–20	1	2	3	4
47.5	28.3	9.6	5.7	0.3	–	359	29	846	193
13.4	8.0	2.7	1.6	0.1	–	100	8	236	54
73.7	48.4	23.1	5.1	0.1	–	586	13	1403	297
13.5	8.9	4.2	0.9	–	–	100	2	239	51
111.7	77.7	49.3	21.9	4.6	1.8	1005	88	2177	452
11.1	7.7	4.9	2.2	0.5	0.2	100	8	216	45
149.1	117.5	83.9	48.3	16.4	0.9	1528	197	2835	540
9.8	7.7	5.5	3.2	1.1	0 1	100	13	186	35
170.3	141.6	108.5	70.2	30.4	8.9	1855	327	3308	632
9.2	7.6	5.9	3.8	1.6	0.5	100	18	178	34
192.5	162.9	128.1	89.8	44.2	15.5	2135	205	3475	624
9.0	7.6	6.0	4.2	2.1	0.7	100	10	163	29
193.8	163.7	127.7	87.9	37.3	12.1	2093	297	3228	569
9.3	7.8	6.1	4.2	1.8	0.6	100	14	154	27
168.7	141,9	106,8	65,3	23,0	5,0	1718	364	2968	486
9.3	7.8	5.9	3.6	1.3	0.3	100	20	163	27
132.7	83.7	57.4	27.2	6.3	–	1311	53	2211	427
10.1	6.4	4.4	2.1	0.5	–	100	4	169	33
85.4	46.9	22.2	5.4	–	–	816	34	1524	322
10.5	5.8	2.7	0.7	–	–	100	4	187	40
40.2	20.5	5.9	0.4	–	–	360	13	976	222
11.2	5.7	1.6	0.1	–	–	100	3	270	62
30.1	15.1	4.6	–	–	–	247	17	682	151
12.3	6.2	1.9	–	–	–	100	7	276	61

The probabilities of the duration daily values* Table 3.

Months	J cm^{-2} day^{-1}	Frequency %	Duration	
			%	day
January	754 — 880	3.0	3.0	1.8
	628 — 753	6.8	9.8	3.0
	502 — 627	12.5	22.3	6.9
	377 — 501	19.4	41.7	12.9
	251 — 376	20.6	62.3	19.3
	126 — 250	25.3	87.6	27.2
	0 — 125	12.4	100.0	31.0
		100.0		
February	1340 — 1425	0.4	0.4	0.1
	1173 — 1339	2.2	2.6	0.7
	1005 — 1172	7.0	9.6	2.7
	838 — 1004	10.6	20.2	5.6
	670 — 837	20.6	40.8	11.4
	502 — 669	16.6	57.4	16.1
	335 — 501	18.1	75.5	21.1
	168 — 334	17.0	92.5	25.9
	0 — 167	7·5	100.0	28.0
		100.0		
March	1884 — 2099	1.8	1.8	0.6
	1675 — 1883	5.7	7.5	2.3
	1466 — 1674	10.4	17.9	5.5
	1256 — 1465	13.0	30.9	9.6
	1047 — 1255	15.5	46.4	14.4
	838 — 1046	17.0	63.4	19.6
	628 — 837	12.7	76.1	23.6
	419 — 627	12.3	88.4	27.4
	210 — 418	9.2	97.6	30.3
	80 — 209	2.4	100.0	31.0
		100.0		

* The boundaries of the intervals seem to be arbitrary due to the conversion of the original caloric values to Joule.

Months	J cm^{-2} day^{-1}	Frequency %	Duration	
			%	day
April	2638 – 2850	1.0	1.0	0.3
	2345 – 2637	4.2	5.2	1.6
	2052 – 2344	12.3	17.5	5.2
	1759 – 2051	17.8	35.3	10.6
	1466 – 1758	22.9	58.2	17.5
	1173 – 1465	16.0	74.2	22.3
	880 – 1172	11.6	85.8	25.7
	587 – 879	8.0	93.8	28.1
	293 – 586	4.9	98.7	29.6
	165 – 292	1.2	100.0	30.0
		100.0		
May	3015 – 3349	2.1	2.1	0.6
	2680 – 3014	6.5	8.6	2.7
	2345 – 2679	15.1	23.7	7.3
	2010 – 2344	19.4	43.1	13.4
	1675 – 2009	19.0	62.1	19.2
	1340 – 1674	15.5	77.6	24.0
	1005 – 1339	11.0	88.6	27.5
	670 – 1004	6.7	95.3	29.5
	335 – 669	4.4	99.7	30.9
	290 – 334	0.3	100.0	31.0
		100.0		
June	3350 – 3520	0.3	0.3	0.1
	3015 – 3349	4.5	4.8	1.4
	2680 – 3014	15.4	20.2	6.1
	2345 – 2679	20.8	41.0	12.3
	2010 – 2344	19.3	60.3	18.1
	1675 – 2009	17.2	77.5	23.2
	1340 – 1674	9.8	87.3	26.2
	1005 – 1339	7.0	94.3	28.3
	670 – 1004	3.9	98.2	29.4
	335 – 669	1.3	99.5	29.8
	167 – 334	0.5	100.0	30.0
		100.0		

Table 3. continued

Months	J cm^{-2} day^{-1}	Frequency %	Duration	
			%	day
July	2931 – 3265	2.7	2.7	0.9
	2512 – 2930	21.7	24.4	7.6
	2094 – 2511	31.7	56.1	17.5
	1675 – 2093	22.0	78.1	24.3
	1256 – 1674	12.7	90.8	28.2
	838 – 1255	5.7	96.5	29.8
	419 – 837	3.2	99.7	30.8
	290 – 418	0.3	100.0	31.0
		100.0		
August	2680 – 2974	1.5	1,5	0.5
	2345 – 2679	12.2	13.7	3.9
	2010 – 2344	25.0	38.7	12.0
	1675 – 2009	26.9	65.6	20.3
	1340 – 1674	17.2	82.8	25.7
	1005 – 1339	10.1	92.9	28.8
	670 – 1004	5.2	98.1	30.4
	335 – 669	1.9	100.0	31.0
		100.0		
September	2010 – 2220	3.0	3.0	0.9
	1759 – 2009	9.5	12.5	3.7
	1508 – 1758	24.0	36.5	10.9
	1256 – 1507	24.2	60.7	18.2
	1005 – 1255	18.6	79.3	23.8
	754 – 1004	8.2	87.5	26.2
	503 – 753	6.7	94.2	28.2
	252 – 502	3.8	98.0	29.4
	40 – 251	2.0	100.0	30.0
		100.0		

Table 3. continued

Months	J cm^{-2} day^{-1}	Frequency %	Duration	
			%	day
October	1508 – 1550	0.3	0.3	0.1
	1340 – 1507	3.2	3.5	1.1
	1173 – 1339	8.4	11.9	3.7
	1005 – 1172	18.7	30.6	9.5
	838 – 1004	23.3	53.9	16.7
	670 – 837	14.3	68.2	21.1
	503 – 669	12.3	80.5	24.9
	335 – 502	9.0	89.5	27.7
	168 – 334	8.1	97.6	30.2
	0 – 167	2.4	100.0	31.0
		100.0		
November	880 – 1005	0.8	0.8	0.3
	754 – 879	3.9	4.7	1.4
	629 – 753	9.6	14.3	4.3
	503 – 628	14.2	28.5	8.5
	377 – 502	17.1	45.6	13.7
	252 – 376	15.8	61.4	18.4
	126 – 251	21.3	82.7	24.8
	0 – 125	17.3	100.0	30.0
		100.0		
December	670 – 710	0.1	0.1	0.05
	587 – 669	1.3	1.4	0.4
	503 – 586	4.7	6.1	1.9
	419 – 502	10.1	16.2	5.0
	335 – 418	12.9	29.1	9.0
	252 – 334	13.4	42.5	13.2
	168 – 251	20.2	62.7	19,4
	84 – 167	23.7	86.4	26.8
	0 – 83	13.6	100.0	31.0
		100.0		

Table 4.

The annual parameters of global radiation
($kJ \cdot m^{-2}\ year^{-1}$)

Summarized annual average value:	$\overline{X}$ = 4423814.7 (for 20 years)
Min. summarized annual value:	Min = 3869231.2 (1960)
Max. summarized annual value:	Max = 5015953.8 (1953)
Range:	Δ = 1146722.6
Standard deviation:	δ = 298476.9
Lower quartile value:	Q_1 = 4222429.6
Upper quartile value:	Q_3 = 4613141.8
Median:	Me = 4443702.0

While Table 1 – 3 are suitable for direct applications, Table 4 provides data for the evaluation of the country's climatic potential. Compared to the regional normal values, Hungary has relatively high solar radiation values. The diagnosed normal value for the 47° latitude is 4333 MJ $m^{-2}year^{-1}$, but this value at Martonvásár – Erdőhát – representing an average condition in Hungary – is 4424 MJ $m^{-2}year^{-1}$, giving a 91 MJ $m^{-2}year^{-1}$ positive anomaly.

The data in Tables 1 – 4 are represented in Fig. 1. The minimum annual energy value is 3869 MJ $m^{-2}year^{-1}$, the maximum is 5016 MJ $m^{-2}year^{-1}$. To get more than 4222 MJ $m^{-2}year^{-1}$ value has a 75% probability. The distribution is moderately skew: $\overline{X} - Me < O$.

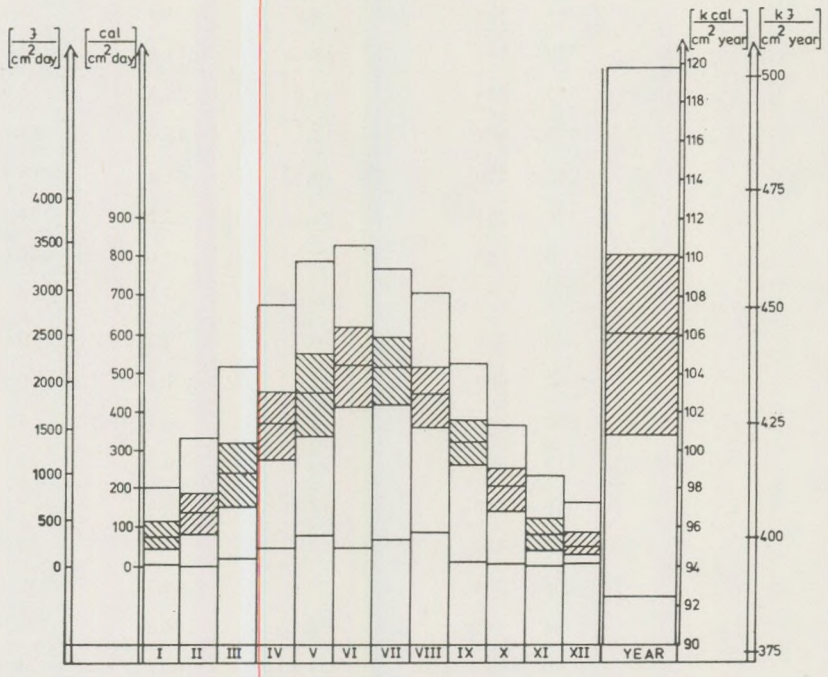

Fig. 1. Daily and annual values of global radiation. Minimum and maximum values, lower and upper quartile values, medians

There are different solar radiation receptors, some can accumulate only the global radiation, or only one of its components, mainly the direct radiation. In the above mentioned OMSZ publication (Major 1976) no informations are found regarding the direct radiation. Our tables neither obtain other data than global radiation ones (Table 1 – 4). However, the technology requires first of all the direct radiation data. Using an empirical formula, the rate of the direct radiation can be estimated. Felméry has found a relationship in 1974 between the ratio of direct to global radiation and the relative sunshine:

$$y = 0.10 + 0.75\,x$$

where x is the relative sunshine, y is the ratio of direct to global radiation. In this way the direct radiation can be obtained from Table 1. and 4. while data of sunshine were published in the Climatic Atlas of Hungary vol. II. (1967). This method also provides some basis for estimating direct radiation as the short-, medium- and long-term forecasts include estimates for the probable rate of cloudiness, too.

Finally a geographical aspect of solar energy application should be mentioned. The receptors of the high capacity solar energy power plants need large territories. Experts generally agree that good agricultural lands should not be used for this purpose but the deserts, which have no agricultural value, and exposed to intense solar radiation with clear sky are the best potential areas. There are no deserts in Hungary and in the neighbouring countries, but there are large areas covered by saltines, of no agricultural potential, and large karst areas like the Dinarides in Yugoslavia, in our vicinity. These karsts, though barren at first sight, have extremely clear atmosphere under the bright Mediterranean sky, providing ideal environment for solar energy plants.

REFERENCES

Felméry, L. (1974): Photosynthetically active radiation during the breeding season. (in Hungarian) Időjárás, v. 78. pp 235 – 239

Major, Gy.: (ed) (1976): Solar radiation in Hungary (1958 – 1972) (in Hungarian). OMSZ official publication. Budapest, 1976.

The Climatic Atlas of Hungary: vol II. Data, Akadémiai Kiadó, Budapest, 1967.

UNTERSUCHUNGEN DER FLUIDEN EINSCHLÜSSE IN DEN ERZHALTIGEN BILDUNGEN DES WEST-MATRAGEBIRGES

(Oberflächliche Indikationen)

GATTER I.

Mineralogisches Institut. Eötvös Universität. Budapest

(Eingegangen dem 15.1.1981.)

ZUSAMMENFASSUNG

Die Fragen im Zusammenhang mit den Entstehungsverhältnissen der hydrothermalen Tagegänge und anderer Ausbildungen im West-Matra wurden durch Untersuchungen der Gas-Flüssigkeitseinschlüsse beantwortet. Nach den Homogenisationsmessungen ist die Entstehungs (minimale)-temperatur 105 – 260°C. Im Zuge der kryoskopischen Untersuchungen sind die Zusammensetzungs-Konzentrationsverhältnisse der Fluide bekannt geworden: die Konzentration der Lösungen entspricht einem Äquivalent von 4 – 8 Gewichtsprozenten NaCl was, vermutlich, hauptsächlich aus Na-Ca-Clorid besteht. Ausserdem ist die Anwesenheit von CO_2 und bituminösen Kohlenwasserstoffen in einer kleinen Menge nachzuweisen. Das letztere ist aus der Tiefliegenden abzuleiten, durch die Migration des hydrothermalen Lösungssystems.

Bei weiteren regelmässigen Messungen auf dem untersuchten Gebiet besteht die Möglichkeit Gänge und andere oberflächliche Indikationen zu parallelisieren, Karten nach Temperatur- und Konzentrationsverteilung zu konstruieren und die Erosionsniveau zu klären.

Einführung

In der Umgebung der in andesit-piroklasstischem Band vorhandenen Erzindikationen im West-Matra (bei Gyöngyösoroszi) hat sich seit dem 18. Jahrhundert – mit mehreren Unterbrechungen – ein Erzbergbau herausgebildet, was auch noch heute funktioniert. Die wichtigsten Verfasser der Pb-Zn- (Cu) -Lagerstätte mit einer gangartigen Entwicklung sind: *Sztrokay*, K. 1939, *Rozlozsnik*, P. 1942, *Vidacs*, A. 1957, 1961, *Koch*, S. 1966, *Siklossy*, S. 1977 usw. Die Vererzung ist von polyzyklischem Charakter und enthält mehrere erzarme (sterile) bzw. sulfidreiche Phasen.

Die Gänge der Sulfidminerale hauptsächlich mit Quarz-Chalcedon- bzw. Baryt (Calcit)-begleitmineralen haben sich in einer bestimmten Streichrichtung angeordnet. Die Tagegänge sind – abgesehen von einigen Beispielen-von weniger klassischer Entwicklung, sie erscheinen nur selten in markanter Form eines Rückens oder Horstes. Die Gänge sind meistens als zerstreuter quarzhaltiger Gesteinsplitter zu finden. Die Gesteinveränderungen (Prophylisation, Verkieselung, Sialitisation usw.) sind in der Nähe der Gänge gut zu untersuchen.

Die von tektonischen Bewegungen verursachte Gliederung, die Streichrichtung der Gänge und die mit der mehrphasigen Vererzung zusammen-

hängenden Gangidentifikationsschwierigkeiten führen zur Überzeugung, dass solche moderne mineralogisch-geochemische Methoden müssen angewendet werden, die über den physisch-chemischen Zustand der Mineralbildung (PTX) zahlenmässige Parameter geben. In der Erzlagerstättenkunde ist der Begriff „geologisches Thermometer" schon seit langem bekannt. In dem betreffenden Fall gibt es mehrere Möglichkeiten zur Bestimmung der PT – Werte. Aufgrund von erzmikroskopisch – paragenetischen Untersuchungen (*Sztrókay*, K. 1939, *Koch*, S. 1966) ist die Vererzung in die „epi-(mezo)thermale Kategorie" zu ordnen. Weitere Angaben könnte die Spurenelementuntersuchung („Sphalerit-thermometer") von erzahltigen und erzleeren Mineralen leisten (*Scott, S. D., Kissin, S. A.* 1973), weiterhin „das Quarz-Al-Thermometer" – *Scotford, D. M.* 1975 (und die Verwendung der isomorphen Ersetzung der Calcitreihe als Thermometer-Capedri, S., *Rivalenti, G.* 1974), usw.

Zur Klärung der Fragen wurde die Methode der Untersuchung der Flüssigkeits-Gaseinschlüsse in Mineralen gewählt.

Die Untersuchungstechnik wird im Ausland heutzutage wieder immer bedeutender. Das wurde durch die Erfindung von immer präziseren Messgeräten und die Anwendung von feineren Musterpreparationsmethoden ermöglicht.

Untersuchung der erzlagerstättenkundlichen Fragen:

- Lagerstätten unsicherer Genese
- Gestreut-stockartige Lagerstättentype
- Lagerstätten von seltenen (wertvollen) Elementen oder Edelsteinen
- Anwendungen von erzgeologischen Reambulierungsuntersuchungen

Untersuchte Ausbildungen

Die Muster für die Untersuchung stammen aus dem Gebiet der Umgebung von Gyöngyösoroszi im West-Matra (Abb. 1). Die Anwendung der Methode wurde auf den folgenden Materialen durchgeführt:

Abb. 1.

Abb. 1.

a) Tagegänge

1. der Gang „Bányabérc" (Gangquarz)
   Tagegang in der Umgebung von alten Stollen „Nedveslyuk" und „Szárazlyuk"
2. Gang mit Baryt bei Kistölgyesbérc (Gangquarz)
   Tagegang und Splitter des alten Stollens im nördlich-westlichen Teil des Ganges und das Material der Grube „Tótrét"
3. Gang „Katalin" (Gangquarz)
   Gangsplitter aus oberflächlichem Tagegang
4. Gang bei Mátraszentimre (Gangquarz)
   Gangsplitter aus oberflächlichem Tagegang

b) „Geisirit" Ausbildungen

1. Baryt bei Asztagkő

c) die hydrothermale Gesteinbildung begleitende Quarzbildung

1. gequarztes Gestein bei Keresztesbérc

Mikroskopische Beobachtungen

Die mikroskopische Betrachtung der auf zwei Seiten polierten 0,1 – 0,5 mm dichten Schnittlagen, die aus Gangmaterialen und dicht gepackten kleinkörnigen Quarzaggregaten, aus aufgewachsenen Barytkristallen gefertigt wurden, ist in den folgenden zusammenzufassen:

Quarz

In den Gangmustern bzw. in dem gequarzten Material ist ein Quarz (Chalcedon) mit dreierlei morphologischen Sonderheiten nachzuweisen:

- fasrig-kugelförmiger, selbständiger oder Quarzstreifen trennender Chalcedon
- hypidomorfer Quarz, in Streifen angeordnet, und Chalcedon mit einem verblassenen Umriss
- Aggregat von xenomorfen, idiomorfen und optisch selten anormalen Körnern

Die Streifen wechseln sich oft untereinander, die letzte Ausscheidung (im allgemeinen aufgewachsener Quarz) ist schon eine xenomorfe Variante.

Baryt

Das besteht aus optisch monokristallen, idiomorfen Körnern.

Die genetische Klassifikation der Einschlüsse geschieht auf stofflich-strukturellem Grund im Vergleich zum Wirtmineral. Es sind zwei Klassifikationstype bekannt: ein sowjetischer (*Ermakov*, N. P. 1972) und ein amerikanischer (*Roedder, E.* 1967) Typ. In der Literatur ist der letzte verbreitet. Zu unterscheiden sind die mit der Mineralbildung gleichartigen, die Mineralisation folgenden Verschiebungen (pseudosekudär) und die Einschlüsse, die im späterem „Leben" des Minerals entstanden sind. Im Zuge der

Untersuchungen ist es möglich über die „ganze Geschichte" des Minerals Informationen zu bekommen. Die Mehrzahl unserer Messungen wurde an primär-syngenetischen Einschlüssen durchgeführt.

Die Einschlüsse befinden sich in den Körnern zerstreut, manchmal selbständig in der Mitte von grösseren Körpern (Bild 1), bei den Wachszonen des Minerals (Bild 2) oder in Streifen (Bild 3), in zersplitterten Körpern kommen sie bei den Klüften vor. Ihr Masstab ist zwischen 2 – 150 μ. Die zweiphasigen Einschlüsse enthalten im Durchschnitt eine Gasphase im Volumen von 10 – 30% bei Zimmertemperatur. Die mit den zweiphasigen Einschlüssen gleichartigen einphasigen (Gas)-Einschlüsse sind untergeordnet, sie erscheinen lieber mit einem stufenweisen Phasenproportionsübergang. Diese Erscheinung ist in den Barytmustern bekannt, ihre Ursache besteht darin, dass der hydrostatische Druck des Lösungssystems kleiner wurde als der Dampfdruck, also das System ist aufgekocht. In solchen Fällen wird bei der Bewertung der Untersuchungsangaben eine grössere Vorsicht gefordert.

In den Chalcedonmustern sind die Einschlüsse seltener zu beobachten, nur im Bereich zwischen den Bündeln sind einige zweiphasige Einschlüsse zu sehen.

An manchen Stellen, in den platten-oder fahnenförmigen sekundären Einschlüssen ist ein dunkelbrauner Tropfen „Erdöl" im Volumen von 10 – 20% zu finden, die Begleitsflüssigkeit ist dunkelbraun gefärbt.

Die in den fluiden Einschlüssen auftretenden festen Ausscheidungen („daughter minerals") können wichtige genetische Merkmale haben. Im Material der Grube „Tórét" in den Einschlüssen kamen kleine, nadel-und plattenförmige Kristallite vor, die letzteren bewiesen sich auf optischem Grund als Baryt. Durch diese Tatsache wird bestätigt, dass im Gang mit Baryt bei Kistölgyesbérc eine gemeinsame Baryt-Quarzausscheidung vorhanden ist. In den Mustern aus Bányabérc sind selten an der Wand der Einschlüsse genau nicht identifizierbare aufgewachsene kleine Nadeln zu beobachten (Bild 4).

Untersuchung der Phasenumwandlungen auf einem Mikroskoptisch mit veränderbarer Temperatur

Die Phasenumwandlungserscheinungen in den Flüssigkeit-und Gaseinsclüssen (Homogenisation, Heterogenisation, kryoskopische Messungen) wurden von uns auf einem Mikroskoptisch „CHAIXMECA", der in einem Intervall von −180 – +600 °C funktioniert und eine Genauigkeit von −100 – +100 ±0,2 °C, +400 ±1,2 °C hat *Poty*, B. et al. (1976), untersucht. Die zur Kalibration der Einrichtung angewendeten Verbindungen sind unter* zu sehen.

* Kaliumdikromat 398 °C, Natrium nitrat 306,8 °C, Phenolphthalein 261 °C, MERCK MSP no. 9847 247,0 °C, MERCK MSP no. 9800 2000 °C, MERCK MSP no. 9735 135,0 °C, MERCK MSP no. 9700 100,0 °C, MERCK MSP No. 9670 70 °C, Natriumsulfat (x 10 H_2O) 32,4 °C, Benzol 5,5 °C, Wasser 0,0 °C. Benzylalkohol – 15,3 °C, Kohlentetrachlorid – 22,8 °C, Chlorbenzol – 45,0 °C, „pro anal" CO_2 Einsschluss (Calanda, Schweiz) – 56,6 °C, Amylazetat – 70,8 °C, N-Kapronylwasserstoff – 94,3 °C.

Homogenisationsuntersuchungen

Wenn die zweiphasigen (Flüssigkeits-und Gas) Einschlüsse Salzlösung in kleiner Konzentration enthalten und das Wirtmetall sich in einem offenen System gebildet hat, weist die bestimmte Homogenisationstemperatur im Verhältnis zur realen Minimaltemperatur in dem hydrothermalen Temperaturbereich eine geringe Abweichung nach. Alles das wird von Vielzahl der laboratorischen Kristallwachsversuchen bestätigt (Naumov, V. B. 1976, Khetchikov, L. N. 1973).

Die nachträgliche Öffnung der Einschlüsse ist nach den stofflich-strukturellen Merkmalen und den Messangaben der Phasenumwandlung zu folgen (untergeordnete Erscheinung), die Migration bzw. Dispersion des den Hohlraum ausfüllenden Fluidums in dem Wirtmineral ist gering, zu vernachlässigen (Roedder, E., Skinner, B. J. 1968).

Die Messungen haben wir auf den 5 – 10 mm² Mustern der vorher schon selektierten Präparate durchgeführt. Das Muster wurde mit einer Geschwindigkeit von 3 – 5 °C/Minute aufgewärmt, vor der zu erwartenden Homogenisationstemperatur wurde die Heizungsgeschwindigkeit auf 0,5 – 1 °C/Minute herabgesetzt. Auf einem gut definierten Wärmegrad konnten wir die Homogenisation beobachten (T_H). Bei den Messungen war die Homogenisation nur in der Flüssigkeitsphase festzustellen. Bei einigen Mustern fand in der Nähe der T_H eine starke Dekripitation statt. Die an der inneren Fläche des Rohres oder der negativkristallförmigen Einschlüsse auftretenden Totalrefraktionserscheinungen machten die Beobachtungen in einigen Fällen unsicher, sogar unmöglich.

Messergebnisse

Die graphisch dargestellten Messergebnisse sind auf den Abbildungen 2/a-h zu sehen. Die möglichst niedrigste Bildungstemperatur der untersuchten Ausbildungen fällt zwischen 105 – 260 °C:

Gang bei Bányabérc („Szárazlyuk" 185 – 230°) (200 – 205°, 210 – 215° max.)
Gang bei Bányabérc („Nedveslyuk" 175 – 230°) (195 – 205°, 210 – 215° max.)
Gang bei Kistőlgyesbérc (Süd-Ost 140 – 235°) (180 – 185°, 165 – 175° max.)
Gang bei Kistőlgyesbérc (Nord-West 160 – 220°) (170 – 180°, 185 – 190° max.)

Gang „Katalin"	170 215° (180 – 190°	max.)
Gang bei Matraszentimre	160 – 260° (195 – 205°	max.)
Keresztesbérc	160 – 220° (185 – 190°	max.)
Asztagkő	105 – 185° (130 – 155°	max.)

Die Messdaten der aus Keresztesbérc stammenden Muster zeigen eine Einmaximumverteilung. Bei den anderen Mustern ist eine markante Zweimaximumverteilung zu beobachten. Die Angaben des Ganges in Mátraszentimre zeigen eine starke Dispersion ebenso wie die des Barytes. Aufgrund der Veränderung des Maximums der Messangaben sind die Ausbildungen präzis zu trennen. Die T_H-Ergebnisse werden auf der Abb. 2. dargestellt. Es ist leicht zu sehen, dass die Angaben der Tagegänge die Daten

der gequarzten Zone fast „überziehen", also es gab keinen relevanten Unterschied in ihrer Bildungstemperatur. Nur die T_H-Werte des Barytes aus Asztagkő befinden sich in einem kleineren Temperaturintervall.

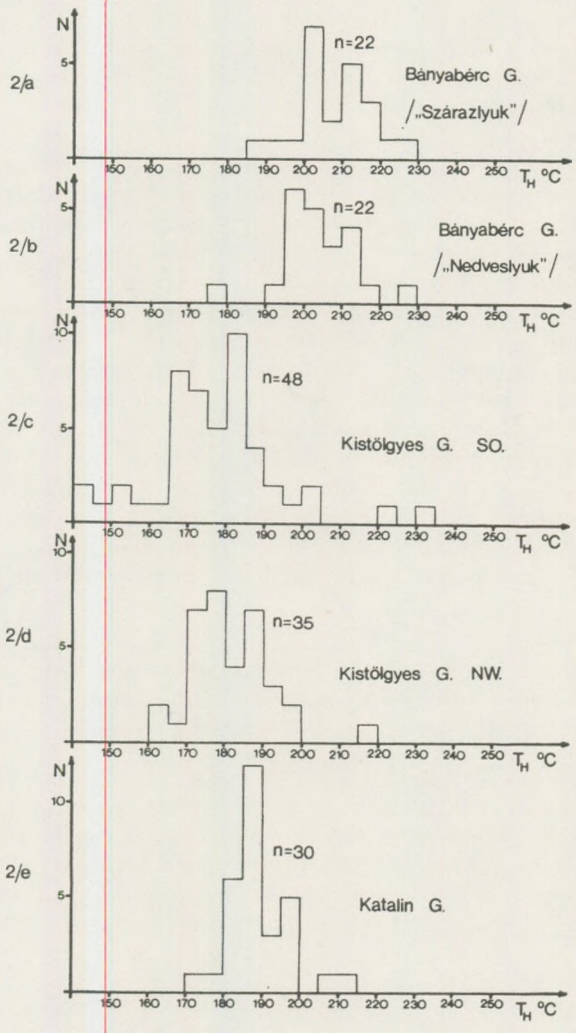

Abb. 2/a—e. Diagramme von Homogenisationsmessungen /I./

Kryoskopische Untersuchungen

Die kryoskopische Untersuchung der Einschlüsse – durch Abkühlen mit Azeton oder Äther – ist bereits seit 1822 (*Davy, H.*) bekannt, aber ihre regelmässige mineralogisch-lagerstättenkundliche Anwendung ist

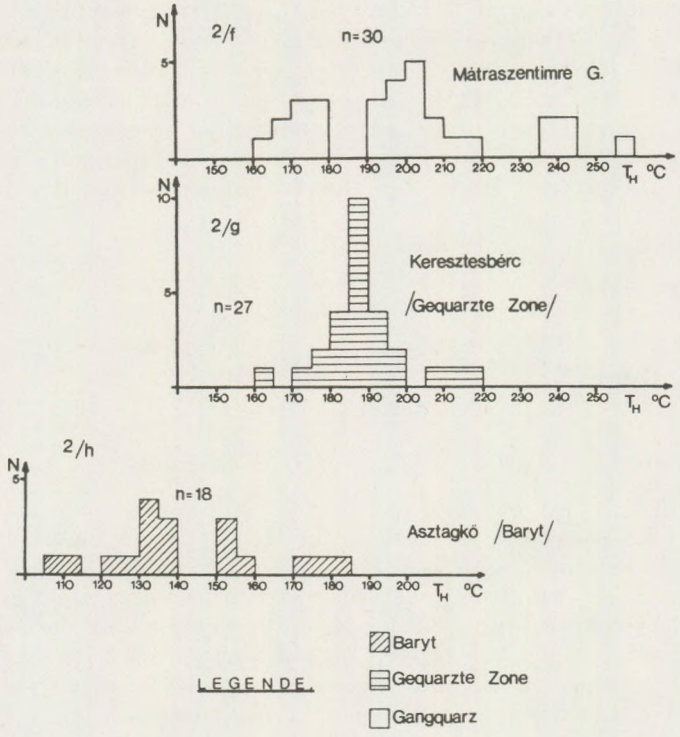

Abb. 2/f—h.

Diagramme von Homogenisationsmessungen /II./

erst seit den 50-er Jahren unseres Jahrhunderts, nach dem Einsatz des Gefrieren mit flüssigem Stickstoff im Jahre 1960, verbreitet.

Durch diese Untersuchungen kann in erster Linie die Konzentration der Salzlösungen bestimmt werden: die den Gefrierpunkt erniedrigende Wirkung von 10^{-10} g Salzes ist schon zu detektieren (*Roedder, E.* 1972).

Die Gase (CO_2, CH-Arten usw.) können nach ihrer Phasenumwandlungstemperatur abgesondert werden, es ist sogar möglich, ihre nebeneinanderliegende Phasenproportion auch zu bestimmen (*Swanenberg*, H. E. C. 1979). Ausserdem kann man mittels des auf 0 °C gemessenen Füllungsgrades der wässrigen Lösungen (im Verhältnis zum vollen Volum des Einschlüsses) Druckbestimmungen auch durchführen.

Der bei den Messungen angewendete aussere Kaltpunkt war Stickstoffgas mit niedriger Temperatur (zirka -160 — -140 °C).

Beim Abkühlen des Musters-wegen der Unterkühlung — im allgemeinen in einem Temperaturintervall von -20 — -100 (!) °C erstarrt die

Lösungsphase zu einem feinkörnigen, leicht durchsichtigen Aggregat (T_0) wobei die Gasblase zusammenbricht oder verschwindet. Beim langsamen Aufwärmen auf Zimmertemperatur rekristallisiert das feinkörnige Aggregat und dann auf einer gut definierbaren Temperatur unter den gerundeten Spitzen der Körnchen erscheint die Flüssigkeitsphase. Dieser Punkt (T_1) ist die eutektische Temperatur der Lösung. Daraus ist in grossen Zügen auf die Zusammensetzung der Lösung zu schliessen.
Solche Zusammensetzungen sind: (°C)

$Na_2CO_3-H_2O$	−2,1
$Na_2SO_4-H_2O$	−1,2
$Na_2CO_3-NaHCO_3-H_2O$	−3,3 (max.)
$KCl-H_2O$	−10,6
$NaCl-H_2O$	−21,2
$CaCl_2-H_2O$	−49,8
$NaCl-CaCl_2-H_2O$	−55,0 (max.)

(*Borisenko*, A. S. 1977).

Alles das beweist, dass das $NaCl-H_2O-$System, das bei den Einschlussuntersuchungen das am besten anzuwendende Modell ist, eine „Übergangsstelle" einnimmt. Einen grösseren eutektischen Punkt haben die Cloride der zweiwertigen Kationen, während die alkalische Sulfat – Carbonat – Systeme einen niedrigeren eutektischen Punkt haben. Auch die optische Untersuchung der beim Gefrieren ausgeschiedenen festen Phasen, meistens bei Lösungen mit grösserer Konzentration, kann eine Hilfe leisten.

Beim weiteren Aufwärmen des Musters erscheint die Gasblase (wenn sie beim Gefrieren verschwunden war), die Menge der festen Phase sinkt. Die Gleichgewichtstemperatur des letzten Körnchens und der Lösungsphase (T_2) gibt Informationen über die Konzentration. Daraus ist die Lösungskonzentration im Gewichtsprozent zu berechnen (*Potter*, R. W. II. et. al. 1978) oder von dem gewöhnlich gebrauchten $NaCl-H_2O-$Diagramm abzulesen (*Roedder*, E. 1963). Den Konventionen nach wird die Salinität der Lösungen „in NaCl Äquvivalent dem Gewichtsprozenten" angegeben, unabhängig davon, wie gross in der Wirklichkeit der NaCl – Gehalt der Lösung neben den anderen Salzgehalten ist. Wenn die chemische Zusammensetzung der Einschlüsse bekannt ist, ist daraus auch die theorethische Gefrierpunktserniedrigung zu berechnen (*Clynne*, M. A., *Potter*, R. W. II. 1978).

Die in den Einschlüssen vorhandenen Gase kondensieren sich beim Abkühlen, gewöhnlich im Augenblick des Gefrierens der Lösungsphase. Das Kondensat kommt im allgemeinen durch einen dünnen Streifen (Reaktionsprodukt) mit der gefrorenen Lösung in Kontakt und es bekommt beim langsamen Aufwärmen eine Form von unsicherem Umriss. In den untersuchten Mustern besteht die Gasphase aufgrund von Brechtisch – „crushing stage" Untersuchungen meistens aus CO_2 (*Roedder*, *E.* 1970). Im H_2O-CO_2-System ist die sogenannte Hydratbildung bekannt, die

über 0 °C in Form von stabilen Kristallen mit unsicherer Kontur zu folgen ist. Aus der Dissoziationstemperatur des Hydrates kann man den CO_2 – Druck berechnen (*Takenouchi, S., Kennedy, G. C.* 1965).

Bei den Einschlüssen mit „Erdölgehalt" (bituminöses Material) sind die Erstarrungserscheinungen des Bitumens auf niedriger Temperatur und die Erscheinung des aus den verschiedenen Ausdehnungsbeiwerten der zwei Flüssigkeitsphasen stammenden, bei der vollen Erstarrung sichtbaren, durchsichtigen Hohlraums mit kleinem Dampfdruck gut zu beobachten.

Messergebnisse

Der Informationswert der T_0 – Werte der kryoskopischen Messungen ist gering, weil ihre Grösse von mehreren Faktoren (Abkühlungsgeschwindigkeit, Stoffzusammensetzung des Einschlusses, Gasdruck, mechanische Eigenschaften des Wirtminerals) abhängt. Die Grösse vertritt für die untersuchte Ausbildungsgruppe einen charakteristischen Wert. Im Zuge der Messungen bei einer Abkühlungstemperatur von 4 – 5 °C ist einjeder der

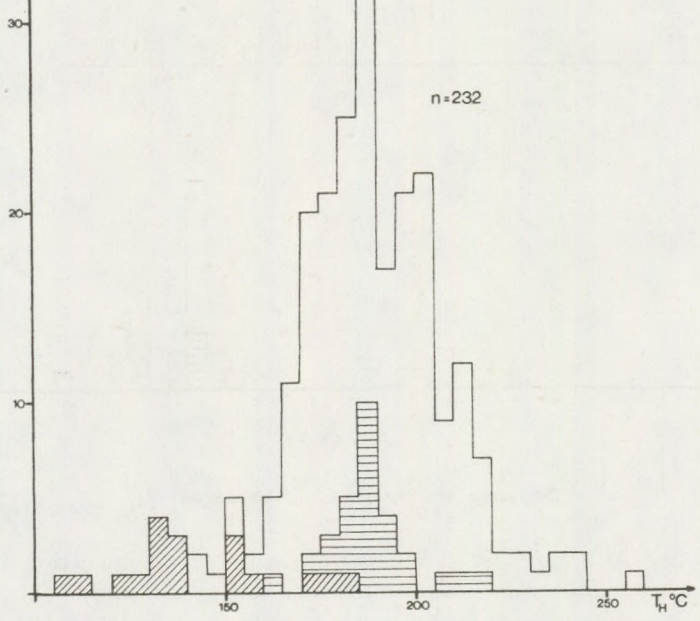

Abb. 3.

Zusammenfassendes Diagramm von Homogenisationsmessungen

untersuchten Einschlüssen bis -55 °C erfroren. Die Verteilung der T_0 – Werte stellt die Abb. 3/a dar: zwischen -43 – -50 °C ist ein Doppelmaximum zu registrieren. Beim Gefrieren ist in manchen Fällen ein Kondensat mit einem Volumen von $1-2\%$ zu beobachten.

Die Verteilung der T_1 – Werte wird auf der Abb. 3/b gezeigt. Aufgrund des ausgedehnten Verteilungsdiagrammes mit Mehrmaximum ist die Zusammensetzung von Fluiden nicht einheitlich. Vermutlich sind Ca^{2+} – $-/Mg^{2+}/-$ Chloride in einer grossen Menge die herrschenden Komponente. Nach dem Diagramm befinden sich die Angaben der gequarzten Zone und des Barytes in der Nähe der niedrigeren T_1 – Werte. Diese Lösungen enthalten wahrscheinlich weniger Alkalien. Nach den durch chemische Analyse kontrollierten Daten ist in der Zusammensetzung der Einschlüsse von polymetallen Barytlagerstätten unter den Kationonen der $Ca^{2+} \gg \gg Na^+ + K^+$) wobei $Na^+ \gg K^+$) und der Anion $Cl^- \gg CO_3^{2-}$ (*Ucsamejsvili*, N. E., *Hitarov, N. I.* 1965).

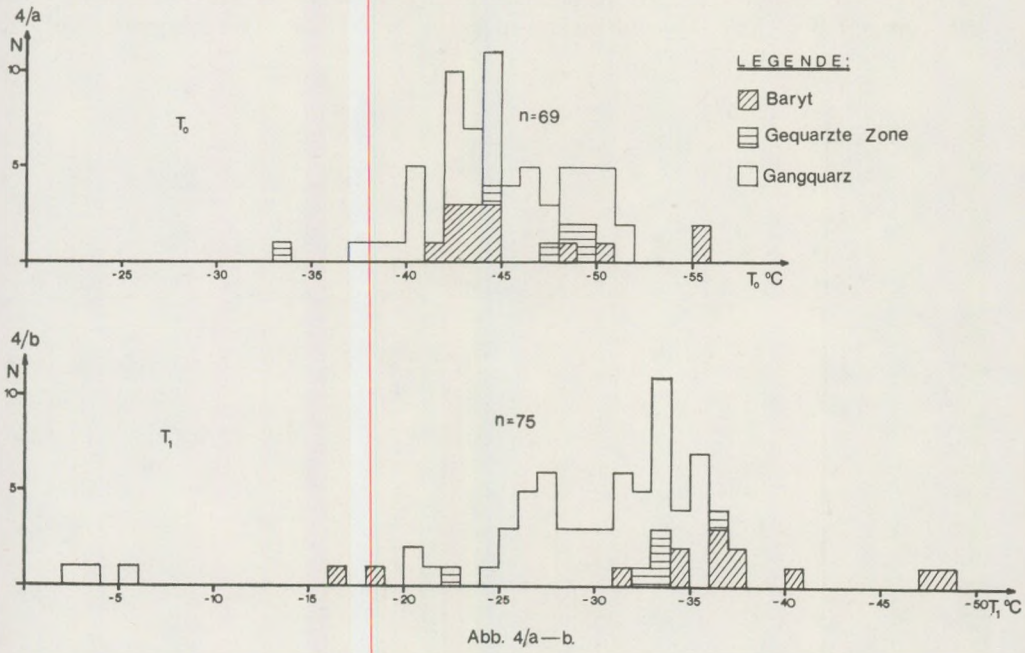

Abb. 4/a—b.

Diagramme von kryoskopischen Messungen /1./

Auf der Abb. 3/c. ist das Diagramm der Konzentrationsverteilung (T_2) zu sehen, mit einem Maximum zwischen -3, und $-5{,}5$ °C. Diese Werte entsprechen 4 – 8 – NaCl Äquivalent Gewichtsprozent. Bei der grossen Ähnlichkeit der Messergebnisse der Gangstoffe ist die starke Dispersion vom Baryt auffallend. Das letztere ist Resultat der lokalen Konzentrationsunterschiede, die beim Auftreten der schon erwähnten Erschei-

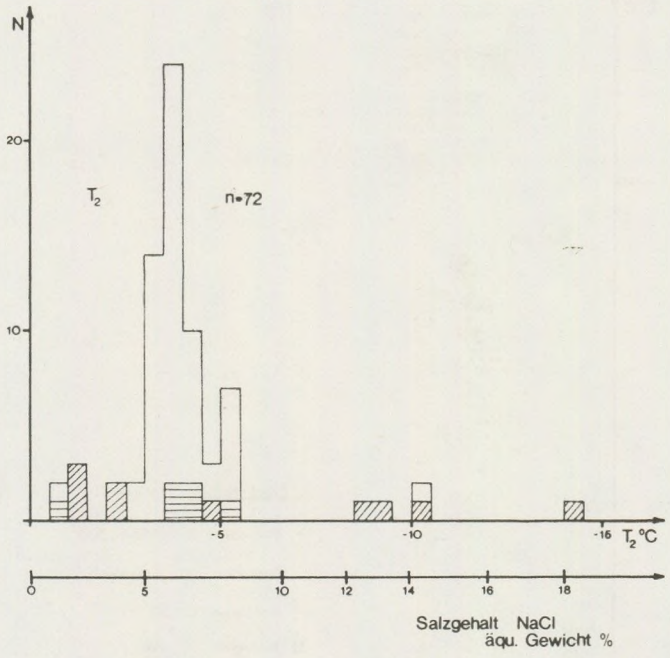

Abb. 4/c.

Diagramme von kryoskopischen Messungen /II./

nung „Aufkochen – boiling –" entsteht. Die Verbindung T_1/T_2 ist auf der Abb. 5 zu studieren. Im Falle bedeutender Dispersion einiger Messangaben (Asztagkő, Mátraszentimre) ist die Mehrheit der gemessenen Ergebnisse im Intervall von $T_1 = -24 - 38$ °C. $T_2 = -2 - 6$ °C. Es ist leicht zu bemerken, dass mit der Erhöhung des eutektischen Punktes eine nicht bedeutende Erhöhung der Konzentrationswerte vollzieht.

Während der Gefrieruntersuchungen der bitumenhaltigen Flüssigkeitseinschlüsse aus Bányabérc ist der Bitumentropfen in gleicher Zeit mit der Flüssigkeitsphase erstarrt, in der Begleitung einer Kontraktion. Die Schmelzerscheinungen sind zwischen $-9{,}4 - +7{,}7$ °C zu untersuchen. Selten kann man in den Barytmustern bis $+2{,}4$ °C CO_2–Hydrat mit einem unsicheren Umriss feststellen.

Der Verfasser dankt der Abteilung für Geologie der Matra–Werke von OÉÁV in Gyöngyösoroszi für die wertvolle Hilfe.

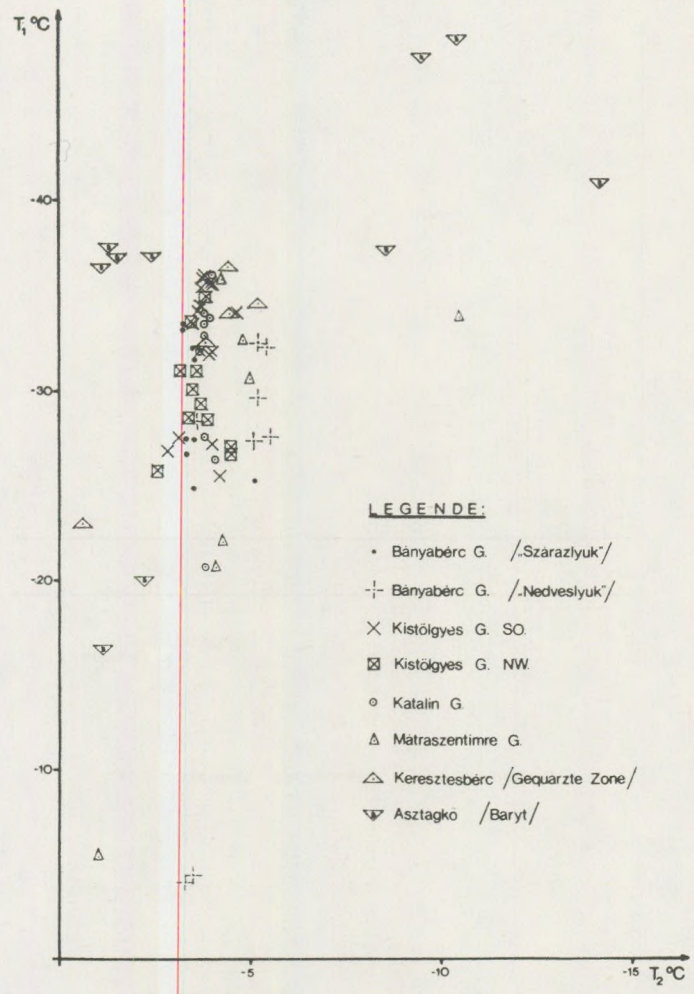

Abb. 5. Verbindung T_1/T_2

Plate I/a.

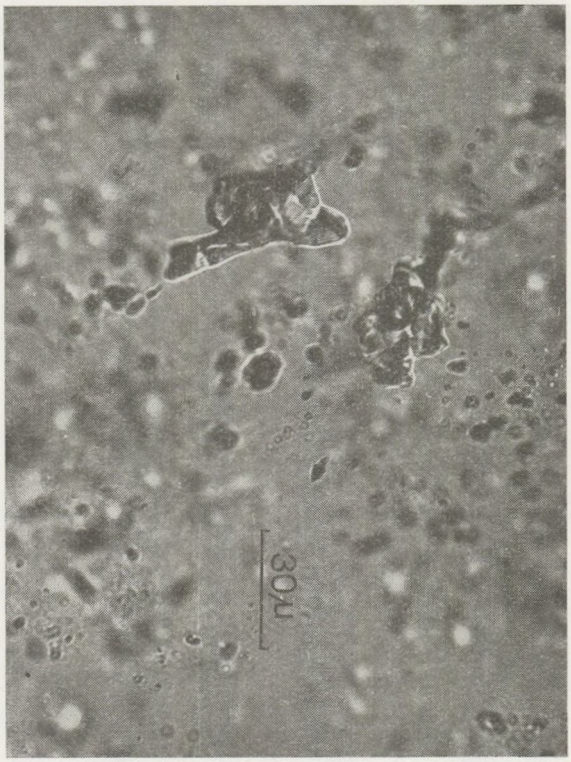

1. Formlose zweiphasige Einschlüsse, die vermutlich von primärem Typ sind. „Nedveslyuk"

Plate I/b.

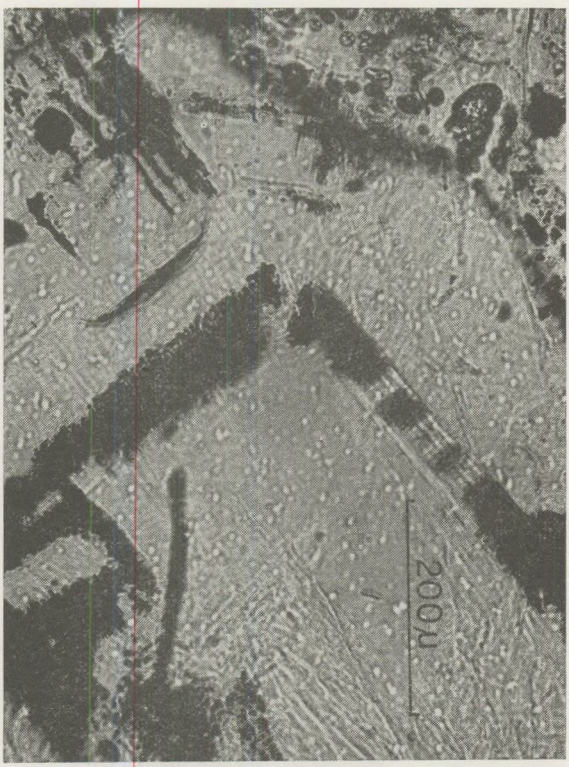

2. Auf Wachstumsfläche erscheinende Einschlussreihen. Gang bei Kistölgyesbérc.

Plate I/c.

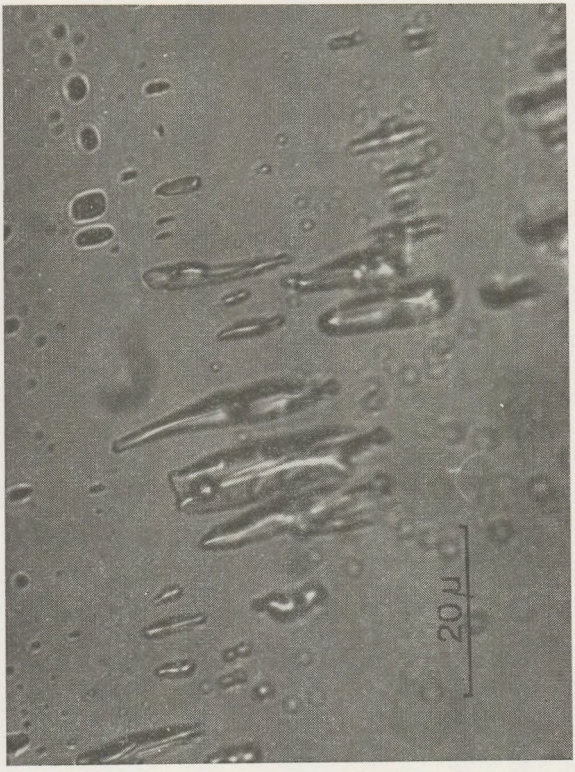

3. Zweiphasige Einschlüsse mit Übergangstyp. „Nedveslyuk“

Plate I/d.

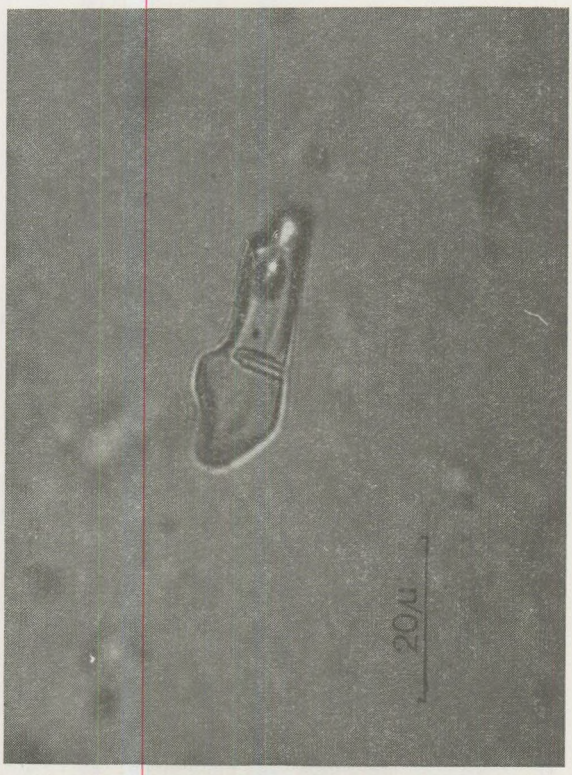

4. Dreiphasiger Einschluss mit einem nadeligen Kristallit aus unbekanntem Stoff. „Szárazlyuk"

Bemerkung: Die Aufnahmen sind in einer parallelen Nikolstellung gefertigt worden.

LITERATURVERZEICHNIS

Borisenko, A. S. (1977): Cryometric technique applied to studies of the saline composition of solution in gaseous fluid inclusions in minerals. Ak. Nauk. SSSR (Sibisrk. no. 8. p. 16–27.) (Russisch)

Capedri, S., Rivalenti, G. (1974): A chemical method for major element determination in calcite coexisting with other carbonats, and its bearing on geotermometry. Tsermaks Min. Petr. 21. p. 61–69.

Clynne, M. A., Potter, R. W. II. (1987): Freezing point depression of synthetic brines Econ. Geol. vol. 73. no. 2.

Ermakov, N. P. (1972) Inclusions as a geochemical systems in minerals „Nedra", (Russisch).

Khetchikov, L. N. (1973): Inclusions of mineral-forming solutions in synthetic crystals, and evidence for thermobarometry. Abst. of Pap. at 4–th Regional Conf. of Thermobarogeochemistry of Min. Form. Proc. – Rostov (Russisch).

Koch, S. (1966): Magyarország ásványai. Akadémiai Kiadó.

Naumov, V. B. (1976): Results of thermometric measurements of inclusions in standard quartz samples carried out in laboratories of the USSSR. Geokhimiya no. 7. p. 1109–1112. (Russisch)

Potter, R. W. II. et. al. (1978): Freezing point depression of aquaeous sodium chloride solutions. Econ. Geol. vol. 73. no. 2

Poty, B. et al. (1976): Un nouvel appareil pour le mesure des temperatures sous le microscope: L installation de microtermométrie Chaixmeca. Bull. Soc. Fr. Mineral. Crist. 99. p. 182–186.

Rozlozsnik, P. (1942): Adatok a Gyöngyösoroszi-környéki érctelérek ismeretéhez. MÁFI évi Jel. 1936–38; II.

Roedder, E. (1963): Studies of fluid inclusions II. Low temperature application of a dual-purpose freezing and heating stage. Econ. Geol. v. 57. p 1045– 1061

Roedder, E. (1967): Fluid inclusions, as a samples of ore fluids. in: Barnes, H.L. ed. Geochemistry of hydrothermal ore deposits. New York... Inc., p. 515–574.

Roedder, E. (1970): Application of the gases in fluid inclusions. Schw. Min. Petr. Mitt. v. 50. pt. 1. p. 41–58.

Roedder, E. (1972): Composition of fluid inclusions. Geol. Prof. Pap. 440–JJ.

Roedder, E., Skinner, B. J. (1968): Experimental evidence, that fluid inclusions do not leak. Econ. Geol. v. 63. p. 715–730.

Scotford, D. M. (1975): A test of aluminium in quartz as a geothermometer. Am. Min. Vol. 60. p. 139–142.

Scott, S. D., Kissin, S. A. (1973): Sphalerite composition in the Zn-Fe-S-system below 300 C. Econ. Geol. vol. 68. p. 475–479.

Siklóssy, S. (1977): Gyöngyösoroszi környékének szerkezeti értékelése. Földt. Közl. 107. p. 348–357.

Swanenberg, H. E. C. (1979): Phase equilibria in carbonic systems and their application to freezing studies of fluid inclusions Contr. Min. Petr. 68. p. 303–306.

Sztrókay, K. (1939): A Gyöngyösoroszi ércelőfordulás mikrószkópi vizsgálata. Math. Term. Tud. Ért. LXIII. 904.

Takenouchi, S., Kennedy, G. C. (1965): Dissociation pressures of the phase $CO_2 5\frac{3}{4} H_2O$ Jour. Geol. v. 73. p. 383–390.

Ucsamejsvili, N. E., Hitarov, N. I. (1965) Chemical composition of fluid inclusions from some barits. Min. Term. Bar. „Nauka" p. 227–232 (Russisch).

Vidacs, A. (1961): A Gyöngyösoroszi ércbánya hidrotermális telérei MÁFI évi Jel. 1957–58. 25.

INVESTIGATION OF THE TEXTURE-FORMING EFFECT OF OXYDATION/REDUCTION PROCESSES IN SOME HUNGARIAN BAUXITES

HIDASI, J.* – PAÁR, M**

Received: 25. February 1980.

SUMMARY

Alteration of goethite and haematite into pyrite and marcasite was observed in the investigated bauxite specimens. The alteration is a result of reaction with downward percolating low-Eh solutions, rich in H_2S. The solutions originate in carbonaceous argillites immediately overlying the bauxite.

Characteristic pyritisation structures recognized in the topmost layers of the ore are automorphous roundgrains and concentrically shaped or irregular aggregates of pyrite and/or marcasite. In porous material and along fissures individual grains of pyrite and marcasite also often occur in the form of aggregates. When postgenetic uplift of the bauxite deposits facilitated close contact with oxygen-rich meteoric waters, oxydation of pyrite and marcasite took place: most pyrite and marcasite grains had been altered into goethite. Part of the ferrous iron present became remobilized by H_2SO_4-rich solutions of oxydation origin.

Dilution of acidic solutions and reaction with the soluble carbonates of the bauxitic groundmass lead to re-precipitation of iron accompanied by a reaction producing gypsum from the cations (Ca) of the carbonate species and the anions (SO_4) of the sulphuric-acidic solutions.

The role of pyritisation and the reoxydation of pyrites are of primary importance in the formation of certain bauxitic textures. Description and partly also genetic interpretation of textures brought about by the processes of pyritisation and and de-pyritisation will be presented here.

Pyritiferous bauxites are rather common in Hungary. They occur at the Szőc, Halimba, Nagytárkány, Iszkaszentgyörgy and Nagyegyháza deposits, as a rule in the uppermost horizons of the bauxite bodies.

Pyritisation is known generally as an evidence of low-pH, oxygen-poor geochemical environments. Bauxites however are mostly held to be the best examples of rocks formed under highly oxydizing conditions. It is the contrasting character of the processes of bauxitization and pyritization which is responsible for the extensive mobilization and transportation of certain elements leading ultimately to multifarious mineralogical and textural rearrangements within the bauxitic material.

As to its relation to the stages of bauxite formation, pyritization may be either of diagenic or – rarely – also syngenetic origin.

* Department of Applied- and Engineering Geology Eötvös L. University, Budapest Múzeum krt. 4/A

** Hungarian Geological Institute Budapest, Népstadion út 14.

It is the epigenic – that is post-accumulation – pyritization, however, that has generally the most significant textural impact on bauxites.

Deposits of the Iszkaszentgyörgy–Rákhegy, Halimba and Nagytárkány occurrences had been intensely affected by this kind of pyritization.

After having been accumulated in karstic hollows of the Mesozoic carbonate terrain bauxites became covered by a terrigenous mottled clay sequence towards the end of the Cretaceous period. The Palaeogen transgression was introduced by a gradual upraisal of the karstic water table, as a consequence of which undrained pools were formed on the top of the bauxite-filled hollows. In these pools – where conditions had been essentially uliginal, i. e. reducing – the uppermost layers of bauxite became resuspended and thoroughly mixed with carbonaceous material. Thus the top of the bauxite profile as well as the immediate cover (consisting of reworked bauxite washed in from the surroundings) became converted into a mixture of carbonaceous clays. The same refers also to that fine non-bauxitic (argillaceous) material, the increased rate of accumulation of which was a result of the increase of the relief differences between the inundated karst plain and the adjoining higher elevated areas.

Solutions rich in humic acids, CO_2 and H_2S but poor in oxygen percolated from the pools downwards into the underlying bauxite, and the alteration of minerals of trivalent iron by reaction with these reducing solutions began. Part of goethite and haematite became converted either into pyrite and marcasite or into some soluble iron-sulphate, and the latter began to migrate downward towards deeper horizons of the profile. The other part of iron was mobilized by CO_2 and humic acids dissolved in the descending solutions.

Reduction by acidic solutions was most effective in the case of the *finest iron-mineral-grains* the high specific surace of which provided for a thorough interaction between reducing medium and subject.

The alteration of *larger* (100 to 500 μm) *grains* took place slowlier and in the presence of a steadily intense solvent-supply only.

The reaction of *concentrically organized textural elements* to reduction is somewhat unusual especially when compared to that of the single grains. *Concentric round grains* formed by rhytmic precipitation of microgranular iron-minerals during diagenesis are characterised by compact, iron-rich, spherical layers in which pores of the microgranular or pelitomorphous groundmass are filled by iron minerals.

Being impermeable for water such concentric round-grains could survive the overall reduction with essentially intact goethite and haematite inside, while ferric iron minerals of the groundmass became altered into pyrite or marcasite (Fig. No. 1).

In the groundmass the alteration of iron minerals resulted in the formation of pyrite and marcasite of widely varying shape and internal structure. As to morphology and size both pyrite and marcasite may occur in the form of automorphous (hexahedral, octahedral or rhombohedral) crystals of 200 tp 300 μm or some times several centimetres size (Fig. No. 2.) *Komlóssy Gy.* (1966) observed the increase of grain size of pyrites in the Iszka-

szentgyörgy grey (reduced) bauxite profiles from top to bottom, down to the upper ironstone layer.

Subsequent re-oxydation results in the formation of pseudomorphs consisting of geothite and haematite but retaining the shape of the original pyrite crystals. (Fig. No 3.)

In addition to automorphous individual crystals also spherical or ellipsoidal grain complexes ("round-grains") of pyrite and marcasite are common, the size of which varies rather widely (Fig. No. 5). Under the standard petrographic microscope they seem to be opaque and thus practically structurelless, i. e. homogeneous. As to size, they vary from several hundreds of a micrometer to some millimeters Concentrically structured *round-grains of pyrite* are also rather common. Their size is practically the same as that of the astructural complexes. As to internal structure, they are built up of alternating spherical layers of some pale iron-poor and an opaque pyritiferous material. Instead of being true spheres, most layers exhibit a rather rough surface with radiately protruding "spurs", scabrid and scraggy hollows.

This "roughness", is such a characteristic feature that it can be used even for a distinctive mark.

Pisoids, as a rule, have smooth surface, while pyritic round-grains – even if subsequently reoxydized – distinguish themselves always bytherough uneven outer surface (Fig. No 7.).

According to our thin-section investigations there are also pyritic round-grains, the outermost shells of which are built up entirely of small automorphous crystals of pyrite. The tiny crystals adhere directly to the underlying iron-poor shells of the round-grain (Fig. No 8.).

Pyritic round-grains may be either single or arranged reularly – like a string of beads as shown by Fig. No. 9.

Irregular precipitations

As to shape the aggregates of pyrite or marcasite formed by reduction of ferric minerals, are for the most part irregular. (Fig. No. 10.)

Dendritic pyrite grains belong also to the group of "irregular precipitaions". Their growth is controlled always by the shape of the open pores of the bauxitic groundmass (Fig. No. 11). Grain complexes built up of individual irregular pyrite grains are generally irregular themselves, too. (Fig. No. 12.)

Pyritic fissure-fillings Pyritisation is most common along fissures or, at places where the porosity of the host rock (bauxite) had originally been greatest. Along fissures pyrite may occur either in the form of automorphous crystals or as irregular aggregates (Fig. No. 13.)

A characteristic sort of pyritic fissure-fillings is the one connected to suncracks or syneresis-cracks formed during diagenesis of the ore (Fig. No. 14).

Pyritisation is generally followed by the deposition of thicker or thinner coverbeds and in most cases a long-lasting period of relative standstill. When subject to subsequent uplift and erosion, coverbeds may be denuded, however, and pyritiferous grey bauxites may reach a near-surface position. As a result of penetration by high-oxygen meteoric waters oxidation of ferrous parts of the profile may begin. Marcasite is the first to decay in contact with groundwater but it is quickly followed by pyrite. Oxydation of the two produces $FeSO_4$ which turns into goethite and haematite on further oxydation. Sulphurous and sulphuric acids thus formed percolate through the bauxite body and promote the alteration of all yet intact iron minerals. Materials thus mobilized may re-precipitate at deeper horizons where neutralisation of acidic solutions is brought about by the proximity of the high-pH bedrock.

Part of the ferro-sulphate formed on pyrite-oxydation is mobilised and impregnates the bauxitic groundmass around the decaying pyrite grains. On contact with oxygenated ground-water percolating through the profile dissolved ferro-sulphate gets oxydized with all the ferrousiron transferred into the trivalent state. The final product of this reaction being sulphuric acid, it results in a sharp decrease of pH and thus in perfect mobilisation of iron. The dissolved from of iron is stabilised as long as the pH of the environment does not decrease below 3 to 4. Since oxydation begins always along the surface of the pyrite (or marcasite) grains it is quite obvious why the oxydized grains are encircled by a distinct pale "halo", the iron content of which is almost completely removed. (Figs. 3., 15. and 16.).

On moving away from decaying pyrite grains the solution gets more and more diluted, allowing a gradual increase of the pH, and thus — sooner or later — also the re-precipitation of ferric iron. That explains why the several micrometer large pale halos arealways enclosed by iron-rich reddish or opaque "crust"-s. The transition from the pale zone towards the dark-colored "crust" is always continuous-there is no sharp boundary between the two.

As to morphology, reoxydation-structures are rather variegated. Their form depends essentially on the rate of indiltration of oxygen-rich waters, on the extent of water-logging of the bauxite-body in question (i. e. on drainage), and on the temporal variations of both.

At places where drainage is blocked (i. e. groundwater is more ore less stagnant) material transport is of the diffusion type, which leads to the formation of iron-bearing precipitations evenly distributed throughout the section (Figs. No. 15. and 17.).

Preferred directions from where the rate of influx of oxygen-rich waters had been higher than from elsewhere are always reflected by an assymetry of the distribution of iron-precipitations, with the iron-rich zone being markedly thicker on the "downstream" side of the groundwater flow. (Figs. No. 18. and 19.)

Steady fluctuation of the groundwater-(or karstic water)-table may lead to the zonation of pyritic bauxites. In such cases the ore consists of

parallel or subparallel zones alternately enriched or depleted in iron (See Fig. No. 20.) The boundary of the zones is wavy in most cases and they are rhytmically arranged. The amount of opaque (iron-rich) concretions is constant throughout the zones, the only difference between the iron-rich and iron-poor bands being the sharp pale iron-poor halos occurring around goethitic concretions in the iron-rich bands. At places where the iron-content of the groundmass is low, the boundary of the concretions is always very sharp.

The interpretation of the above described phenomena is as follows:

Oxydation of pyrite and the precipitation of ferric iron is controlled essentially by slow variations of the karstic water-table. At the time of high-water oxydation of pyrite and marcasite begins and all the dissolved elements are dragged up towards the surface by the raising water-table. At the end of the high-water period when the amount of the solvent (i. e. water) decreases the solution becomes soon saturated in respect of ferric iron and precipitation of iron-hydroxide commences. During the next high-water period the upraisal of the water-table leads to the oxydation of another pyritiferous band.

Formation of *irregular Liessegang-bands* (= groups of several, that is 8 to 10 or even 20 to 30 equal-wide bands alternately iron-poor and iron-rich) in re-oxydized bauxites can be explained similarly.

In the centre of such banded structures there is always some porous remnant of a pyritic or marcasitic concretion, the size of which varies from a few millimeters to several centimeters (The porous or sceletal internal texture is interpreted as a result of the oxydation process.)

In the Liesegang-bands of reoxydized bauxites there are no iron-rich concretions. Iron-minerals of such banded structures are always extremely fine-grained and evenly distributed throughout the pelitic material. In the groundmass, however, the occurrence of the above described concretionary structures is quite common.

The discussed structural-textural phenomena suggest the following mechanism of the oxydation process:

The reaction produces soluble $FeSO_4$ the removal of which is brought about by diffusion. When moving away from the decaying pyrite grain, dissolved $FeSO_4$ meets more and more oxygenated waters which turn its ferrous iron into the ferric form. Being slightly acidic, the solution becomes saturated rather soon in respect of Fe^{3+} and thus precipitation of $Fe(OH)_3$ commences. Later on, by ageing this $Fe(OH)_3$ is converted into goethite. Oxydation of the $FeSO_4$ solution produces also some sulphuric acid which acts toward further decrease of the pH. Precipitation of additional amount of ferric iron is thus prohibited, until — on further diffusion the solution gets again somewhat less acidic. So the above discussed alternating iron-poor and iron-rich stripes form, sometimes as close as a few millimeters to each other. Liessegang-striped textural elements are sometimes very similar to concentric elements like ooids or spastoids (Figs. No. 21 and 22. resp.)

As an accessory most bauxites contain also some calcite which may be turned into gypsum when sulphuric or sulphurous acid percolates through the ore body. Gypsum occurs either in the form of automorphous crystals of several millimeters in size, or as vermicular aggregates of very fine platy grains (Fig. No. 23.).

Percolation of descendant solutions had been facilitated by the porous nature of the ore and by circular or elliptical channelways open and partly interconnected. The topmost section of these channelways may be partially or totally filled by pyrite, or else they have at least a thin film of pyrite along their walls (Fig. 24.). Since later on, during subsequent periods of oxydation partially pyritised channels may have served as conducting water ways also for aerated solutions, reoxydation of channel-filling or channel-lining pyrite is a common phenomenon in these bauxites (Fig. 25.)

Rate of percolation of both aerated and acidic waters had remarkably been accelerated by the presence of such channels and it is easy to understand that the effect of descendant solutions could be most intense at places where the number of open channels per unit volume had been greatest.

Reaching the original, non-reduced, red-russet bauxite, descendant solutions attacked the microgranular ferric minerals (goethite and haematite) of the ore. Mobilisation and local leaching out of ferric iron lead to the formation of icicle-like, pale, vertical elements, the size of which varies from a few centimeters to several maters (For an examples see Fig. 26.)

After the deposition of the coverbeds open pores and channelways may have got sealed by calcite having been precipitated from high pH, Ca-rich descendant solutions (Fig. 26.). The appearance of high pH solutions on the scene is considered to be the sign of termination of the oxydation processes.

Fig. 1. Concentrically shaped textural element with haematiticgoethitic internal shells. The groundmass contains pyrite and marcasite. Halimba – III. M = 10x
Fig. 2. Automorphous grains of pyrite.
Nagytárkánypuszta Nt – 2399; 102,6 – 103,6 m M = 25x
Fig. 3. Pseudomorphs of goethite after pyrite. Halimba – Malomvölgy M = 50x
Fig. 4. Automorphous grains of pyrite along a fissure.
Nagytárkánypuszta Nt – 1838; 89,1 – 89,4 m M = 25x

Fig. 5. Round-grains of pyrite Halimba – III. M = 50x
Fig. 6. Concentrically shaped textural element consisting of pyrite.
Nagytárkánypuszta Nt – 1733; 106,7 – 107,7 m M = 40x
Fig. 7. Concentric-radial textural element.
Nagytárkánypuszta Nt – 2399; 102,6 – 103,6 m M = 50x
Fig. 8. Concentrically shaped textural element with a crust built up of aggregates of automorphous pyrite.
Nagytárkánypuszta Nt – 1733; 106,7 – 107,7 m M = 25x

Fig. 9. Roundgrains of pyrite arranged like a string of beads.
Halimba – III. M = 25x
Fig. 10., Irregular pyrite grain.
Nagytárkánypuszta Nt – 1838; 89,1 – 89,4 m M = 10x
Fig. 11. Dendritic pyrite grain. Halimba – III. M = 25x
Fig. 12. Aggregate of irregular pyrite grains.
Nagytárkánypuszta Nt – 1838; 89,1 – 89,4 m M = 25x

Fig. 13. Fissure-filling pyrite.
Nagytárkánypuszta Nt – 2399; 94,5 – 95,4 m M = 25x
Fig. 14. Diagenic cracks filled with pyrite.
Nagytárkánypuszta Nt – 2407; 94,5 – 95,0 m M = 25x
Fig. 15. Iron-poor halo formed on oxydation of pyrite.
Nagytárkánypuszta Nt – 1838; 88,8 – 89,1 m M = 10x
Fig. 16. Iron-poor halo formed on oxydation of pyrite.
Nagytárkánypuszta Nt – 1838; 88,8 – 89,1 m M = 25x

Fig. 17. Textural element formed by oxydation of pyritic round-grains.
Nagytárkánypuszta Nt – 1838; 88,8 – 89,1 m M = 50x
Fig. 18. Distorted precipitations of goethite formed on oxydation of pyrite.
Nagytárkánypuszta Nt – 1838; 88,5 – 88,8 m M = 10x
Fig. 19. Distorted precipitations of goethite formed on pyrite-oxydation.
Nagytárkánypuszta Nt – 1838; 88,5 – 88,8 M = 25x
Fig. 20. Rhytmical bands, alternately iron-poor and iron-rich in a reoxydized bauxite.
Halimba – Malomvölgy M = 10x

Fig. 21. Pisoid-like textural element of epigenic origin.
Nagytárkánypuszta Nt – 1838; 88,8 – 89,1 m M = 25x
Fig. 22. Spastoid formed from pyrite by oxydation.
Nagytárkánypuszta Nt – 1838; 88,8 – 89,1 m M = 15x
Fig. 23. Epigenic gypsum in bauxite. Halimba – Malomvölgy M = 50x
Fig. 24. Pyrite-lined "channelways" in bauxite. Halimba – III. M = 20x

Fig. 25. Reoxydized "channelways" in bauxite. Halimba – Malomvölgy M = 20x
Fig. 26. Icicle-like textures depleted in iron. Halimba – Malomvölgy M = 10x
Fig. 27. Carbonatic channel-filling in bauxite. Halimba – Malomvölgy M = 10x crossed polars

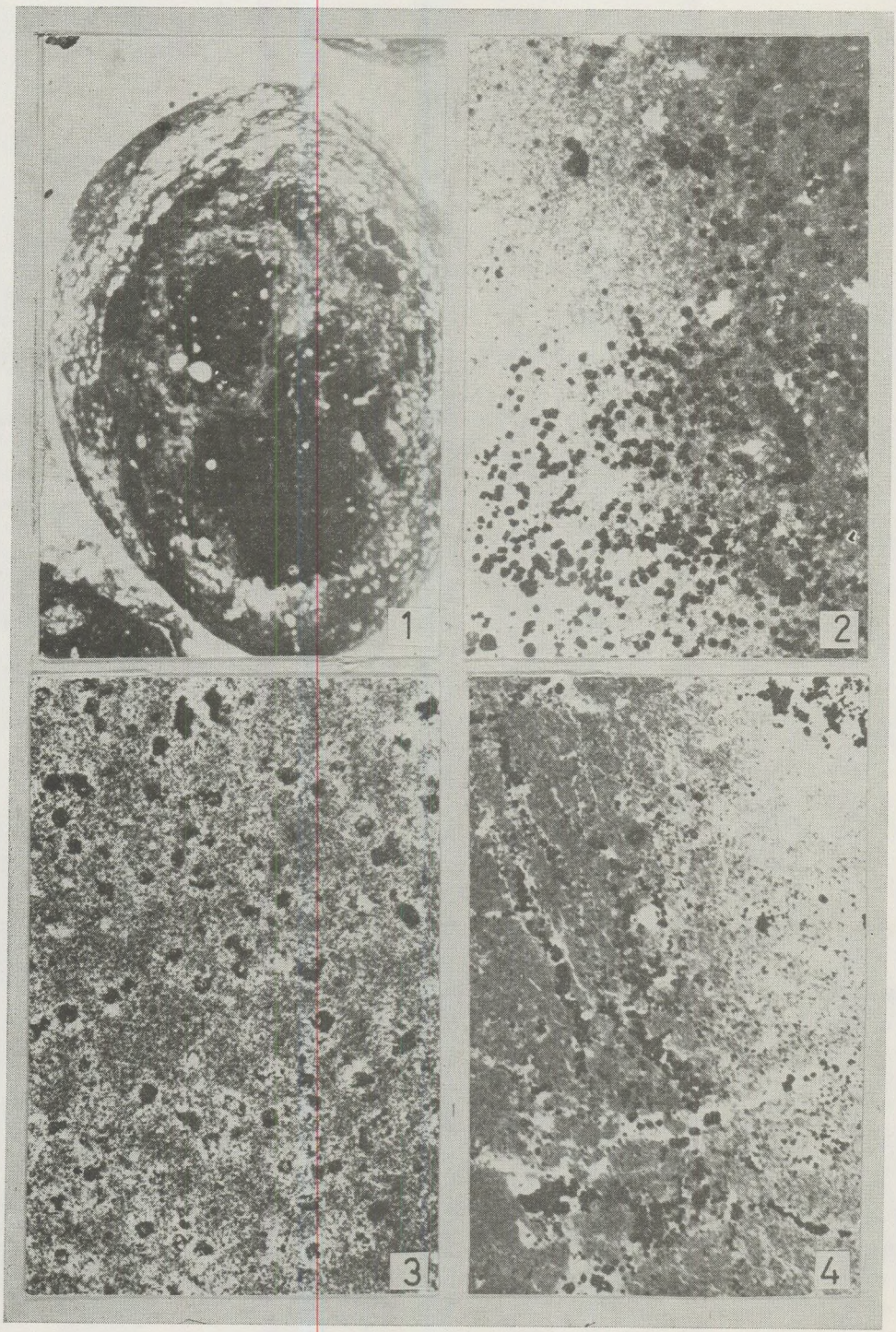
1
2
3
4

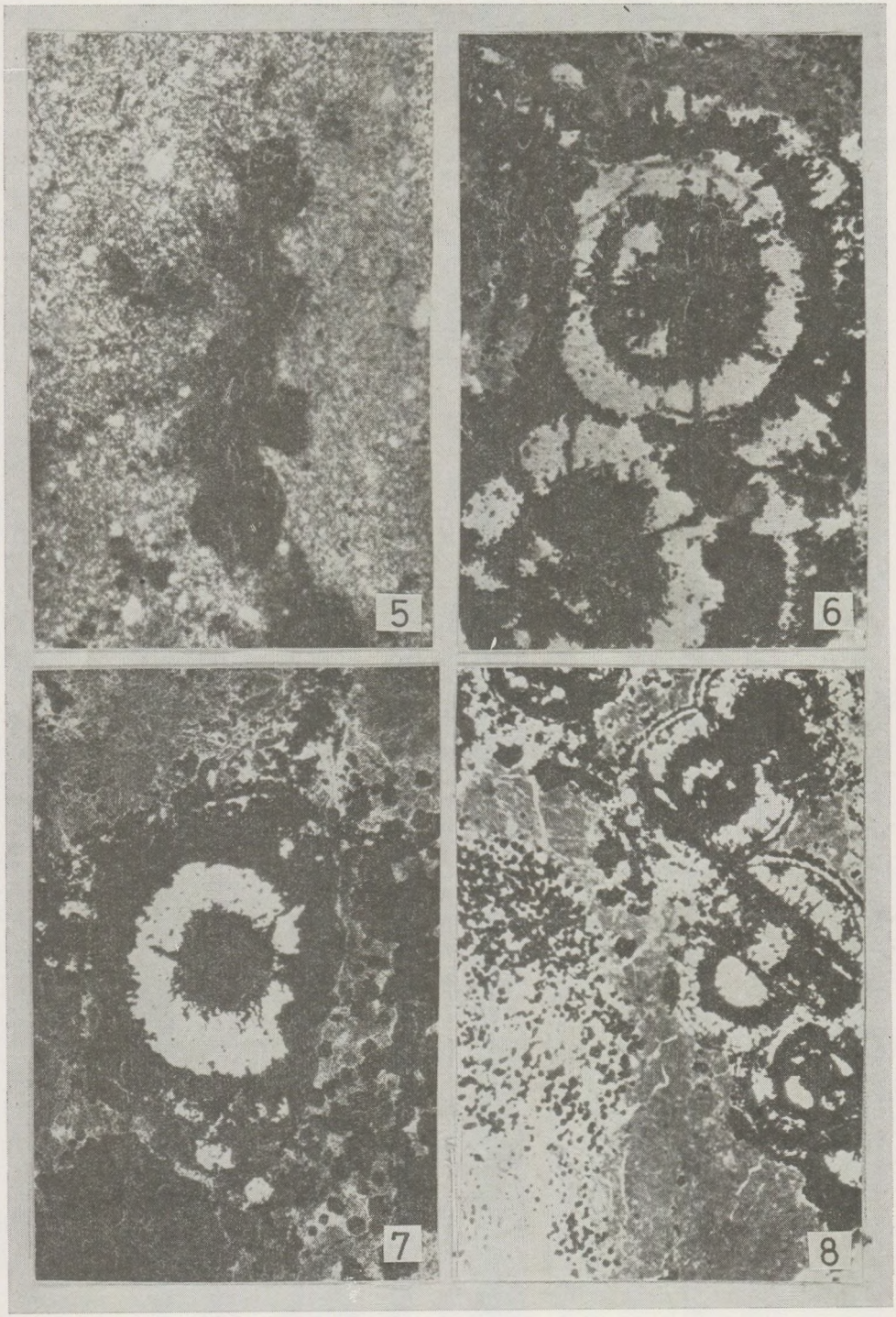
5
6
7
8

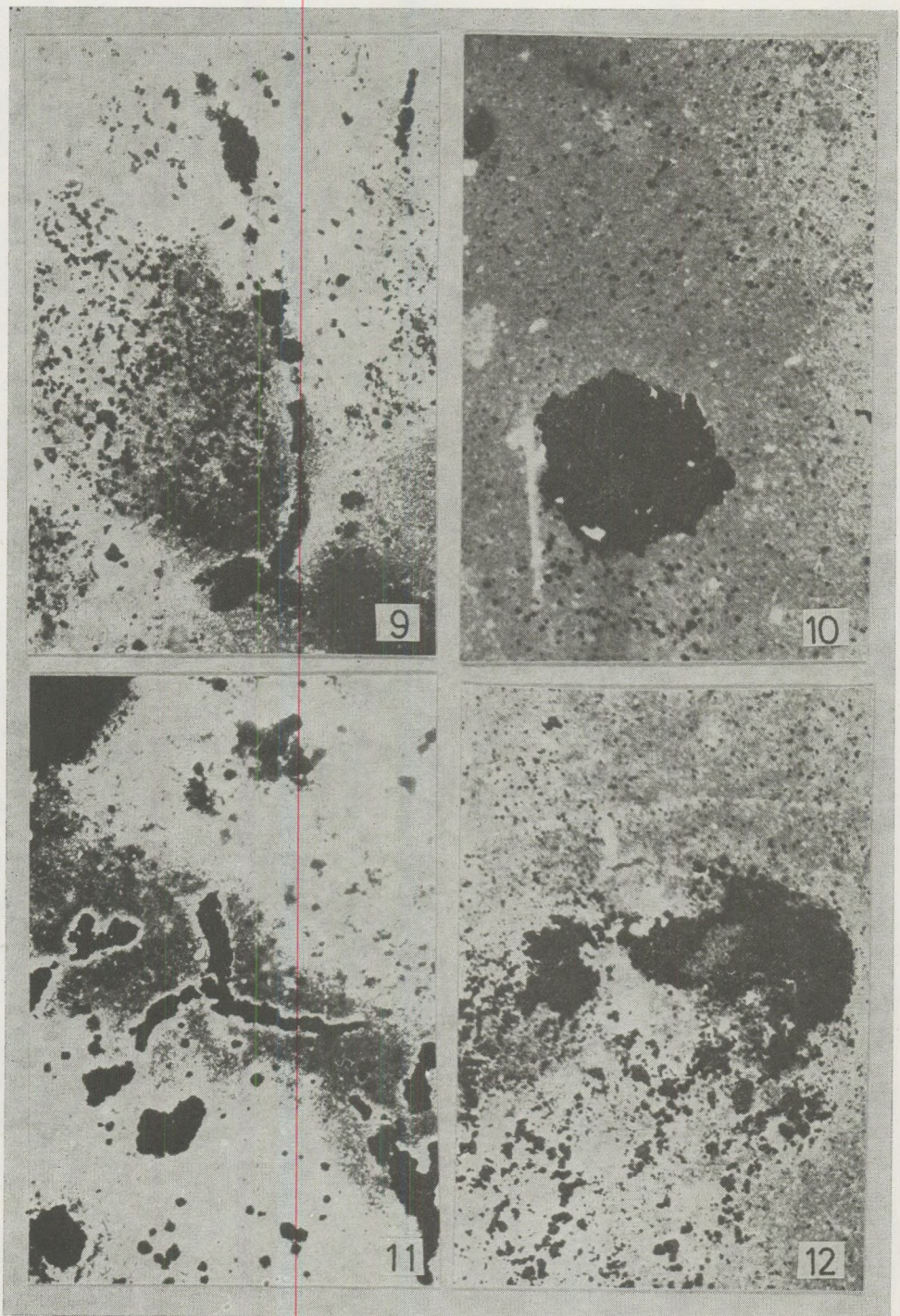
9
10
11
12

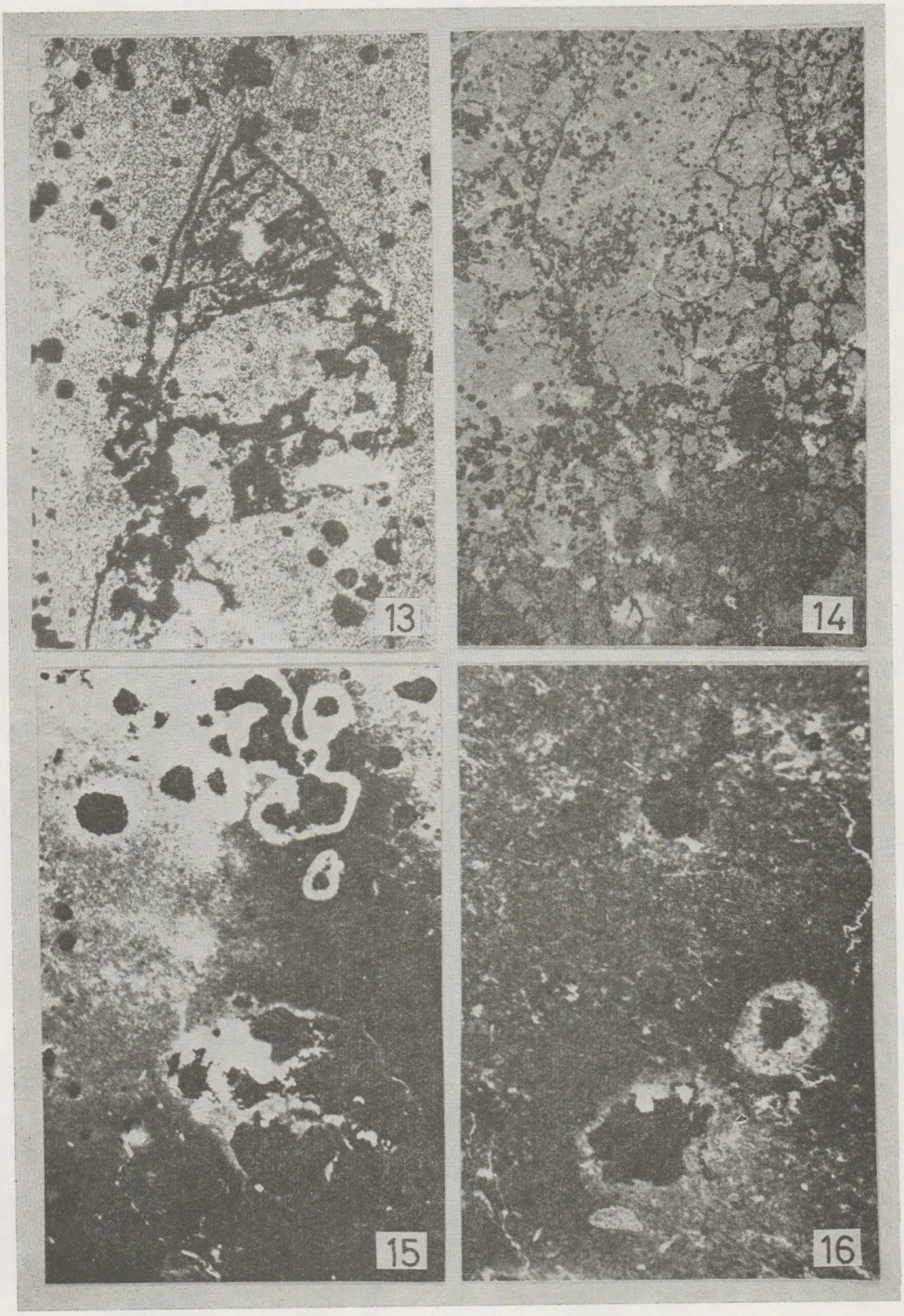
13
14
15
16

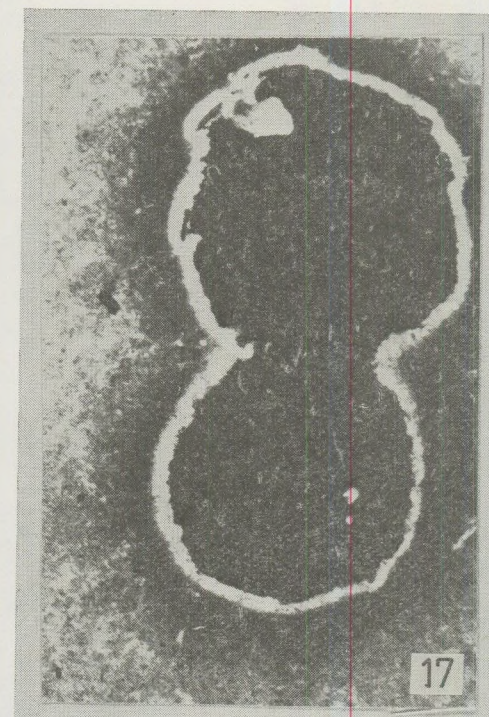
17


18

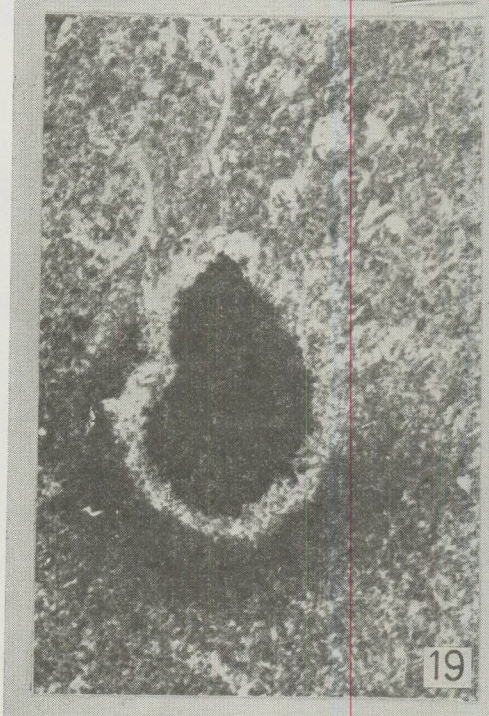
19


20

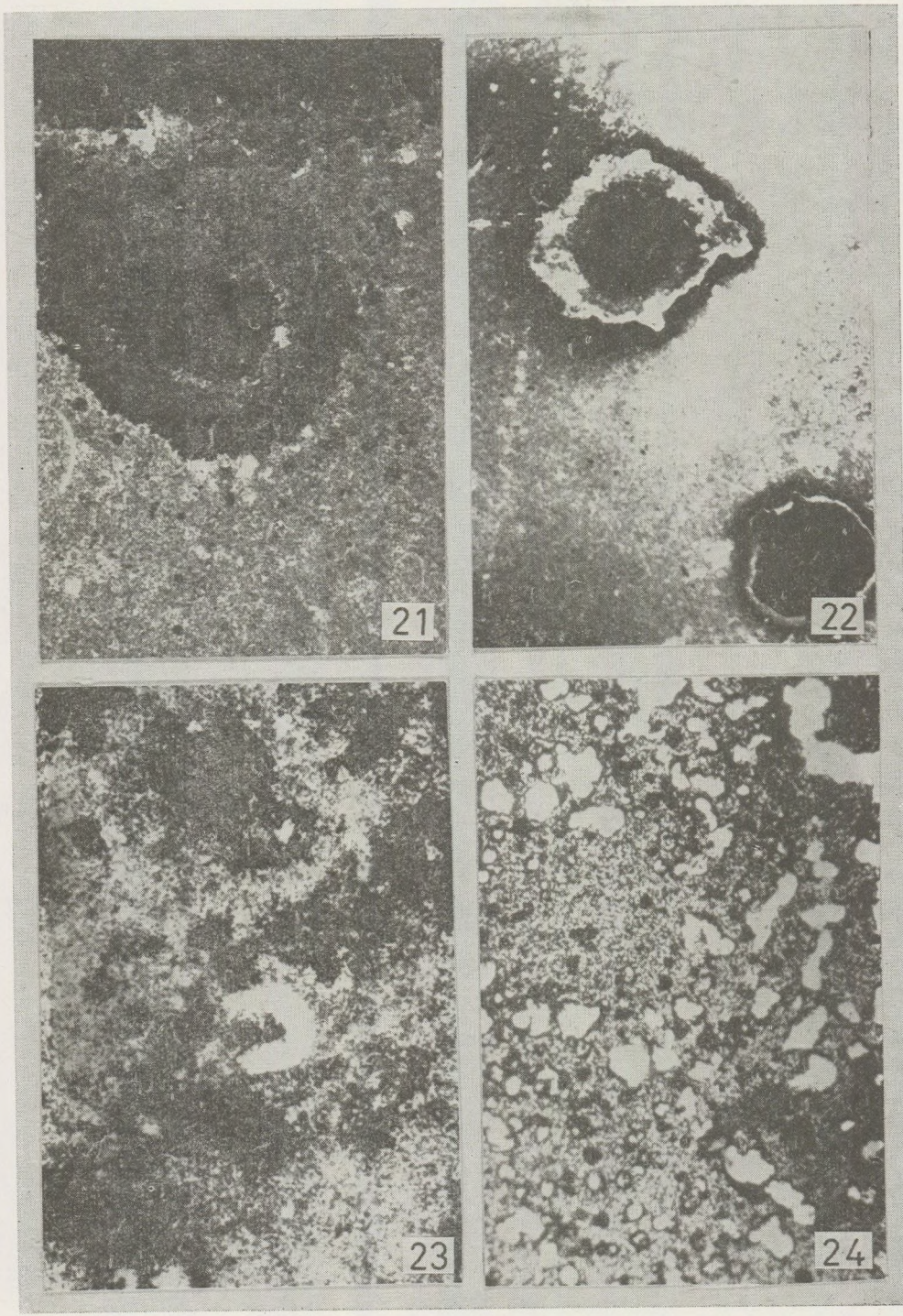
21
22
23
24

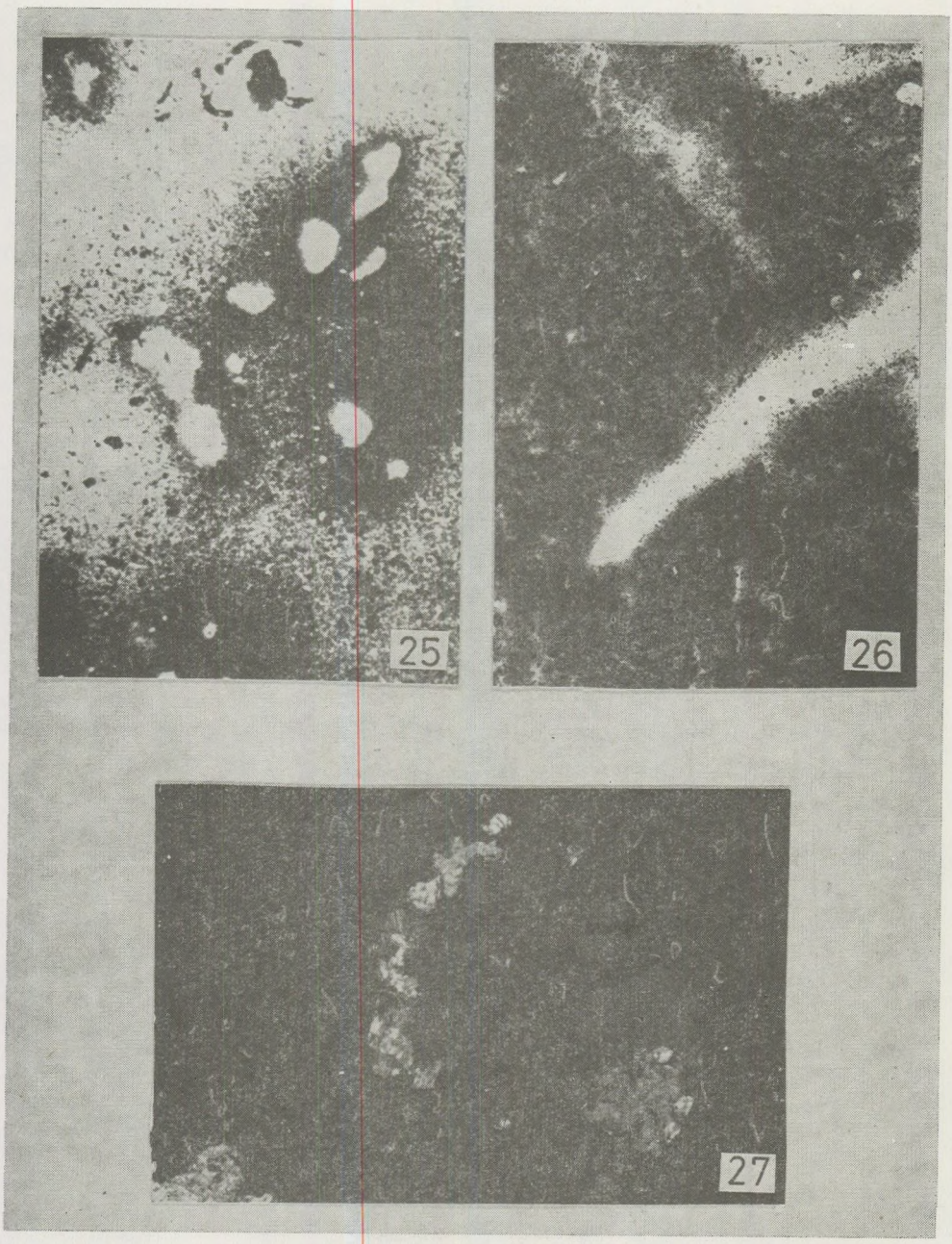
25
26
27

REFERENCES

Bárdossy, Gy. (1961): A magyar bauxit geokémiai vizsgálata (Geochemical investigation of Hungarian bauxites) Spec. Paper of Hung. Geol. Inst.

Bárdossy, Gy.–Pantó, Gy. (1970): A bauxitok vizsgálata elektronmikroszondával (Research of bauxites by electron microprobe) BKL. Bányászat 103/2 pp. 825–837.

Bárdossy, Gy–Pantó, Gy. (1972): On the pyrite types in bauxites Acta Geol. Tom. 16. pp. 3–11.

Bárdossy, Gy. (1977): Karsztbauxitok (Karstic Bauxites) Akadémiai Kiadó Bp. (in hungarian).

Hidasi, J. (1978): Oolitic textural elements in Hungarian bauxites 4th Intern. Congr. ICSOBA Vol. 1. Bauxite. pp. 312–332.

Hidasi, J.–Mensáros, P. (1976): Electron microprobe analyses of karstic and lateritic bauxites. Annal. Univ. Sci. Bp. R. Eötvös Sectio Geol. Tom. XVIII. pp. 3–28.

Dudich, E. jun.–Komlóssy, Gy. (1969): Ősföldrajzi-szerkezeti szempontok a magyar bauxit korkérdéséhez (Considerations paléogeographiques et tectoniques sur la probleme de l'age des bauxites en Hongrie) Földt. Közl. XCIC. 2. pp. 155–165 (in hungarian, with french res.)

Komlóssy, Gy. (1966): A bauxit-piritesedés kérdése (On the problem of the pyritisation of bauxite) Földt. Közl. XCVI. 2. pp. 220–226. (in hungarian, engl. res.)

GEOCHEMISCHE UNTERSUCHUNGEN ÜBER DIE KALKSTEINE AUS DEM SIEBENBÜRGISCHEN BECKEN (RUMÄNIEN)

IMREH, J. – MÉSZÁROS, N. – CIURILEANU, I.

Univ. Bolyai – Babes, Cluj.

Eingegangen dem 15. Marz 1980.

SUMMARY

The paper reports the geochemical investigations of a limestone complex 20 m thick of superior eocene, medium and superior oligocene age. The 22 samples were collected in a vertical row and are designated as 1 Gd (the superior horizon) to 22 Gd (the inferior horizon) as shown in Fig. 1. Chemical and spectral analyses are presented in Tables 1 and 2. Diagrams of the vertical distribution of chemical elements in the investigated limestones are depicted in Figs. 2 – 5. These diagrams were used to establish the correlations between the elements. A parallel distribution between Si, Al, Fe, Ti and Cr on one side, and Ca, Sr, Ba on the other, emerged from these correlation studies, pointing out that Fe, Al, Ti and Cr belong to the insoluble residue, whereas Sr and Ba belong to the carbonated phase.

Am westlichen Ende der Ortschaft GLOD, am südlichen Hang des Berges Dija, erscheint eine Kalksteinserie in einem Steinbruch. Bei den untersuchten Kalksteinen (*Mészáros N., Georgescu, C., Roiban, M.* 1967) handelt es sich um die sogenannten "Culmea Cozlei-Schichten", welche hier bezüglich des Alters mit den Schichten mit Nummulites fabiani, den Bryozoen-Schichten, und den Hoia-Schichten, aus der Umgebung von Cluj-Napoca gleichwertig sind.

In Glod bilden sie eine 20 m starke Serie von organogenen Kalksteinen mit Algen, kleinen Foraminiferen, Nummuliten und Mollusken. Zeitlich betrachtet, bildeten sie sich im oberen Eozän bis zum Beginn des Oligozäns.

Abbildung 1. stellt die lithologische Kolonne dar. Die Stellen, woher Proben entnommen wurden, sind durch Zahlen gekennzeichnet. Es wurden 22 Proben in senkrechter Richtung gesammelt. Die aus dem obersten Horizont entnommene Probe (bioklastischer Kalkstein) wurde mit 1 Gd, und die aus dem untersten Horizont des Kalksteins mit N. fabiani entnommenne Probe wurde mit 22 Gd bezeichnet.

Beim Sammeln der Proben auf der Vertikale, bedienten wir uns unserer Erfahrung, die wir während der Untersuchung anderer Kalksteine aus dem Siebenbürgischen Becken gemacht haben (*J. Imreh, G. Imreh* 1965; *J. Imreh, St. Mihálka* 1965; *J. Imreh, E. Jakab* 1965; *J. Imreh, I. Bedelean* 1967; *J. Imreh, St. Mihálka* 1970; *J. Imreh, G. Imreh* 1971; *J. Imreh, G. Imreh* 1972). Aus diesen Untersuchungen geht deutlich hervor, obwohl der Kalkstein makroskopisch homogen erscheint, die chemische Zusammensetzung grosse Schwankungen aufweist, sowohl bezüglich des Inhaltes in Hauptelementen als auch des Inhaltes in Spurenelementen.

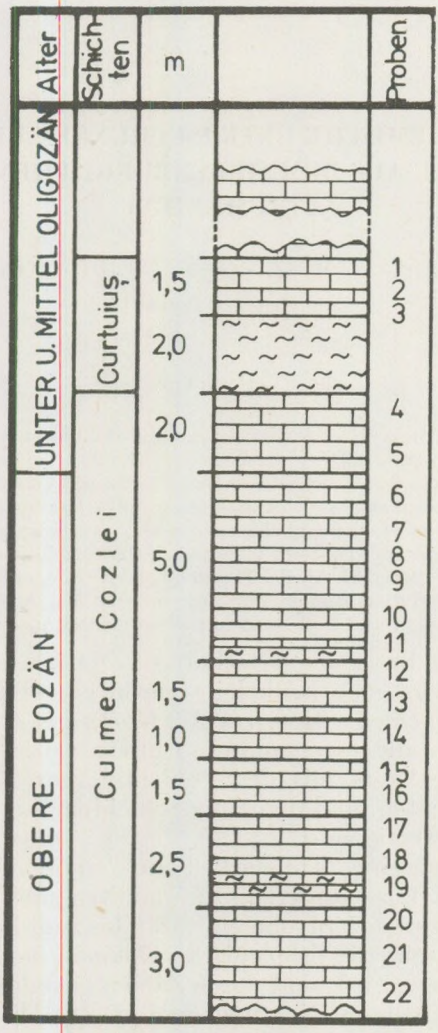

Abb. 1.

Das Studium der senkrechten Verteilung der Elemente aus dem Kalkstein ist nützlich sowohl bezüglich des Chemismus des Gesteines als auch geochemisch, da die senkrechte Verteilung der Elemente uns ein deutliches Bild über die Migration der Elemente und deren Bindung in der Karbonat-Phase gibt. Ausserdem, gibt uns der Vergleich der senkrechten Verteilungen der Elemente aus den *verschiedenen Vorkommen* der Kalksteine desselben Alters die Möglichkeit die untersuchten Horizonte zu parallelisieren, oder durch geochemische Methoden die Bedingungen, unter welchen sich die Kalksteine gebildet haben, festzustellen. Alle diese Probleme wurden weitgehend in unseren vorigen Arbeiten erörtert.

Tabelle 1.

Nr.	Probe	SiO_2 %	Al_2O_3 %	Fe_2O_3 %	Freier Kalzit %	Berechneter Dolomit %
1	Gd	3,25	1,12	1,12	91,61	2,29
2	Gd	3,87	1,04	0,83	92,85	0,67
3	Gd	8,17	1,73	0,78	85,92	1,34
4	Gd	1,49	0,82	1,43	92,89	2,27
5	Gd	4,34	1,83	2,87	88,69	1,81
6	Gd	1,77	0,48	0,40	95,09	1,81
7	Gd	4,60	0,97	0,64	91,77	1,81
8	Gd	3,47	0,65	0,41	94,28	1,34
9	Gd	5,38	0,94	0,56	90,12	2,86
10	Gd	6,90	1,22	0,67	89,40	1,34
11	Gd	7,64	1,39	0,77	88,46	0,89
12	Gd	3,71	0,54	0,34	93,94	1,34
13	Gd	2,84	0,61	0,24	94,63	1,00
14	Gd	3,53	0,49	0,22	94,64	0,67
15	Gd	2,30	0,25	0,15	96,19	0,89
16	Gd	7,96	1,09	0,51	88,11	1,50
17	Gd	1,88	0,30	0,18	96,14	1,56
18	Gd	8,99	2,51	1,02	80,52	5,13
19	Gd	5,26	0,81	0,65	91,95	1,34
20	Gd	2,84	0,45	0,29	94,76	1,13
21	Gd	2,90	0,34	0,31	94,69	0,80
22	Gd	1,54	0,30	0,23	97,89	0,76

Die gesammelten Proben wurden chemisch für die Hauptelemente (Ca, Mg, Fe, Si, Al) und spektral für die Spurenelemente analysiert.

Die chemische Analyse der Proben

Die chemische Analyse der Proben ist in der Tabelle 1 dargestellt, wo die Ergebnisse in Gewichtsprozenten widergegeben sind. Die Werte für das freie $CaCO_3$ und Dolomit aus der Tabelle wurden von uns aus den Ergebnissen der chemischen Analysen berechnet.

Der freie $CaCO_3$ Gehalt. Aus dem auf Klassen von 10% aufgebauten (Abb. 2.) Hystogramm ist ersichtlich dass die häufigsten Werte sich in der Klasse $90\% - 100\%$ befinden und die Häufigkeitskurve einen deutlich asymmetrischen Verlauf hat. Die grosse Häufigkeit der Werte aus der Klasse $90 - 100\%$ beweist, dass dieser Kalkstein einer der reinsten tertiären Kalksteine aus dem NW des Siebenbürgischen Beckens ist. Der kleinste Wert des freien $CaCO_3$ ist 80,52% und der höchste Wert ist 97,89%. Diese Werte, so wie es auch auf Abb. 4 zu sehen ist zeigen eine sehr kleine Schwankung der Veränderung des $CaCO_3$ Gehaltes. Es konnte so eine grosse Ähnlichkeit mit der Verteilung des $CaCO_3$ aus dem Kalkstein von Poiana Blenchii (J. Imre, N. Mészáros, St. Mihálka 1978) festgestellt werden, wo die Schwankung des $CaCO_3$ Gehaltes auch sehr klein ist. Diese Ähnlichkeit ist auf dasselbe Alter der Kalksteine aus den zwei Vorkommen und auf die kleine Entfernung zwischen ihnen zurückzuführen (ca. 14 km).

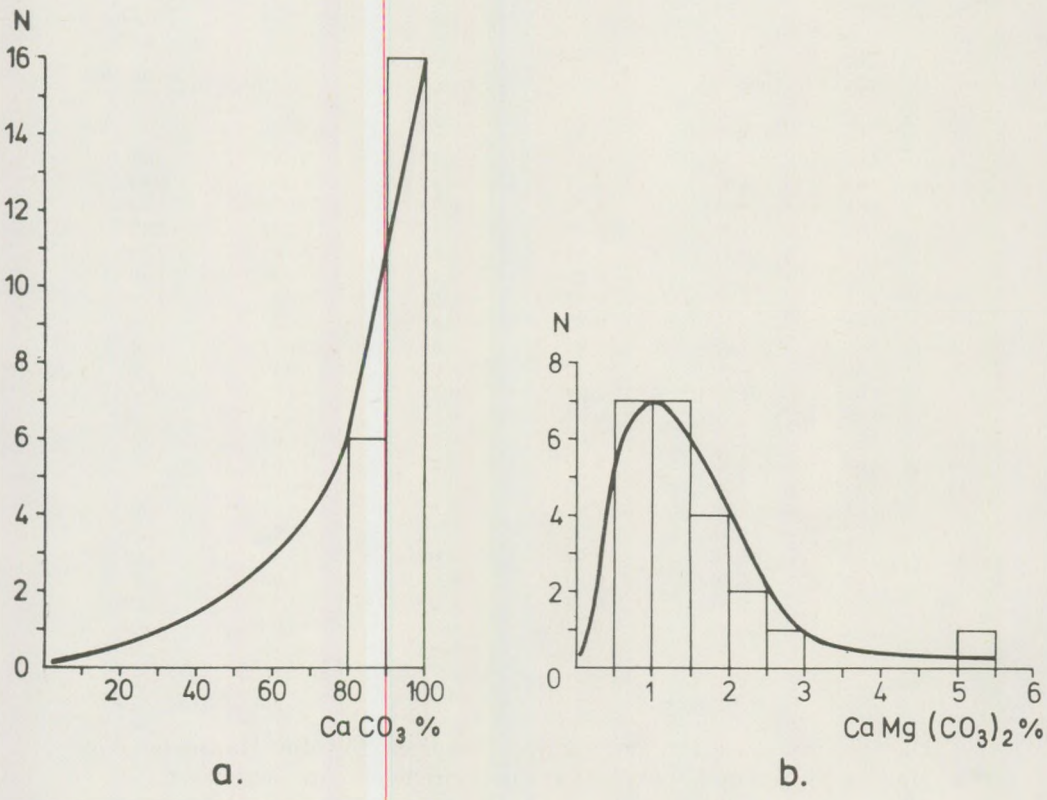

Abb. 2.

Der Dolomit Gehalt. Am auf Klassen von 0,5% aufgebauten Hystogramm können zwei Werte (N = 7) höchster Häufigkeit in den Klassen 0,5–1% und 1–1,5% beobachtet werden, die eine gewönhliche Häufigkeit für die tertiären Kalksteine aus dem Siebenbürgischen Becken darstellen.

Der SiO_2 Gehalt. Der SiO_2 Gehalt weist eine Wertereihe von 1,49% bis 8,99% auf. Das auf Klassen von 0,5% aufgebaute Hystogramm (Abb. 3.) enthält drei Höchstfrequenzen (N = 3) bei drei Klassen.

Der Al_2O_3 Gehalt. Es sind drei Höchstfrequenzen beim SiO_2 festzustellen, aber die Häufigkeitskurve ist asymmetrisch. Die Werte schwanken zwischen dem kleinsten 0,25% und dem höchsten Wert 2,51%.

Der Fe_2O_3 Gehalt. Die Schwankung zwischen den Werten 0,15% und 2,87% ist grösser als beim Al_2O_3. Auch die Werte der höchsten Frequenzen sind grösser als beim Al_2O_3. Auch die Werte der höchsten Frequenzen sind grösser (N = 7–6). Die Häufigkeitskurve ist viel asymmetrischer als die vom Al_2O_3.

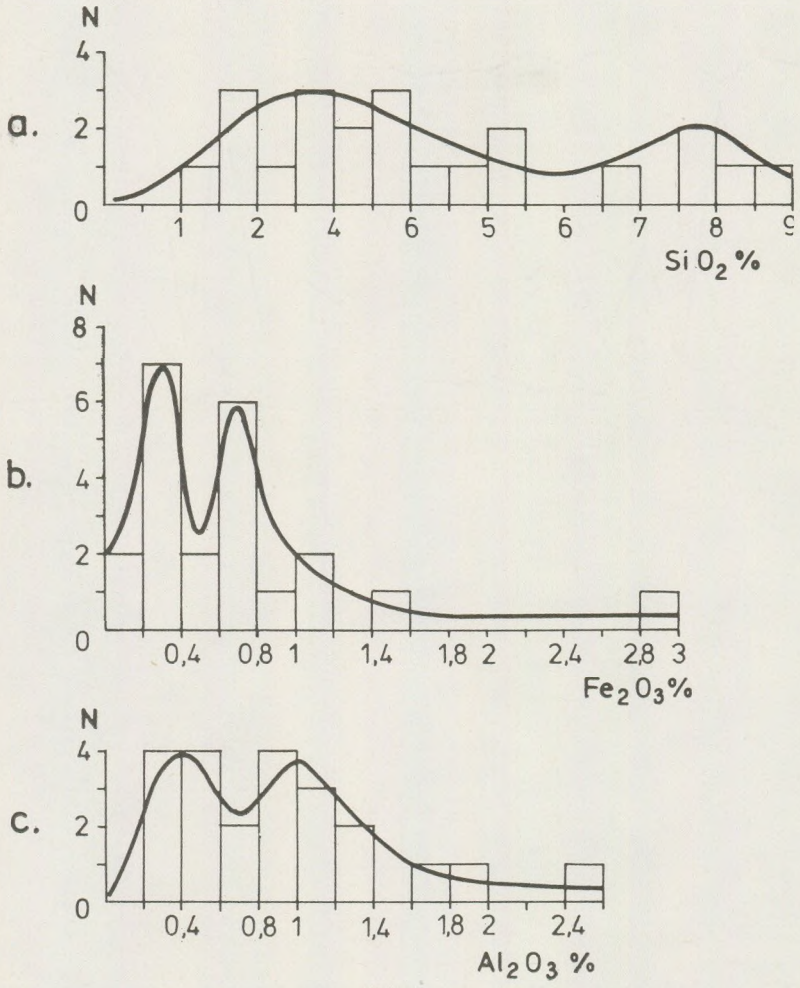

Abb. 3.

In Abb. 4. wurden auf der Ordinate der Gehalt in SiO_2, Al_2O_3 und Fe_2O_3; bzw. $CaCO_3$ in einem anderen Massstab, und auf der Abszisse die Horizonte dargestellt.

Aus der Figur geht deutlich hervor, dass man in den Horizonten wo der SiO_2 Gehalt Spitzen aufweist, auf der Al_2O_3 oder Fe_2O_3 Kurve ebenfalls Spitzen von höchstem Gehalt beobachtet werden können, was eine paralelle Verteilung zwischen Si, Al und Fe beweist. Diese paralelle Verteilung zeigt dass das Eisen und das Aluminium an dem unlöslichen Rückstand des Kalksteines gebunden sind und dass sie zur Bildung der Silikate beitragen. Beim Vergleich der Verteilung in den Horizonten des Al_2O_3 mit der des $CaCO_3$ kann man feststellen, dass zwischen Al_2O_3 und $CaCO_3$ eine antagonische (gegensätzliche) Verteilung besteht, da in den Horizonten,

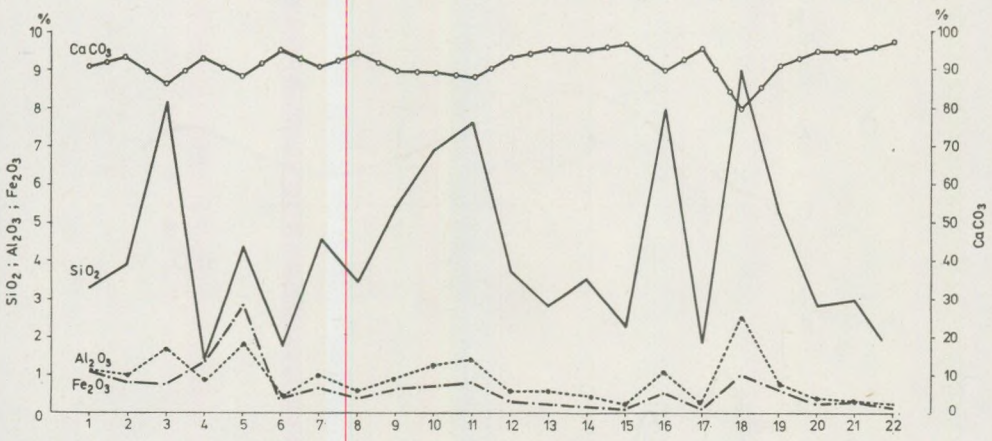
%
CaCO3
SiO2
Al2O3
Fe2O3
SiO2 ; Al2O3 ; Fe2O3
CaCO3
1 2 3 4 5 6 7 8 9 10 11 12 13 14 15 16 17 18 19 20 21 22

Abb. 4.

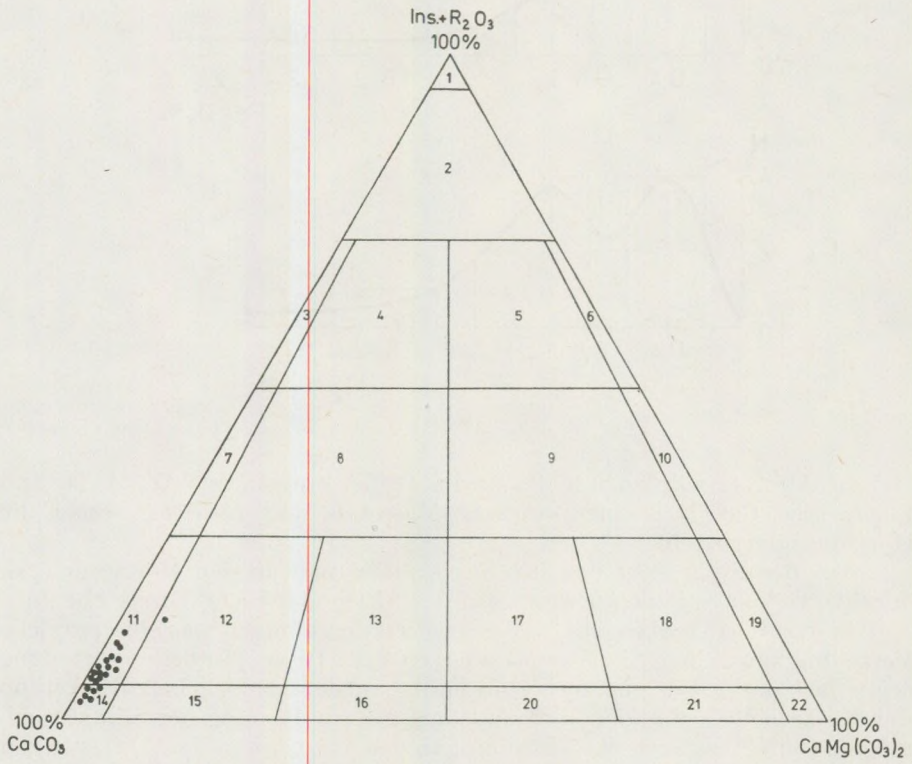
Ins.+R2O3
100%
1
2
3
4
5
6
7
8
9
10
11
12
13
17
18
19
14
15
16
20
21
22
100%
CaCO3
100%
CaMg(CO3)2

Abb. 5.

Das spectrale Studium

Durch die spectrale Analyse wurden die folgenden Elemente bestimmt: Ti, Mn, Cr, Ni, Ba und Sr. Der Gehalt in diesen Elementen ist in der Tabelle 2 wiedergegeben.

Tabelle 2.

Nr.	Probe	Sr	Ba	Ti	Ni	Cr	Mn
1	Gd	1000	3000	170	10	100	150
2	Gd	500	64	180	–	–	360
3	Gd	100	200	160	10	180	410
4	Gd	1000	200	80	10	–	660
5	Gd	300	560	210	–	100	240
6	Gd	1000	200	30	10	–	160
7	Gd	700	76	115	–	160	200
8	Gd	3000	240	90	–	30	320
9	Gd	3000	400	90	–	100	200
10	Gd	1000	310	160	10	160	50
11	Gd	700	120	270	10	180	250
12	Gd	1000	310	80	–	–	100
13	Gd	1000	310	30	–	–	140
14	Gd	1000	350	280	–	–	170
15	Gd	1000	125	30	–	–	160
16	Gd	700	560	500	10	160	100
17	Gd	700	190	145	–	–	200
18	Gd	300	125	260	10	190	180
19	Gd	700	170	30	–	–	150
20	Gd	700	34	80	–	–	210
21	Gd	700	210	80	–	–	290
22	Gd	1000	250	–	–	–	250

in welchen das Al_2O_3 maximale Gehalte aufweist, weist das $CaCO_3$ minimale Gehalte auf. Diese antagonische Verteilung schliesst die Möglichkeit der Angehörigkeit des Fe und Al zur Karbonat-Phase aus. Diese Feststellung ist auch für andere von uns untersuchte tertiäre Kalksteine aus dem Siebenbürgischen Becken gültig.

Eine chemische Klassifikation der Proben

Bei der chemischen Klassifikation der Proben wurde das Vishneakovsche Dreieck (aus L. B. Ruhin 1953) verwendet (Abb. 5). Aus den Projektionen der Proben geht hervor, dass sich die meisten Kalksteine in der Zelle 11 (15 Proben) und 14 (6 Proben) befinden, was einem lehmigen Kalkstein, bzw. einem reinen Kalkstein entspricht. Nur die Projektion einer der Proben befindet sich in Feld 12 (lehmiger, schwach dolomitischer Kalkstein). So unterscheidet sich der Kalkstein von Glod deutlich von den anderen von uns untersuchten tertiären Kalksteinen aus dem Siebenbürgischen Becken, deren Horizonte nur selten in Feld 14 zu finden

sind. Er unterscheidet sich wesentlich auch vom Kalkstein von Poiana Blenchii mit welchem er anderseits viel Gemeinsames hat.

Aus dieser Tabelle geht hervor, dass der grösste Teil der bestimmten Elemente lithofil sind, während die typischen Chalkophilen Elements (Pb, Zn) fehlen. Einige Elemente (Ga, Co, Be, Pb, Zn, V, Cu), welche im Kalkstein aus der Umgebung von Cluj-Napoca erscheinen, fehlen im Kalkstein von Glod. Bei Poiana Belnchii fehlen die Elemente Pb, Zn und Cu, es erscheinen aber das W und Sn die bei Glod nicht erscheinen. Man kann also sagen, dass der Kalkstein von Glod, geochemisch einen Übergang vom Kalkstein aus der Umgebung von Cluj-Napoca zu dem aus dem NW Teil des Siebenbürgischen Beckens darstellt.

Diese geochemische Übergangsposition ist aber sehr relativ, da aus dem Kalkstein von Glod die Elemente Pb und Zn fehlen, zwei sehr typische Elemente für den Kalkstein aus der Umgebung von Cluj-Napoca, sowie W und Sn welche typisch für Poiana Blenchii sind. Manchmal bilden die Elemente Pb und Zn in den Kalksteinen aus der Umgebun von Cluj-Napoca eigenstehende Mineralien: Bleiglanz und Blende (*J. Imreh, N. Mészáros* 1964).

Das Diagram aus der Abb. 6 stellt die Korrelation der Spurenelemente dar, wo wir so wie bei den Hauptelementen, auf der Ordinate die Gehalte in Elementen (in ppm ausgedrückt) und auf der Abszisse die Horizonte dargestellt haben. Die geochemisch wichtigste Verteilung ist die der Elemente Sr und Ba. Aus dem Diagramm geht deutlich die parallele Verteilung zwischen Sr und Ba hervor, und das weist auf die enge Verbindung zwischen den Elementen Sr und Ba in den Kalksteinen hin. Diese parallele Verteilung zwischen Sr und Ba wurde auch von W. Kühn (1976) bei den

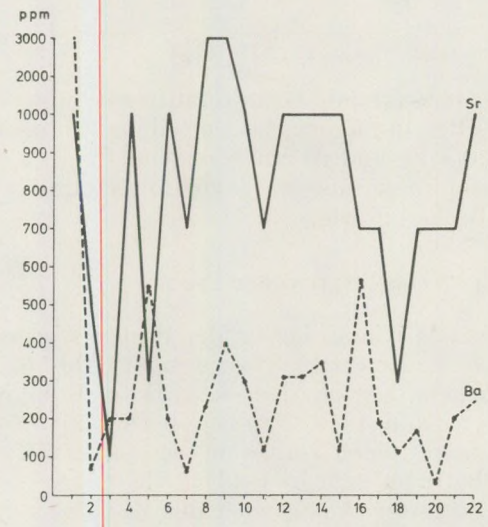

Abb. 6.

Kalksteinen aus dem Thüringer Becken festgestellt. Wenn wir Abb. 4 und 6 vergleichen, können wir eine parallele Verteilung der Elemente Sr und Ba zum $CaCO_3$ beobachten, da die Spitzen der maximalen und minimalen Gehalte aus den Abbildungen bei denselben Horizonten entsprechen, was darauf hinweist, dass Sr und Ba an die Karbonat-Phase gebunden sind. Dasselbe wurde auch von *M. Fornaseri* und *L. Grandi* (1963, 1968) bei der italienischen Kalksteinserie festgestellt. So unterscheiden sich die Kalksteine von Glod von Kalksteinen aus Poiana Blenchii, bei denen die paralelle Verteilung zwischen Sr und Ba nicht so deutlich ist.

Wenn man die Verteilung über die Horizonte von Ti, Ni und Cr untersucht, kann man feststellen, dass diese Elemente eine parallele Verteilung zur SiO_2 Kurve haben, und das beweist, dass sie Bestandteile der unlöslichen Fraktion sind welche sich in den Rezistaten konzentrieren.

Die Betrachtung der Haupt- und Spurenelemente bringt uns zur Schlussfolgerung, dass der Kalkstein von Glod einer der reinsten tertiären Kalksteine ist, die wir im Siebenbürgischen Becken untersucht haben, und die wenigsten Spurenelemente enthält.

LITERATUR

Fornaseri, M., Grandi, L. (1963): Contenuto in stronzio di serie calcaree italiane. Giorn, Geol. Ann. Muzeo Geologico Bologna, 31.

Fornaseri, M., Grandi, L. (1968): Nuovi dati sul contenuto in stronzio di serie calceree italiane. Periodico di Mineralogia, 37.

Imreh, J., Mészáros, N. (1964): Bleiglanz in einigen Schalen von Cyrena sp. N. Jb. Geol. Paläont. Mh., 11.

Imreh, J., Imreh, G., St. Mihálka (1965): Zur Verbreitung des Strontiums in tertiären Kalken. N. Jb. Miner. Abh., 103, 3.

Imreh, J., Jakab, E. (1965): Étude géochimique sur quelques calcaires éocènes du Bassin Transylvain (Roumanie). Bull. Serv. Carte géol. Als. Lorr. 18, 4.

Imreh, J., Bedelean, I. (1967): Étude géochimique des calcaires tortoniens de la bordure occidentable du Bassin Transylvain (Roumanie). Bull. Serv. Carte géol. Als. Lorr. 20. 4.

Imreh, J., Mihálka, St. (1970): Étude géochimique de quelques calcaires éocénes de la partic Nord – Quest du Bassin Transylvain (Roumanie). Bull. Serv. Carte géol. Als. Lorr. 23, 3 – 4.

Imreh, J., Imreh G. (1971): Contenuto in stronzio e bario dei calcari eocènici e tortoniani della parte ovest e nord-ovest del Bacino Transilvanice (Romania). Periodico di Mineralogia, 40, 3.

Imreh, J., Imreh, G. (1972): Geochemische Bedeutung des Sr und Ba beim Studium tertiärer Kalksteine. TMPM, 17.

Imreh, J., Mészáros, M., Mihálka, St. (1978): Studii geochimici sulle serie calcaree terziarie del Bacine Transilvanico (Romania). Periodico di Mineralogia, 47, 1 – 2 – 3.

Kühn, W. (1976): Buntmetallführende Karbonatbänke der Höheren Trias in Thüringer Becken. Chem. d. Erde, 35.

Mészáros, N., Georgescu, C., Roiban, M. (1967): Eocenul si baza oligocenului in regiunea Ileanda Mare – Poiana Blenchii. Studia Univ. Babes – Bolyai, ser. Geol. – Geogr. 1.

Ruhin, L. B. (1953): Osnovi litologii. Leningrad – Moskva.

Rusu, A. (1977): Stratigrafia depozitelor oligocene din nord-vestul Transilvaniei (reg. Treznea – Hida-Poiana Blenchii). Anuarul Inst. Geologie si Geofizica, 51.

NOTE ON THE ARCHAEOMAGNETIC DIPOLE WOBBLE

MÁRTON P.

Geophysics Department, L. Eötvös University
Budapest, VIII. Kun Béla tér 2.

Received 2. June 1981.

ABSTRACT

The present archaeomagnetic results for the last two millenia are consistent with a secular variation pattern of the geomagnetic field in which periods with predominantly dipole variations (rapid shifts in the location of the geomagnetic axis) alternate with intervals of prevailing nondipole variations and a nearly stationary geomagnetic dipole axis.

Introduction

This note has been prompted by two recently published papers (*Barbetti*, 1977), (Braginsky and Burlatskaya, 1979) relevant to the problem of the archaeomagnetic dipole wobble. The idea was thrown out by *Kawai* and *Hirooka* (1967) who postulated a quasi-hypotrochoid motion of the geomagnetic dipole axis as opposed to *Yukutake*'s non-dipole model (*Yukutake*, 1962) for explaining the cause of the archaeosecular variation (ASV) of the geomagnetic field. The true nature of the ASV could have been decided by harmonic analysis over the appointed period of time had there been a sufficient number of spatially well distributed archaeomagnetic observations covering the time period of interest which, however, has never been the case. This is why another, less rigorous approach was taken to test the opposing ideas about the ASV and it was based on *Cox*'s statistical analysis of the 1945 geomagnetic field of *Vestine* et al. (1947).

Discussion

Cox (1962) demonstrated that if a dipole wobble of the expected magnitude is superimposed on the secular variation (SV) of a nondipole field statistically identical with the present (1945) field, then it should be detectable from the time variation of the virtual geomagnetic pole (VGP). *Márton* (1970 a) analized the world archaeomagnetic data available up to 1969 at 50 year intervals for the past two thousand years applying a method that can incorporate any D, I and F observation either separately or in any combination for the determination of the VGP. The results were interpreted formally using *Fourier* expansion of the VGP variation with a basic period of 1800 year and it was believed that the changes in the VGP

location with periods of 1800 and 900 year were predominantly due to the SV of the geomagnetic dipole axis. In such an analytical description of the SV, however, the postulated swings of the geomagnetic dipole axis are largely smoothed out therefore a statistical interpretation of the VGP path was also offered (*Márton*, 1970 b) on the following grounds. A small dispersion of the computed VGP's arises from the differences in the sampling sites used for the analysis at the different times over the studied interval. The dispersion characterizing the deviation of these VGP's from the geomagnetic pole was estimated to be 7.5° of arc for the 1945 geomagnetic field. Thus, it was assumed that changes in the position of the VGP exceeding, say, 10° of arc are caused possibly by swings of the geomagnetic pole.

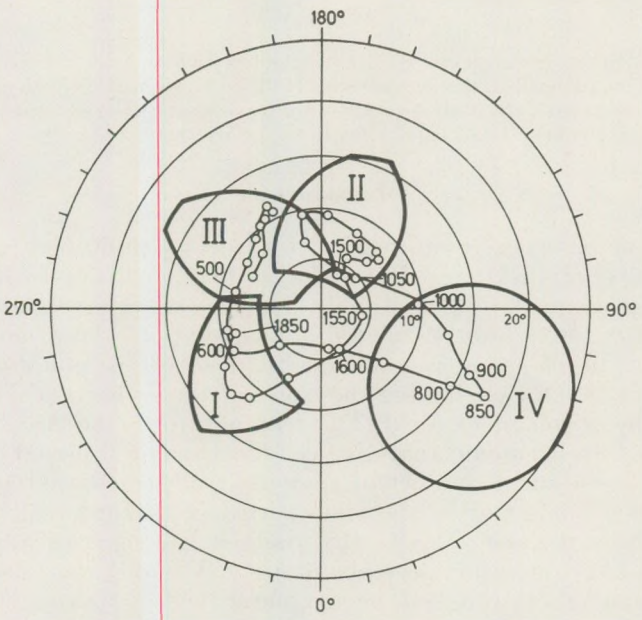

Fig. 1. Secular variation of the virtual geomagnetic pole computed from archaeomagnetic data for the past two thousand years (stereographic projection) Márton; 1970b).

Fig. 1 shows the VGP path on a stereographic plot. A circle of 10° radius was constructed around every computed VGP. The patches labelled I. to IV. in Fig. 2 are those areas which are common to a number of circles and each marks a period of time within which the geomagnetic pole may have been stationary. Based on this construction the following model was set up for the ASV (cf. Fig. 2).

The geomagnetic pole has been practically unchanging four times during the last two millenia namely between about 50 – 100 and 500 – 600 A. D.; about 750 and 950 A. D.; 1000 – 1050 and 1500 A. D. and from

1550 – 1600 A. D. till now. Within these time periods the SV has been dominated by nondipole changes (westward drift). The geomagnetic pole has displayed swings of the order of 20° of arc with a velocity of 0.1 – 0.2 deg./year in between its quasi-stationary periods. The style of the SV during these two thousand years has been such that the position of the mean VGP is identical with that of the geographic pole!

New archaeomagnetic results from Australia were presented by *Barbetti* (1977) and it is asthonishing how well they fit into the above described scheme. Two of the Australian VGP's (numbers 4 an l 5) with ages greater than 1390 A. D. lie close to the present geomagnetic pole and probably belong to area labelled I. in Fig. 2. The VGP's (numbers 2 and 3) dated between 815 and 1385 A. D. fall on area labelled IV. in Fig. 2 and finally the VGP (number 1) at about 550 A. D. lie close to area labelled III. in Fig. 2. The broad agreement between the newer Australian and the older analytical results substantiate the reality of the interpretation of the ASV in terms of the geomagnetic dipole wobble. *Barbetti* (1977) concluded from his own analysis that a large change occured in the orientation of the geomagnetic axis between 1400 and 1650 A. D. which is exactly one of the jerks of the dipole axis suggested above. It may be concluded

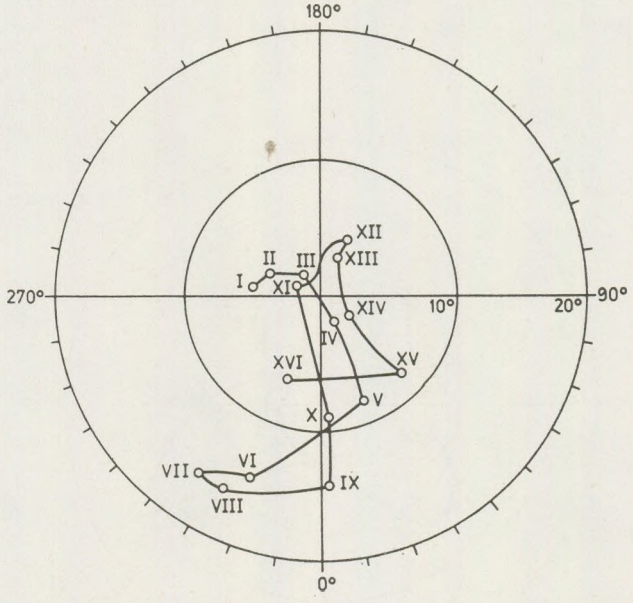

Fig. 2. Areas labelled I. through IV. mark those periods (and domains) within which the geomagnetic dipole is thought to have been stationary. These are as follows:

I.	present	–	1500 – 1600 A. D.
II.	~1500	–	1000 – 1050 A. D.
III.	~500 – 600	–	50 – 100 A. D.
IV.	~750	–	~950 A. D.

(stereographic projection; Márton, 1970b).

further from the Australian VGP locations (numbers 1, respectively 2 and 3) that another swing must also have occured in the orientation of the dipole axis between about 600 and 800 A. D. which, however, has also been proposed (cf. Fig. 2).

Recently, *Braginsky* and *Burlatskaya* (1979) have carried out an harmonic analysis of the accumulated archaeomagnetic data including the Australian results (Barbetti, 1977). They have determined the absolute magnitude of the first eight Gauss coefficients which in fact are, due mainly to the truncation of the potential series at $n = 2$, apparent or virtual values as shown by the RMS errors of g_n^m, h_n^m amounting 28 to 58 percent of the magnitude of the coefficients themselves. Although Braginsky and Burlatskaya (op, cit.) admit that such an error can entirely mask the SV of g_n^m, h_n^m it might be instructive at least to look at the changes the first three coefficients exhibit during the analized period from the first to the sixteenth century A. D., Fig. 3 shows the positions of the "geomagnetic dipole" axes computed from g_1^1, h_1^1 and g_1^0 and again there are similarities between this and Fig. 2. Apart from the last three-four centuries without pole determinations in Fig. 3 there are three quasi-stationary periods (Ith – IVth, VIth – VIIIth and XIth – XIVth centuries A. D.) of the 'geomagnetic" axis from which the first and the third are essentially dentical with the periods labelled III. and II. in Fig. 2. The period between

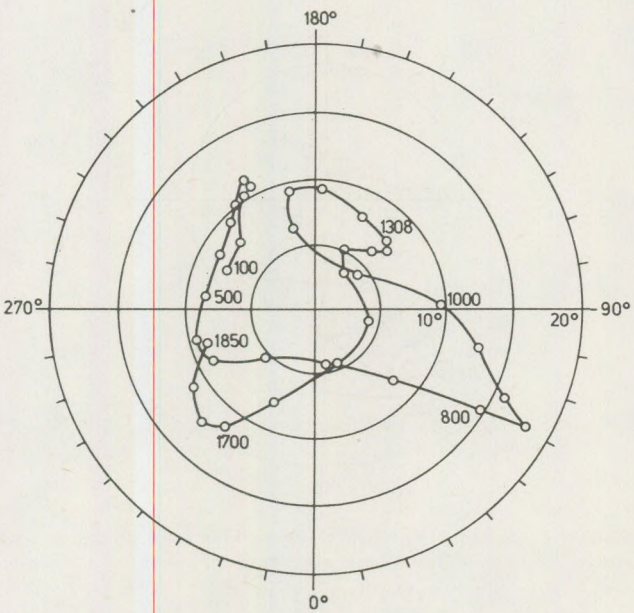

Fig. 3. "Geomagnetic pole" positions from the Ist to the XVIth century A. D. computed from the first order Gauss coefficients of Braginsky and Burlatskaya (1970) (stereographic projection).

the VIth and VIIIth centuries A. D. is new with respect to Fig. 2 but its existence (and the pole path between the VIth and XIth centuries A. D.) are not supported by the Australian data either.

Conclusion

In spite of this last possible disagreement it can be concluded that the present archaeomagnetic data for the past two thousand years are consistent with an SV pattern of the geomagnetic field in which periods with predominantly dipole variations (rapid changes in the orientation of the dipole axis) alternate with intervals of prevailing nondipole variations and a nearly stationary geomagnetic dipole axis.

REFERENCES

Barbetti, M., 1977: Measurements of Recent Geomagnetic Secular Variation in Southeastern Australia and the Question of Dipole Wobble, EPSL., Vol. 33,pp. 207–218.

Braginsky, S. J, Burlatskaya, S. P., 1979: Spherical analysis of the geomagnetic field using archaeomagnetic data (in Russian), Fizika Zemli, Vol. 12, pp. 59–66.

Kawai, N., Hirooka, K., 1967: Wobbling Motion of the Geomagnetic Dipole Field in Historic Time during These 2000 Years, J. Geomagnet. Geoelectr., Vol. 19, pp. 217–227.

Yukutake, T., 1962: The Westward Drift of the Magnetic Field of the Earth, Bull. Earthquake Res. Inst. Tokyo Univ., Vol. 40, pp. 1–65.

Vestine, E. H., Laporte, L., Lange, I., Cooper, G., Hendrix, V., 1947: Description of the Earth's Main Magnetic Field and its Secular Change, 1905–1945, Publ. Carneg. Inst. No. 578.

Cox, A., 1962: Analysis of Present Geomagnetic Field for Comparison with Paleomagnetic Results, J. Geomagnet. Geoelectr., Vol. 13, pp. 101–112.

Márton, P., 1970a: Secular Variation of the Geomagnetic Virtual Dipole Field During the Last 2000 Years as Inferred from the Spherical Harmonic Analysis of the Available Archaeomagnetic Data, Pageoph., Vol. 81, pp. 163–176.

Márton, P., 1970b: Palaeosecular Variation of the Geomagnetic Field During the Last 2000 Years (in Hungarian), Thesis.

CLIMATE MODEL BASED ON THE ENERGY-BALANCE OF THE EFFECTIVE SEA-SURFACE

MIKA, J.

Department of Meteorology, Eötvös Loránd University Budapest, Múzeum krt. 6 – 8.

Received: 20. july 1980.

SUMMARY

The paper deals with a zonally averaged, stationary energy-balance model based on the heat-exchange of the quasi-isothermal layer of the ocean. It is assumed that the climatic changes of the continents are caused by changes over the ocean, which has great heat capacity. The experimental coefficients are altering themselves, this is why in case of a significant climate change the validity of the model is getting worse, moving away from the present climate. The result of the first test is positive, i. e. the sensitivity of the model lays in the region of the best avaible estimation. Further development can be reached by modification of the numerical algorithm and the boundary conditions at the South-Pole.

Introduction

A real aim for numerical modeling of the climate can be the elaboration of so-called "predictions of the second kind" (LORENZ 1967). Such kind of computations avoid to treat the uncertainities connected with the time-evolutions of the effective factors, that is the consequences of hypothetical, isolated climatic changes are investigated only. The validity of these predictions can be guaranteed by the adequate model description and by a reliable model sensitivity. We have an estimated value for the sensitivity of the real climate against different external forcings, which is expressed in the

$$\beta = \frac{\Delta T}{\Delta S_0} S_0$$

form. This β equals about 140 – 150 K, i. e. in case of 1% change of the solar constant S_0, the average temperature of the Earth alters by 1,4 – 1,5 K. This value should be average sensitivity of the different models with more or less different structures, and/or could be regarded as a base of comparison in judging of individual models (BUDYKO 1969, CESS 1975, GAL-CHEN – SCHNEIDER 1973, KONDRATIEV 1976, OERLEMANS – VAN DEN DOOL 1978)

The role of predictions of the second kind is to give information about the possible climatic changes due to anthropogenic effects. Nowadays,

the physical climatology cannot answer these question in every detail, so the numerical predictions of the different models can only be regarded as estimations of the order. It would be more close to the reality, if the same investigations were made with the help of several models, which have structures different from each-other, as much as possible. When most of these results would take place around an average value, then this value could be considered as a better estimation of the real climatic consequence.

It means that the proviso of this "probability approximation" is a sufficient number of climate models having independent structures. In this paper such a stationary energy-balance model is introduced, what has mainly such parameterizations, which first time are used in a climate model.

Physically, our model is zonally averaged and stationary, the energy-balance is required for the ocean with real extent, and it is assumed that over the continents – which have lower heat-capacities –, the temperature changes are only consequences of the oceanic ones. In our judgement, the omitting of processes over the continents is in accordance with the given degree of the space- and time-resolution, and is advantageous for execution of further numerical simulations.

1. Model description

1.1 Notations

γ – quotient of actual and present-time meridional temperature gradients.

γ_w – quotient of actual and present-time meridional sea-surface temperature gradients.

Γ, Γ_0 – actual and present-time meridional gradients [°C].

Γ_w, Γ_{0w} – actual and present-time meridional sea-surface temperature gradients [°C].

ε – sea-surface emissivity coefficient, equals to 0.91.

σ – $5.67 \cdot 10^{-8}$ Wm^{-2} $grad^{-4}$, the Stephan-Boltzman constant.

a – empirical constant in the (1.2) equation, depending on the latitude.

A_0, A – albedos of the ocean for clear- and for ordinary cloudy sky.

b – empirical constant in the (1.2) equation, depending on the latitude.

B – energy term, containing oceanic horizontal and vertical heat-currents [Wm^{-2}].

C – empirical constant depending on the latitude in the (1.5) relationship.

C_p – heat capacity of the air, equals to 1011 $m^2 s^{-2} K^{-1}$.

e, e_w – water vapour pressure at the higher level, as well as at the sea-surface. [mb]

E – quantity of water evaporating from a unit surface in a unit time $[kgm^{-2}s^{-1}]$.
f – relative humidity expressed in fraction of the unit.
H – turbulent heat-transfer $[Wm^{-2}]$.
k, k_a, $k_E = k_H$ – latitude dependent empirical constants in equations (1.12), (1.3), (1.8) and (1.9).
k_R – temperature dependent coefficient in eqution (1.6).
L – heat of evaporation, equals to $24.7 \cdot 10^5\ m^2\ s^{-2}$.
n – cloudiness expressed in fractions of the unit.
q, Δq – specific himidity and its vertical gradient in equation (1.8).
Q_0^+, Q_0 – latitude dependent values of the global radiation for cloudless sky in case of ideally absorbing- and in case of real surface (maximum possible insolation) $[Wm^{-2}]$.
R_S, R_L – short- and long-wave radiation balances $[Wm^{-2}]$.
S_0 – latitude dependent intensity of solar radiation, on the top of the atmosphere $[Wm^{-2}]$.
t, T – air-temperature, expressed in °C as well as in K.
t_w, T_w – sea-surface temperature, expressed in °C as well as in K.
ΔT – vertical temperature gradient in equation (1.9). [°C].
t_E – air-temperature, extrapolated to the Equator.
T_{we} – sea-surface temperature, extrapolated to the Equator.
u – wind speed at the 8m level $[ms^{-1}]$.
W – water vapour content of a unit surface vertical air-column ranging from the surface to the top of the atmosphere [kg].

1.2 Energy exchange of the effective surface

The fundamental equation of our model is an energy-balance one, written for the quasi-isothermal effective surface of the ocean:

$$R_S = R_L + L \cdot E + H + B \tag{1.1}$$

The law of energy conservation is only a necessary condition for the natural processes, i. e. to make the consequence unique, other relationships must be prescribed too in the model.

First, let us express the energy terms as (experimental) functions of yearly averaged climate elements. The theoretical background for this is supplied by the works done at the Geophysical Main Observatory of Leningrad. The purpose of these investigations started in 1954, was to calculate the measurable terms of the surface energy exchange from the data of standard meteorological elements.

The function of these connections has been changed during their inclusion into the model, that is, according to our aims, this time the meteorological elements are being calculated – beside altered external conditions –, using the energy balance condition.

The most important quantity in the parameterization of the short-wave energy balance is the maximum possible irradiation Q_0 (BERLJAND 1961). Its value, determined from direct measurement, shows the quantity of the global radiation at the surface in cloudless condition, for a given geographical location and for a given season. In comparison with the average, attenuated (by clouds) irradiation it has a maximum value. In the presence of clouds the short-wave balance is the following:

$$R_S = (1-A) \cdot Q_0 \cdot (1-an-bn^2). \tag{1.2}$$

According to measurements and computations done by TER MARKARJANCH, the ocean's albedo depends on the cloud coverage at middle and high latitudes, i. e. at middle and low Sun-elevation angles (KONDRATIEV 1965). Physically, this dependence is based on that fact, that for the radiation under high zenith angles, a greater part of it is reflected, than for low zenith angles. The cloudiness – beside the absorption effect –, scatters the radiation depending on its direction. For this reason, at low Sun-elevation angles the albedo decreases when the cloud coverage increases, while at high Sun-elevation angles slightly increases. In case of total cloudiness – according to the measurements –, the albedo becomes nearly independent on the Sun-elevation angle. The above-mentioned relationship can be succesfully approximated by the

$$A = A_0 \cdot \exp(k_a \sqrt{1-n}) \tag{1.3}$$

equation, where the coefficients are functions of the geographical latitude.

For a given latitude, the value of Q_0 is determined by the water-vapour- and ozone amounts. (The amounts of gas-components active in the short-wave absorption are regarded constant.) MÖLLER's calculations show that the absorption by water-vapour is proportional to the 0.3-rd power of water-vapour content taking place in the path of the radiation. There exist no such a simple relationship for treating the aerosol effect. The amount of the global radiation reaching the surface is only slightly dependent on the albedo, because of the radiation, reflected from the surface is scattered back again by the atmosphere.

Following AVERKIEV, this is taken into account as the

$$Q_0 = \frac{1}{1-0.2\,A}\, Q_0^+ \tag{1.4}$$

relationship, where Q_0^+ is the total radiation, absorbed by a black-body having ideal surface, as well as the sky is cloud-free.

So, we obtain:

$$R_S = (1 - A_0 \cdot \exp(k_a \sqrt{1-n}) \cdot S_0 (1 - C \cdot W^{0.3}) \cdot \cdot \frac{1}{1 - 0.2\, A_0 \cdot \exp(k_a \sqrt{1-n})} \cdot (1 - an - bn^2). \tag{1.5}$$

Here C accounts for the aerosol absorption, the effect from increase of the radiation path-lenght, as well as the absorption and scattering by gases.

In the parameterization of the long-wave backward radiation we use, that there is a strong correlation between the temperature and the vapour tension above sea-surface (GIRDYUK – MALEVSKI – MALEVICH 1973), and so the number of parameters determining the effective outgoing radiation can be reduced:

$$R_L = \varepsilon \sigma T_W^4 - \varepsilon(1.63\sqrt{\sigma T^4} - 0.775)(1 + k_R n^2) \tag{1.6}$$

The term k_R is not constant strictly, therefore its tabulated values (BUDYKO 1978) were applied, approximated as:

$$k_R = 0.35 \cdot \exp(-0.0316t). \tag{1.7}$$

A common feature of the evaporation and of the turbulent heat-transport is that both are transport processes, i. e. they are linearly proportional to the gradients of the appropriate intensive quantities. The coefficients depend on the wind-speed and on the balance-conditions of the air at the sea-surface. The first connection is taken into account – according to the references –, as being linearly shaped, while the second is regarded as an empirical constant depending on the latitude.

This way:

$$E = k_E \cdot u \cdot \Delta q \tag{1.8}$$

and

$$H = c_p \cdot k_H \cdot u \cdot \Delta T, \tag{1.9}$$

where Δq and ΔT are gradients between the bottom of the turbulent layer and the 8 meters level of the standard oceanic measurements. Experience shows that the gradient between the real surface and a level laying in the turbulent layer, is a constant-times multiple of the above difference – independently from the weather conditions –, and this constant depends only on the selection of the upper measurement level (KONSTANTINOV 1963). Replacing this constant to the expressions determining k_E. and k_H., and using the approximate relationship

$$Q = 0.62 \cdot 10^{-3} e \tag{1.10}$$

between the specific humidity and the vapour tension, as well as that $k_E = k_H$, we get finally for the evaporation heat and for the turbulent heat-transfer:

$$L \cdot E = 1.5\, ku(e_W - e), \tag{1.11}$$

$$H = ku(T_W - T) \tag{1.12}$$

Here e_W equals to the saturated water-vapour tension at t_W, because of decrease of the balance vapour tension is negligible at the used level of accuracy (2 digit number). This low level of accuracy is explained by that fact, that the present-time energy values applied in determining k, were also 2 digit numbers only (BUDYKO 1978).

The remaining term of the oceanic heat-transport is resulted from two processes. Possibly, the greater contribution to it comes from the horizontal transport within the isothermal effective surface, driven by wind-created streams and transient eddies. Its other part is connected with the vertical transport with the deep ocean. The $50-100$ m thick isothermal layer transmits just a very small fraction of the incoming short-wave radiation into the deeper regions, while the long-wave vertical transport seems to be negligible, because of the strong absorption of the water. According to recent theories, the molecular- and the slightly turbulent transport also play role in the heat-conduction under the isothermal layer. As could be seen, the term B is a result of several processes, this is why the folloving solution procedure was chosen, instead of explicit modelling: For reproducing the recent climate the B values themselves were used, while at changing of the solar constant the global feedbacks were treated in a manner described under point 1.4.

1.3 Local feedbacks

The energy-balance equation for the effective surface is such a one, which enables us to calculate any of the meteorological elements, knowing all the others. It is evident, that their present values should be inserted into this equation. By the way, most of these elements are internal factors, i. e. during the change of an element for which the solution goes-they do not remain unchanged themselves. In fact, because of our quanti, tative knowledges restrict mainly to the very present-time-, or to a similar climate, we have to include and fix certain parameters empirically, in spite of that we know exactly: in a real situation these also are altering, when the climate undergoes excursions. So, the validity of any climate model depends mostly on that, how "far" are these values from the values of such parameters, which directly affect the temperature, and how great are the obeyed variations of the internal factors. Since these variations finally react upon the changes of the temperature – the most significant climate indicator –, the equations regulating these processes are called feedbacks.

Two of these feedbacks were described in the previouos Section; one between the cloudiness and the albedo, while the other between the albedo and the global radiation [(1.3), (1.4)].

The using of fixed cloudiness is also not suitable, therefore a regression equation

$$n = -0.30\, f - 0.0085\, t + 1.02 \qquad (1.13)$$

was determined from the 16 elements of the 10° latitude-belt averages. The correlation coefficient was 0.9.

In accordance with the experience, the relative humidity f, also can not to be an unrestricted quantity over the ocean (within the $0-1$ range). E. g. at a perfect calm the saturation is possible in a several meters thick air-layer above a greater water-surface, while it is not possible when the wind speed is high enough, because of the strong turbulence. Based on

observations over ice-free domains of the Pacific Ocean, a negative relationship with high correlation was found by STOLOVNIKOVA between the monthly mean relative humidity and the 850 mb wind speed (SERGIN – SERGIN 1978). These results were adapted into our model in the form:

$$f = 1.0 - 0.024\,u. \tag{1.14}$$

The water-vapour content w of a vertical column, playing role in the short-wave radiative balance, can be expressed according to REITAN as the following relationship (SELLERS 1973):

$$w = 0.124 + 0.16\,e. \tag{1.15}$$

The saturation vapour tension regarding temperature t is determined from an approximated form of the MAGNUS-formula:

$$e^{+} = 6.1 \cdot \exp(0.066\,t) \tag{1.16}$$

The (1.1) energy-balance equation is solvable for T_w, using the (1.3), (1.4) and (1.13) – (1.16) local feedbacks, if – beside the constants denoted by letters or numerals –, the values of internal factors B, u and T were prescribed. The variations of these three quantities are governed – as a first approximation –, by the global feedbacks.

1.4 Global feedbacks

A key problem – regarding the feedbacks connected with the meridional temperature gradient –, is that – experimentally –, the yearly zonal means of air-and water temperatures are changing with the geographical latitude, as follows:

$$t(\varphi) = t_E - \Gamma \sin^2 \varphi\,, \tag{1.17}$$

and

$$t_w(\varphi) = t_{wE} - \Gamma_w \sin^2 \varphi\,. \tag{1.18}$$

The hemispheric temperature curves are described by no more than 2 parameters in these equations. The temperature gradients Γ and Γ_w show actually the differences between the Equator and the Pole. This difference plays a significant role in the horizontal transport.

Referring to considerations done by SERGIN – SERGIN (1978), it is assumed in our model, that the velocity u is linearly proportional to the gradient Γ.

Considering the feedbacks regarding to the oceanic heat-transport, we take into account that the increasing of the velocity (through the dinamic velocity u_*) thickens the scene of transport – the isothermal layer (KITAYGORODSKI 1970). Accepting the equation of turbulaent diffusion we get that the second derivative of t_w is proportional to Γ_w, according to (3.18), and the transport velocity – as in the atmosphere –, is also proportional to Γ_w, This way:

$$B \sim \Gamma \cdot \Gamma_w^2. \tag{1.19}$$

Dividing the actual meridional differences by the recent values of Γ_o and Γ_{ow}. we obtain the

$$\gamma := \frac{\Gamma}{\Gamma_0} \tag{1.20}$$

and

$$\gamma_w := \frac{\Gamma_w}{\Gamma_{0w}} \tag{1.21}$$

quantities, characterizing the hemispheric climate.

[°C]	Northern hemisphere	Southern hemisphere
T_E	27.1	27.1
Γ_o	34.5	35.2
Γ_{ow}	33.3	37.0

Based on present-time data, the -1.8 °C and the -2.9 °C values of the sea-temperatures are regarded as ice-boundaries in the Northern- and in the Southern hemispheres, respectively. It corresponds to -3.0 °C and -1.6 °C sea-surface air temperatures. Both pairs of these values were extrapolated from data, concerning to lower latitudes. Usually, the air temperature values are regarded to be the smaller ones (SERGIN – SERGIN 1978; BUDYKO 1974), but the ice-boundary is determined by interpolation in those models. The above-mentioned values can be determined in such a way, that the sea-ice boundaries coincide with the border of an ice-cup formed by gathering round all of the icebergs (69 °N, 64.5 °S – KARPEC 1975).

2.2 The calculation procedure

The computation process consisted of the following steps:

1. Reading in of the hemispheric values of two parameters of equation (1.17), which concerns to the air temperature γ, $\gamma_w = 1.0$.
2. Solving of the energy-balance equation for t_w at ice-free points of both hemisphere, in 10° latitude steps.
3. Producing of equation (1.18) with the least squares method for each hemisphere, using the obtained water temperatures.
4. Substituing the critical hemispheric sea-water temperatures into the left side of equation (1.18), the ice-boundary φ_j will be obtained.
5. Solving equation (1.17) for Γ, using the ice-boundary position and that fact, that

$$t_E = t_{we} - 0.15\,°\text{C}.$$

6. Producing γ and γ_w, based on relationships (1.20) and (1.21).
7. Here follows step 2. again with new t_E, Γ, γ and γ_w values for points inside the ice-boundary. If t_E is not the same for each hemisphere, then their arithmetic mean would be used in the new computation.

According to our experiments, the 1 – 7. iteration procedure converges rather slowly, therefore the variations appearing in t_{we} were regarded ten-times greater, and this affected the procedures under points 4. and 5. too. It is suitable to investigate the effect of an other-than-ten multipliing factor in the future, in order to make the convergence even faster.

The solution of the energy-balance equation for t_w is also a rather slow process, but is is always converging, because of the using of the interval-halving procedure or the tangent method, alternatively. This equation is a monotonous function of t_w, therefore it has no more than one root in an interval, selected depending on t, then a border-point corresponding to the direction of the equilibrium will be regarded as an intermediate solution, in order to avoid the obtaining of an unreal difference between the water- and air-temperatures.

3. Preliminary results of model testing

The predictions of the second kind were simulated in the form of differences between the climatic values corresponding to a hipothetical change, and a recent climate being also model-generated. It is important that the reference climate has to be not a real- but a model one, because of the alteration between these would be even greater, than the climate excursion to be simulated itself.

2. Numerical realization

2.1 Input data

There are two kinds of input data for the numerical procedure to be described in the next Section. One group contains those data, which remain unchanged iteration step by iteration step, during computations regarding to a given point (local data). Oppositely, the global data change at every iteration step, but remain constant within an iteration step for both hemispheres.

Table 1. contains the data of the "local group". The initial values of the global data – which characterize the recent climate – ,are the followings:

The first accomplished calculation was the reproducing of the present-time climate, which proved not to be perfectly succesful. It happened, that there was no ice-forming around the South-pole, according to the Antarctic boundary. The ocean remained ice-free even at the 75 °S latitude circle. However, at the Northern hemisphere, the ice-boundary, and so the temperature too, was found to be close to the real situation. Forcing the climate by a solar constant 1% less than its recent value, the ice appeared around the South-pole, although even this time, its extension was less than nowadays (Table II.). This model behaviour can be explained in terms that in the Southern hemisphere, the sea-ice is a consequence of the antarctic ice-sheet and the low air temperature of the sorroundings. If it was taken into account in the southern boundary condition, by prescribing some constant, low air temperature, then perhaps, a real ice-sheet

Table I.

	80 N	70	60	50	40	30	20	10	0	10	20	30	40	50	60	70 S
$\sin^2\varphi$	.970	.883	.750	.587	.413	.250	·117	.030	.000	0.30	.117	.250	.413	.587	.750	.883
B	–20.0	–20.0	–28.5	–22.0	–20.0	–12.5	–4.0	5.0	17.5	11.0	–4.0	–3.5	7.0	9.0	5.0	–5.0
C	.295	.285	.256	.246	.224	.202	1.85	.181	.175	.183	.189	.205	.216	.230	.229	.290
u	5.42	5.84	6.67	8.34	9.17	8.76	7.51	6.26	5.84	6.26	7.51	8.76	9.17	8.34	6.67	5.84
$\exp(k_a)$	1.878	1.632	1.419	1.234	1.073	.932	1	1	1	1	1	.932	1.073	1.234	1.419	1.632
$-S_0$	–130.2	–145.0	–173.7	–209.7	–242.4	–270.4	–290.8	–304.9	–307.2	–304.9	–290.8	–270.4	–242.4	–209.7	–173.7	–145.0
b	–.153	–.385	–248.	–.280	–.312	–.278	–2.93	–2.76	–.276	–.276	–.293	–.278	–.312	–.280	–.248	–.385
a	.706	1.090	.770	.800	.824	.756	.746	.713	.713	.713	.746	.756	.824	.800	.770	1.090
–k	–.80	–.80	–.83	–.76	–.79	–.76	–.91	–1.71	–2.29	–1.95	–.130	–.83	–.47	–.39	–.40	–.40
A_0	.074	.073	.072	.071	.070	.069	.060	·060	0.60	.060	.060	.069	.070	.071	.072	.073

would had formed. Because of the fault in the simulation of our recent climate conditions, the consequences of solar constant changes were investigated by a comparison of equilibrium climates concerning to $+1\%$ and -1% solar constant alterations. This way, the climate sensitivity parameter β was approximated by constituing of central differences instead of one-side ones. Owing to that there was no adequate southern boundary condition, and so the temperature changes of the Southern hemisphere were found too high, we evaluate quantitalively only the results concernig to the Northern hemisphere:

Table II.

Northern hemisphere	+1%**	0*	−1%**
φ_j	72.3°	69.0°	65.5°
Γ	35.1°	34.5°	35.9°
Γ_w	33.9°	33.9°	34.7°
Southern hemisphere	**+1%****	**0***	**−1%****
φ_j	75.0°	64.5°	68.0°
Γ	26.6°	35.2°	33.0°
Γ_w	27.9°	37.0°	34.7°

* real climatological values
** model values

TABLE II. shows the northern- and southern ice boundaries, as well as the Γ and Γ_w meridional gradients of the air- and water temperatures. The change of the northern ice-boundary corresponding to the extreme values of the solar constant is somewhat less than the double of the annual amplitude (KARPEC 1975). The arithmetic mean of the two extreme values is in the vinicity of the real northern ice-boundary. The meridional temperature gradients of the Northern hemisphere were decreased only slightly, when the solar constant had an increased value. Oppositely, the gradient-decrease is considerable in the Southern hemisphere because of the ice-free conditions.

Table III. shows the temperature changes and the sensitivity values of the ice-free, northern middle latitudes, for the altered solar constants. It was found for every latitudes, higher temperatures correspond to the greater solar constant. The climate sensitivity, derived from the differences is somewhat less than the $140-150$ °C value, what corresponds to the results of other climate models, but those models account for the variations of high latitudes too. For middle latitudes, the sensitivity of our model is in the region of the results of up-to-date climate models, according to our knowledge.

Table III.

Northern hemisphere	60°	50°	40°	30°	20°	10°	0°N
+1%	2.3	8.3	14.4	20.2	25.0	28.1	29.1°C
−1%	−0.3	5.6	11.9	17.8	22.7	25.8	26.9°C
β	130	130	125	120	115	115	110°

Beside the simulation of ice-boundary-and temperature changes, the model provides the possibility of simulating the atmosphere-related part of the hidrologic cycle too. For example, the cloud coverage has decreased by 0.02 at every points of the Northern hemisphere in consequence of a 2% solar constant increase. The change of the relative humidity – variations of which are influenced by wind speed alterations in our model –, was less than 1% for both hemisphere. Nevertheless, the vapour tension e has increased everywhere, by about 15%, because of the temperature rising.

It is possible to determine the terms of surface energy-transfer too, beside the simulation of the meteorological elements. The change of the surface short-wave balance can be seen in Fig. 1. in percents, what is worth to compare with the appropriate results due to 2% change of the solar constant. Owing to the cloudiness decrease, the 2% decrease in the short-wave balance at the top of the atmosphere remains unchanged. However, the energy-increase at the surface will be less considerable, because of changes in the atmosphere – first of all due to increase of the water vapour content.

Another important term of energy-balance of the sea-surface is the heat of evaporation, and its relative change is shown on Fig. 2. The increase of this term becomes lower and lower going equtorward, but it is greater than 5%, even there. The latitude distribution of its relative increase is very similar to the behaviour of the short-wave balance, at least in tendency.

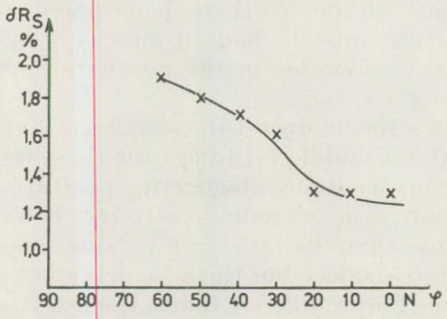

Fig. 1. Relative variation of the short-wave radiation balance.

Summarising, we could regard the results of the first testing to be positive: the simulated changes qualitatively seem to be real; the sensitivity is sufficiently close to the average value extracted from other, more sophisticated models.

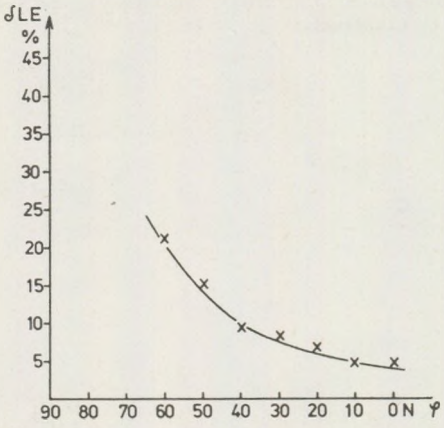

Fig. 2.: Relative variation of the latent heat.

ACKNOWLEEGEMENTS:

The author gratefully acknowledges Prof. Z. Dobosi and Assist. Prof. L. Erdős for their useful advices.

REFERENCES

Berljand, T. G. (1951): Raspredelenie solnechnoy radiacii na continentah. Leningrad, Gidrometizdat.

Budyko, M. I. (1969): The effect of solar radiation variations on the climate of the Earth. Tellus 21. N. 5. pp. 611–619.

Budyko, M. I. (1978): "Teplovoy balans Zemli" Leningrad, Gidrometizdat 40.

Cess, R. D. (1975): Climate change: An appraisal of atmosferic feddback mechanisms emlploying zonal climatology. J. Atm. Sci. v. 33. N. 10. pp. 1831–1843.

Gal Chen, T. Schneider, S. H. (1973): Numerical experiments in climate stability. J. Gaophys. Res. v. 78. N. 27. pp. 6182–6194.

Girdyuk–Malevski–Malevich (1973): "Methodika rascheta effektivnovo izluchenia poverhnosti okeana. Vsb. Fizika pogranichovo sloya atmoszfern. Trudu GGO v. 297. p. 124–132.

Karpec, A. N. (1975): Vlianie teplovovo rezima prizemnovo sloya atmosferu na ploschad morskih Ldov. "Isledovanije sistemu ledniki-okean-atmosfery" p. 14–22. Vladivstok.

Kitaygorodskij, Sz. A. (1970): Fizika vzaimodejstvija atmoszferu i okeana. Leningrad, Gidrometeoizdat.

Kondratiev, K. Ja. (1965): Aktinometrija. Leningrad, Gidrometeoizdat.

Kondratiev, K. Ja. (1976): Novoje v teorii klimata. Leningrad, Gidrometizdat.

Konstantinov, A. R. (1968): Iszparenije v prirode.

Lorenz E. N. (1967): The nature and theory of the general circulation of the atmosphere. WMO

Oerlemans J. – H. M. – Van den Dool (1978): Energy balance climate models: stability experiments with a refined albedo and updated coefficients for infrared emission. J. Atm. Sci. 35. N. 3. pp. 371 – 381.

Sellers W. D. (1965): Physical climatology. The Univ. Chicago Press p. 272.

Sergin V. Ja. – Sergin S. Ja. (1978): Sistemnij analiz problemi bolsih kolebannij zemli Leningrad, Gidrometizdat.

DETERMINATION OF THE VELOCITY AND DIRECTION OF THE GROUNDWATER FLOW BY GEOELECTRIC METHODS

ORSOVAI, I.

Department of Applied and Engineering Geology Eötvös Loránd University
H – 1088 Budapest, Múzeum krt. 4/A

Received: 30th July 1980

SUMMARY

These tests are the first steps toward the development of this method, where the new problemes, requirements may modify the final solution.

The accuracy and reliability of the measurements can be been colmated towards the Danube's aquifer. In this way the temporal changes of the comation could have also been detected.

Since the pumps of the producing wells are powered with three-phase 380 V motor, which is earthed to the taps the electric noise is significant. Using 1.2 kHz carrier frequency and 3.6 kHz measuring frequency along with phase/frequency selective instruments, this electric noise could not have been eliminated. The instrument was then modified adding a 20 dB input separating circuit (complimented by an MN circuit sensitivity meter), fitted to the specifications of the instrument and the field – artificial ground. In this way the feed current became tenfold, so did the signal/noise ratio. This improvement has also reduced the induced impulse noises, and proved to be both necessary and useful in urban areas too.

Several attempts were made to quantify the possible flow velocities in different depths in an inhomogeneous aquifer. Vertical geoelectric logging was used, with different AB spacings. The first step in the method of evaluation was similar to that of the vertical geoelectric logging. These tests were carried out on areas with dense observation well network, where the ground-water level was well-known, and permeabilities were determined with reliable accuracy from core samples taken from the wells. About 30 areas were tested. A non-linear correlation was found between the "k" factor and the flow velocity, where $k^{1.2-2} = v$, if there were no large differences between the highly permeable and less conductive strata.

Improved by the optimisation of the electrode arrangements as well as the quantity and quality of the marker materials used, furthermore, the more accurate design of timing and spacing of the tests.

The method, with further improvements, may become suitable for engineering practice and for the determination of ground-water flow distortions around structures.

Introduction

The direction and velocity of the ground-water flow is a significant parameter in the engineering geology, water supply and sewage disposal problems. Mainly indirect methods are used as measurement techniques, by introducing different marker materials into the aquifer, and the migration different marker materials into the aquifer, and the migration of these materials are detected with appropriate devices. The most commonly used marker materials are sporae, bacteria, colouring and soluble salts, and more recently radioactive or activable materials. The detection methods are variable and depend on the marker material used.

In our present work an alternative method of the measurements are suggested, the electrolytic marking and ground geoelectric detection is discussed. The electric resistivity of the ground water, and its variation in space and time has been detected by two techniques:

a) in case of dense well spacing and high flow velocities (in the vicinity of producing wells or in urban environment) the observation is made in one point, and the temporal changes were measured;

b) if large open areas are available for the measurements, and the flow velocity is smaller, simultaneous horisontal ground geoelectric survey is also used to detect the path of the saline marker salts.

1. A review of the techniques used for the determination of the velocity and direction of the ground-water flow

The ground-water flow can be investigated by indirect methods. This can be done by introducing marker materials into the aquifer and the observation of their migration with suitable techniques.

In selecting the marker material the following parameters should be evaluated:

a) the approximate solubility (inhomogenity) of the media and its probable flow velocity;

b) mineralogical composition (ionic exchange capacity of the clay minerals show considerable variation):

montmorillonite	60 – 100 mg-equivalent/100 g
kaolinite	3 – 15 mg-equivalent/100 g

c) the environmental pollution; materials, which already present in the water (chloride, ammonia, etc) should not be used;

d) the necessary protection of the environment (in the vicinity of domestic water producing wells radioactive materials and heavy metal salts must not be used);

e) the number and the arrangement of observation wells;

f) tools and devices available for detection;

g) other miscellaneous aspects, like in the case of larger aquifer inhomogeneity, the level of water consumption, e.g. the actual and local flow or the long-term regional flow characteristics are to be determined, etc;

When water-colouring is applied, sampling wells are needed. If the direction of the ground-water flow is known, one well, if it is unknown, 4 – 8 wells are required, depending on the accuracy of the measurements. The fluorescein, fuchsine and rhodamine B are the most commonly used chemicals. The mode of detection is relatively simple. The fluorescein is easily recognisable with naked eye in 10^7, or with fluoroscope in 5×10^8 dilution. In argillaceous aquifer it tends to be absorbed to a small extent, while in acidic soils, humus and peat its absorption is intesive.

The fuchsine can be detected with naked eye in 2×10^7 dilution, though it strongly absorbed on clay minerals.

The water colouring method is the most suitable technique in its classical field of application, i. e. in the search of karst cavities, determination of the connections between sinkholes and springs.

When fine-grained solid matter (pollen, bacteria etc) is used for marking, several, wells are required, and the mode of detection is more complex. With use of plankton-net, the first appearance of the marker is hard to determine. This method can be successfully used in highly permeable rocks only, where the marker material is not filtered out. Even if the method is properly used, the similarity of flow velocity and the migration velocity of the pollen cloud is often very hard to determine.

The quantitative determination of the above mentioned markers are very difficult, thus the lognormal plot necessary to the accurate analysis of flow velocities is hard to compile.

More accurate velocity data can be obtained with the application of soluble salts. Their detection can be made by getting samples in series from observation wells. With adequately frequent sampling the lognormal distribution of concentrations can be properly determined.

In areas isolated from domestic water supply network heavy metal salts (Cu^{2+}, Zn^{2+}) can be used. Their first appearance can be detected by dithizone even in very dilute solutions.

The application of salts is suitable for the determination of the regional flow in erratically inhomogenous aquifers where the addition of the NaCl in considerable quantities (10 – 20 t), the considerable distances between wells, and the long duration of the observations (several months) make the accurate determination of the average regional ground-water flow possible.

The application of the radioactive marker materials can be considered as the most advanced amongst the methods, and discussed frequently in the technical literature. Here only a few notes are made concerning these techniques:

It is advantegous, since the network of the observation wells is no longer necessary, if the recently developed "one-hole" methods are used. However, the duration as well as the areal influence of the tests are relatively small, therefore the results are strongly effected by the local inhomogeneities of the aquifer, so does the relationship of the well with the strata and the design of the well.

The electrolytical markering and the detection by surface geoelectric resistivity measurements have several advantages as far as accuracy, reliability, feasibility and simplicity is concerned.

The earlier techniques, with the determination of equipotential curves (*Biczók* 1954) has been developed twenty-five years ago, and does not meet with the present-day requirements. The presently available sensitive, simple, low-noise instruments are associated with the development of the new detection methods.

2. The description of the new detection method

The method has been developed on practical basis, with the application of the mathematical and physical principles of geoelectric resistivity measurements.

Theoretically, the electric conductivity of a rock is predominantly derived from the conductivity of pore fluids which are functioning as electrolytes. (The role of the conductive ore minerals can be neglected in the hydrogeology.)

The electric conductivity of the ground-water is increased by the addition of soluble salts. The dissolved salt content is included in the ground water flow.

The following considerations should be followed in selecting the marker salts:

a) it should be soluble even in cold water;

b) its diffusion coefficient should be small enough to maintain the distinct interface of the salted and non-salted waters;

c) its electric activity should be adequately high even in high dilutions;

d) it should not be absorbed on clay minerals of the rocks in the aquifer.

e) it is preferably easily available and inexpensive,

f) it should not cause significant environmental pollution even when it is used in large quantities.

A salt, which meets all these standards, certainly does not exist. The NaCl and a few fertilizers, like NH_4NO_3 and KNO_3 may be the optimal choices. In the vicinity of domestic water wells the use of heavy metal salts should be avoided, so does that of the fertilizers.

The solubilities of some salts in water (in g/100 ml)

	20 °C	100 °C
NaCl	36,0	39,8
KNO_3	31,6	246,0
NH_4NO_3	192,0	871,0

Thus, the dissolution of NaCl in warm water does not increase the efficiency significantly. When, for some reasons, large amount of salt have to be added with small amounts of water, the boiling NH_4NO_3 solution gives the best results. When the hot (100 °C) saturated solution is poured in the well, the cooling and contamination is taking place simultaneously, and the salt is not precipitated. However, the high diffusion coefficients of the otherwise suitable salt impose great difficulties. The velocity of the natural ground-water flow (when it is not effected by pumping) is generally much lower than the rate of diffusion at such a high difference of concentrations.

It is therefore advisable to design the timing and arrangement pattern of the observations carefully since after the marker salts are suitably diluted, the rate of the ground-water flow exceeds the velocity of the diffusion.

The feed-in of the marker salts can generally be made in any of the wells. If non-screened observation wells are involved in the tests, the electrolyte should be flushed out the well properly by sufficiently large amount of water. A screened observation well ideally provides less resistance than the aquifer rockes themselves, thus the direction and velocity of the ground-water flow remains unchanged during the feed of the marker electrolyte.

In certain cases, when large quantities of feed-water are available, this method can be applied in areas, where observation wells do not exist. The electrolyte is poured in smell pits, which have been dug beneath the A+B layers of soils, and flushed out by about ten times as much water, as fast as the sinking capacity of the pit permits.

The spot-like and instantaneous feed of the marker salt is essential. These conditions can be achieved by using concentrated electrolytes in well screened observation wells. In any other cases the accuracy decreases, and this fact should be encountered in the evaluation.

The field tests provided the following results for the amount of salts required. Using ohmmeters of $10-6$ V sensitivity, $5-10$ kg is necessary at expected $0.2-2.0$ m/day ground-water flow.

If the natural ground-water flow is faster than 2.0 m/day, or in the vicinity of producing wells, $2-5$ kg NaCl should be used. These quantities are referred to bank-gravel aquifers, with neglectable amount of clay mineral content in the rocks. The amount of salts also depend on the ionic exchange capacity of the clay minerals. Consequently, if tests are being carried out in relatively unknown areas, a couple of preliminary tests are sometimes necessary for the prediction of the optimal salt concentrations. Overdosing may diminish the spotlike and instantaneous nature of the tests, while inadequate quantities may make the detection uncertain.

The detecting instrument may be any type of geoelectric ohmmeters, commonly used in the engineering geophysics, with $5-10$ W capacity, and at least 10^{-5} ΔV/grade sensitivity.

In high noise environment (i. e. near to producing wells) or urban areas frequency and phase selective AC detectors can be successfully used. In places of high noise, screened measuring cables, with screen connected to neutral wire are advisable.

Instead of actual resistivities, their reciprocal amounts, i. e. conductivities are involved in the evaluation. The maximum value indicates the direction of flow. If two adjacent directions are coupled with high values, then the resultant direction is given by the addition of the two vectors. In non-homogenous aquifers the resistivities should be measured before and after the feed-in of the salt, in eight directions. The ratios of the two measurements are calculated and plotted on diagrams.

For example:

Table 1.

1. Homogenous aquifer, Makád, at the southern end of the Csepel Island

	Ohmm	$\frac{1000}{\text{Ohmm}}$
N	38	26.3
NE	36	27.8
E	39	25.6
SE	31	32.2
S	22	45.5
SW	25	40.0
W	33	30.3
NW	36	27.8

Table 2.

2. Inhomogenous aquifer, Tököl, in the middle of the Csepel Island

	Before salting Ohmm	After salting Ohmm	Ratio
N	48	44	1.02
NE	46	42	1.09
E	45	43	1.05
SE	46	41	1.12
S	44	36	1.22
SW	46	29	1.59
W	45	27	1.67
NW	47	34	1.38

If the proper direction of flow is known, the velocity measurements can be carried out in 10—30 days after the feed-in of marker salts. The commonly used horisontal geoelectric surveying method should be capable to penetrate the depth of the aquifer, therefore AB electrode spacing should be three time larger than the depth of the aquifer. The grid used was chosen as AB/4, this is necessary, but at the same time adequate.

It is known (*Schmassmann* 1971) that the concentration of salts show lognormal temporal distribution at constant ground water flow since the effects of diffusion and flow are superimposed to each other. Thus, the mean flow velocity of the salt marker is smaller than that of estimated from the maximum concentrations.

With the comparison of nearly 250 data the differences of the mean and maximum velocities were found to be negligible, and did not exceed the magnitude of the error introduced by other factors. Thus, the velocity calculated from conductivity maximums is applicable in practice.

Since 10 – 30 day time-lapse is involved, the measurements can be considered as simultaneous, since one reading needs two minutes, and the transfer of the equipment from one point to another (with the help of two field assistants) need 5 – 10 minutes on the field.

The following example illustrated the evalution of the velocity measurements:

Makád, the depth of the impervious strata: 15 – 16 m $\overline{AB}$ electrode spacing 50 m, spacing between measuring points: 12.5 m; The measurements were carried out on the 30th day after salting.

Table 3

Measuring points	Distance from the salting point	Resistivity
1	12.5	42
2	25.0	39
3	37.5	35
4	50.0	31
5	62.5	29
6	75.0	27
8	87.5	31
9	100.0	48
10	112.5	49
11	125.0	47

The maximum was measured at 75 m, thus velocity is 75/30 = 2.5 m/day.

If high accuracy is required, the area of the minimum resistivity should be more dansely measured.

With repcated horisontal measurements, the temporal changes of the ground water flow were frequently observed. This phenomenon was found

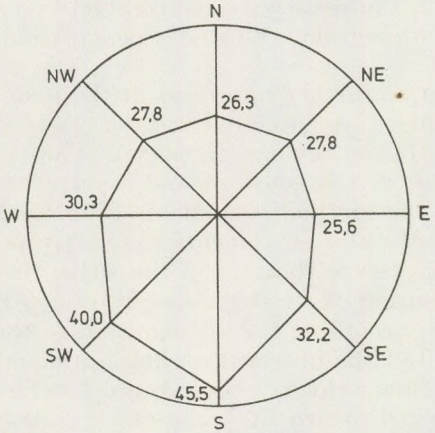

Fig. 1. Data of groundwaer movement direction in homogeneous medium repres ented as $\frac{1000}{\text{ohmm}}$

dominantly in the ground-water aquifers, which are closely connected with the Danube, where flow velocities varied depending on the Danube water level, an is some cases the direction of flow has been even reversed.

If the direction of flow is known from the water-level values of the neighbouring observation or producing wells, an alternative method seems to be more practical to use. This is the fixed location measurement series.

The electrodes are set up normal to the expected direction of flow, in permanent arrangement. The electrodes should be positioned 1 – 2 weeks before the actual tests in orde to allow the galvanic processes to become stationary. This can be promoted by sprinkling copper sulphate solution onto the ground around the electrodes.

The reliability and accuracy of the measurements can be increased if two or more parallel profiles are laid down in the direction of flow.

The resisitivity measurements should be done both before and after salting, in pre-determined periods.

Several aspect have to be encountered in choosing the spacing of salting points and profiled, as well as the timing of the measurements.

Close to the salting point disturbances caused by diffusion are decreasing abruptly, in non-linear manner. Thus the measurements should be done at a certain distance from the salting point. According to our field tests, this distance is min. 10 m if 5 kg NaCl is used, and the expected flow welocity is about 2.0 m/day, or 5 meter, if the flow velocity is around 5 m/day. In the former case the measurements should start after 72 hours from salting, initially in every two hours, then, if the expected maximum is being approached, in every 30 minutes. The measurements should continue until the conductivity does not fall down to the minimum level.

If the flow velocity is larger, and the distance between the feed-in point and the observation wells is smaller, the the measurements should start after 12 hours from the salting, in a similar manner as described above. In the evaluation the resistivity (or conductivity) values are plotted on the vertical axis, while time is plotted (in logarithmic scale) on the horisontal axis.

The method can be further improved in the case of producing wells, if only temporal changes are measured and the electrode arrangement can be different from that of the Schlumberger-type. The electrode coefficient is negligible in this case, if it is constant and known for the replicability of the measurements. The method was successfully used in the determination of the direction of water movements to (waterpipe with tap). Current electrodes were connected to the taps of the wells, the other current electrodes and the measuring electrodes were positioned radially around the well, in 10 directions, according the arrangement of the taps. With simultaneous salting in all of the observation holes in equal distance from the measured hole, the flow velocity was precisely determined. The results have later been checked in-situ by scuba-divers, who measured the temperature and the rate of discharge in each taps, and sampled the water on spot. The results of the geoelectric survey have coincided well with the data from these control tests, far better than with the evaluation derived

from the deformation of the cone of depression, since this has considerably been disturbed by clogging of the river-facing side of the aquifer by colmatation.

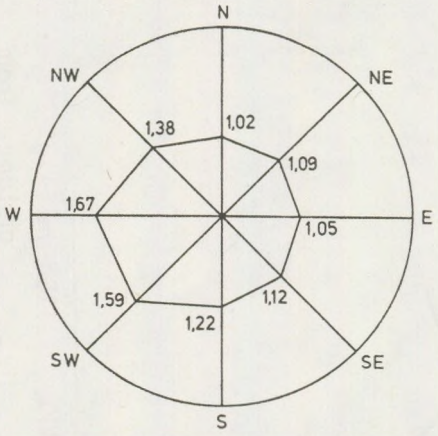

Fig. 2. Data of groundwater movement direction in inhomogeneous medium represented as quotients of resistance with and without salt.

Since the three-phase 380 V pump-motors are generally put to earth at the waterpipes, the electrical circuit noise is very much increased and can not be eliminated by the 1.2 kHz conduction current frequency, the 3.6 Hz measuring frequency or the frequency- and phase-selective equipment either. The basic instrument was installed therefore with a 20 dB input diving current and a circular resistivity-measuring unit attached to it – both having been carefully adjusted to the basic characteristics of the instrument and also of the artificial ground there on the field. Thus both the power-supply and the sign/noise ratio has been increased by about an order of magnitude. Also the inductive noices were considerably reduced by this method. In addition to this, the measurements – when repeated several times, and under the same standard conditions – produced information concerning the progress of colmatation, too.

Experiments to measure the flow velocity were carried out several times and at various depths, essentially by means of the widely known vertical geoelectric soundung method (i.e. by changing the A–B distances). The first steps of the evaluation of the results thus attained were also the same as in the case of the VES measurements. Since the experiments were not restricted to one of the observation wells, but were carried out in several of them, the ground-water level could be taken for known it was the transmissivity of the aquifers that was to be established.

Based on measurements carried out at 30 different places, it can be stated that the relation of transmissivity to the actual flow velocity is exponential rather than linear and can be represented by the following approximate formula: $k^{1,2-2,0} \approx v$, providing that the difference between the thickness of the individual aquifers is not too much.

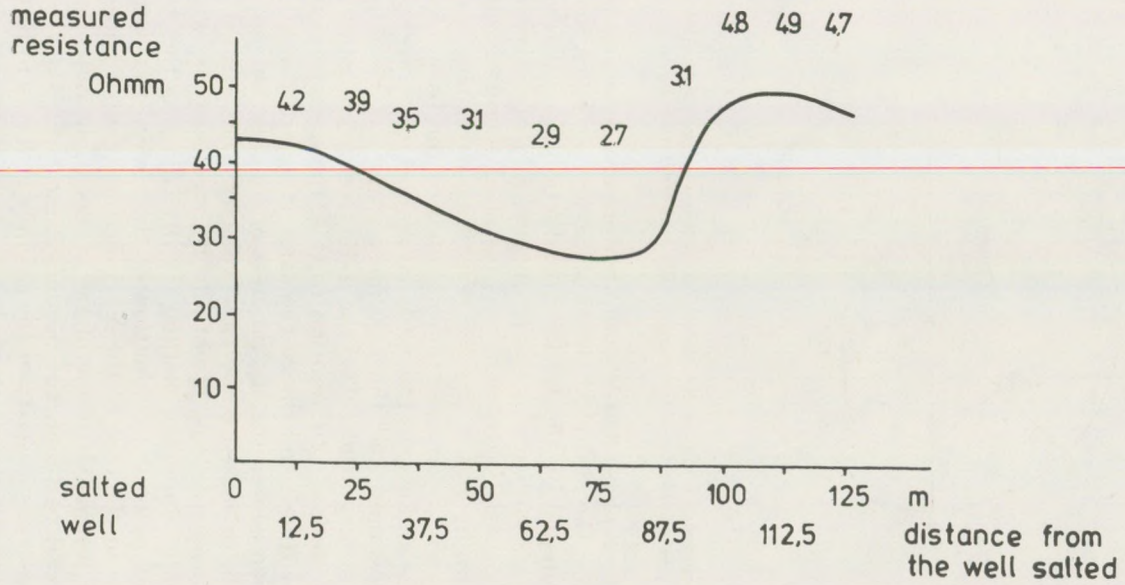

Fig. 3. Data of groundwater movement velocity, Makád, 12. 05. 1977.

REFERENCES

Biczók, Il. (1954): Geoelektromos mérés a vízkutatás szolgálatában – Hidr. Közl. XXXIV. 3–4. pp. 121–128

Buchtela, K.–Mairhofer, J.–Maurin, V.–Papadimitropoulos, T.–Zötl, J. (1964): Vergleichende Untersuchungen an neueren Methoden zur Verfolgung unterirdischer Wässer – Die Wasserwirtschaft 54. Jahrg., 9. H. pp. 260–270

Dimitroulas, C.–Papadimitropoulos, T.–Papakis, N. (1962): Groundwater investigation by the use of neutron activation analysis "Memoires" de l'Association International des Hydrogeologues, 5, pp. 83–103.

Feely, H. W.–Walton, A.–Barnett, C. R.–Basan, F.: The potential applications of radioisotope techniques to water resource investigation and utilization – NYO 9040 A. E. C. Research and Development Report

Hull, D. E. (1958): The Total-Count Technique: A New Principle in Flow Measurements Int. J. appl. Rad. Isotopes 4. 1.

Johnston, W. H. et al. (1960): The development of principle and methods of high dilution on stream isotopic tracers A. E. C. contract AT (11–1)–650–Soc., May.

Leipunskaja, D. J.–Pruslin, J. A. (1958): Radioactive Methods for Studying Liquied Flow in a Porous Medium. Izdatelstwo Akademii Nauk U. S. S. R. (OID abstr. 394).

Maierhofer, C. R. (1954): Behavior of subsoil water table under a systemof irrigation and a drainage. Trans. Second Congr, on Irrigation and Drainage.

Quirico, D. (1979): Determination of the direction and velocity of ground water flow as a source of information for sludge disposal 3rd Conference on Water Quality and Technology Budapest 1/a/6.

Schmassmann, H. (1971): Quantitative Auswertung von Kochsalzmarkierungen in Schotter–Grundwasserströmen Gas–Wasser–Abwasser 5. pp. 122–127.

Straub, C. P.–Ludzack, F. J.–Hagee, G. R.–Goldun, A. S. (1958): Time of Flow Studies, Ottawa River, Lima Ohio. Trans. Am. Geoph. Union, 39., pp. 420–426

Véssey, E.–Csernyi, Gy. (1957): A talajvíz mozgásának vizsgálata radioaktív izotópok és nyomjelző ionok segítségével – Hidr. Közl. 1. pp. 44–56.

VISCOSITY OF HUNGARIAN TERTIARY ANDESITIC LIQUIDS AND ITS RELATIONSHIP WITH THE STRUCTURE OF THE MELTS

PUSKÁS Z.

Department of Petrology – Geochemistry Eötvös Loránd University
H – 1088 Budapest, Múzeum krt 4/A

Received 6. October 1980.

Introduction

The Department of Petrology-Geochemistry of the ELTE has carried out extensive research program with anhydrous silicate melts since 1967. Several rock types in Hungary (i. e. intermediate and basic igneous rocks – andesite, microgabbro, basalt –, sedimentary rock mixtures (sand + dolomite or limestone + Na_2CO_3) as well as power plant cinders were involved in the experiments which have revealed several aspects of the melting and crystallization characteristics. The physico-chemical features of the melts and the mineralogical compositions of the crystallized products were also investigated (*Kubovics*, 1974). The principal aim of this research was to produce artificial polishable crystalline rocks for ashlar-stone applications, though several interesting results have been born on the field of igneous experimental petrology too. It has been revealed that the structure and viscosity of the silicate melts have strong influence on other physico-chemical features of the molten phase, the crystallization process, the types of the solid phases formed, as well as their textural characteristics. The viscosity of melts was systematically studied and related to the chemical and mineralogical compositions of the initial components.

The mineralogical and petrological investigations of the artificial magmatic solid phases produced by re-crystallization from melts have provided valuable informations for the crystallization and structure of the melts.

In the present experiments a number of Tertiary andesite types from Hungary were sampled and used in the experimental petrological tests, and their characteristics were studied. Different additives (bauxite, dolomite, limestone, Na_2CO_3) were used to investigate the effect of the variation in the proportions of the main components to the viscosity of the melts. The recrystallized products of natural and blended andesites were studied by mineralogical and petrological methods. These data have been compared to the respective characteristics of the initial materials to evaluate the petrological aspects of the relationship of chemical composition, temperature and viscosity in intermediate silicate melts.

Methods

The melting temperatures of the initial andesite materials were measured by Zeiss/Jena/MHO – 2 type heating-stage microscope. These measurements have indicated that a temperature of 1460 °C were required to produce rock melts for viscosity measurements.

The melting process was carried out in alundum crucibles, using mullite-lined electric kilns. The temperature of the melts was determined by UHER pyrometer, and this pyrometer has also been used to control the heating during the whole process.

The viscosity of the melt was determined by a modified version of Endell's ball-pulling method (*Kocsis*, 1966). Using the

$$\eta = A \cdot e^{\frac{E}{RT}}$$

relationship between the temperature and viscosity, the data were plotted in a

$$\left[x = \frac{1}{T} 10^4; \quad Y = \log \eta\right]$$

diagram. Regression analysis of data has been made by a HP 65 programmable hand calculator.

Mostly optical, less frequently XRD and DTA analyses were used to determine the mineralogy of the initial rocks of the recrystallized products. The quantitative mineralogical compositions were investigated with a MICRO-VIDEOMAT – 1 Image Analyzer (C. Zeiss, Oberkochen, Germany).

Samples of about 1.5 kg weight each were used in the tests. The amount of additives were 10 per cent in all cases but the Csódi-hegy andesite, where 20 per cent additive was applied owing to the extremely high viscosity of the original andesite melt. The application of greater amount of additives have maintained the internal friction of the melts within the limits of the ball – pulling method ($10 - 10^4$ Pa. s) in the temperature range of the viscosity determinations.

The rocks were melted at 1460 °C temperature. The degasification and homogenisation of the melts was followed by 6 – 8 hours conditioning period. The viscosity of the melt was measured at 30 °C temperature intervals from 1460 °C. Before each measurements, the actual temperatures were stabilised for 40 – 60 minutes to ensure the uniformity of the temperature distribution in the melt. The lower temperature limit of the viscosity determinations was the commencement of the spontaneous crystallization, or the 10^4 Pa · s limit of applicability of the ball-pulling method.

The viscosity tests were followed by the crystallization at – or below – the temperature of the spontaneous crystallization for 5 – 23 hours, in two or three steps.

Results

13 different andesite samples from Hungary were used in the experiments (Table 1).

Table 1.

The location and the petrological characteristics of the andesite samples used in the experiments

No.	Petrological name	Location	Sample code
1	Augite hornblende andesite	Sukoró, Velence mts.	Sa
2	Uralitic augite andesite	Nadap, quarry, Velence mts.	Np
3	Hypersthene biotite andesite	Dunabogdány, Csódi-hill, quarry, Visegrád mts.	Cs
4	Biotitic oxi-hornblende andesite	Visegrád, Visegrád mts.	Vo
5	Biotitic hypersthene andesite	Szob, Csákhill quarry, Börzsöny mts.	Sza
6	Biotitic hypersthene hornblende dacite	Szob, Csákhill, quarry, Börzsöny mts.	Sz
7	Hypersthene pigeonite andesite „bronsitic hypersthene augite andesite"*	Cserhátszentiván Cserhát mts.	Ba
8	Pigeonite trachy-andesite „andesite with pigeonite-augite groundmass"*	Zsunypuszta, quarry Cserhát mts.	Ta
9	Pigeonite augite andesite „amafitic andesite"*	Szandahegy, quarry Cserhát mts.	Am
10	Augite pigeonite andesite „alveolar microandesite"*	Zsunypuszta, Nagy-Zsunyi-hill, Cserhát mts.	CsMa (2)
11	Pigeonite augite andesite „microandesite"*	Alsótold, Bableves-csárda, Cserhát mts.	CsMa (1)
12	Hypersthene pigeonite andesite „alveolar andesite"*	Mátrakeresztes, Mátra mts.	MMa (2)
13	Augite pigeonite andesite „microandesite"*	Mátrakeresztes, Mátra mts.	MMa (1)

* The names in quotation marks represent the volcanic levels for the Middle Miocene volcanism of the Mátra (Kubovics, 1966), which has later been adapted to the Cserhát by Árkai (1970).

Chemically these types covered the range of the intermediate group from the more basic members to the almost acidic varieties. The experiments have taken place in atmospheric pressures, therefore the chemical composition of the anhydrous system formed after the release of the volatile components has to be used in the evaluation (Table 2).

The chemical compositions and the proportions of the main components were modified by mixing the andesite samples with different additives (Table 3). In this way the simulation of the effects of natural assimilation on the flowability of magma and on the mineralogy and texture of the igneous rocks has been attempted.

Table 2.

The calculated chemical compositions of the "dry" andesite melts formed after the release of volatile components

	Sa	Np	Cs	Vo	Sza	Sz	Ba	Ta	Am	CsMa(2)	CsMa(1)	MMa(2)	MMa(1)
SiO_2	61,72	65,32	68,09	61,67	67,39	66,46	60,23	60,93	60,50	59,64	60,27	57,51	63,11
TiO_2	1,25	0,89	0,76	0,96	1,03	0,97	1,53	1,77	2,15	1,75	1,96	1,70	2,41
Al_2O_3	18,06	17,28	17,02	17,68	16,69	17,35	18,34	17,12	17,26	19,30	16,45	19,58	14,88
Fe_2O_3	4,38	3,68	4,82	6,78	2,30	1,87	3,15	2,82	3,21	2,67	4,75	3,23	4,61
FeO	3,07	2,55	1,54	0,51	2,84	3,52	4,57	4,85	4,69	5,09	4,06	4,48	4,04
MnO	0,01	0,02	0,02	0,02	0,01	0,01	0,01	0,02	0,01	0,01	0,01	0,01	0,02
MgO	3,13	2,35	0,61	3,30	1,65	1,75	2,36	2,52	2,81	2,34	3,03	2,34	1,64
CaO	6,27	4,94	4,03	6,40	5,15	5,21	7,80	6,67	6,85	6,11	6,90	9,22	5,90
Na_2O	1,66	1,98	2,18	1,91	2,12	2,08	1,65	1,77	1,81	2,11	1,94	1,71	2,05
K_2O	0,34	0,97	0,92	0,75	0,78	0,78	0,35	1,32	0,69	0,96	0,53	0,21	1,03
P_2O_5	0,11	0,02	0,01	0,02	0,02	0,01	0,01	0,20	0,02	0,01	0,10	0,01	0,31
Total	100,00	100,00	100,00	100,00	99,98	100,01	100,00	99,99	100,00	99,99	100,00	100,00	100,00

x = Analysed by K. Ikrényi

Table 3.

The chemical composition of the additive materials

	1.	2.	3.
SiO_2	5,80	0,02	4,66
TiO_2	2,53	0,05	0,05
Al_2O_3	52,73	0,80	2,80
Fe_2O_3	20,61	0,64	0,79
FeO	–	–	–
MnO	–	0,01	0,01
MgO	–	18,78	2,96
CaO	–	31,93	49,37
Na_2O	–	0,02	0,02
K_2O	–	0,06	0,18
P_2O_5	–	–	–
Loss	18,34	47,69	39,15
Total	100,0	100,00	99,99

1 = bauxite, Iszkaszentgyörgy (Analysed by Almásfüzitői Timföldgyár)
2 = dolomite, Pilisvörösvár (Analysed by K. Ikrényi)
3 = limestone, Pilisvörösvár (Analysed by K. Ikrényi)

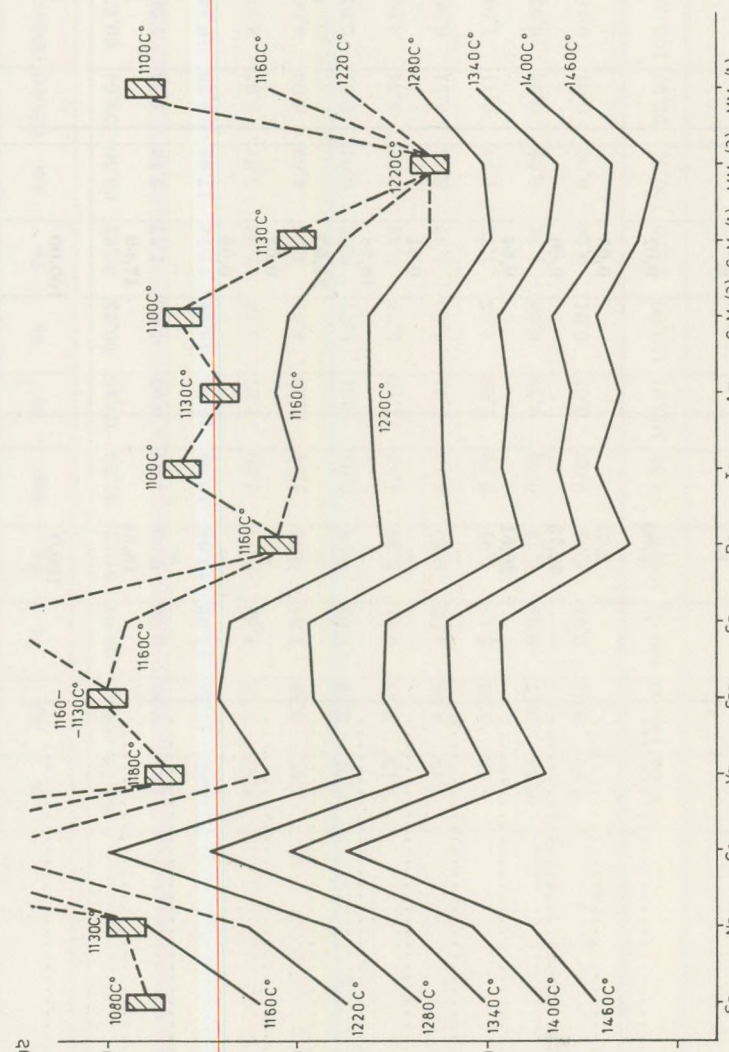

Fig. 1. The viscosity, spontaneous crystallization temperature and the maximum viscosity values of the andesites used in the tests. For legend see Table 1.

The viscosities of the andesite melts starting from 1460 °C, and using 60 °C intervals were plotted on Fig. 1. The lower temperature limit was determined by the start of the spontaneous crystallization, or by the measurement range of the method. The viscosity values (in Pa · s) were plotted in logarithmic scale. The temperatures of the spontaneous crystallization and the viscosity values immediately prior to crystallization are also presented on the diagram.

The experiments have shown that at 1460 °C maximum melting temperature the hornblende andesites from Sukoró (Velence) and the pyroxene andesites from the Cserhát and Mátra produce low viscosity melts (13 – 27 poise). The andesites from Nadap (Velence), oxi-hornblende from Visegrád and the micro-andesites from the Mátra have higher viscosities (36 – 59 Pa · s), while the dacite from Csákhill (Börzsöny) and andesite from Csódihill (Dunabogdány) have shown significantly high viscosity (83 – 575 Pa · s).

The spontaneous crystallization has begun in the temperature range of 1220 °C (alveolar andesite, Mátra) and 1080 °C (hornblende andesite, Sukoró, Velence). However, the formation of crystallites has not been observed at 1160 – 1070 °C temperatures after 9 – 23 hours heat treatment from the melts of the andesite (Csódihill) and dacite (Csákhill). The values of the internal friction at the beginning of the crystallization were also variable: for the alveolar andesite (Mátra), at 1220 °C crystallization temperature the viscosity was 160 Pa · s, while for the Csákhill andesite, at 1160 – 1130 °C temperature it was 10^4 Pa · s.

In the majority of the andesite melts the crystallization has started at $10^3 - 10^4$ Pa · S viscosity values.

The effects of additives on the viscosity in andesite melts are illustrated on the diagrams of Fig. 2 – 12.

Discussion

The following aspects were considered in the evaluation of experimental data:

1. The variation of viscosity with chemical composition and temperature.

2. The dependence of the activation energy of viscosity from the viscosity, chemical composition and temperature.

1a. *The influence of the variation of main component ratios of the melts on the viscosity (more accurately, the viscosity vs. temperature function) in pt-conditions higher than the liquidus point.*

As it is seen from the viscosity vs. temperature plots the addition of bauxite lowers the viscosity least effectively. The largest drop on viscosity was recorded with the use of dolomite (or occasionally limestone or Na_2CO_3) at 1300 – 1200 C°, and of Na_2CO_3 at lower temperatures.

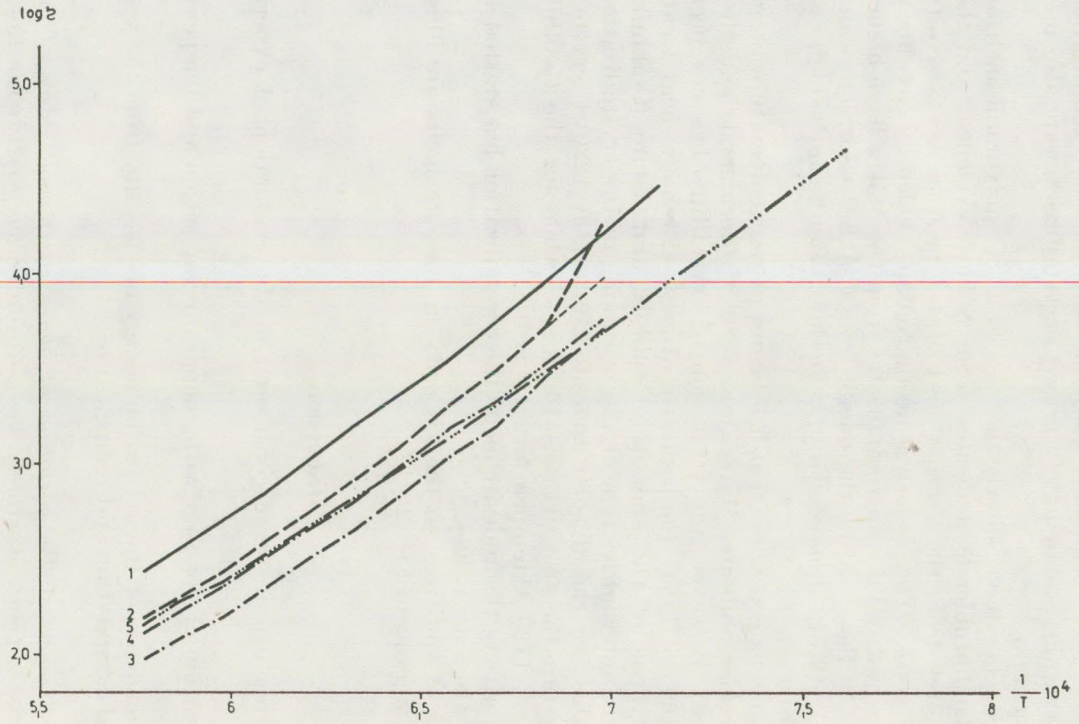

Fig. 2. The viscosity values of the Sa sample series. Legend:
1 = 100 weight % andesite
2 = 90 weight % andesite + 10 weight % bauxite
3 = 90 weight % andesite + 10 weight % dolomite
4 = 90 weight % andesite + 10 weight % limestone
5 = 90 weight % andesite + 10 weight % Na_2CO_3

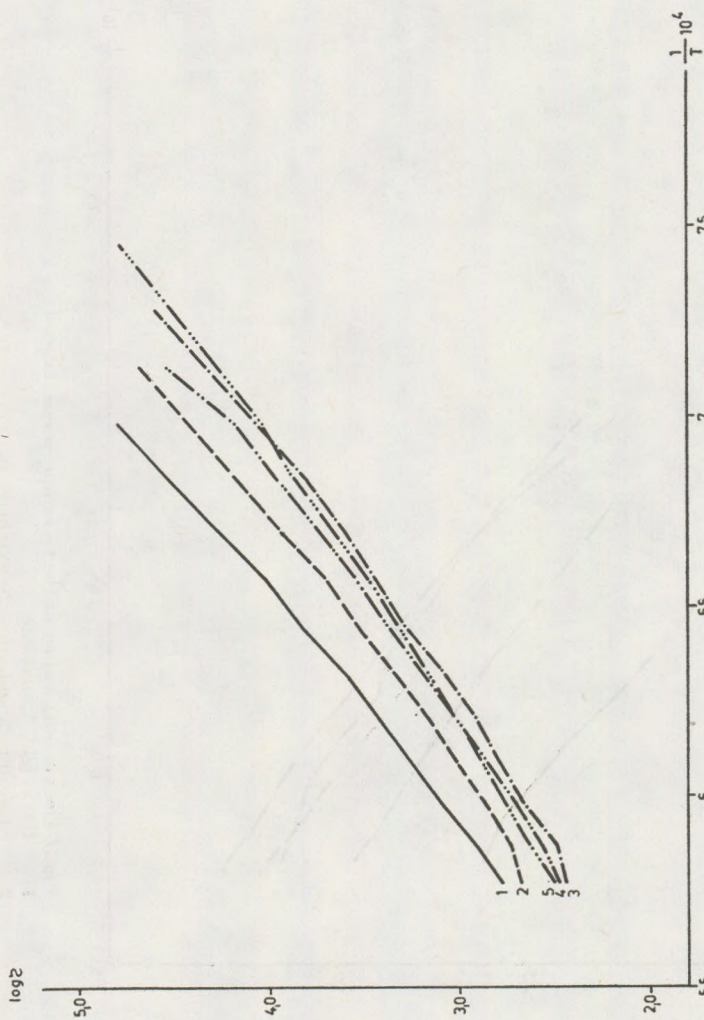

Fig. 3. The viscosity values of the Np sample series. For legend see Fig. 2.

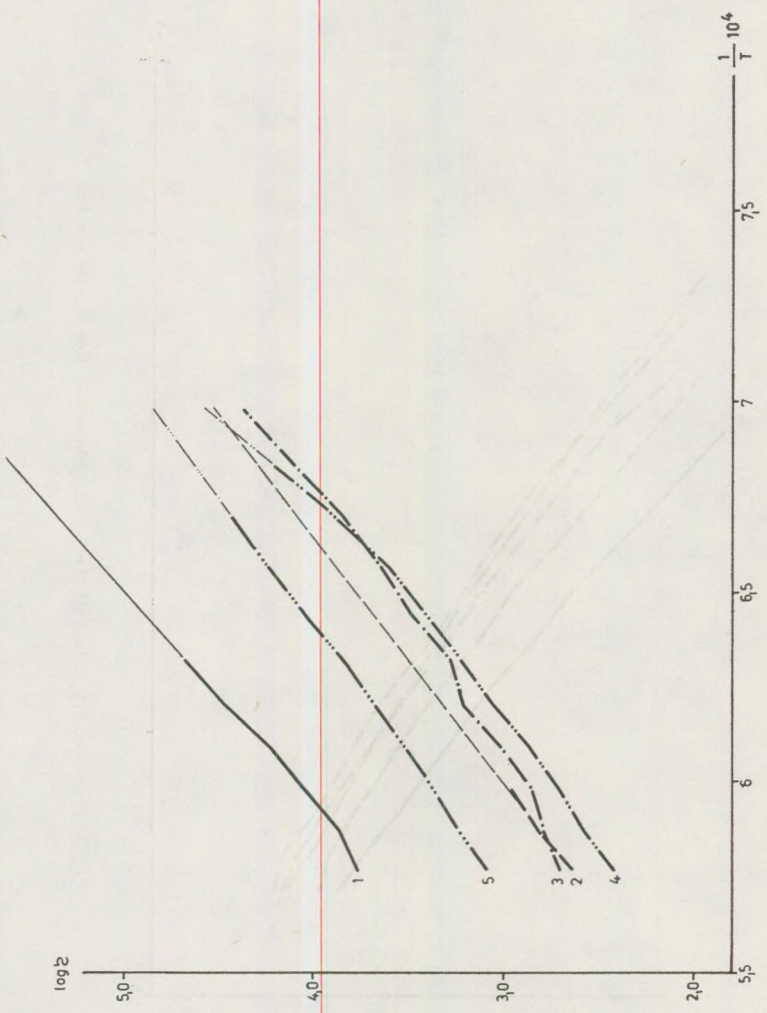

Fig. 4. The viscosity values of the Cs sample series. Legend:
1 = 100 weight % andesite
2 = 80 weight % andesite + 20 weight % bauxite
3 = 80 weight % andesite + 20 weight % dolomite
4 = 80 weight % andesite + 20 weight % limestone
5 = 90 weight % andesite + 10 weight % Na_2CO_3

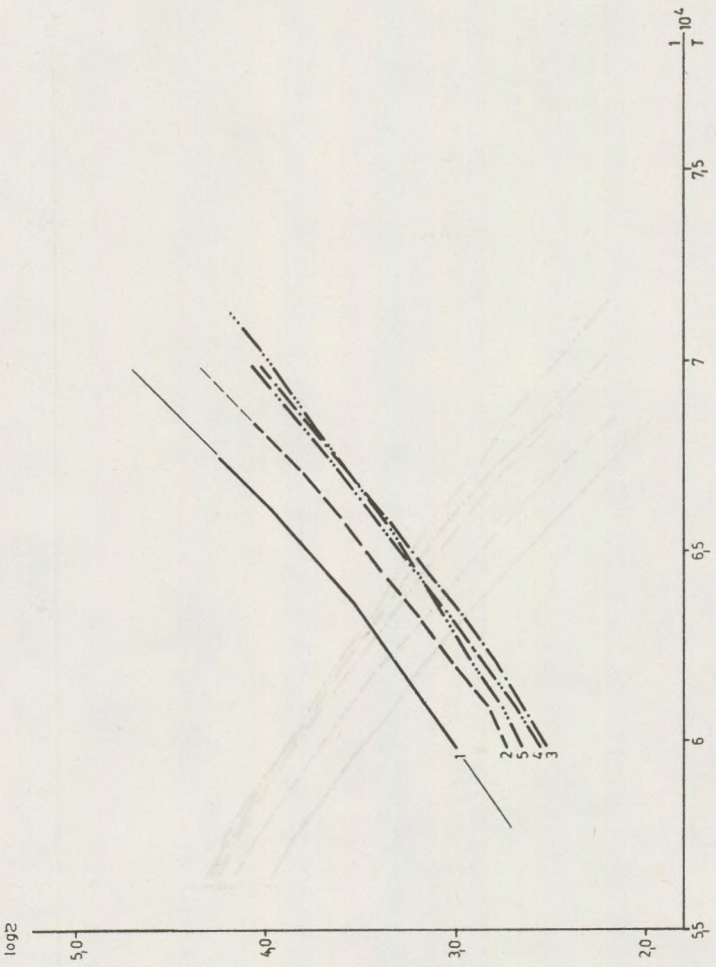

Fig. 5. The viscosity values of the Vo sample series For legend see Fig. 2.

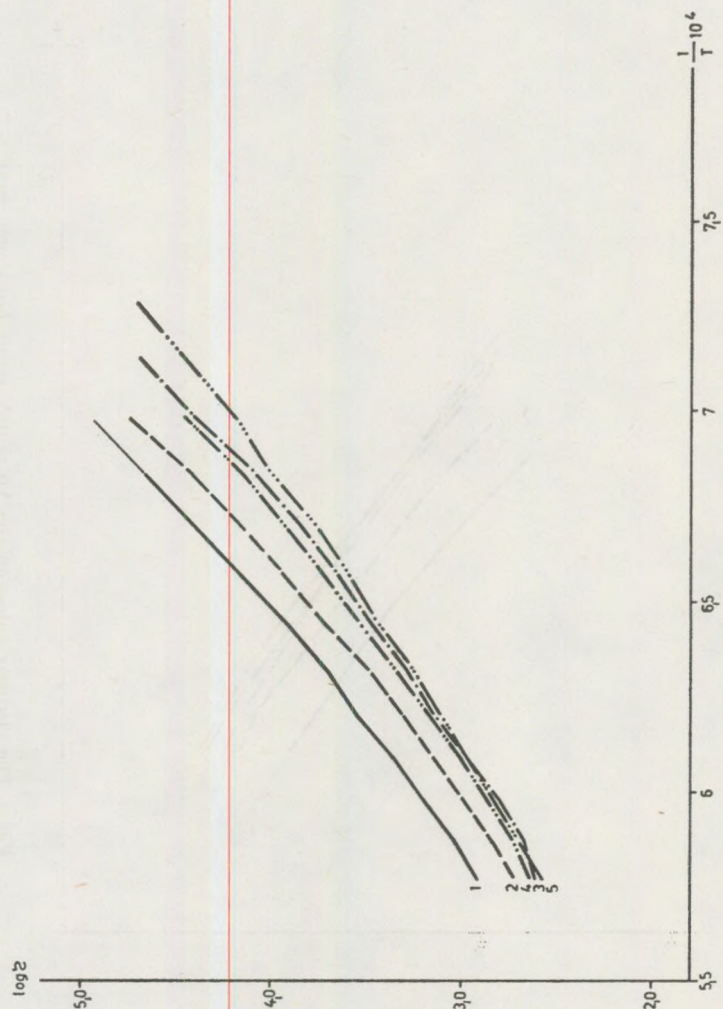

Fig. 6. The viscosity values of the Sza sample series For legend see Fig. 2.

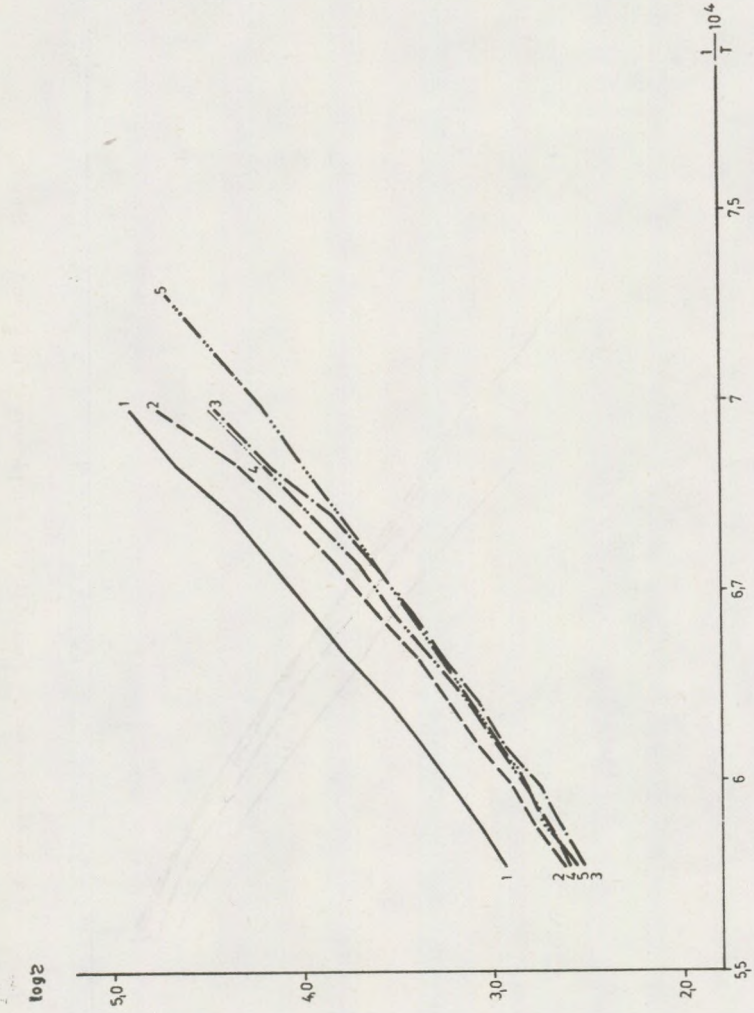

Fig. 7. The viscosity values of the Sz sample series For legend see Fig. 2.

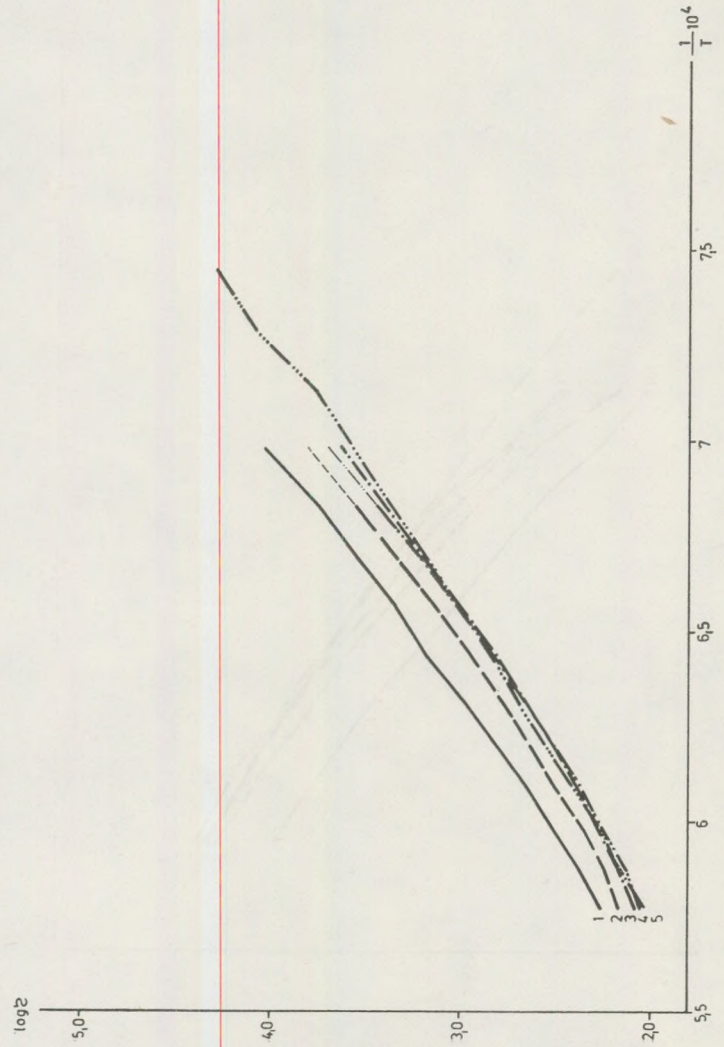

Fig. 8. The viscosity values of the Ba sample series For legend see Fig. 2.

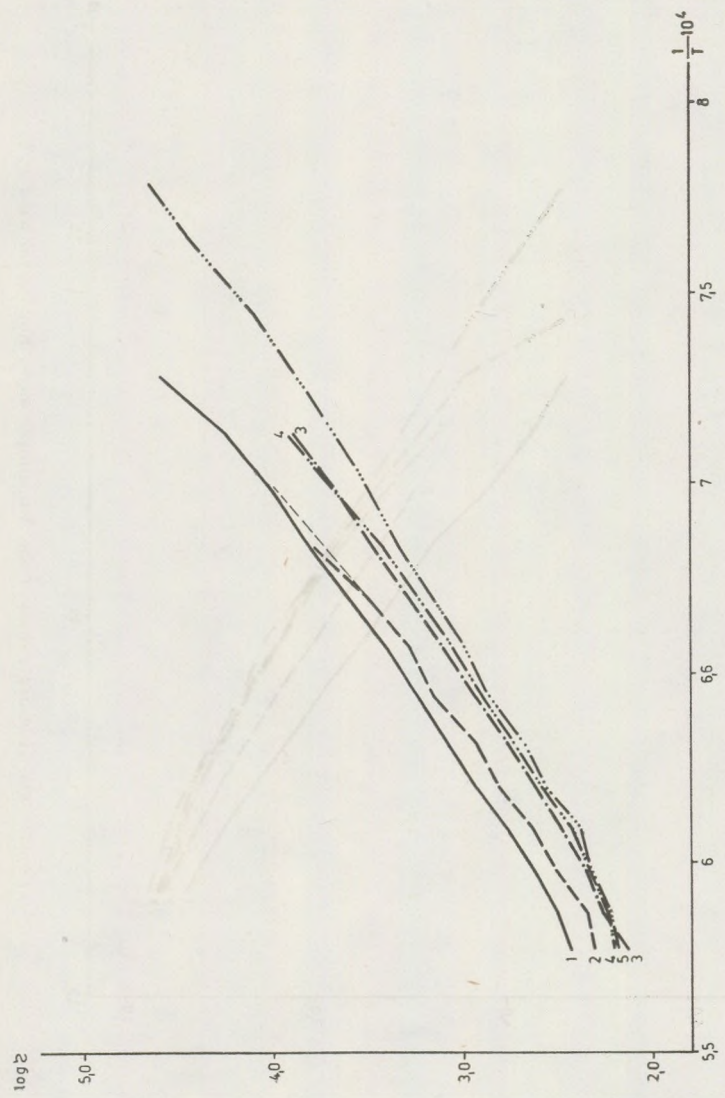

Fig. 9. The viscosity values of the Ta sample series For legend see Fig 2.

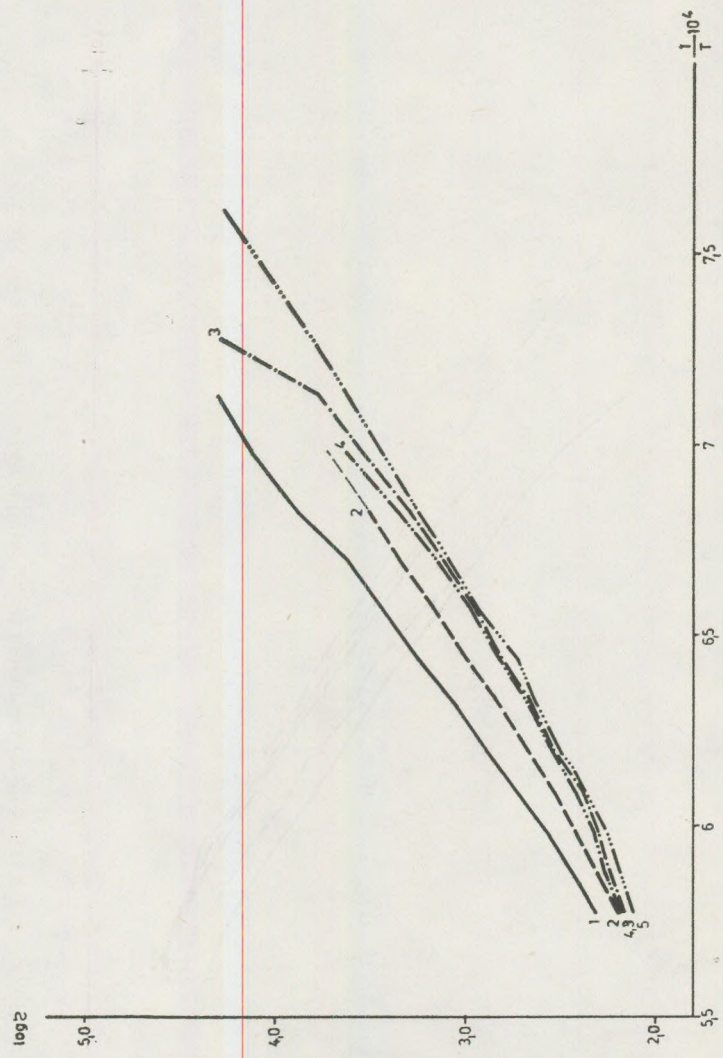

Fig. 10. The viscosity values of the Am sample series For legend see Fig. 2.

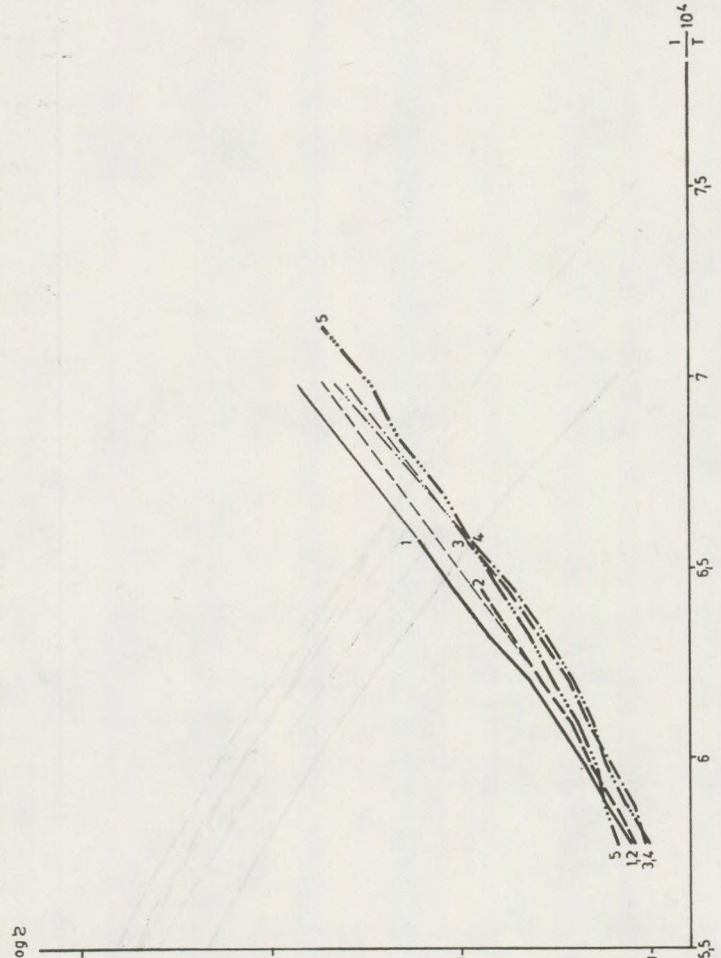

Fig. 11. The viscosity values of the MMa (2) sample series For legend see Fig. 2.

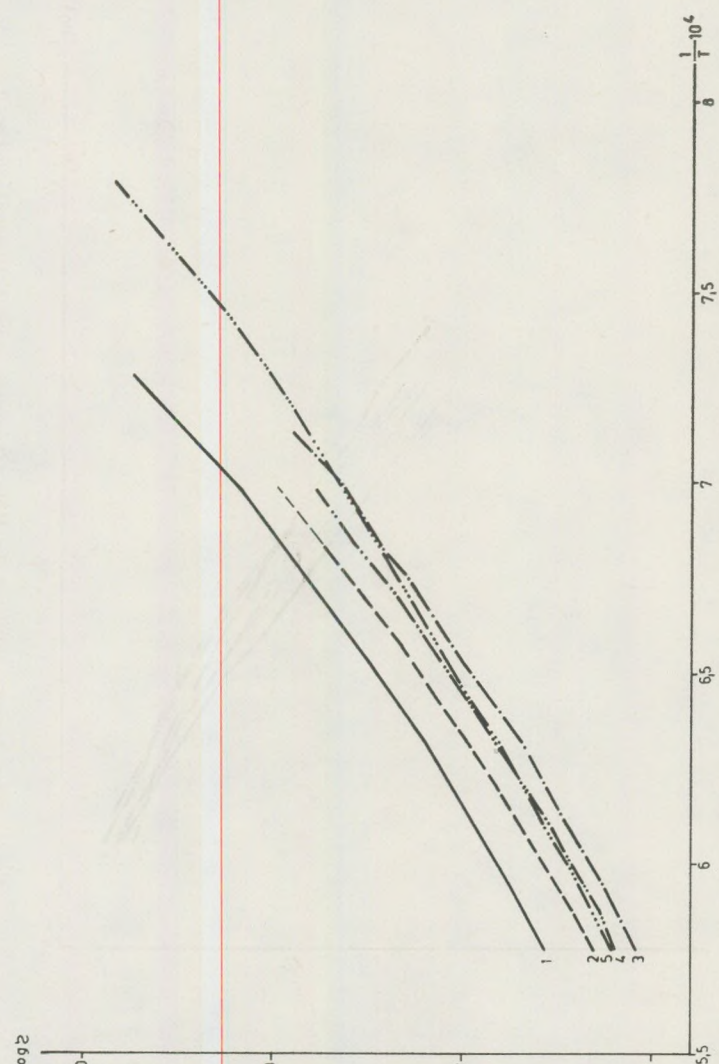

Fig. 12. The viscosity values of the MMa (1) sample series For legend see Fig. 2.

1b. *The variation of viscosity with temperature*

In a liquid the empirical relationship between the viscosity and temperature is as follows:

$$\eta = A \cdot e^{\frac{E}{RT}} \tag{1}$$

The validity of this equation is limited to simple non-associable liquids, where the structure is independent from the temperature (*Erdey-Grúz*, 1972). The rate of variation is considerably larger in more complex associable liquids, where the structure varies with temperature.

For this latter type of liquids a number of alternative equations have been suggested for the variation of viscosity with temperature in silicate melts (*Knapp* and *Korányi*, 1964, Lőcsei et al., 1965; Khitarov et al., 1976).

Since the dependence of viscosity from temperature in silicate melts can be experimentally determined, these measurements can provide one of the best informations regarding the variation of the structure of the melts.

Our viscosity data were plotted in

$$\left[X = \frac{1}{T} 10^4; \quad Y = \log \eta\right]$$

systems (Fig. 2 – 12). These plots have shown characteristic deviation from the linear distribution, indicating that the viscosity of andesite melts follow a relationship which differs from that of given in (1).

Assuming that the viscosity of associable liquids also vary exponentially with temperature, there are two or three alternatives which may influence the viscosity vs. temperature function:

– with constant activation energy the logarithm of viscosity varies linearly with the higher powers of 1/T·

$$\eta = A \cdot e^{\frac{E}{RT^n}} \tag{2}$$

where $n = 1, 2, 3, 4, 5$.

– the logarithm of viscosity varies lineraly with 1/T, but the activation energy (E) is temperature dependent;

– the above mentioned two factors have combined effect on the variation of viscosity, and the deviation of $\log \eta \left(\frac{1}{T} 10^4\right)$ from linear distribution.

It is probable that these three cases may lead to different physical interpretations of the melt structure. The determination of the most realistic functions and their appropriate interpretation still needs further experimental and theoretical studies.

Having these considerations in mind, we have investigated if the logarithms of the measured viscosity values show linear correlation with any of the higher powers of 1/T. The activation energy was assumed to be independent from the temperature.

It was revealed that there are such $n \leq 5$ positive integers (typical to each system) by which the logarithm of internal friction varies almost linearly with $1/T^n$. Therefore, the viscosity of silicate melts can be adequately represented in a

$$\left[X = \frac{1}{T^n} 10^{3n+1}; \quad Y = \log \eta\right]$$

$$(n = 1, 2, 3, 4 \text{ or } 5)$$

diagram, where n is characteristic to the system.

Thus, unlike the simple (non-associable) liquids, the viscosity of the silicate melts varies significantly with the temperature, as a consequence of structural changes in the molten phase. The magnitude of this variation differs widely in each system.

1c. *The relationship between the main component ratios and the temperature dependence of viscosity of melts.*

The amounts of main elements in natural andesite varieties were altered, and the temperature dependence of viscosity was studied (Fig. 13).

The viscosities of the natural andesites, as well as mixtures containing 10 weight per cent bauxite and limestone are in most cases expressed by

$$\eta = A \cdot e^{\frac{E}{RT^3}} \tag{3}$$

formula.

With the addition of dolomite, the viscosity shows more intimate relationship with the temperature, according to the

$$\eta = A \cdot e^{\frac{E}{RT^4}} \tag{4}$$

equation.

However, using Na_2CO_3 additive, the variation of viscosity could be expressed as

$$\eta = A \cdot e^{\frac{E}{RT^2}} \tag{5}$$

According to the data described in the former section, the application of dolomite promotes the temperature dependent structural changes of the melt most effectively, while the use of the Na_2CO_3 is the least effective in this respect.

The (6) curve on Fig. 13. illustrates the frequency distribution of the linearity of log η[1/T] functions according the different exponents of 1/T,

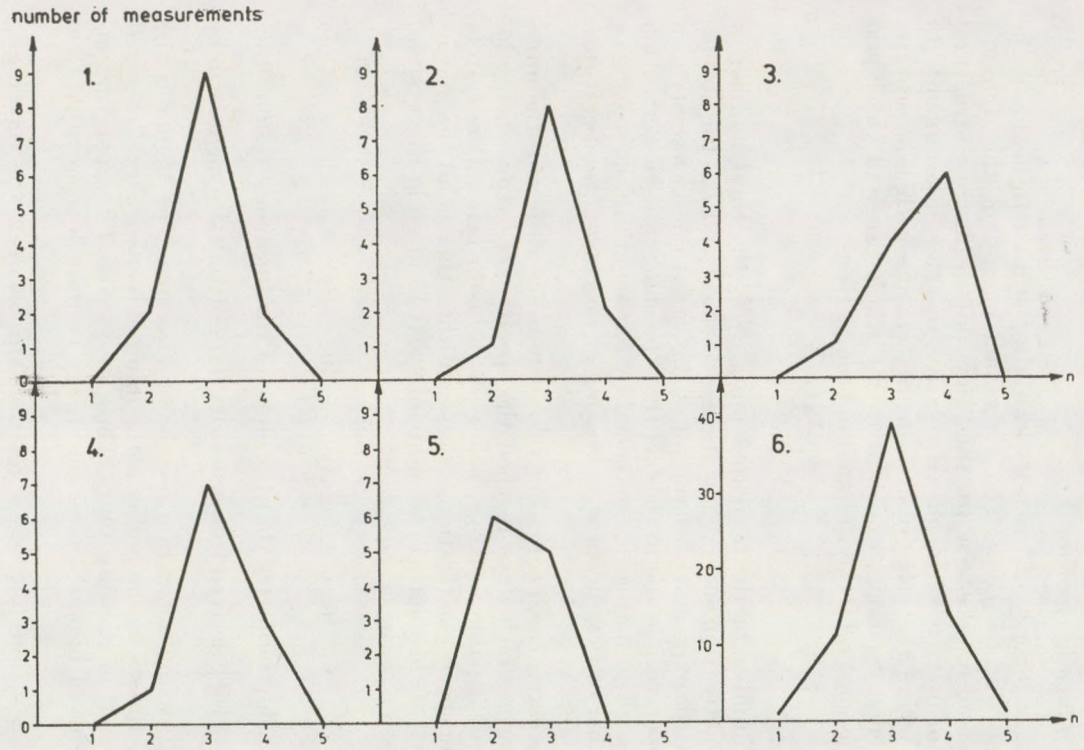

Fig. 13. The frequency of linearity of the log $\eta\left(\frac{1}{T^n}\right)$ functions of the andesite melts as a function of (n). Legend:

1 = natural andesite
2 = mixed materials with 90 weight % andesite and 10 weight % bauxite
3 = mixed materials with 90 weight % andesite and 10 weight % dolomite
4 = mixed materials with 90 weight % andesite and 10 weight % limestone
5 = mixed materials with 90 weight % andesite and 10 weight % Na_2CO_3
6 = natural and mixed materials together

based on 66 viscosity measurements in chemically different systems. This curve indicates that the temperature dependence of the internal friction in intermediate silicate melts is best estimated by the (3) relationship in most cases.

2. *The variation of the activation energy of viscosity with the temperature, chemical composition and viscosity*

The activation energy of viscosity can also be used to evaluate the structure of the silicate melts. The activation energy of the dynamic viscosity is the energy necessary for the "flow units" (discrete structural elements) of the melt to be displaced relative to their environment. In simple liquids, where the "flow units" do not change with temperature, the activation energy remains constant in the whole range of the liquid phase stage. As is shown by the Boltzmann-theory, i. e.

$$N_i = N \cdot e^{\frac{-\Delta E}{RT}}, \tag{6}$$

(where N_i the number of the activated units, N is the total number of units, ΔE is the activation energy, R is the gas constant and T is the absolute temperature), the exponential character of the variation of viscosity as a function of temperature is due to the fact that the characteristic activation energy level of a given material is exceeded by exponentially increasing or decreasing number of flow units at increasing or decreasing temperatures, respectively.

Thus, if the activation energies of two systems are different, the number of the particles which have reached the specific activation energy level, hence became capable to move, will grow in faster rate in the system which has higher specific activation energy. On the other hand this means that the viscosity of the melt will be more intensely reduced in this system. With the conversion of the (1) equation:

$$\log \eta = \log A + \frac{E}{RT} \log e \tag{7}$$

The relationship indicates that the slope of the linear regression functions, $\log \eta \left(-\frac{1}{T} \; 10^4 \right)$ derived from viscosity data of andesite melts, will be steeper with increasing activation energy of viscosity. The higher is the tangent of these functions the higher is the minimum energy level required to the displacement of the flow units. Thus, at a given T temperature interval the systems of higher activation energy contain less movable flow units.

These considerations outline a relationship between the "average" viscosity (here is taken as

$$\bar{\eta} = \frac{\log \eta_{1460} + \log \eta_{1160}}{2} \Bigg)$$

and the activation energy of a melt, as it is seen on Fig. 14.

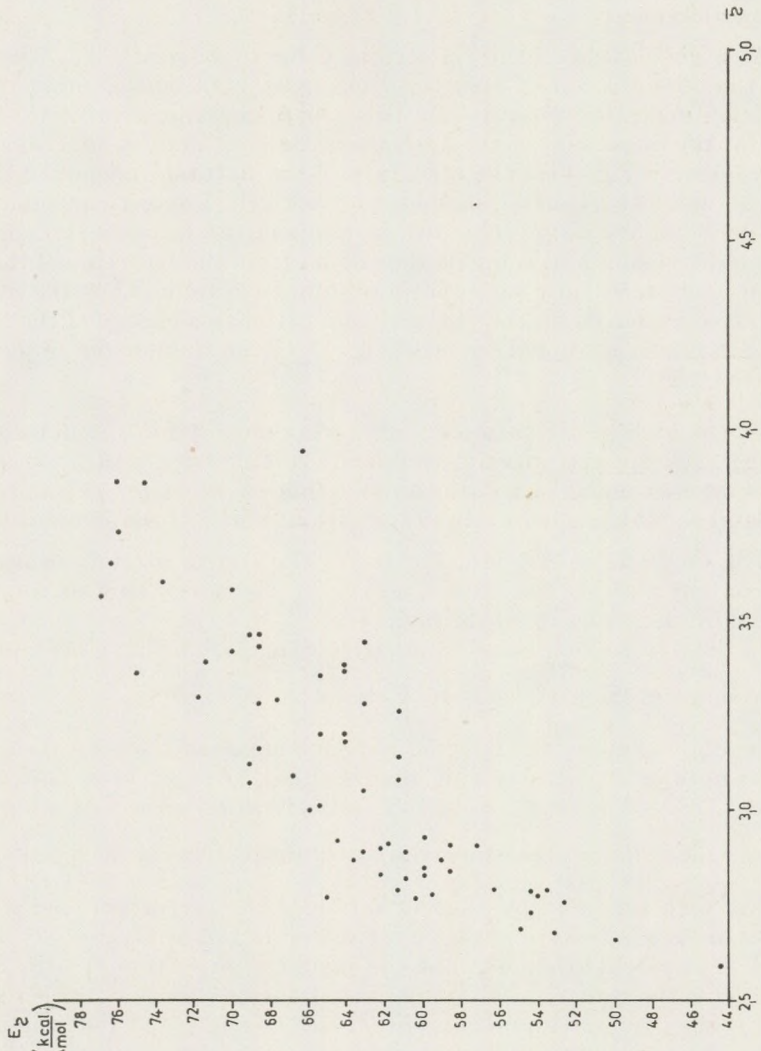

Fig. 14. The activation energy of viscosity of andesite melts as a function of the "average viscosity"

Our experimental results concerning this correlation are in coincidence with Shaw's (1972) conclusions, who suggested the convergency of the $\log \eta \left(\frac{1}{T}\ 10^4\right)$ functions of the silicate melts, based on numerous viscosity measurements.

At a given temperature, a certain value of viscosity may be derived from the combination of structural elements with considerably different activation energies (*Shaw* 1972). This phenomenon can provide explanations for the dispersion of the activation energy values as function of average viscosity (Fig. 14). The structure of the natural and mixed andesite melts is therefore a controlling factor for both the viscosity and the activation energy of viscosity. In a certain temperature interval the effect of a given additive material is highly dependent from the structure of the silicate melts, which in turn varies from system to system. Thus the influence of additive materials on the viscosity and activation energy of the andesite melts can not be predicted directly (Fig. 15.) Even though, our observations indicated, that:

– the highest activation energies were recorded in the natural andesite melts (except the andesite and dacite sample from Szob);
– in increasing order, the application of bauxite, dolomite, limestone and Na_2CO_3 has reduced the activation energy of the silicate liquids.

The diagram on Fig. 16. illustrates the complex relationship of the SiO_2 content and the activation energy of viscosity. This relationship is affected by the structure of the melts too.

In the 1b. section three alternative explanations have been proposed for the shape of the $\log \eta \left(\frac{1}{T}\ 10^4\right)$ curves.

Several examples can be cited for the increase of the activation energy of silicate liquids with reducing temperatures (*Kocsis*, 1966; *Bonetti* and Lazzari, 1969). The actual values of the activation energy of a liquid system over the liquidus point are given by the derivatives of the $\log \eta \left(\frac{1}{T}\ 10^4\right)$ function with temperature. The variation of the activation energy of viscosities of the melts have not been estimated in this study.

It is apparent, though, that the higher is the value of n in Eq. (2), the larger is the rate of variation of the activation energy with temperature in the range over the liquidus point. It can be suggested that the increase of the activation energy in lower temperatures is a consequence of the change in size of the independent movable discrete flow units of the silicate melt. This relationship is in accordance with the conclusions drawn for the effects of additive materials, and been described in 1c. section.

It can be stated, that the variation of the activation energy of viscosity of silicate liquids over the liquidus point range indicates the rate of alteration of the structural elements as a function of temperature. This re-

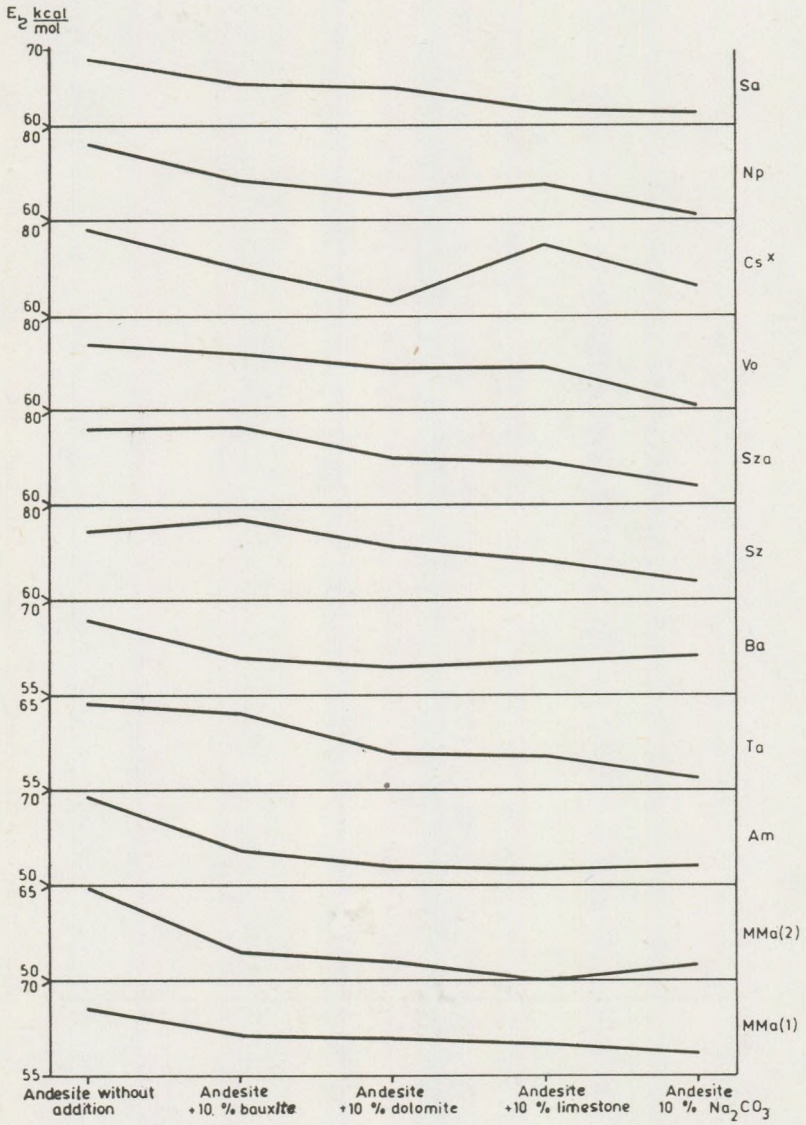

Fig. 15. The activation energy of viscosity of andesite melts as a function of the additive materials

Legend: see Table 1.
x = the amount of additive bauxite, dolomite and limestone is 20 weight %

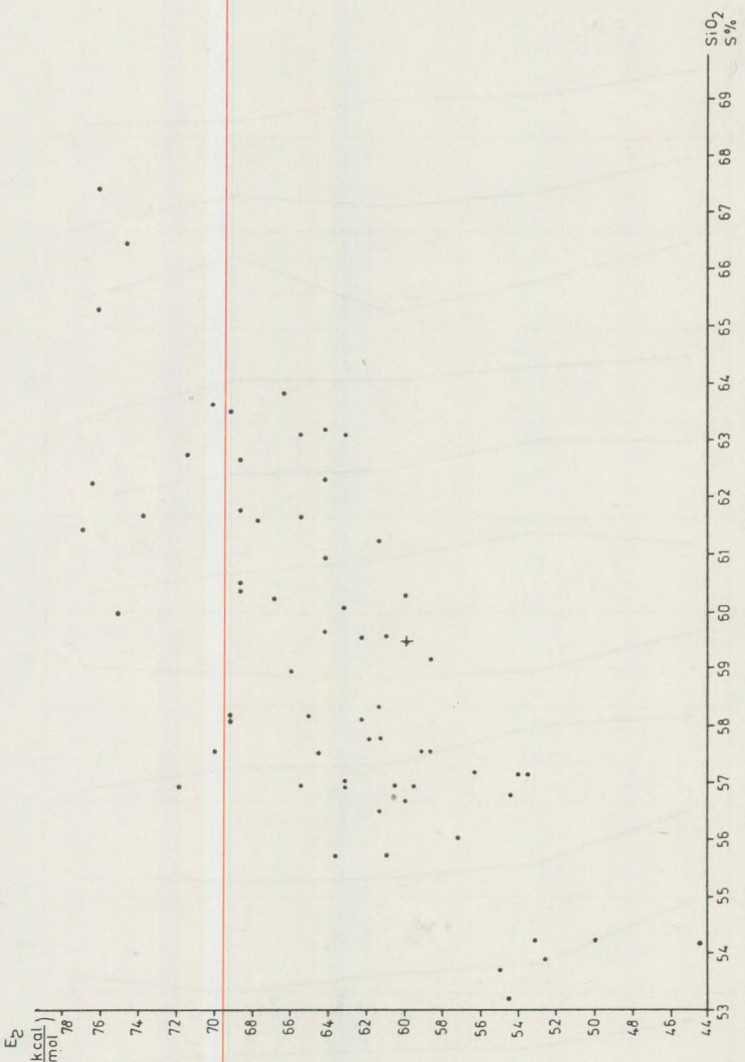

Fig. 16. The activation energy of viscosity of the andesite melts as a function of the SiO_2 content of the volatile-free liquids.

lationship is reflected in the shape of the $\log \eta \left(\frac{1}{T} 10^4\right)$ curves, which have been determined with experiments. This factor is therefore suitable for the determination of structural variability of silicate liquid systems.

Conclusions

The experimental petrologist generally agree, that at a given pt-condition a silicate melt is composed of silicate anion-polymers and cations, in types and proportions characteristic to the system (*Hess*, 1971; *Kubovics*, 1974). The structure and the viscosity of the melt is dominantly controlled by the features of silicate anion-polymers, which have been formed from $(SiO_4)^{4-}$-tetrahedra.

However, the temperature dependence of the viscosity of a silicate liquid system is not governed solely by one component, namely the SiO_2 (*Bonetti* and *Lazzari*, 1969). The rate of polymerisation, and internal friction of the melt is influenced by the cations too. Experimental data are available for different viscosities in binary liquid systems having the same SiO_2 content (Anfilogov 1973). Our measurements have also shown that the viscosity of an anhydrous andesite melt is not directly correlable to its SiO_2 content (Fig. 17).

Based on a large number of viscosity data, it was concluded, that the cations may have both network-former and network-modifier role (*Bottinga* and *Weill*, 1972). The most important and extensively known is the dual role of the alumina. Conductivity measurements have indicated the four-fold coordination, hence network-forming role of the alumina (Lengyel et al., 1966) in a system where the mol-fraction of alkali metals has exceeded that of the alumina. In natural silicate liquids mainly tetrahedral Al coordination is encountered, which is stabilised by alkali metal and calcium cations (*Bottinga* and *Weill*, 1972). In case of extremely non-equilibrial crystallization the Al may enter into six-fold coordination sites and may be incorporated in structures as network-modifier, i. e. in pyroxenes (*Rasin*, 1959).

Assigning sole tetrahedral coordination for the Al, the relationship between the ratio of the

$$\frac{\text{network} - \text{former} \; (= SiO + Al_2O_3)}{\text{network} - \text{modifier} \; (= TiO_2 + Fe_2O_3 + FeO + MnO + MgO + CaO + Na_2O + K_2O + P_2O_5)}$$

components and the viscosity of the melts has been calculated (Fig. 18). The unpredictable trends of variation may imply, that the above grouping of the elements is an oversimplification. It is probable that the Al occupies both tetrahedral and octahedral sites, i. e. has both network-former and network – modifier role already in the liquid phase. Above a certain temperature limit, however, all of the tetrahedral $(AlO_4)^{5-}$ polymers dissociate,

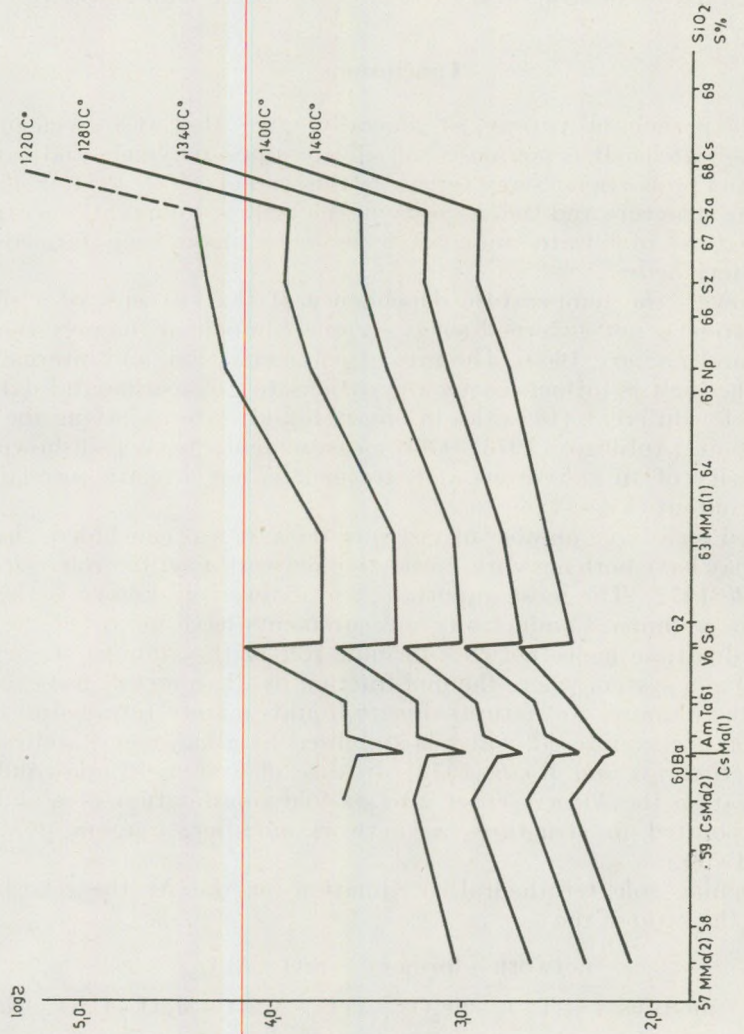

Fig. 17. The variation of viscosity of the andesite melts as a function of the SiO_2 content of the volatile-free melts
For legend see Table 1.

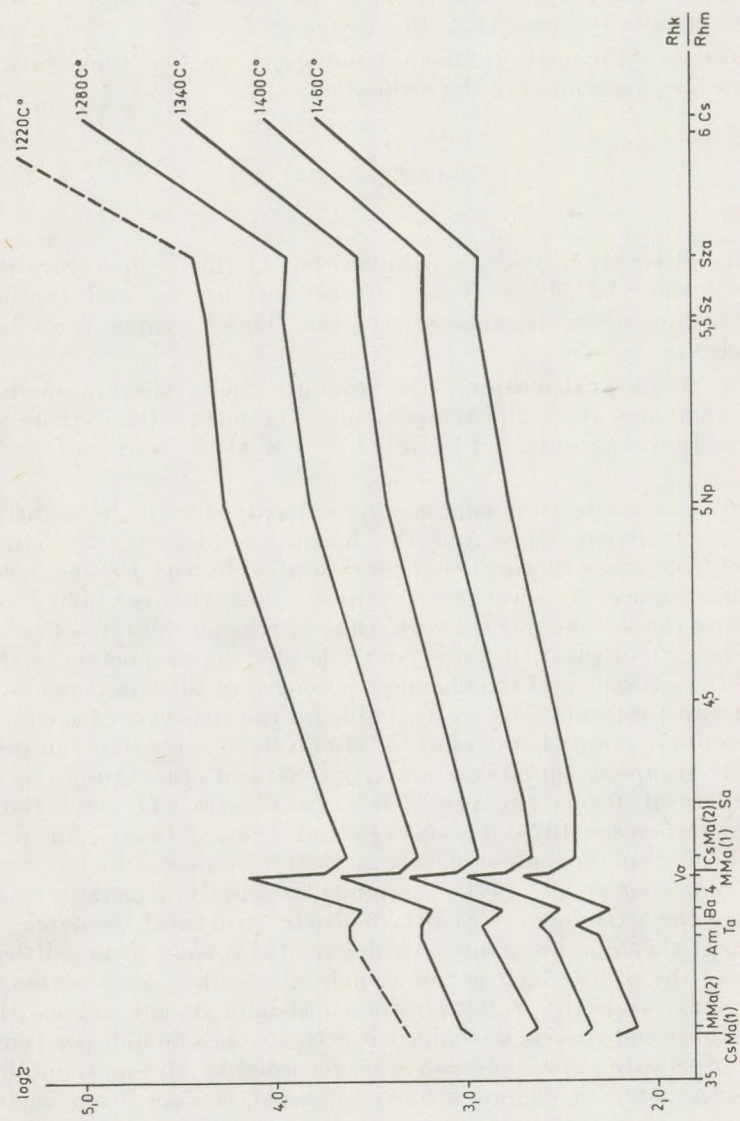

Fig. 18. The viscosity of the andesite melts as a function of the ratio of the network-former (= $R_{nf.}$) and network-modifier (= $R_{hm.}$) components.
For legend see Table 1.

therefore only the silica may exist in tetrahedral position, since this element has the highest ionic potential. The lowest polymerisation stage of the andesite melts was calculated, with the assumption, that all of the oxygene was linked to silica. In this way mainly $(SiO_3)^{2-}$, less frequently $(SiO_2)^0$ ions were encountered, except for the MMa(2) sample, where $(SiO_4)^{4-}$ ions were also recorded (Fig. 19).

The viscosities of the melts on the maximum – 1460 °C – temperature could not have been correlated to the estimated

$$\frac{(SiO_3)^{2-}}{(SiO_2)^0}$$

ratio (Fig. 20).

From this observation it was concluded that at this temperature the dissociation of the $(AlO_4)^{5-}$ polymers is still incomplete, and the lowest polymerisation stage characteristic to the "high" temperatures has not been reached.

According to our calculations, the andesite melts contain mainly $(SiO_3)^{2-}$ silicate anions at "high" temperature. The most advanced stages of depolymerisation is represented by $(Si_3O_9)^{6-}$, $(Si_4O_{12})^{8-}$ and $(Si_6O_{18})^{12-}$ rings.

The increase of viscosity during cooling is partly due to the additive polymerisation of silicate rings and the formation of $(SiO_3)^{2-}$ chains, partly derived from the structural changes described by the *Frenkel* hole-theory regarding liquids. At lower temperatures – but still over 1460 °C – the Al may enter the tetrahedral network, thus increasing the rate of polymerisation. The rate of substitution is controlled by the proportion of the network-modifier cations, and the chemical potential of the components.

Mainly indirect informations are available for the structure of the melt close to the liquidus point. Lengyel at al. (1966) have suggested the presence of silicate groups based on conductivities. Several other studies have indicated structural formation prior to crystallization (*Lőcsei*, 1967, *Zhuravkov* and *Baranceve*, 1975; *Yermolenko* and *Trunec*, 1975). The presence of the elements of diopside structure at 1550 °C temperature has been suggested by *Zhunina* et al. (1971). Yermolenko and Manchenko (1975) have indicated the existence of $SiAlO_7$ feldspar structural elements in conditions above the liquidus point. Anfilogov (1975) has concluded that the structure of the silicate melt is "ionic-molecular": the ionic fraction is formed by cations, while the molecular one consists of silicate anions. He stated that infinite network is developed if SiO_2 exceeds 50 mol per cent. The presence of silicate anion polymers were recorded by chromatography and mass-spectrometry in glasses formed by rapid cooling from melts (*Yesin*, 1976).

Besides the actual pt-conditions, the structure of the silicate melt is probably affected by its "inherited" thermal history too (*Zhunina* et al., 1971, 1975).

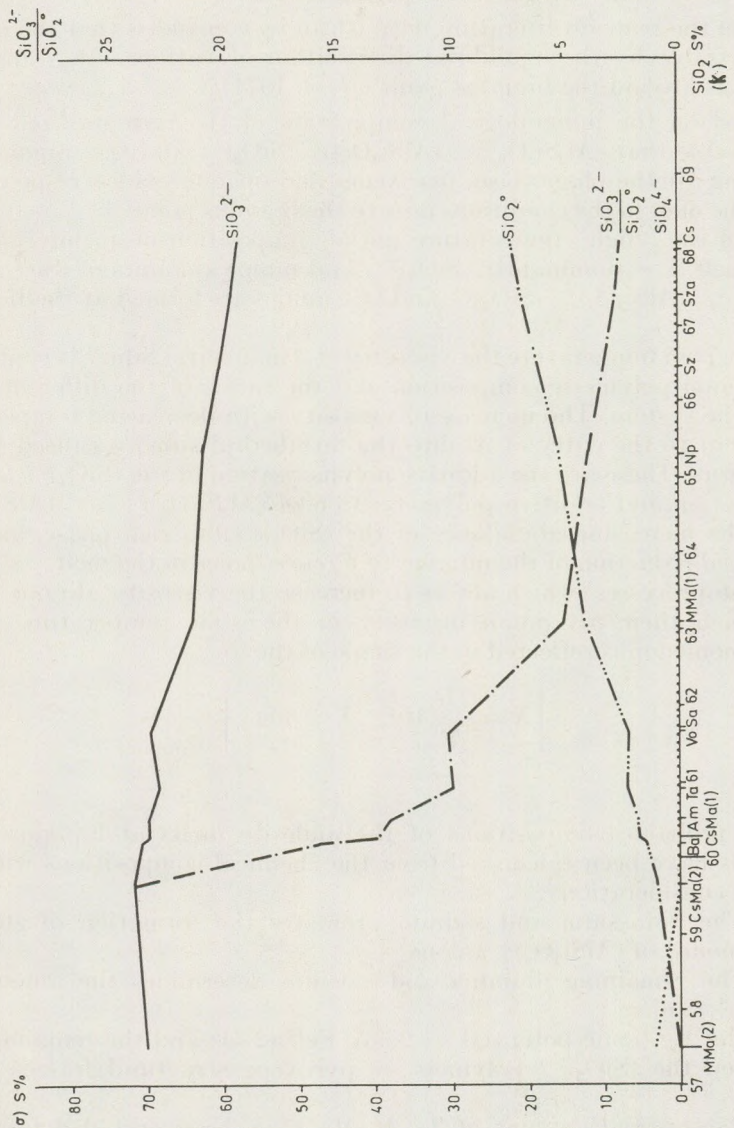

Fig. 19. The calculated $(SiO_3)^{2-}$, $(SiO_2)^0$, $(SiO_4)^{4-}$ contents and $(SiO_3)^{2-}/(SiO_2)^0$ ratios vs. the SiO_2 content of the volatile-free melts.
For legend see Table 1.

The crystals formed at the liquidus point may also provide information about the structure of the melt near to the liquidus point. Their structural elements are probably present in the melt (*Hess*, 1971). This assumption has been successfully used in our experiments too.

From the relevant literature data it can be concluded that the melt is characterizable by the equilibrial distribution of cations, O^{2-} and silicate anions around the liquidus point (*Hess*, 1971).

Based on the mineralogical composition of the recrystallized rocks, it is probable that $(Al_2Si_2O_8)^{2-}$, $(AlSi_3O_8)^{-}$, $(SiO_3)^{2-}$ and O^{2-} anions, corresponding to the plagioclase, pyroxenes and opaque oxides respectively, exist in the melt in the conditions near to the liquidus point.

From the "high" temperature initial composition of an intermediate silicate melt, i. e. dominantly $(SiO_3)^{2-}$, and minor amounts of $(SiO_2)^0$; the $(Al_2Si_2O_8)^{2-}$, $(AlSi_3O_8)^{-}$, $(SiO_3)^{2-}$ and O^{2-} anions are formed at the liquidus point.

At a given temperature the viscosity of a magmatic liquid is controlled by the anion polymeric composition and the ratios of the different polymers in the system. The increase of viscosity with decreasing temperature (subsequent to the entry of Al into the tetrahedral sites) is caused by several factors. These are the additive polymerisation of the $(SiO_3)^{2-}$ anions, the formation and additive polymerisation of $(Al_2Si_2O_8)^{2-}$ and $(AlSi_3O_8)^{-}$ anions, the increasing abundance of the $(SiO_2)^0$ silica-rich phase, and the exponential reduction of the number of *Frenkel*-holes in the melt.

These processes, which act as to increase the viscosity, do not necessarily reach their maximum intensity in the same temperature range. This phenomenon is reflected in the shape of the

$$\left[X = \frac{1}{T}10^4; \quad Y = \log \eta\right]$$

curves.

The probable compositions of the andesite melts at liquidus point conditions have been calculated from the chemical compositions with the following considerations:

a) The potassium and sodium promotes the formation of stochiometric amount of $(AlSi_3O_8)^{-}$ anions;

b) The remaining alumina and calcium determines the amount of $(Al_2Si_2O_8)^{2-}$ anions;

c) The Mg (ionic potential = 2.56), Fe^{II} (2.41) and the remaining Ca (1.89) keep the $(SiO_3)^{2-}$ polymers – pyroxene structural frames – in balance.

The accessorial amount of Ti, P, Mn have been excluded from the calculations since their effect on the structure of silicate melts is questionable. [The role of manganese is probably similar to that of the Fe^{II}. The Ti might be a network modifier, according to *Bottinga* and *Weill* (1972)].

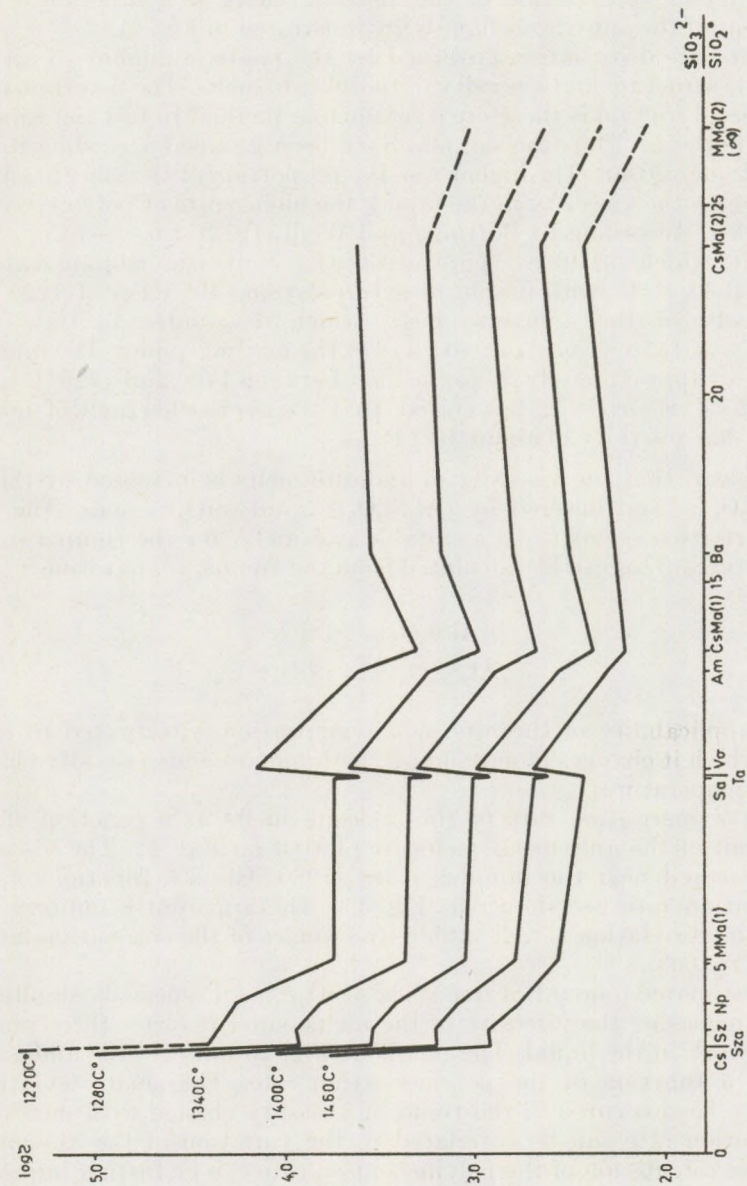

Fig. 20. The viscosities of the andesite melts vs. the $(SiO_3)^{2-}/(SiO_2)^0$ ratio of the volatile-free melts.
For legend see Table 1.

Besides these anion polymers, significant amount of $(SiO_2)^0$ has also been estimated. This has been formed simultaneously with the entry of Al into the tetrahedral network, and the increase of the polymerisation rate, during the cooling of the melt.

The anionic composition of the andesite melts as a function of the SiO_2 content of the anhydrous liquids are illustrated in Fig. 21.

The anionic distribution governed by the relative amount of cations controls the structure and viscosity of the silicate melts. The determination of the internal friction is therefore a reasonable method to test the validity of the hypothesis. Thus the samples have been grouped according to the rate of polymerisation. The higher was the proportion of the silicate anions which increase the viscosity in the liquid, the higher rate of polymerisation was assumed. According to Bottinga and Weill (1972), the viscosity of an albite melt, which produces "pure" $(AlSi_3O_8)^-$ anion in molten state, is 10^4 Pa·s at 1400 °C (with graphical extrapolation, 10^6 Pa·s at 1220 °C). The viscosity of the anorthite melt, which dissociates to Ca^{2+} and $(Al_2Si_2O_8)^{2-}$ at 1550 °C, is about 10 Pa·s at the metling point. The internal friction of an approximately diopsidic melt between 1400 and 1220 °C is less than 10 Pa·s, *Shaw* (1972) has stated, that the overcooled melt of quartz at 1220 °C has viscosity of about 10^{13} Pa·s.

It is clear, that the viscosity of andesite melts is increased by $(SiO_2)^0$ and $(AlSi_3O_8)^-$, and lowered by $(Al_2Si_2O_8)^{2-}$ and $(SiO_3)^{2-}$ ions. The rate of polymerisation seems to be a suitable parameter for the comparison of melt structures. This can be calculated from the anionic composition:

$$P^0 = \frac{(AlSi_3O_8)^- + (SiO_2)^0}{(Al_2Si_2O_8)^{2-} + (SiO_3)^{2-}}$$

The applicability of the rate of polymerisation is restricted to those cases, in which it changes monotonously with monotonous viscosity change at lower temperatures.

The polymerisation rate of the andesite melts as a function of the SiO_2 content of the anhydrous melts are plotted on Fig. 22. The viscosity values measured near the liquidus point (1280 °C) as a function of the polymerisation rate are shown in Fig. 23. The apparently uniform and monotonous correlation is well visible (the square of the correlation factor, r^2 is equal to 0.93).

The estimated amount of free silica, $(SiO_2)^0$ is an especially significant factor in increasing the viscosity of the melts, since it forms three-dimensional network in the liquid. The points at Fig. 23 indicate the amount of $(SiO_2)^0$ as a function of the polymerisation rate. The small deviations, which have been occured in the trend of viscosity change with increasing polymerisation rate can be correlated to the variation of the amount of $(SiO_2)^0$. The calculation of the polymerisation rate can be further improved if the amount of anion polymers are weighted according to their role in the ontrol of viscosity.

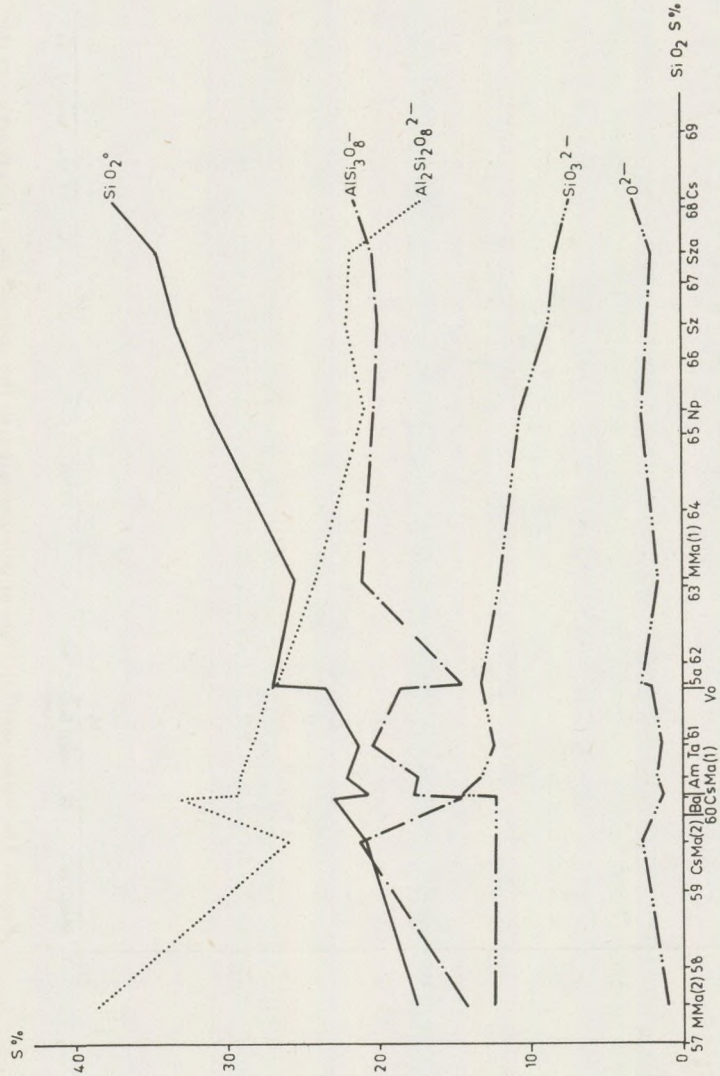

Fig. 21. The anionic composition near the liquidus point in the andesite melts as a function of the SiO_2 content of the anhydrous melts.
For legend see Table 1.

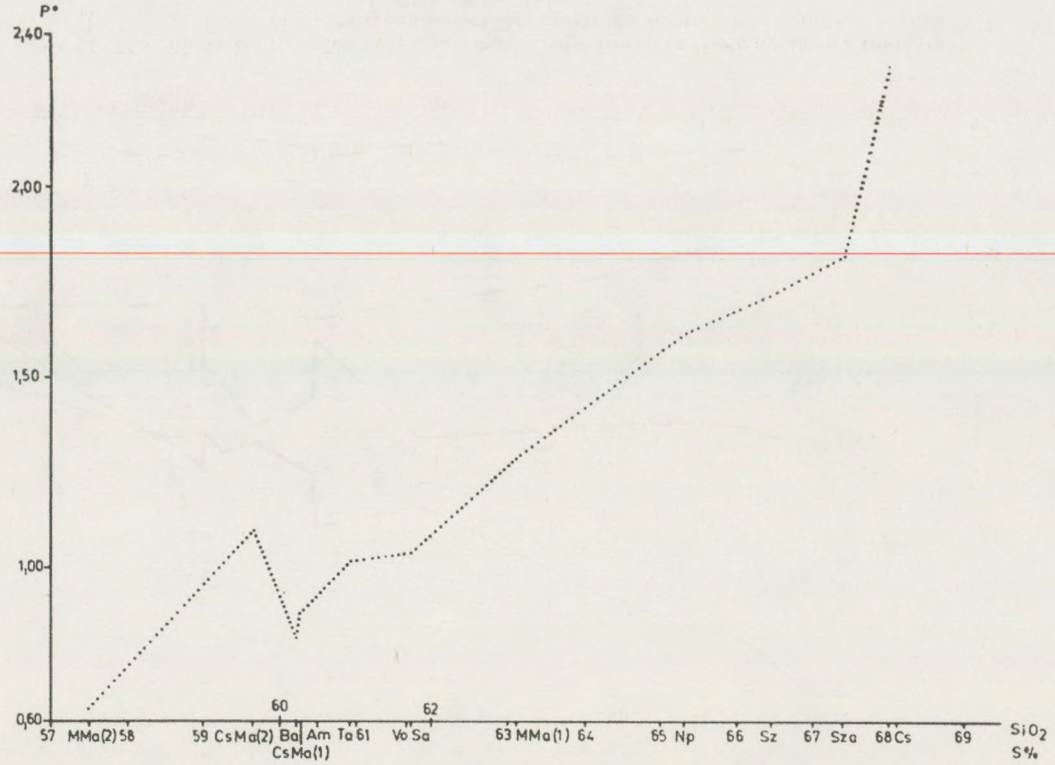

Fig. 22. The variation of the rate of polymerisation in the andesite melts as a function of the SiO_2 content of the volatile-free melts.
For legend see Table 1.

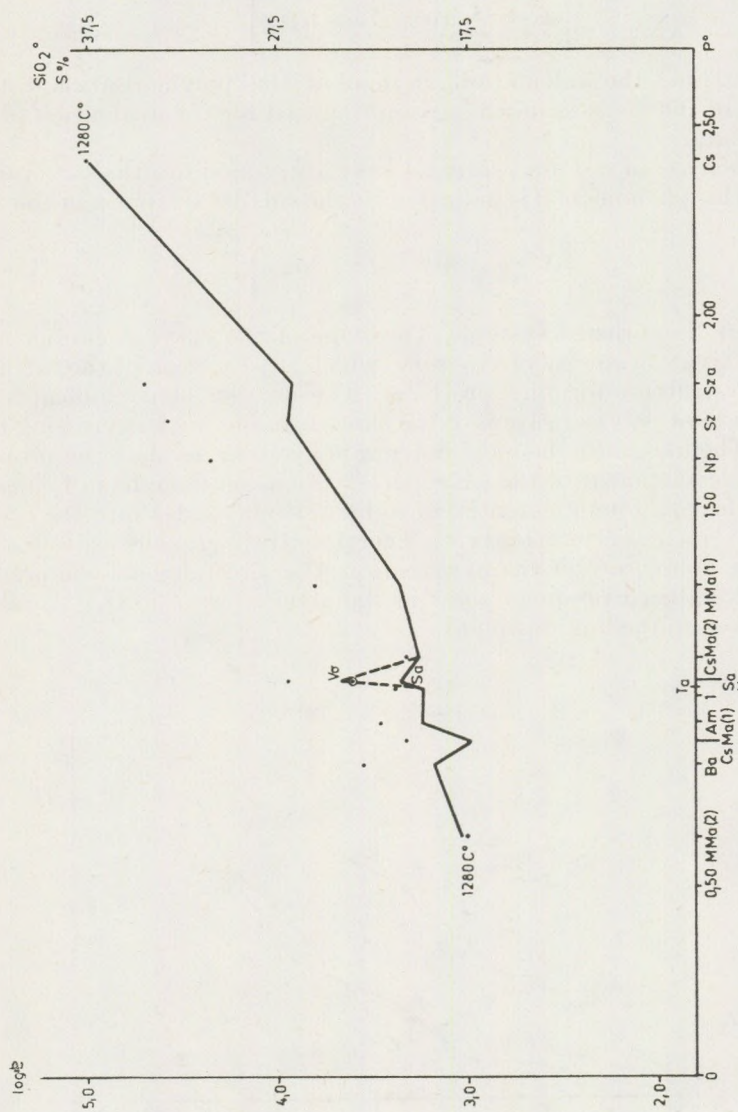

Fig. 23. The viscosities (continuous line) and the calculated $(SiO_2)^0$ contents (dots) in the andesite melts as a function of the calculated polymerisation rate.
For legend see Table 1.

The bauxite, dolomite and limestone additives have negligible effect on the structural evolution and anion polymerisation of the melts, as is shown by the approximately identical steepness of the

$$\left[X = \frac{1}{T}10^4; \quad Y = \log \eta\right]$$

functions. Thus, the calculation method of the polymerisation rate is applicable in these cases, its change can be used for the evaluation of the viscosity data.

The increase of sodium content significantly modifies the structure of the melt. This phenomenon is indicated by the smaller steepness of the

$$\left[X = \frac{1}{T}10^4; \quad Y = \log \eta\right]$$

functions in Na-enriched systems. The slope of the curve is proportional with the activation energy of viscosity, which is a function of the intensity of anionic structure-forming processes. The smaller slope indicates the smaller grade of polymerisation of the silicate anions with decreasing temperature. The increased chemical potential of sodium reduces the probability of the development of the $(Al_2Si_2O_8)^{2-}$ anions on the effect of calcium. Owing to the small ionic potential of sodium, it may enter into the crystal lattice only in lower temperatures. Therefore the melt can easily be overcooled. The dominance of the pyroxenes in the mineralogical composition of the recrystallized products point to the abundance of $(SiO_3)^{2-}$ units in the melt close to the liquidus point.

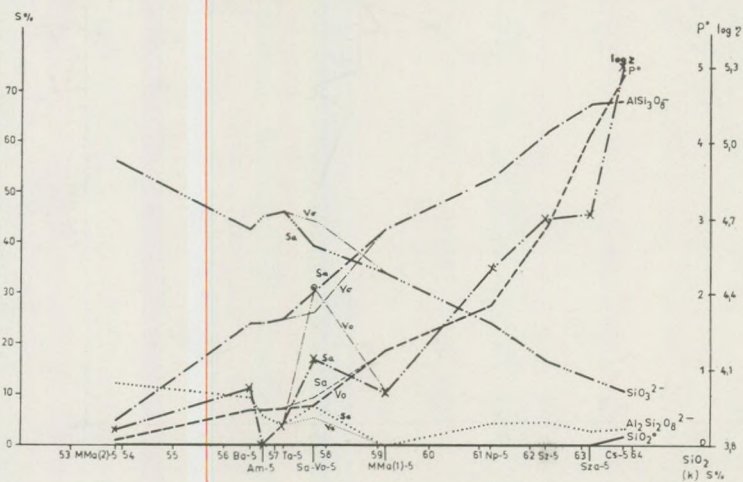

Fig. 24. The anionic polymer composition of the samples with 10 weight % Na_2CO_3, their polymerisation rate, and viscosity values on 1100 °C vs. the SiO_2 content of the volatile-free liquids.
For legend see Table 1.

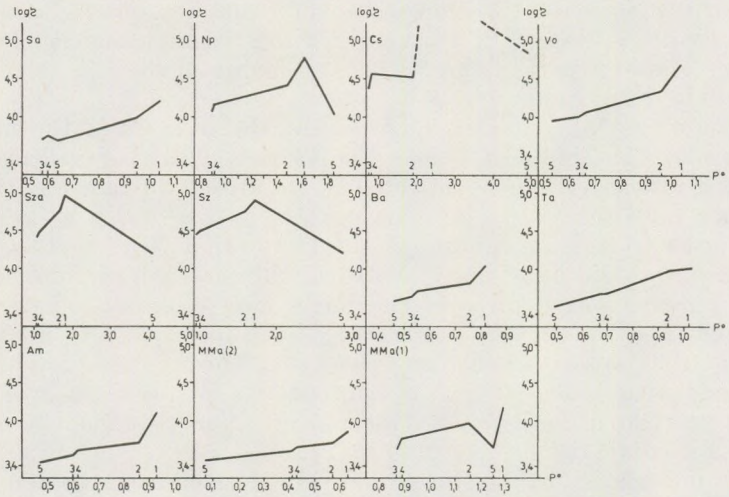

Fig. 25. The variation of the viscosity near the liquidus point, at 1160 °C as a function of the calculated polymerisation rate.
For legend see Table 1.

If the sodium concentration of the melt is significantly increased, the above mentioned method to calculate the rate of polymerisation is no longer applicable, since the system becomes unsaturated due to the limited amount of silica, and the amount of the $(AlSi_3O_8)^-$ anions is less than that of the sodium cations. Thus it is assumed that the potassium promotes the formation of proportional amount of $(AlSi_3O_8)^-$, the sodium – in the first step – is connected to $(Al)^* \rightarrow (Si_2O_6)^{4-}$ units, the Ca is related to the $(Al_2Si_2O_8)^{2-}$ structures (the amount of which is limited by the availability of remaining Al), the remaining Ca, the Mg and Fe leads to the formation of $(SiO_3)^{2-}$ anions. The amount of the $(SiO_2)^0$ controls the type and ratio of the anion polymers – i. e. $(AlSi_3O_8)^-$ and $(Al)^* \rightarrow (Si_2O_6)^{4-}$, which are kept in balance by the sodium. Thus, the formation and abundance of these polymers is a function of the SiO_2 content and the cationic composition of the melt.

A direct consequence of these calculations is the fact that a varying, though significant amount of Al may act only as network-modifier.

The intense viscosity lowering effect of the sodium at lower temperatures may be due to two principal factors:

– incremental increase of Na content may lead to the development of stochiometric amount of $(AlSi_3O_8)^-$ anions, and the system still remains saturated. However, the ratio of $(SiO_2)^0$ beside the anion polymers bonded to cations show sharp decrease;

$(Al)^*$ = network-modifier alumina, in octahedral coordination.

– if the Na content is significantly increased, the $(SiO_2)^{0-}$ component completely disappears (as it was recorded in all samples except for Cs – 5 and Sza – 5) and a part of the Na cations maintain the equilibrium state of the $(SiO_3)^{2-}$ anionic polymers.

Thus, if the Na content is increased by the addition of 10 weight per cent Na_2CO_3, the anionic polymer composition of the silicate melts also changes significantly. This is reflected by the strong difference in the polymerisation rates (Fig. 24).

In order to test the validity of our assumption about the viscosity of andesite melts, the relationship between the internal frictions and the anionic polymerisation rates of the melts have been systematically investigated (Fig. 25). It was shown that – except for Na_2CO_3 mixtures – the value of log η shows linear increase with P^0 near to the liquidus point. In systems with increased Na_2CO_3 content and SiO_2 content over 61 – 62 per cent, the rate of the estimated increase of P^0 grows, thus it is no longer suitable for comparison.

This increase is virtual, since it has been derived from the non-proportional change of the anion polymer ratios. The estimated amounts of the $(SiO_2)^0$-component are very low even in the most acidic alkali enriched systems, thus the measured viscosity values are much lower than expected from P^0.

The increase of the Na content causes significant changes in the

$$\left[X = \frac{1}{T}\,10^4; \quad Y = \log \eta\right]$$

function, the activation energy of viscosity, the estimated anion polymer composition, the rate of crystallization, the mineralogical composition and texture. These phenomena can be considered as equivalent with the differences between the formation of alkali and calc-alkaline rocks in natural conditions.

SUMMARY

The most interesting petrological-mineralogical results of our experiments can be summarised as follows:

1. The Tertiary andesite melts have had $10^2 - 10^4$ Pa · s viscosity even at the highest eruptive temperatures – at 1100 – 1200 °C. The low viscosity types – i. e. the magmas at Velence, Cserhát and Mátra mts. – have tended to form extensive lava flows while the more viscous, less flowable magmas at Csódihill and Csákhill formed more isometric forms, i. e. extrusions or laccoliths. The viscosity is a main controlling factor in the development of eruptive forms.

2. In most cases the recrystallized products have had different mineralogical composition and texture than that of the original rocks. The only exception is the micro-andesite, which occurs in the Mátra and Cserhát. It is probable, that the conditions of crystallization of these rocks were similar to the experimental conditions of the heating treatment.

3. The skeleton crystals are abundant in the crystallized products – due to the lack of currents in the silicate liquids. The scarcity of these skeleton crystals in the majority of natural andesites – except for certain micro-andesites – indicate the existence of convection, gravitative etc. type currents during the crystallization.

4. The assimilation does not affect the viscosity of the andesite lavas to a great extent even if assimilated materials are contaminated, and comprise up to 10 per cent of the total volume. Thus the flowability of the magmas in the Earth's crust is basically controlled by the initial characteristics of the melt.

5. The viscosity vs. temperature function and the activation energy of the viscosity in the andesite-based liquids can be interpreted by means of the anion polymerisation theory for silicate melts. It can be assumed that at "very high" temperatures an andesite melt is composed mainly of $(SiO_3)^{2-}$ anionic polymers. Around the liquidus point this structure changes to an $(Al_2Si_2O_8)^{2-}$, $(AlSi_3O_8)^{-}$, $(SiO_3)^{2-}$, $(SiO_2)^0$, O^{2-} composition. The viscosity grows with decreasing temperature. This is due to several factors, the additive polymerisation of $(SiO_3)^{2-}$ anion, the formation and additive polymerisation of $(Al_2Si_2O_8)^{2-}$, $(AlSi_3O_8)^{-}$ anions, the increase of the $(SiO_2)^0$ silica-rich phase, and the decrease of the number of Frenkel-holes. The intense viscosity change with decreasing temperature in andesite melts is largely due to the incorporation of alumina into tetrahedral positions.

Bonds are developing between the cations and the silicate anions at the liquidus point. The crystallization of a silicate melt is thus preceded by a preliminary phase in molten state, with complex processes of development of anions.

REFERENCES

Anfilogov, V. N. (1973): Szilikátolvadékok egyensúlyi polikondenzációja és szerkezete (Ravnovesnaya polikondensacia i stroenie silikatnih rasplavov). Geokhimia No. 12. pp. 1793–1800.

Anfilogov, V. N. (1975): Magmaolvadékok likvációjának természete és kőzettani kritériumai (Priroda i petrograficheskie kriterii likvacii magmaticheskih rasplavov) Geokhimia No. 7. pp. 1035–1042.

Bonetti, G.–Lazzari, S. (1969): Conducibilita elettrica di alcuni vetri ternari SiO_2-Na_2O-/CaO e Al_2O_3/ad alta temperatura e relazione con la viscosita. Vetro e Silicati XIII. No. 77. pp. 5–11.

Bottinga, Y.–Weill, D. F. (1972): The viscosity of magmatic silicate liquids: a model for calculation. American Journal of Science, Vol. 272. pp. 438–475.

Erdey-Grúz, T. (1972): A fizikai kémia alapjai. Műszaki Könyvkiadó, Budapest.

Ezekiel, M.–Fox, K. A. (1970): Korreláció- és regresszió-analízis. Közgazdasági és Jogi Könyvkiadó, Budapest.

Hess, P. C. (1971): Polymer model of silicate melts. Geochimica et Cosmochimica Acta. No. 3. pp. 289–306.

Khitarov, N. I. et al. (1976): Fizicheskie svoystva sistemi kremnezom-voda pri visokih parametrah. Geokhimia No. 2. pp. 217–222.

Khitarov, N. I. et al. (1976): (Vliyanie davleniya na vyazkost risplava bazatta. Geokhimia No. 10. pp. 1489–1497.

Yermolenko, N. N.–Manchenko, Z. F. (1975): Issledovanie vliyaniya dobavok dvuokisi cirkoniya na svoystva is struktura visokoglinozomistih stekol i sitallov sistemi SiO_2-TiO_2-B_2O_3- Al_2O_3-CaO. Steklo, sitalli i silikatnie materiali. Vip. 4. Minsk. pp. 115–120.

Yermolenko, N. N.–Trunec, I. A. (1975): Vliyaniya termoobrabotki na svoystva i struktura stekol sistemi SiO_2-TiO_2-B_2O_3-Al_2O_3-MgO. Steklo, sitalli i silikatnie materiali. Vip. 4. Minsk. pp. 136–140.

Yesin, D. A. (1976): O primenenii statisticheskoj termodinamiki polimerov k rasplavlennim silikatam. Geokhimia, No. 7. pp. 1005–1020.

Knapp, O.–Korányi, Gy. (1964): Üvegipari Kézikönyv. Műszaki Könyvkiadó, Budapest.

Kocsis, G. (1966): Szilikátüvegek aktiválási energiájának alakulása olvasztásgyorsító adalékok hatására. Építőanyag 5. pp. 167–174.

Kubovics, I. (1974): A neutrális-bázisos magmatitok, erőműi salak és üledékes kőzetek összehasonlító petrurgiai vizsgálata. Akadémiai doktori értekezés, Budapest.

Lengyel, B. et. al. (1966): A szilikátüvegek elektromos tulajdonságai. Akadémiai Kiadó, Budapest.

Lőcsei, B. et. al. (1965): Húzott síküveggyártás kapacitásának befolyásolása a technológiai paraméterek módosításával. A Veszprémi Vegyipari Egyetem közleményei, 9. pp. 53–69.

Lőcsei, B. (1967): Olvasztott szilikátok és tulajdonságaik. Akadémiai Kiadó, Budapest.

Rasin, G. A. (1959): Rol aluminiya v mineraloobrazovanii pri kristallizacii osnovnih silikatnih rasplavov. IAN. SSSR. Seriya geologicheskaya. No. 12. pp. 60–68.

Shaw, H. R. (1972): Viscosities of magmatic silicate liquids: an empirical method of prediction. American Journal of Science, Vol. 272. pp. 870–893.

Zhunina, L. A. et. al. (1971): Obrazavanie piroxenovih strukturnih gruppirovok na otdelnih etapah steklo-i sitalloobrazovaniya i ih rol v processah kristallizacii stekla). Eksperimentalnoe issledovanie mineraloobrazovaniya. Izdatelstvo Nauka, Moskva, pp. 158–163.

Zhunina, L. A. et. al. (1975): (Mineraloobrazovanie v processe kristallizacii slakosoderzhaschevo sitalla piroxenovovo sostava). Eksperiment v oblasti tehnicheskovo mineralabrazovaniya. Izdatelstvo Nauka, Moskva. pp. 68–75.

Zhunina, L. A. et al. (1975): Issledovanie vliyaniya grupp OH^- na kristallizacii slakovih stekol. Steklo, sitalli i silikatnie materiali. Vip. 4. Minsk. pp. 8–14.

Zhuravkov, N. M.–Baranceva, S. E. (1975): Izmenenie nekotorih svoystvo stronciysoderzhaschevo stekla v processe evo kristallizacii. Steklo, sitalli i silikatnie materiali. Vip. 4. Minsk. pp. 108–115.

GEOCHEMISTRY OF UPPER OLIGOCENE SEDIMENTS OF THE WEST-CSERHÁT AREA (NORTH HUNGARY)

by

RÓZSAVÖLGYI J.

(Department for Petrology and Geochemistry of the Eötvös L. University, Budapest, Múzeum krt. 4/A)

Received: 18. June 1980.

SUMMARY

In the West-Cserhát area discontinuous regression of the Parathetys has lead to the deposition of a fine grained clastic sequence during the Late Oligocene. The sequence is built up of calcite-cemented sediments consisting of various mixtures of sand, aleurolite and argillite. Accumulation of the above sediments took place mostly in a litoral-marine environment with subordinate signs of the lagoonal-brakish facies at places. As a whole, the sequence can be taken for an intramontan-molass complex.

Trace elements were analysed in 122 sand-specimens and 62 aleuritic argillites. Trace element content of the aleuritic-argillite layers proved to be anomalously high as compared to that of the sandy strata. The average trace element contentration of the complex, however, corresponds to the global average of trace-elements in fine clastic sediments. The trace element concentration of any clastic sediment depends on several factors – primarily on the nature and proportion of clays and heavy minerals. In the case of the Cserhát Mts, however, also telethermal solutions generated by Miocene andesite volcanism and the reworked material of Cretaceous bauxites at Nézsa are to be considered as important sources of trace elements. Due to the polygenetic nature of the accumulation process, frequency distribution curves of most trace elements are of the polymodal type. Copper, cobalt and partly zincum are the only elements which exhibit unimodal curves both in sands and in aleuritic argillites. Frequency distribution of boron, barium, nickel, plumbum and vanadium is unimodal in sands but polymodal in aleuritic clays. Chromium and titanium, on the other hand have polymodal curves in sandy strata, but unimodal in argillites. Frequency distribution curves of gallium, manganese and strontium are polymodal both in sands and in argillites. Interpretation of the above observations is given in the text. It should be noted that the results of geochemical facies analysis carried out by the statistical method of Potter, and by a study of boron to gallium ratio, do not conform with those of stratigraphical-palaeontological analysis.

Introduction

The first comprehensive review of the geology of the Cserhát Mts. was published in 1940 by *Noszky J.* Although it is a standard work on the subject even today, it is quite natural that more than 40 years ago the author's interest was focussed on stratigraphical and palaeontological problems rather than on geochemistry. Similarly, the latest overall syntheses on Hungarian Upper Oligocene Formations – including those of the Cserhát Mts. – are also based on palaeontological and sedimentological data (*Báldi, T.* 1966, 1973).

Geochemical data concerning sedimentary formations of selected areas of the Cserhát Mts were first published in the early seventies (*Andó, J.* 1973, *Pécsi-Donáth, É.* 1973, *Rózsavölgyi, J.* 1973).

The subject of the present study is the trace element distribution of Upper Oligocene sediments between the Börzsöny Mts. and the valley of the Galga-creek in the W-Cserhát area (See Fig. 1.) Oligocene formations are covered here by an essentially continuous soil-blanked and most of the area is arable land. In situ rock surfaces are exposed in small village-quarries or in road-cuts and gullies where their outcrop is sometimes simply he result of intense soil erosion.

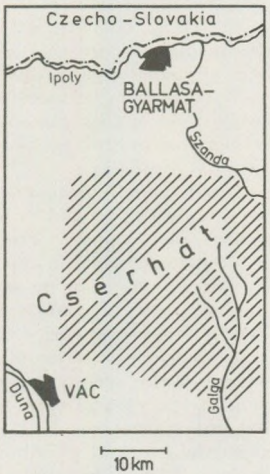

Fig. 1. Topographic map of the West-Cserhát area

Altogether 184 specimens of Upper Oligocene clastic sediments were collected from this area. Trace element concentration of the samples was determined semiquantitatively by using a Q – 24 quartz-spectrograph. The analysis was carried out by semiquantitative accuracy (*Mrs. J. Nagy-Balogh* 1971). Grain-size distribution was determined by wet-sieving and weighing on a Sartorius – 4600 Sedimentation-Scales. $CaCO_3$ was assayed by using the standard Scheibler-calcimeter. Part of the samples were separated, and the heavy minerals were identified from the 0.25 –.0.125 mm fraction, while the clay fraction was investigated by the differential thermal gravimetric method. Results of the standard petrological investigations will be detailed here restricted to the interpretation of the geochemical data.

Geology and petrology of the Upper Oligocene

Interrupted by shorter or longer periods of oscillation, the regression of the Upper Oligocene sea had been discontinuous in the area of present-day W-Cserhát. The sedimentary complex deposited during this oscillatory regression consists of various mixtures of calcite-cemented sand, aleurolite and clay. Gravellites are subordinated. Based on bore-hole information the average thickness of the complex is 300 to 400 metres, definitely decreasing towards the North.

In the Legénd—4 bore-hole thickness of the Upper Oligocene does not exceed 260 metres.

As to regional tectonics the W-Cserhát Upper Oligocene complex is an integral part of the "intramontan" molasse sequence filling the Tertiary basins of Hungary. Individual layers of the complex are never persistent on the regional scale, they vary capriciously in the vertical sense: mayor may not be repeated, and are not confined to any given stratigraphic horizon. That is why they can not be mapped properly even on the large scale. Beside the vertical inconstancy they exhibit a remarkable variability also in the horizontal sense: formations of fairly different grain-size distribution may be heteropic substitutes of each other. There are also brakish trata in the complex (*Noszky, J.* 1940). According to *Báldi, T.* (1966) the palaeoecological picture suggests a predominantly shallow-sublitoral and partly litoral-lagoonal/or central-sublitoral environment.

No closed lagoons had been formed in this area, however. The connection with the open sea had been firmly established towards the ENE. That is why, unlike the Pomáz area (Pilis Mts), the Upper Oligocene of the Cserhát contains no gypsum-bearing layers, (*Koch, A.* 1877).

The Late Oligocene regression — brought about by the Savian orogeny — was followed by a comparatively short continental period and again an inundation, during which sea advanced from the ENE towards the SW. Corresponding sediments are those of the Lower and Middle Miocene gravellites, coarse sands, reworked rhyo-dacite tuffs, tuffites and argillaceous aleurolites, the latter called "slir" in N-Hungary. They occur at places and in the form of smaller or larger isolated patches only. The Middle Miocene paroxysm of the Inner-Carpathian subsequent volcanism produced lava-flows, dykes and tephra of pyroxene-andesitic composition. Although there is no industrial-scale mineralisation known in connection with the Cserhát volcanism, thermal effect of volcanic or subvolcanic bodies intruded into or penetrating the Upper Oligocene sediments is to be considered as a plausible factor which by mobilising the volatiles, might have modified the original distribution of trace elements in prae-volcanic rocks.

Grain-size analysis of the Upper Oligocene sediments lead to the conclusion that the coarser or finer nature of any given stratum depends essentially on the proportion of the sandy and aleuritic constituents in it. The percentage of clays rarely exceeds 50. Grouping of the investigated samples was carried out therefore on the basis of the proportion of sand-size

and aleurolite + clay fractions. According to this classification 122 of the 184 samples proved to be "sandy", with the rest belonging to the group of "argillaceous.aleurolites".

The group of sandy formations includes sandstones (coarse-, medium- and fine-grained sands and aleuritic-argillaceous sands cemented by a calcite matrix).

The group of aleuritic-argillites consists of clayey-sandy aleurolites, marly-sandy aleurolites, aleuritic-sandy clayey-marls, aleuritic-sandy marls, and calcareous marls. All sandy formations are more of less homogeneous, i. e., when plotted in a triangle they are represented by a close aggregate of dots near to the "100 precent sand" symbol or the triangle. The group of aleuritic-argillites is somewhat less homogeneous: the dots occupy an area considerably larger than that occupied by the sand-dots (See Fig. 2.). Heavy and light minerals were separated in 2.95 spec. weight tetra-bromenthane. After separation the amount of heavy minerals was determined and it proved to be of the order of magnitude of X, 0 percent to 0, X percent. Based on predominant minerals the separates were divided into theree main groups. The first group is characterised by predominant garnet and opaque minerals (ilmenite and magnetite); the second by chlorite and the third by autigenic pyrite and epigenic limonite. Although in lesser amounts also rutile, tourmaline, disthene, hornblende, tremolite, actinolite, staurolithe, epidote and zircon are common in almost all separates.

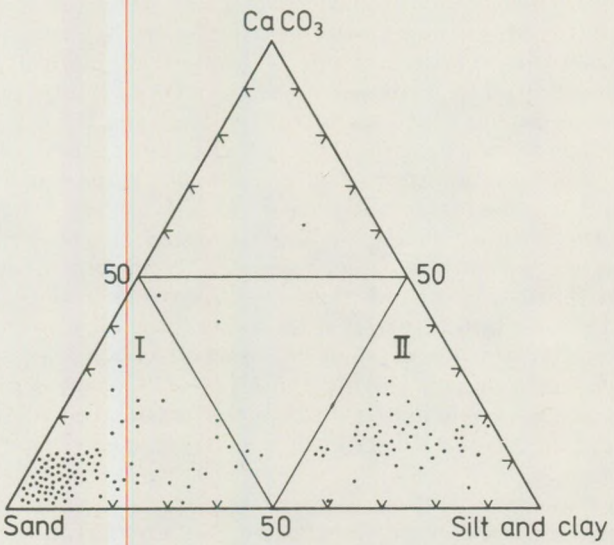

Fig. 2. Grain size composition of the investigated rock samples
I. Sandy formations
II. Aleuritic-argillites

The light-mineral fraction consists mainly of quartz and quartzite with subordinate muscovite, orthoclase, Na-plagioclase, microcline and fragments of non-identifiable metamorphics.

Since high percentages of garnet, ilmenite and magnetite are strictly bound to sandy strata, which suggest an intensely moving transportation medium, whereas chlorite, autigenic pyrite and epigenic limonite are characteristic of aleuritic-argillites laid down is slowly-moving, gently agitated, oxygen-poor waters, the observed inhomogeneous distribution of heavy minerals can be satisfactorily explained by assuming changes in the intensity, but not necessarily in the direction or the source of transportation.

Minerals, identified in the heavy- and the light fractions suggest that the source area had been build up of epi- and meso-zonal metamorphics with some subordinated igneous formations. When only heavy-minerals are taken into consideration, the investigated samples resemble the Lower Miocene sandstones of Salgótarján (*Mrs. Örkényi-Bondor, L.* 1969), and are quite unlike the Upper Oligocene clastics of the Dorog basin, where heavy minerals of igneous (volcanic) origin are rather frequent (*Mrs. E. Csánk* 1969). The above sequence of thoughts suggests that the source of the Upper Oligocene clastics of the Cserhát must have been somewhere to the NNE at the crystalline mass of the presentday Vepor and Gemer Mts.

Derivatographical analyses proved the presence of kaolinite- and illite-type clay minerals in the argillite fraction of the investigated rocks. In the sandy strata the argillitic fraction consists mostly of kaolinite while the aleurolites are generally rich in illite.

When assuming all the clay minerals to be of detrital origin, the above distribution – namely that kaolinite is confined to the sands and illite to the aleurolites – can not be explained by the principle of differential sedimentation. The deposition of kaolinite, which takes generally much more time than that of illite, would namely result in the increase of the percentage of the latter in sands and the former in aleurolites – the opposite of which was observed. It seems highly probable that illite may be not only of detrital but also of dia-or epigenic origin. (*Nemecz, E.* 1973).

Trace elements

33 trace elements were analysed by the emission spectral analytical method. Limits of detectability for the individual elements are shown by table 1. Conditions of the analyses were as follows:

Instrument: Q – 24 quartz-spectrograph
Photographic material: Agfa Gaevert Scientia 23 D – 50
Diaphragm: 10 μm
Aperture: 3.2
Current: 10 A
Exposition time: 120 sec
Collimator: 2.4
Elektrodes: Al 99.99
Distance of electrodes: 3 mms

Table 1.

Detectability of the investigated trace elements
(in g/t)

Elements	Limit of detectability g/t	Elements	Limit of detectability g/t	Elements	Limit of detectability g/t
Ag	1	Ge	10	Sn	10
As	160	Hg	250	Sr	< 100
B	< 10	In	4	Ta	1000
Ba	< 100	Li	400	Te	60
Be	60	Mn	< 16	Ti	60
Bi	40	Mo	10	Tl	1
Cd	40	Nb	250	V	< 4
Co	< 16	Ni	< 6	W	100
Cr	< 2.5	Pb	< 6	Y	300
Cu	< 10	Sb	60	Zn	< 100
Ga	< 2.5	Sc	100	Zr	1000

The amount of Be, Bi, Cd, Ge, Hg, In, Nb, Sb, Sc, Ta, Te, Tl, W, Y, and Zr was undetectable in all the investigated samples. Since the global average of these elements is much less than the lower limit of sensitivity of our spectral analytical method, we must be content with the statement that there are no anomalously high percentages in any of the investigated samples. Ag was detected in a few samples only, and its amount never proved to be more than 6 g/t. The same refers to As (max 160 g/t), Li (max 1000 g/t), Mo (max 6 g/t) and Sn (max 25 g/t). Local enrichment of

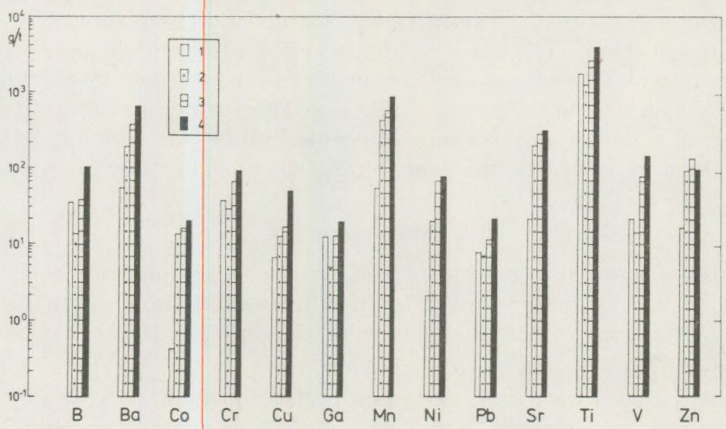

Fig. 3. Comparison of the average trace element content of Upper Oligocene sediments of the West-Cserhát area to the global averages of sandstones and clays.
1. Global average of sandstones as calculated by Turekian, K. K. and Wedepohl. K. H. (1961)
2. Average trace element content of sandy strata
3. Average trace element content of the aleuritic argillites.
4. Global average of clays according to Turekian, K. K. and Wedepohl, K. H. (1961)

the above elements may be explained by some episodic rease of the relative percentage of "granitoid" calstics in the sediment. Apart from some exceptions all the other specimens contained detectable amounts of B, Ba, Co, Cr, Cu, Ga, Mn, Ni, Pb, Sr, Ti, V, and Zn thus allowing the calculation of mean values and standard-deviations as well as closer investigation of the frequency distribution curves.

The amounts of all investigated trace elements were found to be higher in the aleuritic-argillitic strata than in the sandy formations (see Table 2.) Comparison of the means with the global averages calculated by *Turekian, K. K.* and *Wedepohl, K. H.* (1961) for the corresponding rock types shows that the mean trace element content of the W-Cserhát fine-clastics falls either between the averages of sandstones and clays of may be even less than that calculated for sandstones (see Fig. 3.) To sum up all, the general trend of the mean trace-element concentration of the Upper Oligocene fine clastics in the W-Cserhát area is fairly conformable with the global average of fine clastics as known from the literature.

Table 2.

number of specimens / elements	1		2		3	4
	122		62		25	26
	$\overline{X}$	S	$\overline{X}$	S	$\overline{X}$	$\overline{X}$
B	11.5	6.2	36.8	28.2	224.0	114.6
Ba	186.5	133.0	353.6	274.0	141.4	380.5
Co	14.2	1.5	16.7	3.8	27.2	26.2
Cr	28.0	42.0	64.3	42.0	525.2	185.4
Cu	12.2	16.0	15.3	15.0	128.4	144.2
Ga	3.9	1.9	12.6	8.9	14.9	34.8
Mn	398.0	773.0	531.2	778.0	7925.4	1173.5
Ni	18.6	12.0	57.4	44.0	35.8	161.2
Pb	6.0	3.7	11.5	7.1	168.5	233.3
Sr	180.8	214.0	282.3	246.0	200.0	336.1
Ti	1138.7	1230.0	2438.3	1596.0	9480.0	6334.6
V	12.0	10.0	69.3	67.0	62.1	271.9
Zn	91.9	16.0	122.5	57.0	181.6	216.5

Average concentration (X) and standard deviation (S) of trace elements in the sandy strata (1) and in the argillitic-aleurolites(2).
Average concentrati on in the heavy-mineral separates (3) and in the argillitic—aleuritic fractions (4)

The only difference is that the average zincum content of the W-Cserhát aleuritic-argillites (122.5 g/t) is somewhat higher than the 95 g/t figure for the global average of clays. Based on purely theoretical considerations it is quite understandable that the trace element association of any clastic sediment will not be as coherent as it is in the case of an igneous rock or a chemical sediment. Concentration and distribution of the trace ele-

ments in clastic sediments are mainly controlled by the character of the source area and by the physico-chemical environment of the accumulation including all diagenic and epigenic processes. Mineralogy and petrology of the source area are of primary importance since they are responsible for the "inherited" geochemical properties of the clastic sediment. These inherited properties are sustained to a considerable extent by the trace elements of the heavy mineral fraction.

Physico-chemical conditions of the depcsition, diagenesis and epigenesis affect mainly the trace element distribution of the clayey and carbonatic (calcite) fraction of the sediment.

Based on the above considerations trace elements of heavy mineral separates from 25 specimens and of aleuritic-argillite fractions separated from 26 specimens were analysed as shown in Table 2. The heavy mineral separates proved to be unambiguously rich in B, Co, Cr, Mn and Ti while in the clay fractions Ba, Cu, Ga, Ni, Pb, Sr, V and Zn were concentrated (Fig, 4.)

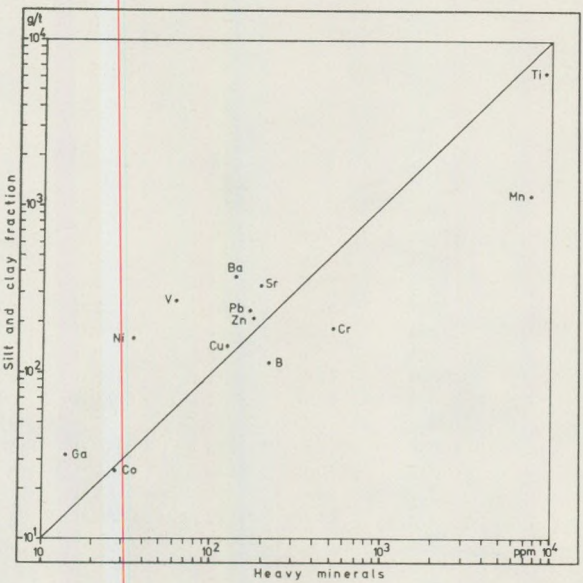

Fig. 4. Mean trace-element content of the heavy-mineral separates and the argillaceous-aleuritic fractions

Considering the mineralogy of the heavy mineral separates it is clear that B must be bound to tourmaline, Co is a probable associate of pyrite, Cr is contained in magnetite, ilmenite and chlorite, Mn in garnets and epidote and Ti in ilmenite and rutile. In other words: part of the trace elements detected in the investigated rock samples are bound to the heavy minerals either in the form of some stochiometric components or in some cases as isomorphic substituents in the lattice. Trace element distribution

of the sedimentary sequence as a whole however, seems to be determined essentially by trace elements of the clay fraction, although trace elements are bound to the clay particles by adsorption rather than stochiometrically. The fact that clays play such decisive role in the trace-element distribution of the investigated sedimentary sequence can be explained by the assumption that all allotigenic clastic particles having been accumulated together with the clay were originally poor in trace elements and that the relative percentage of clays is at least by one order of magnitude higher than that of the allotigenic heavy minerals in all the investigated rock types.

Boron: Frequency distribution of boron is unimodal and exhibits a positive skewness in sands while the curves of aleuritic-argillites are of the multi-modal type with several small maxima (See Fig 5/a). The small maximum at 6 ppm seems to be coincident with the large maximum of the curves of the sandy strata and is probably due to the aleurite-size torumaline present in this type of rocks. There are two other smaller maxima at 25 and 60 ppm which may be explained by different adsorption capacities of kaolinite and illite respectively.

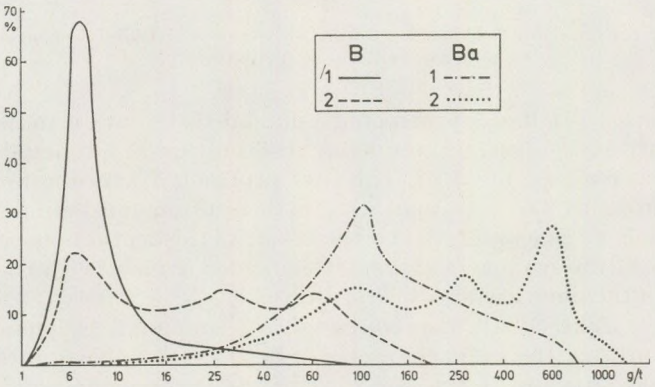

Fig. 5/a. Frequency distribution of trace-elements in the sandy (1) and in the aleuritic-argillaceous formations (2).

Barium: Frequency distribution curves of the sandy formations are unimodal, protracted and of positive skewness, while in the aleuritic argillites the distribution is unimodal and exhibits a definite negative skewness (see Fig. 5/a). The single large maximum of the sands and the small maximum of aleuritic-argillite at 100 g/t probably points to the presence of feldspar-bound Ba in both. Small maxima at 250 and 600 g/t in the aleuritic-argillites may be due to the concentration of the low ionic-potential Ba which is exceptionally apt to adsorption. The complexity of its distribution together with the relatively large standard deviation suggests, however, that its frequency may have been affected also by some remote low-temperature telethermal solution related to Middle Miocene andesite volcanism.

Cobalt: Its frequency distribution is essentially the same in sands and in aleuritic argillites (see fig 5/b). The unimodal nature of the frequency distribution curves and the low standard deviation figures suggest that a single process is responsible for the concentration. One of the plausible variants is the precipitation of ferrous sulphide (pyrite) accompanied by an enrichment in Co.

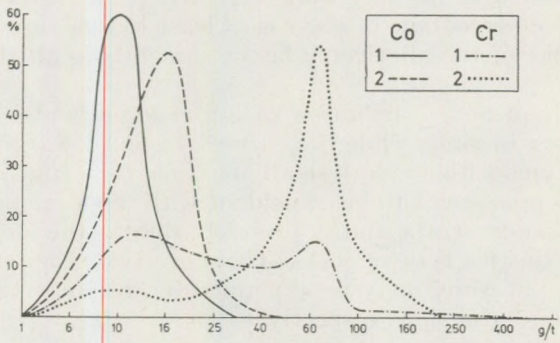

Fig. 5/b Frequency distributio of trace-elements ie the sandy (1) and in the aleuriticargillaceous formations (2).

Chromium: It has a protracted bimodal distribution ind sands while in the aleuritic argillites its frequency distribution is unimodal and of negative skewness (see Fig 5/b). The first protracted maximum observed in sands is probably the representative of heavy-mineral-bound chromium, while the second is thought to be the result of adsorption-concentration of chromium on the surface of clays. (It coincides namely with the maximum observed in the aleuritic-argillitic strata.)

Copper: Like cobalt also copper shows unimodal ferquency-distribution of essentially the same character in both sands and argillites (Fig 5/c). The unimodal nature of the curves suggests that copper is bound to the sulphide pase, but its large standard deviation points to the possibility of organogenic concentration (– local enrichment in coalified plant relics).

Gallium: Its frequency distribution is bimodal in both sands and aleuritic-argillites (see Fig. 5/c). According to the well-known affinity of Ga to hydrolisates both maxima occur at higher ppm figures in the argillites than in the sands. A plausible explanation of the biomodal-character of the distribution of Ga is that the Ga is bound to allotigenic clastic alumosilicates which came from the Vepor source area, while the rest is an associate of accessory diaspore, a product of denudation of the Upper Cretaceous bauxite deposits at Nézsa.

Manganese: Distribution curves of manganese are complex and polymodal with several maxima of various size and shape both in the sands and in the argillites (see Fig. 5/d). Part of the Mn present is undoubtedly bound to allotigenic heavy minerals like garnet and epidote, another part is concentrated within the carbonate cement, while the rest is adsorbed on

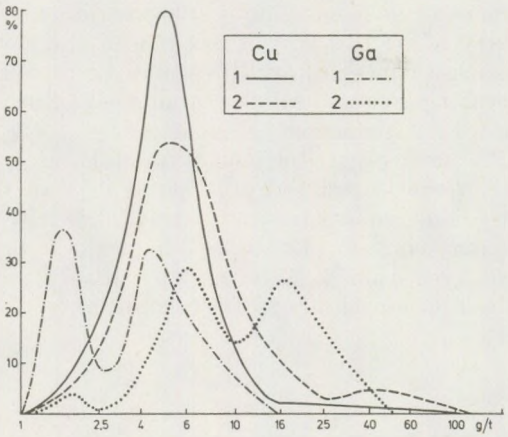

Fig. 5/c. Frequency distribution of trace-elements in the sand (1) and in the aleuriticargillaceous formations (2).

the surface of the clay particles. The polymodal character of the distribution curves and the large standard deviation suggest, however, that as in the case of Ba, also here the effect of postvolcanic activity due to Middle Miocene andesite volcanism can not be excluded either. Manganese is the only trace element in the Upper Oligocene sediments of the W-Cserhát the behaviour of which justifies further more detailed geochemical study.

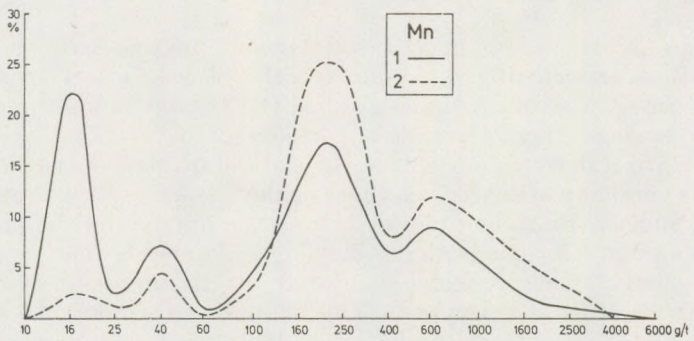

Fig. 5/d. Frequency distribution of trace-elements in the sandy (1) and in the aleuriticargillaceous formations (2).

Nickel: Frequency distribution: unimodal and of negative skewness in sands but polymodal in argillites (see Fig, 5/e). Although the behaviour of Ni and Co is thought to be similar during the sedimentary cycle, the frequency distribution of Ni is quite different from that of Co in the Upper Oligocene sediments of the W-Cserhát. None of the heavy minerals identified so far proved to be nickeliferous: they do not contain nickel, either as

the main constituent or as isomorphous substitution. Corresponding to the well-known affinity of Ni to hydrolisates one of the several peaks of the frequency distribution curves of argillites may be representative of nickel absorbed on colloidal particles. All the other peaks however, require further investigation for a satisfactory explanation.

Plumbum: Frequency distribution: unimodal and of positive skewness in the sands and of the protracted polymodal type in the argillites (Fig. 5/e). Of the clastic constituents in sandy strata it is feldspar and probably also epidote that may contain plumbum. The peaks of argillites reflect the probability of concentration of plumbum by adsorption on clays, on the one hand, and by the enrichment of Pb-containing plant debris on the other.

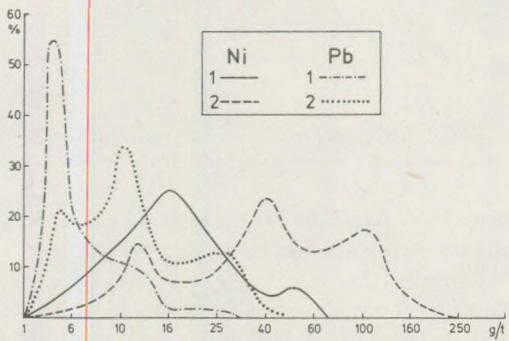

Fig. 5/e Frequency distribution of trace-elements in the sandy (1) and in the aleuriticargillaceous formations (2).

Strontium: It is of polymodal distribution with one main peak accompanied by several smaller maxima in both the sands and argillites (see Fig. 5/f). Since in all the samples studied $CaCO_3$ and Sr show a weak but definitely positive correlation, Sr is considered to be bound primarily to the carbonate (calcite) cement. The large standard deviation and the presence of several subordinated maxima on the frequency distribution curve however, suggest that the amount of Sr may not be determined by the changing amount of cement alone. It is highly probable that, Sr is accommodated partly by the K-feldspars, partly by the fragmentary carbonate (calcite) shells of fossil Pelecypods. This supposition seems to be confirmed by seven pieces of Ostraea- and Pecten-shells recovered form the Upper Oligocene sediments which proved to contain 635 g/t of Sr on the average.

Titanium: Frequency distribution — protracted bimodal in the sands and widely protracted unimodal in the argillites — and the large standard deviation suggest that the concentration of Ti has been controlled by several factors (see Fig. 5/f). Although it has its own mineral phases in the heavy mineral fraction (ilmenite and rutile) considerable amount of it is obviously associated with clay particles and comes from the main source area — the Vepor — with minor contribution from the denudation of the Nézsa bauxite deposit.

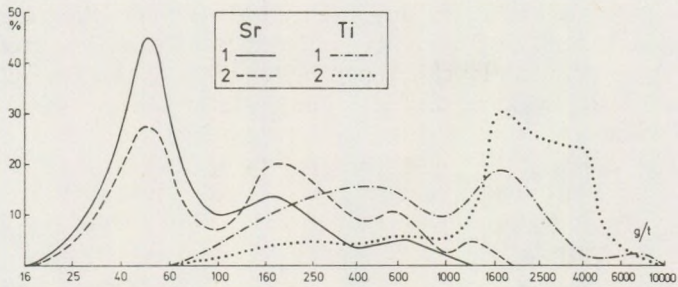

Fig. 5/f Frequency distribution of trace-elements in the sandy (1) and in the aleuriticargillaceous formations (2).

Vanadium: Its frequency distribution is represented by broad unimodal curves of positive skewness in the sands and protracted polymodal curves in argillites (see Fig. 5/g). Of the clastic minerals of sandy strata it is the Fe-Ti phases (magnetite and ilmenite) that accommodate V for the most part, but – to a lesser extent – V may also be associated with amphiboles. In the aleuritic-argillitic formations it is probably bound to the colloidal fraction and to coalified plant remnants.

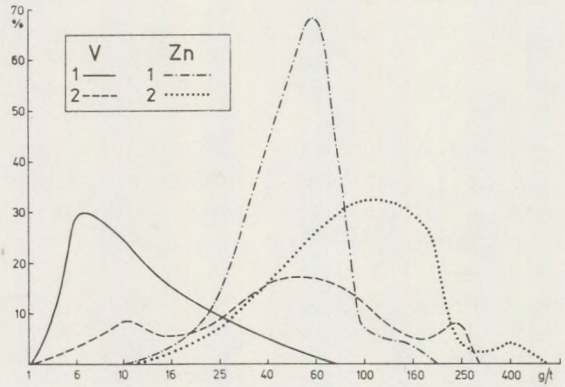

Fig. 5/g Frequency distribution of trace-elements in the sandy (1) and in the aleuriticargillaceous formations (2).

Zincum: Frequency distribution: unimodal in the sands and unimodal of positive skewness with a single widely protracted maximum in the argillites (see Fig. 5/g). It is associated probably with garnet and to a lesser extent with amphiboles in sands. The widely protracted maximum in the argillites is probably the joint result of Zn in the carbonatic matrix, in the clay fraction and in coalified plant detritus.

Geochemical facies analysis: According to *Keith, M. L.* and *Degens, E. T.* (1959) differentiation between marine-, brackish- and fresh-water sediments is possible on the basis of the ratio of B to Ga. Stratigraphical

and palaeontological evidence suggest that the Upper Oligocene sequence of the W-Cserhát is predominantly of neritic-sublitoral character containing also some brackish layers. When plotting the B and Ga figures of the aleuritic-argillitic fraction of 26 samples in the *Keith-Degens* diagram, we found 16 are of freshwater character and only the rest (10) proves to be marine (see Fig. 6.). The apparent contradiction between the stratigraphical-palaeontological and the geochemical facies, the latter based on the B : Ga ratio, may probably be due to the difference in the mineralogy of the clay fractions.

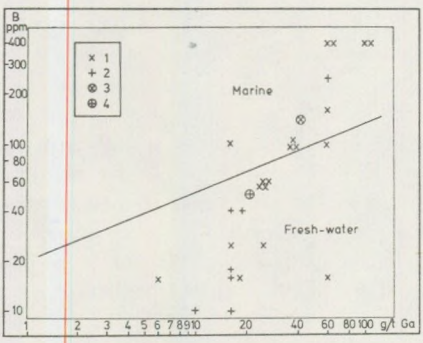

Fig. 6. B : Ga ratio in the argillaceous-aleuritic fractions 1 — of illitic compostition; 2 — of kaolinitic composition; 3 — average of all illitic fractions; 4 — average of all kaolinitic fractions

Apart from one exception, all the samples falling into the "marine" field of the diagram are namely of illitic composition while the rest of the illitic and all kaolinitic samples fall within the "fresh-water" field. That means that due to different adsorption capacities of the clays, the B : Ga ratio depend not only on the physic-chemical enviroment of sedimentation but also on the clay mineral species present. When comparing the average trace element content of the illitic and kaolinitic fractions it turns out that — corresponding to the higher adsorption capacity of illite — all trace elements tend to concentrate in the illitic rather than in the kaolinitic fraction (see Fig. 7). It must be admitted, however, that in addition to their different adsorption capacities, the different origin of the two must also be taken into consideration as a potential factor affecting trace element concentration. Kaolinites of the sandy strata were most probably deposited from a suspension originally poor in trace elements, i. e. they are of detrital origin while the illites of the aleuritic-argillitic strata were formed by reaction with the sea-water facilitated by ion-exchange processe, thus illitic clays can be considered as of diagenic origin. Based on statistical analysis *Potter, P. E.* (1963) suggested that argillaceous sediments are in 88% probabylity of marine origin if their trace element content exceeds the following limit values: 75 ppm for boron, 60 ppm for chromium, 26 g/t for copper, 18 g/t for gallium, 32 g/t for nickel and 107 g/t for vanadium.

Comparison of *Potter*'s limits with the data in the 4th column of Table 2 shows that the Upper Oligocene sedimentary sequence of the West-Cserhát is of marine character, with no signs of brakish or fresh-water members at all. It is to be pointed out, therefore, that due to the heterogenetic nature and the remarkably different adsorption capacities of clay minerals, geochemical facies analysis has not led to results in full agreement with those of stratigraphical-palaeontological investigations.

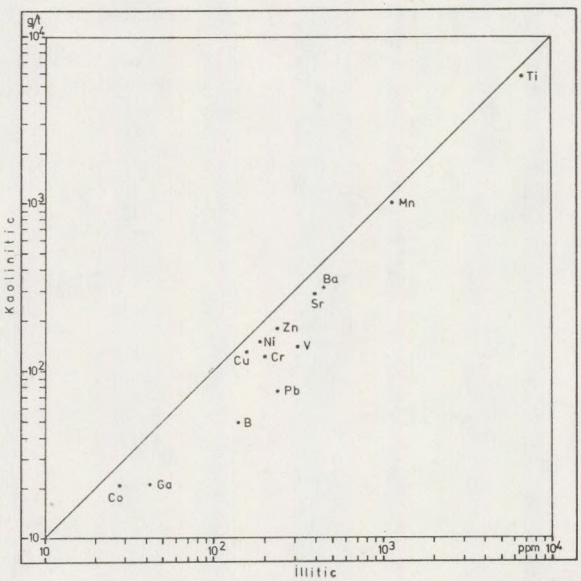

Fig. 7. Mean trace-element content of the illitic and kaolinitic fractions.

REFERENCES

Andó, J. (1973): Geochemical investigation of sedimentary rocks in the northern Cserhát hills. – Annales Univ. Sc. Bp. Rolando Eötvös Sectio Geologica XVI. pp. 3–17.

Báldi, T. (1973): Mollusc fauna of the Hungarian Upper Oligocene (Egerian). – Akadémiai Kiadó Bp. pp. 511.

Csánk, E.-né (1969): A Dorogi-medence oligocén képződményei-ásvány-kőzettani vizsgálata. – MÁFI Évi Jelentése 1967 évről pp. 83–133.

Keith, M. L.–Degens, E. T. (1959): Geochemical indicators of marine and fresh-water sediments. (In: Researches in Geochemistry. pp. 38–61. Editor P. H. Abelson). John Wiley Ed., New York.

Koch, A. (1877): A dunai trachytcsoport jobbparti részének földtani leírása. (MTA. Math. és Term. Tud. Oszt. Kiadása Bp. p. 298.

Nagyné, Balogh J. (1971): Vorrichtung zur halbquantitativen Auswertung von Emissionsspektren. – Spectrochimica Acta 268. pp. 609–611.

Nemecz, E. (1973): Clay minerals. Akadémiai Kiadó Bp. p. 507 (in hungarian)

Noszky, J. (1940): Geology of the Cserhát Mts. (in: Geology of Major Geogr. Units of Hungary. Hung. Geol. Inst). p. 283 (in hungarian)

Pécsiné, Donáth É. (1973): Geochemical investigations of sedimentary rocks from the vicinity of Felsőpetény. – Annales Univ. Sc. Bp. R. Eötvös Sectio Geologica XVI. pp. 157–185.

Potter, P. E.–Shimp, N. F.–Witters, J. (1963): Trace elements in marine and fresh-water argillaceous sediments. – Geochimica et Cosmochimica Acta 27. pp. 669–694.

Örkényiné, Bondor, L. (1969): The allothigenic minerals of a glauconotic sandstone sequence in the vicinity of Salgótarján. – Ann. Mus. Nat. Hung. 61. pp. 45–61.

Rózsavölgyi, J. (1973): Petrographical and geochemical investigations of the Mesozoic on the left bank of the Danube. – Annales Univ. Sc. Bp. R. Eötvös Sectio Geologica XVI. pp. 197–206.

Turekian, K. K.–Wedepohl, K H. (1961): Distribution of the elements in some major units of the Eart's crust. – Bull. Geol. Soc. America 72. pp. 175–192.

THE GENESIS OF GARNETS IN THE ANDESITES OF THE KARANCS-HILL

SZABÓ CS. – NAGY B.-NÉ – G. SOLYMOS K.

Petrological – Geochemical Department Eötvös Loránd University
H – 1088 Budapest, Múzeum krt. 4/A

Received: at 15th May 1980.

SUMMARY

Neither the contact effects of the neighbouring sediments, nor the contamination of the basement xenoliths provide acceptable explanation of the existence of garnets in the hornblende andesite of the Karancs-hill.

The garnet is a common constituent of the andesites in the early phase of crystallization, at higher pt conditions. However, it may become unstable with decreasing pressure and temperature in the uprising igneous melt.

The zonation of the garnet crystals is rather due to their inclusion content than compositional changes. The chemical composition of the garnet is either unchanged or gained equilibrium during crystallization.

Introduction

Two alternative ideas are known about the genesis of the garnets in the hornblende andesites of the Karancs-hill. The first one suggests that the ascending magma have assimilated the argillaceous, micaceous sediments along its path, thus its Al-content increased, and almandine garnet has formed on (or near to) its contact. The alternative explanation relates the garnets to the partially or completely contaminated basement xenoliths, which contain plagioclase and hornblende, suggesting, that the reactions between the neutral magma and the xenoliths were responsible for the development of garnets.

The subvolcanic hornblende andesite of Miocene Badenian age is exposed in several quarries in the area. Most of the garnet samples were collected in the Bobonyér quarry, where the contact of the andesite and the sedimentary "slir" formation is also exposed. Samples were also collected from the Sátoros and Farkaskő quarries. In the former location basement xenoliths are abundant, while in the latter one the central parts of the intrusive laccolith are exposed.

Field observations

In the Bobonyér quarry the "slir" sediments have been altered to compact, hard contactised rocks on the selvage of the laccolith.

The andesite has become a reddish-greenish, pyritic variety along this contact. The contact zone is 20–50 cm thick. The 2–15 mm large garnets are the only visible phenocrysts among the primary constituents of the andesite in this zone. The garnet grains generally have a deep red lustrous core, surrounded by a white-red mottled outer zone with indefinite contours. Euhedral grains have been abundantly released from the weathered andesite. The surface of these grains are uneven and the grains themselves frequently fall into pieces.

Away from the chilled margin, and in the Farkaskő quarry the andesite is more brittle and dark coloured, with plagioclase and hornblende phenocrysts along with the garnets.

The central core occurs only in a part of the grains, its appearence and size is independent from the size of the garnet grains. There are crystals composed exclusively from the darker or the lighter "varieties". The abundance of garnets, as well as the occurence of these varieties are not related to the distance from the contact zone. Similar observations were made in the Sátoros quarry, except that the basement xenoliths (amphibolites, quartzites, gneisses) were not surrounded by garnetiferous rims (Photo 1). These field data indicate that the origin of the garnets is not connected with the contaminated sediments or basement xenoliths.

Microscopic studies

During this work the attention was focussed on the differences between the cores and the outer zones of the garnet grains, the relationships of the garnets with their environment, and the distance from the contact zone.

There were no significant optical differences between the macroscopic darker cores and outer zones of the garnets. However, the type of inclusions in these two zones are completely different. Short prismatic, and needle-shaped apatite, euhedral magnetite and occassional sphene were observed in the less fractured inner cores (Photo 2). Mainly plagioclase was found in the outer zones, though prismatic apatite, magnetite (and sphene) have also occured. Both the garnet – and the andesite as a whole – is characterised by the abundance of the magnetite (and sphene) – apatite assemblage. The sphene is an alteration product of the Ti-rich magnetite or titanomagnetite. It is associated with calcite, which is either interstitial, or surrounds the sphene grains. Among the inclusions of the garnet only the sphene indicates correlation with the distance from the contact zone, being much – more abundant near the contact than in the fresh andesite.

The plagioclase does not comprise a continous inclusion – rich zone in the outer rims of the garnets, but it generally subdivides this outer zone into two or three distinct-concentric bands (Photo 3). The size of the plagioclase inclusion vary between 0.5–0.05 mm, the grains are mainly subhedral or anhedral, with erratic contours. The plagioclase crystals are frequently zoned and twinned, with average An content of 52–63 percent (measured by symmetric extinction angle method). *Nemecz* (1944) has studied the

plagioclase phenocrysts of these rocks and measured 60 – 65% An in the central, 53 – 54% An in the middle and 41 – 44% An in the outer zones. The existence of the plagioclase phenocrysts in the outer zone, and their lack in the central cores indicate that the formation of the garnet had preceded that of the plagioclase, and similarly, the crystallization of garnet had been completed earlier than that of the plagioclases. The plagioclase in the different inclusion rich zones are similar in composition and no change has been encountered with the distance from the contact zone.

The alterations in the phenocrystal and inclusion forming types of the plagioclase are similar. The dominant calcitisation is associated by argillitisation and sericitisation. The type of alteration does not depend seemingly on the distance from the contact, though its intensity increases towards the contact zone.

It can be suggested therefore, that the zonal colouration of the garnets is caused by the change in the amount and character of the inclusion content. These features have been tested by Micro-Videomat image analyser (Table 1).

Table 1.

The average inclusion content of garnets from the hornblende andesite of the Karancs-hill (in volume percents)

Magnetite + sphene	2 – 3
Plagioclase, apatite, calcite	12 – 14

The average inclusion content of the core and outer zones of garnets (in volume percent)

	Plagioclase	Apatite	Magnetite + sphene
Outer zones	15,0	0,2	1,6
Cores	1,1	1,0	2,6

The garnets are frequently surrounded by plagioclase-rich rims (Photo 4), associated by calcite, magnetite, sphene and apatite. The plagioclase generally occurs in uncomplete crystals interlocking with the garnet. In this zone the abundance of euhedral magnetite and prismatic apatite is similar to that found in garnets, but the anhedral magnetite locally shows enrichments. The hornblende, or its altered remnants are rare in this zone, but irregularly shaped garnet fragments were observed (Photo 5). It is possible, that the plagioclase, calcite and anhedral magnetite, which surrounds the garnet, are products of partial resorption, and the garnet fragments occur as remnants after this alteration. The plagioclase-rich zones of the garnets certainly indicate changes in the crystallization of the garnet (and the magma). This phenomenon is probably associated with the asvending migration of the magma, therefore decreasing pt conditions. The new conditions had stopped the further growth of garnets until temperature rise with further supply of igneous melt or pressure increase due to release of volatiles had not occured.

Microscopic evidences indicate contemporaneous crystallization of garnet, apatite and magnetite in the early stages of solidification. The outer zones have formed along with the crystallization of the plagioclases. According to the inclusions of the garnet the following sequence of crystallization can be suggested: apatite + magnetite + garnet-core → outer zones of garnets + basic plagioclase → more acidic plagioclase → quartz → calcite. This sequence coincides with the observations of *Nemecz* (1944) who placed the hornblende between the garnet and the plagioclase.

Geochemical studies

Árkai (1975) has shown that the metamorphic garnets retain their non-equilibrium character owing to their crystal structure and small ionic diffusion rate. It can be suggested, that the magmatic garnets, having similar features, reflect the changes of the composition of the parent melt during crystallization.

Several samples of garnets were analysed by AAS and thermometric method, giving results shown on Table 2.

The average chemical coposition of the garnets from the Bobonyér quarry (in weight percent):

SiO_2	40.25
TiO_2	0.50
Al_2O_3	21.00
Fe_2O_3	5.50
FeO	20.00
MnO	0.50
MgO	3.58
CaO	7.25
Na_2O	1.00
Total:	99.58

Analysed by L. *Hoffmann*

Though the chemical composition is influenced by the inclusions, the data indicate essentially almandine composition, with a small shift towards the pyrope – grossularite range.

The distribution of the main components of the garnets (Fe, Ca, Mg, Al, Si, Mn, Ti) and the chromium were determined by microprobe, with linear scanning. Three garnet samples were selected. Two crystals had a definite core, the smaller one was collected close to the contact zone, while the larger one at a greater distance from the contact. The third, coreless sample was collected from the least altered intrusive rock. The linear scanning intersected the centre of the crystals and crossed the boundaries of the particular grains. These analyses have shown, that except for the inclusions, the main chemical components are uniformly distributed. In one sample the Mn content decreased at the edge of the outer zone.

A larger garnet, which had a central core, was investigated along with its vicinity, by laser- microspectral analysis, with results shown in Fig. 1. The analysis gave higher Mn, Fe, Mg, Si values, lower Ti, Ca values for the garnet than for the andesite. The Al has shown variable distribution. More Ti, Si, less Mn, Ca, Al content, variable amounts of Mg and Fe were recorded in the core as compared to the outer zones. By statistic estimations, the standard deviations indicate that the average Si, Al, Mg, Fe contents in the core and the outer zones are similar, with 95% probability level. The Ti content is roughly on the limit, while the Mn content is less in the core, with 99% probability. Homogenous distribution of Ti and Si was recorded in the core, while that of the Al, Mg, Fe and Mn in the outer zone. The Mg and Fe, and to a less extent the Mn have shown similar variation trends.

The two micro-analyes gave similar results with the exception of the manganese, therefore the distribution of the main elements in the garnet can be considered as homogenous.

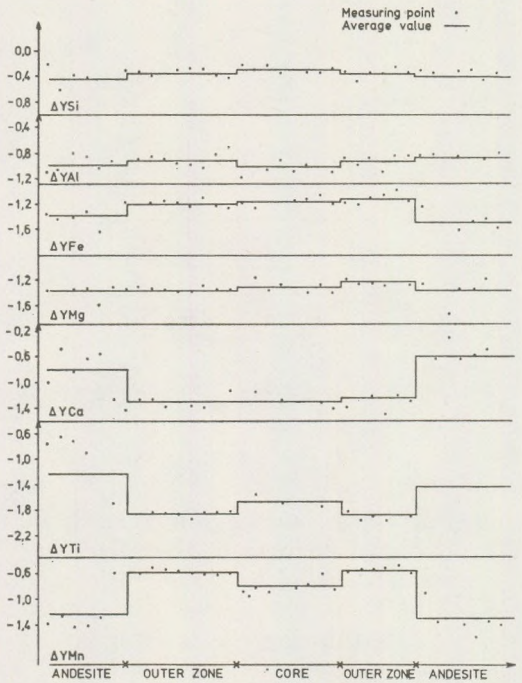

Fig. 1. Laser microspectral analysis data from linear scanning analyses on garnets and the neighbouring andesite material in the andesite from Karancs (Bobonyér quarry). The values on the vertical axis are proportional with the concentration of each given element. Spacing between measuring point 150 μm.

Separated garnet cores, outer zones and garnet-free andesites were analysed by emission spectrometry. The results are summarised in Fig. 2. These data have shown, that the cores and the outer zones of the garnets are virtually identical in their trace element content. A slight enrichment of Cr, Cu, B, Zn was found in the garnet compared to the host andesite. The amounts of Co and Ni were roughly similar. The lithophile Ba and Sr, and the pegmatophile V and Ga were concentrated in the surrounding andesite. The early crystallization of the garnet is evidenced by the higher amounts of the calcophile and siderophile Cu, Cr and Zn. The high boron content of the andesite (compared to the average of the intermediate igneous rocks) can be explained by possible precrystallization effects of sedimentary or low grade metamorphic country rocks in greater depths.

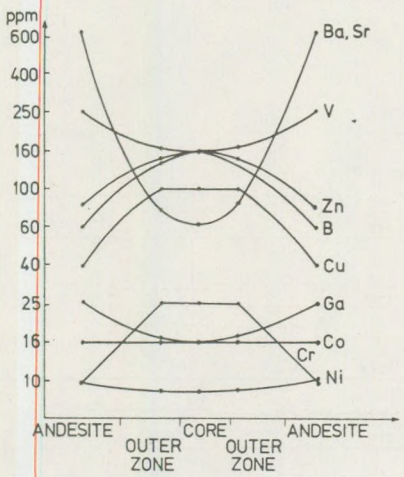

Fig. 2. Trace element distribution of the garnet and the andesite (Karancs, Bobonyér quarry).

The geochemical investigations have indicated, that the garnets do not reflect the compositional changes of the ascending magma. The zonality of the garnets is solely caused by the inclusion content and not differences in chemical composition. It is possible that the composition of the garnets remained unchanged during the later stages of solidification. Alternatively, the garnets could repeatedly restore equilibrium compositions during the long period of crystallization, by resorption, ionic diffusion, or alternation to plagioclase, calcite, magnetite. These questions would need further studies in the whole mountain, as well as in the garnetiferous igneous rocks in the Carpatians.

PLATE I.

1. An inclusion from the garnetiferous hornblede-andesite in the Sátoros quarry at Karancs-hill.

PLATE II.

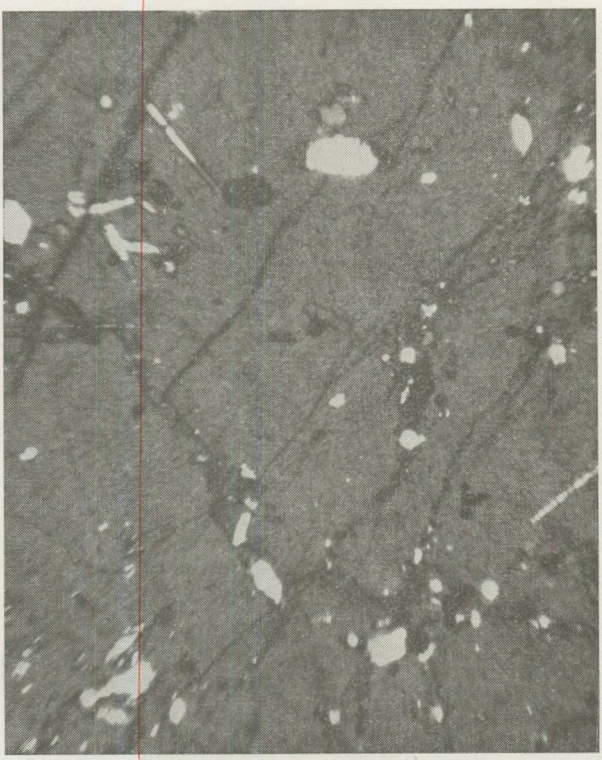

2. Inclusions of apatite and magnetite in the core of a garnet, (hornblende-andesite, Karancs, Bobonyér quarry), +N, 62,5 x.

PLATE III.

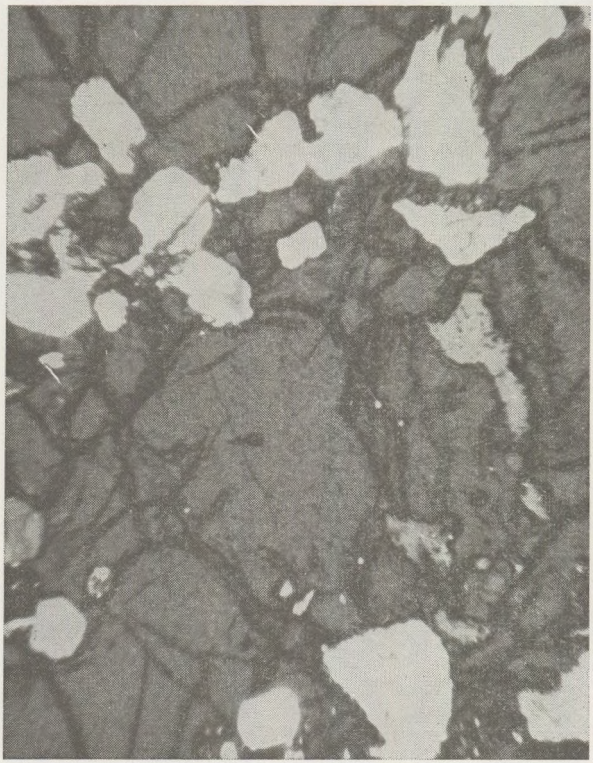

3. Plagioclase inclusion in the outer zone of garnet (hornblende andesite, Karancs, Bobony quarry) +N, 62,5x.

PLATE IV.

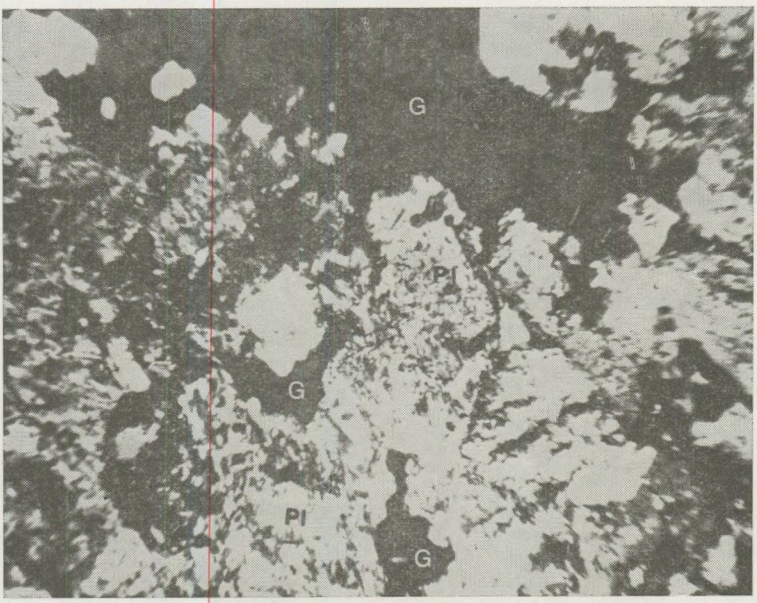

4. Plagioclase rim around garnet (hornblende andesite, Karancs, Bobonyér quarry) + N, 62,5x.

PLATE V.

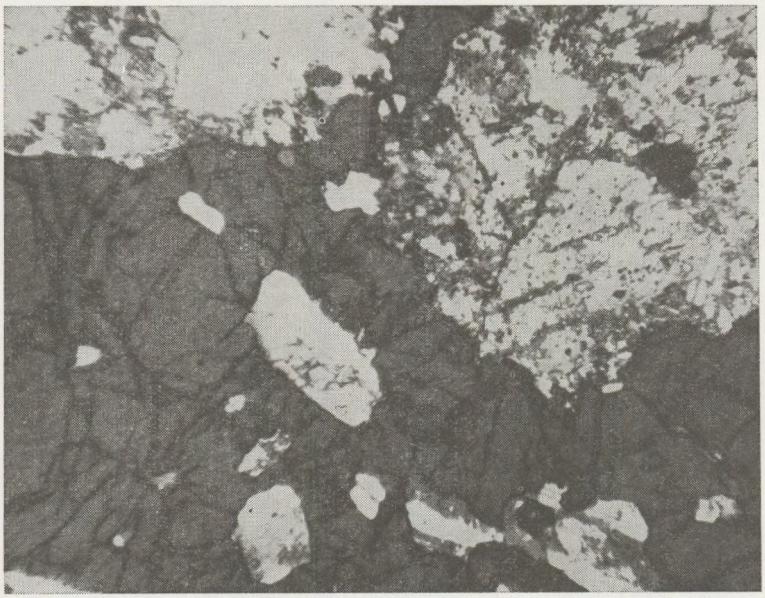

5. Garnet "fragment" from the plagioclase zone surrounding a garnet grain (hornblende andesite, Karancs, Bobonyér quarry), + N, Magnifcation: 62,5 x.

REFERENCES

Árkai P.–Nagy G.–Pantó Gy. (1975): A ciklusos folyamatok szuperpozíciója (polimetamorfózis) és azok ásványtani kimutatása. MTA X. Oszt. Közl. 8/3–4. p. 383

Árkai P.–Nagy G.–Pantó Gy. (1976): Összetétel-zónásság típusai polimetamorf kőzetek gránátjában. Manuscript.

Erdélyi J. (1942): A sátorosi andezitbánya hidrotermális ásványai. Föld. Közl. 72. p. 192.

Hermann M. (1953): A magmás kőzetek szövetének mennyiségi értelmezése. Föld. Közl. 83. p. 129.

Kárpáti F. (1972): Összefoglaló földtani jelentés és készletszámítás a karancs-hegyi andezitkutatás területéről. Manuscript.

Korpás L.–Peregi Zs.–Szendrei G. (1967): A Dunazug-hegység északi részének kőzettani és földtani vizsgálata. Föld. Közl. 97. p. 211.

Kubovics I.–Pantó Gy. (1970): Vulkanológiai vizsgálatok a Mátrában és a Börzsönyben. Budapest. Mátra hegység (1975) MÁFI Évkönyve LVII. Magyarázó Magyarország 200 000-es földtani térképsorozatához. Salgótarján (1965).

Nemecz E. (1944): A Karancs-hegységi andezit kőzettani vizsgálata. D. Sc. Thesis.

Noszky J. (1915): A Mátrától északra levő dombos vidék földtani viszonyai. Évi jel. p. 364.

Noszky J. (1919):A Cserhát északi részének földtani viszonyai. Évi jel. p. 342.

Noszky J.—Hermann M.—Nemesné Varga S. (1952): A kelet-nógrádi andezitek vulkanológiája és földtani viszonyai. Föld. Közl. 82. p. 8.
Ódor L. (1961): A Karancs-hegység földtani, kőzettani viszonyai. Thesis.
H. Rössler und H. Lauge (1975): Geochemische tabellen Leipzig.
Schafarzik F. (1889): Trachytaink néhány ritkább zárványairól. Föld. Közl. 19. p. 406.
Scholtz M. (1917): A Karancs-hegység andezitjei. Föld. Közl. 47. p. 224.
Szabó J. (1871): A trachitok makrográfiai osztályozása. Föld. Közl. 11.
Szádeczky-Kardoss E. (1955): Geokémia. Budapest.
Szádeczky-Kardoss E. (1958): A vulkáni hegység kutatásának néhány alapkérdéséről. Föld. Közl. 88. p. 171.
Vadász E. (1960): Magyarország Földtana. Budapest.

DEPENDENCE OF PROTON SIGNAL IN PROTON MAGNETOMETERS AND NUCLEAR MAGNETISM WELL LOGGING INSTRUMENTS ON ELIMINATION RATE OF POLARIZING FIELD

by

SZEMERÉDY P.

Geophysics Department, L. Eötvös University Budapest, VIII. Kun Béla tér 2.
Received: 2. June 1981.

Introduction

As well known, the operation of proton magnetometers as well as nuclear magnetism well logging (NML) instruments assumes three basic phases. At first, a strong magnetic field is established in a suitable hydrogen-containing fluid in order to polarize the greatest amount of protons along the resultant of this field and the earth's field. The polarizing field is produced by an electric current flowing through a coil of wire. After the polarizing field has been applied long enough to developed adequate polarization, it is rapidly removed by switching off the polarizing current, leaving the polarization to precess around the earth's field. In the third phase, the precessing polarization induces a damped sinusoidal emf., called proton signal, in the same coil previously used to establish the polarizing field. (In fact, usually the second phase involves two steps. At first the high polarizing field strength, applied to induce a sufficiently strong polarization in the material, is reduced to a lower value. Only this low field is removed so rapidly that it trigger the precession. However, in the subsequent discussion the step of reducing the polarizing field to a lower value, for the sake of simplicity, will be disregarded and the precession of the polarization attributed to the abrupt elminiation of the same field used to establish the polarization.)

The proton magnetometers serve to measure the frequency of the proton signal, and the NML instruments to determine its initial amplitude. The induced signal in the coil is expressible as [1], [2]:

$$U = -\frac{\omega_0}{I_p} \cdot \int \overline{H}_p \cdot \dot{\overline{M}}\, dv \tag{1}$$

where ω_0 is the angular frequency of precession. $\overline{H}_p$ and I_p are the polarizing magnetic field and the current procuding it, respectively. $\overline{M}$ denotes the nuclear magnetic polarization precessing in the earth's field. The volume integration must be performed over the volume containing the polarized fluid, which, for the sake of simplicity, will be referred to as the proton sample. The expression above involves, explicity or implicity, the polar-

izing field intensity and geometry compared to those of the earth's field, as well as the characteristics of the proton sample.

In this paper special attention will be paid to the process taking place in the second phase of measurement during which the polarizing field is being eliminated. Especially, the question of how the precession of the polarization depends on the way of removing the polarizing field in the third phase will be considered. The removal of polarizing field in the second phase and the motion the polarization performs at this time will be referred to as the field removal (f. r.) process.

Significance of the f. r. process

In the theory of both proton magnetometers and NML instruments the f. r. process is considered as extremely rapid, that is, as non-adiabatic. Within the short time interval of such a process the polarization has no time to make a displacement. Thus, as shown in Fig. 1., the initial angle between the earth's field and the polarization remains unchanged resulting in the same angle, ε, of the free precession. It is the non-adiabatic process that is considered most efficient in transforming the polarization, established in the first phase, into a precessing polarization for the third phase. This demand involves using a coil with negligible self-inductance which, however, for technical reasons, is in contradiction with the most favourable conditions of the polarizing phase. Namely, a polarizing field of sufficiently high intensity can only be realized by means of a coil having a considerable self-inductance. Consequently, the available signal-to-noise ratio of the proton signal is basically determined by the correct balance of two inconsistent factors, in particular, that of the polarizing field strength and the rapidity of the f. r. process.

When the f. r. process is slower than non-adiabatic, its course takes a finite amount of time. Thus, the free precession in the earth's field begins later than it would after the non-adiabatic case. In the meantime the polarization performs a displacement characteristic of the magnitude, shape and duration of the current transient appearing in the coil when the polarizing field is reduced to zero. In addition, the particular dis-

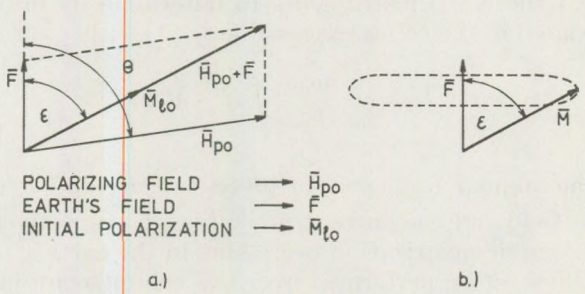

Fig. 1.

placement also depends on the initial condition of the motion. Obviously, this circumstance affects the angle of precession too, by making the relationship between the initial angle ε and the angle of precession more complex than in the case demonstrated in Fig 1. a and b. Also, the displacement and the delayed beginning of the free precession combine to cause a specific change in the phase angle of the precessional motion in comparison with the motion triggered by a very abrupt f. r. transient. In the adiabatic case, that is if the removal of the polarizing field is extremely slow, the polarization is able to follow the direction of the changing resultant field without a detectable precession.

Between the two extreme cases (adiabatic and non-adiabatic) there is the family of the polytropic processes having characteristic times comparable with the precessional period in the earth's field, the matter of the present interest. To demonstrate the situation, Fig. 2. shows two trajectory projections of the motions of a constant-magnitude polarization vector. Here, the earth's field points upwards along with the z coordinate axis. The polarizing field, in the $x-z$ plane, is chosen to be ten times stronger than, and to make an angle of $+135°$ with, the earth's field. The outermost dashed line is a trajectory projection of the motion belonging to a particular polytropic process. The motion takes place in an exponentially decaying polarizing field whose decay constant is identical with the precessional ferquency, ω_0, in the earth's field. The next soild line refers to the non-adiabatic variant of the motion performed by the same polarization vector. This trajectory projection corresponds to a circle, because the polarization starts precessing in the earth's field immediately from the $x-z$ plane after the infinitesimally short f. r. process at $t = 0$. The radius of the circle is equal to the magnitude of the polarization vector times sin ε where ε is the initial angle with the same meaning as shown in Fig. 1a. With diminishing polarizing field the polytropic trajectory also approximates a circle whose radius, however, differs from that of the previous case.

At a selected point of time t, also are indicated in Fig. 2. the phase angles of the motions and denoted as τ and τ' for the non-adiabatic and polytropic processes, respectively. As can be seen, there is a phase shift between the two motions. In particular, the polarization component B, belonging to gradually decaying polarization field, lags behind A revolving after the non-adiabatic f. r. transient and having a phase angle of $\tau = \omega_0 t$. Obviously, with the progress of time, also the phase lag, $\Delta\tau$, tends to be a constant value, which, in the present example, is about 145°.

Both the phase lag and the phase angle of precession are independent of the magnitude of the polarization. For this very reason, it is convenient to study their values by considering the motions of the unit polarization. In this case, the initial condition can be defined unambiguously by specifying the angle, Θ, between the earth's field, $\overline{F}$, and the polarizing field, $\overline{H}_p$, and, by prescribing the relative intensity, $K = H_p/F$, of the polarizing field. Thus, the stationary phase lag and trajectory radius have the general forms of $fp(\Theta, K, f(q))$ and $fr(\Theta, K, f(q))$, respectively, where the

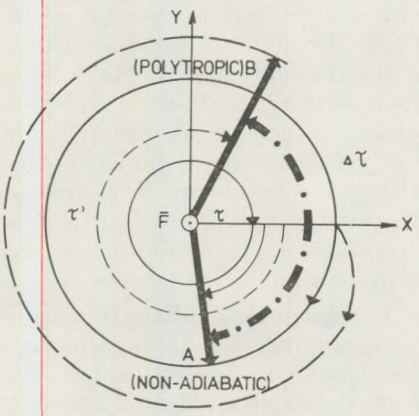

Fig. 2.

former may be defined as $fp(\Theta, K, f(q)) = \lim\tau \to \infty \Delta\tau(\tau, \Theta, K, f(q)) = \lim\tau \to \infty [\tau - \tau(\tau, \Theta, K, f(q))]$. In these expressions the polarizing field decay rate is assumed to be desribed by a single quantity q which must be defined on the basis of some reasonable convention. In the arguments, instead of q, the notation $f(q)$ is used. It is intended to emphasize that the selection of q depends on the actual form of the particular transient function. In the preceding example, this is an exponential function with a real argument: $\exp(-\alpha t)$. In this case, as it will be pointed out in the subsequent discussion, the most convenient selection is $q = \alpha/\omega_0$.

As has been referred to, the theoretical considerations on the magnitude of proton signal, for both proton magnetometers and NML devices, are based on the assuption that the f. r. process is perfectly non-adiabatic. In this case, the proton signal amplitude is obtained to be proportional to $\sin \varepsilon \cdot \sin \Theta$, which, however, due to the great polarizing field strength, is almos perfectly equal to $\sin^2\Theta$. Since the f. r. process realized in instruments fail to be exactly non-adiabatic, smaller or greater deviations from the ideal $\sin^2\Theta$ characteristic can be experienced.

On the usual coil and sample geometry of proton magnetometers the polarizing field may be fairly well approximated with a homogeneous magnetic field. Thus, the functions fp and fr have nearly the same individual values within the whole sample volume, and also their dependence upon Θ are homogeneous. Obviously, the approximately homogeneous phase shift, described by the fp function, means an almost perfect phase coherency of the emf. contributions induced on the coil by the polarization precessing at any place of the sample volume. Under such condition the behaviour of the fp function does not affect the signal amplitude. In case of proton magnetometers, the consequences of the polytropic f. r. processes have been studied by Bullard et al. both experientally and theoretically [3].

As a matter of fact, practical consequences of the phenomena occuring in the polytropic region are totally negligible in geomagnetic prospecting. On the one hand, proton magnetometers with nearly perfect $\sin^2\Theta$ characteristic can be built without any difficulty. On the other hand the deviations from the theoretical characteristic has no effect on the signal frequency. The only precondition to correct operation of the proton magnetometers is that a proton signal with sufficiently high signal-to-noise ratio be available for the frequency measurement. To meet this requirement poses no major problem due to the favourable coil and sample geometry.

The problem of signal-to-noise ratio is much more crucial in case of NML measurements where the signal amplitude is the quantity of interest. Thus, it is not indifferent any longer that the f.r process is actually takes place in the polytropic region. The coil is situated in the hole and the sample around it in the formation which inevitably involves a very inhomogeneous polarizing field. This fact causes place dependent *fp* phase shifts in the sample, adversely affecting the phase coherency and, in this way, the signal amplitude as well.

There have been theoretical considerations for the signal amplitude supplied by NML hole devices, but they concern only the non-adiabatic case, [1], [2], [4], [5], [6], [7]. Based on the above reasoning, the author believes that the extension of these investigations to the polytropic case would be of very profitable, at least for two reasons. At first, such an approach may help to improve the very poor signal-to-noise ratio of the proton signal in the NML devices, by offering a more precise designing method. Secondly, the knowledge of the relationship between the f. r. transients and the corresponding signal amplitudes raises the possibility to develop a new variant of the NML method. In particular, the knowledge of this relationship enables to study the spatial distributions of free fluid phases at the vicinity of the borehole in the invaded zone.

This possibility is inherent in Eq. 1. The magnetic moment of a volume element, dv, in the formation is proportional to the local free content, $\sigma(\bar{r})$, where $\bar{r}$ is the position vector of dv. By using the distribution function $\sigma(\bar{r})$ and by indicating only the most relevant parameters explicitly in Eq. 1. we obtain an expression of the following form:

$$U(t;\, q) = \int \sigma(\bar{r})\, G(t, \bar{r};\, q)\, dv \tag{2}$$

where the integration must be performed over the formation. Hence, the signal amplitude measured by the instrument at a fixed polarizing-field decay rate q, may be written as

$$U_0(t;\, q) = \sqrt{[\int \sigma(\bar{r})\, S(\bar{r},\, t;\, q)\, dv]^2 + [\int \sigma(\bar{r})\, C(\bar{r},\, t;\, q)\, dv]^2} \tag{3}$$

Here, the functions S and C are identical with the G function taken at a suitable point of time t and at $t+\pi/2\omega_0$, respectively.

If, at a given time t, U_0 is measured as a function of q and the functions S and C are computed for the same moment and q values, Eq. 3. provides a non-linear integral equaton for $\sigma(\bar{r})$ without an unambiguous solution. However, imposing certain realistic simplifying conditions upon the magnetic-field geometry, the tool position in the hole and on the group of the acceptable distribution functions, the correct approximate solution of the problem can be obtained numerically. The conceptual possibility of establishing the radial free fluid distribution profiles around the boreholes, by means of the suggested method, has been checked by computer simulation. The measurement of the signal amplitude as a function of q was

simulated by the computation of the $U_0(q)$ function on the basis of Eq. 3. using a theoretical $\sigma(\bar{r})$ profile. Subsequently, by solving Eq. 3. with the computed $U_0(q)$ values the original $\sigma(\bar{r})$ profile could be reproduced. This experiment has been succesfully carried out with several "smooth enough" theoretical $\sigma(\bar{r})$ profiles.

The applicability of the delineated method in well logging may be questionable due to random noises which in NML works pose a major problem. However, this difficulty seems to be reconcilable by means of statistical methods [8.], [9]. A more detailed report on this study will be published elsewhere.

Determination of the functions *fp* and *fr*

For the present treatment, the nuclear magnetic polarization may be considered as a gyroscope having an angular moment $\overline{M}/\gamma$, where γ is the gyromagnetic ratio of the proton. In the course of an f. r. process the motion of polarization obeys the equation as follows:

$$\dot{\overline{M}}(t) = \gamma\, \overline{M}(t) \cdot [\overline{F} + \varphi(t;\, \alpha)\, \overline{H}_p] \tag{4}$$

where $\overline{F}$ and $\overline{H}_p$ are the earth's field and the static polarizing field, respectively. The function $\varphi(t;\, \alpha)$ serves to describe the transient when the polarizing field is decaying. α is a suitable parameter to characterize the polarizing-field decay rate. The polytropic or non-adiabatic nature of an f. r. process is primarily determined by the ratio of time necessary for the collaption of the polarizing field to the precessional period in the earth's field. For this very reason, it is convenient to use the substitution of $\tau = \omega_0 t$ in Eq. 4. resulting in

$$\overline{M}'(\tau) = \overline{M}(\tau)\, x[\overline{F}_0 + \Phi(\tau; q)\, K\, \overline{H}_0] \tag{5}$$

where $\overline{F}_0$ and $\overline{H}_0$ are unit vectors in the directions of the earth's field and the polarizing field, respectively. $K = H_p/F$ is the polarizing field intensity expressed in terms of that of the earth's field. The polarizing field decay constant is also given as the relative quantity q, whose actual form depends on the function $\varphi(t;\, \alpha)$.

In order to establish a particular pair of the *fp* and *fr* values the corresponding asymptotical solution of Eq. 5. should be known, with the initial condition that the unit polarization is paralel to the $\overline{F}_0 + K\overline{H}_0$ vector at $\tau = 0$. Unfortunately there is no general analytical solution for the type of the differential equation shown. Neither proved the usual numerical methods suitable for evaluating a great amount of asymptotical solutions belonging to a given transient function $\Phi(\tau;\, q)$.

With respect to the different technical realizations in the instrument, a mass of the possible transient functions ought to be considered. Amongst them the simplest one is the exponential function. With this selection Eq. 5. becomes

$$\overline{M}'(\tau) = \overline{M}(\tau) \cdot [\overline{F}_0 + K\, \overline{H}_0\, e^{-q\tau}] \tag{6}$$

where $q = \alpha/\omega_0$ which is obtained from $\varphi(t;\, \alpha) = \exp(-\alpha t)$ by the substitution of $\tau = \omega_0 t$. The asymptotical solutions of Eq. 6. for different q and K

values and various angles Θ between $\overline{F_0}$ and $\overline{H_0}$, have been determined by means of an iteration procedure. The procedure is based on the Taylor's expansion of the functions $M(\tau)$ and $\exp(-q\tau)$, in the differential equation system. From each asymptotical solution the corresponding fp and fr values can be immediately computed.

In the present method used to obtain the asymptotical solutions the iteration follows the trajectory of motion. Therefore, a more efficient procedure is expected to be developed on the basis of going immediately towards the asymptotical solution. The derivation of the method is in progress [10].

The function fr obtained from Eq. 6. is demonstrated in Fig. 3. for real q values with $K = 100$ at several angles Θ. In the special case of $\Theta = 90°$ and $K \gg 1$, corresponding to the solid-line curve, a very simple expression can be deduced by means of quantum mechanics, whose details are given in the appendix.

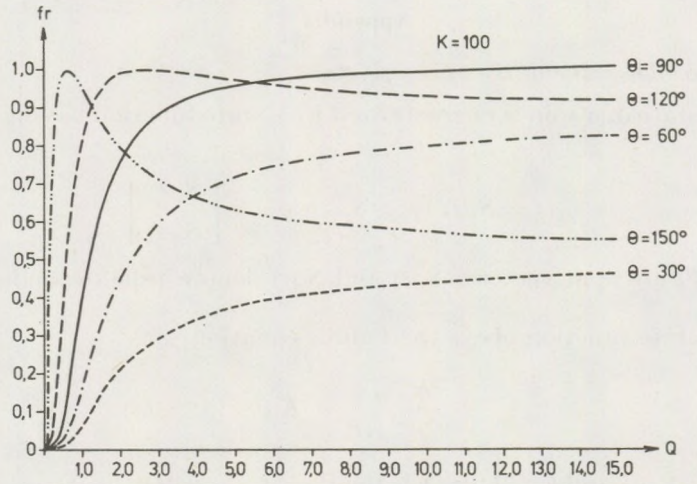

Fig. 3.

$$\lim_{K \to \infty} fr(\pi/2, K, q) = \frac{1}{\cosh \dfrac{\pi}{2q}} \tag{7}$$

For the dependence of the phase lag fp on the variation of the different parameters, Fig. 4. shows an example. Here, fp (in degrees) is plotted against the relative polarizing field intensity K for a few values of q at the angle of $\Theta = 90°$. As can be seen, the phase shift fp is highly influenced by the intensity of the polarizing field and this influence increases as the f. r. process is shifted deeper into the polytropic region, with the decreasing q values.

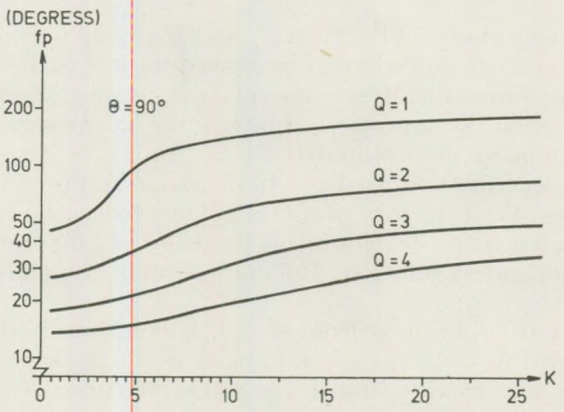

Fig. 4.

Appendix

Expectable value of the spin operator

The state of a spin is characterized by a state function having the form of

$$\psi(t) = S_1(t) \cdot \psi_1 + S_2(t) \cdot \psi_2 = \begin{bmatrix} S_1(t) \\ S_2(t) \end{bmatrix} \tag{A.1}$$

Ψ_1 and Ψ_2 are spin vectors; $S_1(t)$ and $S_2(t)$ denote time dependent scalar factors.

The state function obeys the Pauli's equation

$$\frac{\bar{h}}{j} \frac{\partial \psi}{\partial t} = \boldsymbol{K} \psi \tag{A.2}$$

where $j = \sqrt{-1}$ and $h = h/2\pi$; h is the Planck's constant.

$\boldsymbol{K}$ is an operator expressed as

$$\boldsymbol{K} \equiv \mu \overline{H} \sigma \equiv \mu\{H_x \sigma_x + H_y \sigma_y + H_z \sigma_z\} \tag{A.3}$$

In the operator's expression μ represents the nuclear magnetic moment; $\overline{H}(H_x, H_y, H_z)$ is the magnetic field acting upon the particle. The σ operators are the Pauli's matrices:

$$\sigma_x = \begin{bmatrix} 0 & 1 \\ 1 & 0 \end{bmatrix} \quad \sigma_y = \begin{bmatrix} 0 & -j \\ j & 0 \end{bmatrix} \quad \sigma_z = \begin{bmatrix} 1 & 0 \\ 0 & -1 \end{bmatrix} \tag{A.4}$$

Spins in a spin system, in thermal equilibrium, subject to a magnetic field are in eigen states. Their directions align partly parallel and partly antiparallel to the direction of the ambient field. The state of spins paral-

lel to the field is characterized by the quantum number $m = +1/2$, while $m = -1/2$ refers to their antiparallel position. These states change during the decay of polarizing field and may be described by one state function for each, denoted as $\varphi_+(t)$ and $\varphi_-(t)$, respectively. The signs in the subscript refer to the spin direction at $t = 0$. For the general form of these state functions we have

$$\varphi_+(t) = S_{1+}(t) \cdot \psi_1 + S_{2+}(t) \cdot \psi_2 \tag{A.5}$$

$$\varphi_-(t) = S_{1-}(t) \cdot \psi_1 + S_{2-}(t) \cdot \psi_2 \tag{A.6}$$

In order to take the initial conditions into account first we deduce from ψ_1 and ψ_2 two vectors with eigen values $m = +1/2$ and $m = -1/2$, respectively.

If we assume that in a direction given by the unit vector $\bar{e}$ the quantum number is $+1/2$, then, apart from a factor, the necessary coefficients for ψ_1 and ψ_2 may be obtained from equation

$$\bar{e} \cdot \sigma \cdot \psi_+ = a \cdot \psi_1 + b \cdot \psi_2 \tag{A.7}$$

Hence

$$\frac{a}{b} = \frac{e_x - je_z}{1 - e_z}, \quad \text{or} \quad \frac{a}{b} = \frac{1 + e_z}{e_x + je_y} \tag{A.8}$$

Choosing the last equation we get

$$\psi_+ \alpha (1 + e_z) \cdot \psi_1 + (e_x + je_y) \cdot \psi_2 \tag{A.9}$$

This equation must be normalized by requiring that

$$|1 + e_z|^2 + |e_x + je_y|^2 = 1 \tag{A.10}$$

At the same time for the components of the unit vector $\bar{e}$

$$e_x^2 + e_y^2 + e_z^2 = 1 \tag{A.11}$$

holds.

According to Eqs. (A.10) and (A.11), Eq. (A.9) can be written as

$$\psi_+ = \frac{1}{\sqrt{2}\sqrt{1 + e_z}} \cdot \{(1 + e_z) \cdot \psi_1 + (e_x + je_y) \cdot \psi_2\} \tag{A.12}$$

The vector belonging to $m = -1/2$ can be derived from Eq. (A.7) in the same way if the direction of the unit vector $\bar{e}$ is reversed. Whence

$$\psi_- = \frac{1}{\sqrt{2}\sqrt{1 + e_z}} \cdot \{(e_x + je_y) \cdot \psi_1 + (1 + e_z) \cdot \psi_2\} \tag{A.13}$$

In the present treatment the polarizing field is supposed to be normal to the earth's magnetic field. The Cartesian coordinates are directed in such a manner that the z axis coincides with the direction of the earth's

magnetic field vector, $\overline{F}$, and the y axis with that of the polarizing field vector, $\overline{H}_p$. The magnitude of the polarizing field is assumed to be time-dependent in the form of

$$H_p(t) = \begin{cases} H_p = \text{const. if } -\infty \geq t \geq 0 \\ H_p(t) \qquad \text{if} \qquad 0 < t \leq \infty \end{cases} \tag{A.14}$$

Hence, at $t = 0$

$$e_x = 0, \; e_y = \frac{H_p}{\sqrt{F^2 + H_p^2}}, \; e_z = \frac{F}{\sqrt{F^2 + H_p^2}} \tag{A.15}$$

Considering these components of the unit vector $\bar{e}$ and by introducing the new notations as follows

$$\frac{H_p}{F} = K \tag{A.16}$$

$$\frac{1 + \sqrt{1 + K^2}}{\sqrt{2}\sqrt{1 + K^2}\sqrt{1 + K^2}} = c_1(K) \tag{A.17}$$

$$\frac{jK}{\sqrt{2}\sqrt{1 + K^2}\sqrt{1 + K^2}} = c_2(K) \tag{A.18}$$

Eqs. (A.12) and (A.13) may be written in simpler forms as

$$\psi_+ = c_1(K) \cdot \psi_1 + c_2(K) \cdot \psi_2 \tag{A.19}$$

$$\psi_- = c_2(K) \cdot \psi_1 + c_1(K) \cdot \psi_2 \tag{A.20}$$

As initial conditions for Eqs. (A.5) and (A.6) we require the identities of

$$\varphi_+(0) = \psi_+ \tag{A.21}$$

$$\varphi_-(0) = \psi_- \tag{A.22}$$

Hence

$$S_{1+}(0) = c_1(K), \qquad S_{2+}(0) = c_2(K) \tag{A.23}$$

and

$$S_{1-}(0) = c_2(K) \qquad S_{2-}(0) = c_1(K). \tag{A.24}$$

From the proper state functions $\varphi_+(t)$ and $\varphi_-(t)$, the corresponding expectable values of spin operators can be deduced. The expectable values belonging to the operator σ_x are

$$\big((\varphi_+(t), \sigma_x \cdot \varphi_+(t)\big) = S_{1+}^* S_{2+} + S_{2+}^* S_{1+} \tag{A.25}$$

and

$$\big(\varphi_-(t), \sigma_x \cdot \varphi_-(t)\big) = S_1^* S_{2-} + S_{2-}^* S_{1-} \tag{A.26}$$

where, on the right side, we disregarded the indication of the variable t, and the asterisks denote complex conjugates. In a similar manner, the expectable values of the operator σ_y are

$$(\varphi_+, \sigma_y \cdot \varphi_+) = -j S_{1+}^* S_{2+} + j S_{2+}^* S_{1+} \tag{A.27}$$

$$(\varphi_-, \sigma_y \cdot \varphi_-) = -j S_{1-}^* S_{2-} + j S_{2-}^* S_{1-} \tag{A.28}$$

In the present consideration the expectable values of the operator σ_z have no significance.

Magnitude of the polarization component perpendicular to the earth's field after the f. r. process

The discussion will be confined to the case when the intensity of the earth's field is negligible as compared with that of the polarizing field. Then, according to Boltzmann's statistics, the longitudinal polarization existing at $t = 0$ is espressible as

$$\overline{M}_1 = \chi \cdot \mu_0 \cdot \overline{H}_p = \overline{\mu}(N_+ - N_-) \tag{A.29}$$

where χ denotes the relative nuclear magnetic susceptibility of the proton sample. N_+ and N_- are numbers of spins per unit volume, directed parallel and antiparallel, respectively, to the magnetic field. μ_0 is the magnetic permittivity of vacuum. Considering the number densities and using Eqs. (A.25) to (A.28), the magnitude of the polarization component perpendicular to the earth's field is

$$M_{tr} = \mu \cdot \sqrt{[N_+(\varphi_+, \sigma_x \varphi_+) + N_-(\varphi_-, \sigma_x \varphi_-)]^2 + [N_+(\varphi_+, \sigma_y \varphi_+) + N_-(\varphi_-, \sigma_y \varphi_-)]^2} =$$

$$= 2\mu \cdot$$

$$\cdot \sqrt{N_+^2 S_{1+}^* S_{2+} S_{2+}^* S_{1+} + N_+ N_- (S_{1+}^* S_{2+} S_{2-}^* S_{1-} + S_{2+}^* S_{1+} S_{1-}^* S_{2-}) + N_-^2 S_{1-}^* S_{2-} S_{2-}^* S_{1-}} \tag{A.30}$$

In order that M_{tr} may be determined the S functions should be known, which, in turn, depend on how the polarizing field decays. The magnitude of the transverse polarization $\overline{M}_{tr}$ must be known only for the case when the polarizing field has already decreased to zero.

The case of exponentially decreasing polarizing field

If the polarizing field decreases exponentially

$$H_p(t) = \begin{cases} H_p = \text{const.} & \text{if } -\infty \leq t \leq 0 \\ H_p \exp(-\alpha \cdot t) & \text{if } 0 \leq t \leq \infty. \end{cases} \tag{A.31}$$

Hence, for Eq. (A.2) we obtain

$$\frac{dS_1}{dt} = \frac{\mu}{\hbar}(H_p e^{-\alpha \cdot t} S_2 + j F S_1) \tag{A.32}$$

$$\frac{dS_2}{dt} = \frac{\mu}{\hbar}(H_p e^{-\alpha \cdot t} S_1 + j F S_2) \tag{A.33}$$

Introduction of the new independent variable $\xi = \exp(-\alpha \cdot t)$ and elimination of S_1 result in a second order differential equation

$$\xi \cdot \frac{d^2 S_2}{d\xi^2} + S_2 \left(\xi^2 \frac{K^2}{p^2} + \frac{1}{p^2} + \frac{j}{p} \right) = \tag{A.34}$$

where $\omega_0/2 = \mu F/\hbar$ and $p = 2\alpha/\omega_0 = 2q$. Eq. (A.34) is a Bessel's equation whose general solution may be obtained in the form of

$$S_2(\xi) = \xi^{1/2} \cdot Z_\nu \left(\frac{K}{p} \cdot \xi \right). \tag{A.35}$$

Z_ν corresponds to a linear conbination of Bessel's functions of first kind such as $J_\nu\left(\frac{K}{p}\right)$ and $J_{-\nu}\left(\frac{K}{p}\right)$, where $\nu = \pm(1/2 - j/p)$.

After returning to the variable t and taking Eq. (A.33) into account we obtain

$$S_1(t) = e^{\alpha t/2} \cdot A \cdot \left[J_\nu \left(\frac{K}{p} e^{-\alpha t} \right) \frac{2\nu p}{K} - e^{-\alpha t} \cdot J_{\nu+1} \left(\frac{K}{p} e^{-\alpha t} \right) \right] -$$

$$- B \cdot e^{-\alpha t} \cdot J_{-\nu+1} \left(\frac{K}{p} e^{-\alpha t} \right) \tag{A.36}$$

$$S_2(t) = e^{-\alpha t/2} \cdot A \cdot \left[J_\nu \left(\frac{K}{p} e^{-\alpha t} \right) + B \cdot J_{-\nu} \left(\frac{K}{p} e^{-\alpha t} \right) \right] \tag{A.37}$$

In Eq. (A.36) also the relations of

$$\frac{d}{dt} J_\nu \big(f(t)\big) = \frac{1}{2} \cdot [J_{\nu-1} - J_{\nu-1}] \frac{df}{dt} \tag{A.38}$$

and of

$$2 \frac{J_\nu(x)}{x} = J_{\nu-1}(x) + J_{\nu+1}(x) \tag{A.39}$$

have been considered.

From the general solutions we must choose those of satisfying the initial conditions given in Eqs. (A.23) and (A.24), which, in accordance with Eqs. (A.5) and (A.6) means assigning the particular state functions. The necessary coefficients corresponding to Eqs. (A.23) can be determinded by solving the equation system as follows

$$c_1(K) = S_1(0) = A \cdot \left[\frac{2p}{K} J_\nu \left(\frac{K}{p} \right) - J_{\nu+1} \left(\frac{K}{p} \right) \right] - B \cdot J_{-\nu+1} \left(\frac{K}{p} \right) \tag{A.40}$$

$$c_2(K) = S_2(0) = A \cdot J_\nu \left(\frac{K}{p} \right) + B \cdot J_{-\nu} \left(\frac{K}{p} \right) \tag{A.41}$$

Hence, after using the transformation given in Eq. (A.39),

$$A_+ = \frac{c_1 J_{-\nu} + c_2 J_{-\nu+1}}{J_{\nu-1} \cdot J_{-\nu} + J_{-\nu+1} \cdot J_\nu} \tag{A.42}$$

$$B_+ = \frac{c_1 J_{\nu-1} + c_2 J_\nu}{J_{\nu-1} \cdot J_{-\nu} + J_{-\nu+1} \cdot J_\nu} \tag{A.43}$$

The coefficients A_- and B_- belonging to Eq. (A.24) are to be deduced in a similar way.

The present derivation utilizes only the asymptotical expressions of the particular solutions. From the expansion of the corresponding Bessel's functions we have

$$S_1(\infty) = \frac{2p}{K} \frac{e^{(j/2)\omega_0 t}}{\Gamma(\nu)} \cdot \left(\frac{K}{2p}\right)^\nu \cdot A\left(\frac{K}{p}\right) \tag{A.44}$$

$$S_2(\infty) = \frac{e^{-(j/2)\omega_0 t}}{\Gamma(\nu-1)} \cdot \left(\frac{K}{2p}\right)^{-\nu} \cdot B\left(\frac{K}{p}\right) \tag{A.45}$$

Substituting A and B by A_+ and B_+ in Eq. (A.44) and (A.45), respectively, we obtain the particular asymptotical solutions $S_{1+}(\infty)$ and $S_{2+}(\infty)$. The other pair of the asymptotical solutions, that is $S_{1-}(\infty)$ and $S_{2-}(\infty)$, can be similarly composed of A_- and B_-.

The expressions of A_+ and B_+ and also those of A_- and B_- can be evaluated only if we introduce certain simplifying assumptions:

1. We consider only the region of $K/p \gg 1$. In this case, the Bessel's functions in Eqs. (A.40) and (A.41) may be approximated by expressions of the following kind

$$J_\nu = \sqrt{\frac{2p}{\pi K}} \cdot \sqrt{\frac{1}{1 - \frac{\nu^2 \cdot p^2}{K^2}}} \cdot \cos\left\{\frac{K}{p} \cdot \sqrt{1 - \frac{\nu^2 p^2}{K^2}} - \right.$$

$$\left. - \arccos\frac{\nu \cdot p}{K} - \frac{\pi}{4}\right\} \tag{A.46}$$

which can be derived on the basis of the steepest descent method.

2. In addition to the above restriction, we also assume that $K \gg 1$. According to Eqs. (A.17) and (A.18), this requirement is equivalent to selecting the values of $c_1 = 1/\sqrt{2}$ and $c_2 = j/\sqrt{2}$, respectively.

With respect to the relation

$$\frac{1}{\Gamma(z) \cdot \Gamma(1-z)} = \frac{\sin \pi z}{\pi}, \tag{A.47}$$

after evaluating Eq. (A.30) we have the final result as follows

$$\frac{M_{tr}}{M_l} = \frac{1}{\cos h \dfrac{\pi}{p}} = \frac{1}{\cosh \dfrac{\pi}{2q}} \tag{A.48}$$

where Eq. (A.29) has also been taken into account.

REFERENCES

[1] Praxmayer, T. (1966): On the amplitude of the nuclear magnetic logging signal Acta Geophys. Polonica, 14. p. 301.

[2] Аксельрод, С. М., Даневич, В. И., Запорожец, В. М., Евдокимов, А. Ф., Мелик-Шахназаров, А. М., Неретин, В. Д., Орлов, Г. Л. (1976): Ядерные магнитные исследования скважин, Недра, Москва, 127 стр.

[3] Bullard, E. C., Mason, C. S., Mudie, J. D. (1964): Curious behaviours of a proton magnetometer, Proc. Camb. Phil. Soc., 60. p. 287.

[4] Brown, R. J. S., Gamson, B. W. (1960): Nuclear magnetism logging, Petroleum Transactions 219. p. 201.

[5] Аксельрод, С. М., Даневич, В. И. (1967): К расчету сигнала, индуктируемого в датчике аппаратуры ядерно-магнитного каротажм, Изв. вузов. Сер. Нефть и газ, Но. 2, 107–110.

[6] Даневич, В. И. (1963): К теории ядерно-магнитного каротажа, Изв. вузов. Сер. Нефть и газ, Но. 12, 97–102.

[7] Даневич, В. И., Керимов, З. Г (1969): К методике расчета датчиков ядерномагнитного каротажа, Изв. вузов. Сер. Нефть и газ, Но. 8, 93–97.

[8] Robinson, J. D., Loren, J. D., Vajnar, E. A., Hartman, D. E. (1974): Determining residual oil with the nuclear magnetism log, Journ. of Petr. Techn., p. 226.

[9] Brown, R. J. S., Neuman, C. H. (1980): Processing and display of nuclear magnetism logging signals, SPWLA 21-th annual logging symposium.

[10] Schipp, F.: Personal information.

CONTENTS – INHALT

A kiadásért felelős az Eötvös Loránd Tudományegyetem rektora — A kézirat nyomdába érkezett:
1981. július — Megjelent: 1982. június — Terjedelem: 19,6 (A/5) ív+1 melléklet —
Példányszám: 650 — Készült monószedéssel, íves magasnyomással,
az MSZ 5601—59 és az MSZ 5602—55 szabvány szerint
81.631. Állami Nyomda, Budapest
Felelős vezető: Mihalek Sándor igazgató